UNIVERSITY OF CALIFORNIA, SAN DIEGO

Modeling and Characterization of Strongly Coupled Silicon-on-insulator Nanophotonic Devices

A dissertation submitted in partial satisfaction of the
requirements for the degree
Doctor of Philosophy

in

Electrical Engineering (Photonics)

by

Michael Lawrence Cooper

Committee in charge:

Professor Shayan Mookherjea, Chair
Professor Prabhakar R. Bandaru
Professor Dimitri N. Basov
Professor Joseph E. Ford
Professor Vitaliy Lomakin

2010

The dissertation of Michael Lawrence Cooper is approved, and it is acceptable in quality and form for publication on microfilm and electronically:

_____

_____

_____

_____

_____

Chair

University of California, San Diego

2010

DEDICATION

To my love, Amy Chia-Yun Chen

EPIGRAPH

We see the world clearly when were children,
and we spend the rest of our lives,
trying to remember what it was we saw.
—Garrison Keillor

TABLE OF CONTENTS

LIST OF FIGURES

LIST OF TABLES

ACKNOWLEDGEMENTS

I started at University of California, San Diego a little over four years ago as a Masters of Engineering student, and will soon graduate with a Ph.D. in electrical engineering (photonics) having worked and published with one of the top research groups in the world, in some of the top journals. By any account, this experience far exceeded all expectations that I had when entering the University. And none of this would have happened without the tremendous time, effort, and chance, afforded to me on behalf of my advisor, Shayan Mookherjea. Throughout my years here I received excellent personal and professional advice that I will always carry with me. For all of this, I am truly incredibly grateful.

I also owe a tremendous debt to William M. J. Green at the IBM Thomas J. Watson research center. Throughout my Ph.D. studies, whether researching coupled mode theory, dispersion engineering, or coupled resonator optical waveguides, his communications to me were always incredibly detailed, insuring that I fully understood various aspects of the projects. These e-mails were of no doubt time consuming, and of no personal benefit to him. I cannot express how grateful I am for all of the opportunities he provided me, and the research group I am a part of. I am also very appreciative of the research efforts by many of the other IBM members in which I directly benefited from, specifically, Solomon Assefa, Fengnian Xia, and Yurii Vlasov. I am further grateful for advice that I received from Dawn K. Gifford at Luna Technologies in performing high accuracy time delay statistics.

I am truly thankful to the other members of my committee: It was wonderful to work with Professor Prabhakar Bandaru on my first project on slot-waveguides. I will never forget the incredible sense of humor that was shared at those group meetings. Professor Vitaliy Lomakin, I have never seen another professor who exposed such a high degree of passion for electromagnetism in his lectures, the effects of which were contagious to his students. I am grateful to the council provided to me on two of my projects by Professor Joseph E. Ford, and the conversations and encouragement given by Dimitri N. Basov.

I am grateful for the early years of my Ph.D. where I shared a lab space with Jung Soo Park. There are numerous memories that I carry quite fondly, and am incred-

ibly grateful for all of the conversations we had together, and advice he provided. We were the first students in this group, and our competitive natures undoubtedly improved both of us in every aspect (except, perhaps, our foosball game). I cannot express the gratitude I feel for Greeshma Gupta, whom joined the lab in my final year. She provided tremendous council and structure in every way, and I am truly looking forward to when she completes her mission. I am grateful to Mark Schneider for his advice and feedback throughout the years on basically every project I was a part of (including, among many things, the ability to solve the modes of a slab waveguide in a single line of code). I enjoyed the time spent with Marco Antonio Escobar Acevedo, who taught me many things, among them LaTeX in which this dissertation was composed. I am also grateful for the support through the years provided by several other group members and friends, including but not limited to, Yiran Shen, Junrong Ong, Ben Ellis, Shun-Hui Yang, Jonmei "Johanna" Yan, Bill Norton, Matthew Chen, Dawn Tan, and Maurice Ayache.

This would not have been possible without the tremendous support of my family. Most especially my fiancé, Amy Chia-Yun Chen, who sat alongside me for hours at coffee shops while I worked on various projects. I cannot thank my parents enough for all of their persistent encouragement through the years, my step father, for his wonderful since of humor, and also my sister, whom has provided me tremendous council, shaping my life in a positive direction.

For all of this, I am grateful,
Michael L. Cooper

1. Chapter 2 contains material published in:

   M. L. Cooper, G. Gupta, M. A. Schneider, W. M. J. Green, S. Assefa, F. Xia, D. Gifford, and S. Mookherjea, "Waveguide dispersion effects in silicon-on-insulator coupled-resonator optical waveguides," *Optics Letters*, 35, 2010.

   The dissertation author was the primary author of this paper.

2. Chapter 2 contains material that was submitted to *Optics Express*:

   M. L. Cooper, G. Gupta, M. A. Schneider, W. M. J. Green, S. Assefa, F. Xia, D. Gifford, Yurii A. Vlasov, and S. Mookherjea, "Statistics of light transport in 235-ring silicon coupled-resonator optical waveguides," submitted to *Optics Express*.

   The dissertation author was the primary author of this paper.

3. Chapter 3 contains material published in:

   S. H. Yang, M. L. Cooper, P. R. Bandaru and S. Mookherjea, "Giant birefringence in multi-slotted silicon nanophotonic waveguides," *Optics Express*, 16, 2008.

   The dissertation author is the secondary author of this paper.

4. Chapter 5 contains material published in:

   Michael L. Cooper and Shayan Mookherjea, "Numerically-assisted coupled-mode theory for silicon waveguide couplers and arrayed waveguides," 17, pp. 1583-1599 (2009).

   The dissertation author was the primary author of this paper.

5. Chapter 5, in part, has been submitted for publication Journal of Lightwave Technology, 2010, M. L. Cooper and Shayan Mookherjea.

   The dissertation author was the primary author of this paper.

6. Chapter 6 contains material published in:

   M. L. Cooper, G. Gupta, J. S. Park, M. A. Schneider, I. B. Divliansky, and S. Mookherjea, "Quantitative infrared imaging of SOI microring resonators," *Optics Letters*, 35, 2010.

   The dissertation author was the primary author of this paper.

7. Chapter 6 contains material submitted to *Photonics Technology Letters*:

   M. L. Cooper, Mark A. Schneider, Greeshma Gupta, and Shayan Mookherjea, "Filter-less amplification for rapid swept-wavelength interferometric measurement of silicon nanophotonic waveguide group delay statistics," submitted to *Photonics Technology Letters*.

   The dissertation author was the primary author of this paper.

VITA AND PUBLICATIONS

2004	B. S. in Physics with Minor in Mathematics *magna cum laude*, Arizona State University
2006-2008	M. S. in Electrical Engineering (Photonics), University of California, San Diego
2010	Ph. D. in Electrical Engineering (Photonics), University of California, San Diego

M. L. Cooper, G. Gupta, M. A. Schneider, W. M. J. Green, S. Assefa, F. Xia, Yurii A. Vlasov, and S. Mookherjea, "Statistics of light transport in 235-ring silicon coupled-resonator optical waveguides," submitted to *Optics Express*.

M. L. Cooper and S. Mookherjea,"Multi-band slow light in coupled-resonator waveguides: modeling and comparison with experiment," submitted to *Applied Physics Letters*.

M. L. Cooper and S. Mookherjea, "Modal perturbations due to high confinement and strong coupling in silicon-on-insulator arrayed waveguides," submitted to *Journal of Lightwave Technology*.

M. L. Cooper, Mark A. Schneider, Greeshma Gupta, and Shayan Mookherjea, "Filterless amplification for rapid swept-wavelength interferometric measurement of silicon nanophotonic waveguide group delay statistics," submitted to *Photonics Technology Letters*.

M. L. Cooper, G. Gupta, M. A. Schneider, W. M. J. Green, S. Assefa, F. Xia, D. Gifford, and S. Mookherjea, "Waveguide dispersion effects in silicon-on-insulator coupled-resonator optical waveguides," *Optics Letters*, 35, 2010.

M. L. Cooper, G. Gupta, J. S. Park, M. A. Schneider, I. B. Divliansky, and S. Mookherjea, "Quantitative infrared imaging of SOI microring resonators," *Optics Letters*, 35, 2010.

M. L. Cooper and S. Mookherjea, "Numerically-assisted coupled-mode theory for silicon waveguide couplers and arrayed waveguides," *Optics Express*, 17, 2009.

S. H. Yang, M. L. Cooper, P. R. Bandaru and S. Mookherjea, "Giant birefringence in multi-slotted silicon nanophotonic waveguides," *Optics Express*, 16, 2008.

M. L. Cooper, G. Gupta, W. M. J. Green, S. Assefa, F. Xia, Y, A. Vlasov, and S. Mookherjea, "235-Ring coupled-resonator optical waveguides," *CLEO 2010 Proceedings of the Conference on Lasers and Electro-Optics*, CTuHH3, 2010.

M. L. Cooper, G. Gupta, J. S. Park, M. A. Schneider, I. B. Divliansky, and S. Mookherjea, "Characterization of SOI Microrings Using IR Imaging," *CLEO 2010 Proceedings of the Conference on Lasers and Electro-Optics*, CThAA1, 2010.

M. L. Cooper and S. Mookherjea, "Field perturbations due to strong coupling and modal confinement in SOI arrayed waveguides," *CLEO 2010 Proceedings of the Conference on Lasers and Electro-Optics*, JThE70, 2010.

G. Gupta, M. L. Cooper, J. S. Park, M. A. Schneider, W. H. Steier and S. Mookherjea, "Tuning of microring resonators," *SPIE Photonics West Conference*, 7612, 2010.

J. S. Park, S. Zlatanovic, M. L. Cooper, J. M. Chavez-Boggio, I. B. Divliansky, N. Alic, S. Mookherjea, S. Radic, "Two-pump four-wave mixing in silicon waveguides," *FiO 2009 OSA Annual Meeting, Frontiers in Optics*, FML2, 2009.

M. L. Cooper and S. Mookherjea, "When and how coupled-mode theory fails in high-index contrast arrayed and multi-slot waveguides," *CLEO 2009 Proceedings of the Conference on Lasers and Electro-Optics*, JThE94, 2009.

S. H. Yang, M. L. Cooper, P. R. Bandaru, and S. Mookherjea, "Tuning giant birefringence in multi-slot silicon optical waveguides," *CLEO 2009 Proceedings of the Conference on Lasers and Electro-Optics*, CThU3, 2009.

S. Mookherjea, M. L. Cooper, J. S. Park, S.-H. Yang, P. R. Bandaru, "Design, fabrication, and measurement of giant birefringence at telecommunications wavelengths in multi-slotted silicon nanophotonic optical waveguides," *XXIX URSI General Assembly*, 2008.

S.H. Yang, P. R. Bandaru, M. L. Cooper, J. S. Park, S. Mookherjea, "Multi-slot silicon optical waveguides," *CLEO 2008 Proceedings of the Conference on Lasers and Electro-Optics*, CThT1, 2008.

ABSTRACT OF THE DISSERTATION

Modeling and Characterization of Strongly Coupled Silicon-on-insulator Nanophotonic Devices

by

Michael Lawrence Cooper

Doctor of Philosophy in Electrical Engineering (Photonics)

University of California, San Diego, 2010

Professor Shayan Mookherjea, Chair

Silicon photonics is technologically attractive because of the possibility of monolithically integrating multi-element photonic waveguide circuits with complex electronic circuits. To reduce the footprint of the photonic components, it is possible to fabricate strongly-coupled waveguides and resonators, e.g., with sub-100 nm separation gaps. The most insightful design tool used for photonic devices, coupled mode theory (CMT), is considered suspect for high-index contrast strongly coupled waveguides. Using a numerically assisted coupled mode theory (NA-CMT) developed for arrayed waveguides, it was shown how one may modify the basis parameters within CMT to calculate more accurate modal profiles and more accurate estimates of the value and the wavelength dependency (i.e., dispersion) of coupling coefficients. Traditional CMT inaccurately

predicts both the field peak locations and the exponential decay rates of the field envelopes in the cladding regions.

Examples of strongly-coupled silicon photonic devices based on waveguides and couplers include giant birefringence multi-slot waveguides, and large-bandwidth coupled-resonator optical waveguides (CROWS) consisting of several hundred coupled silicon microring resonators. Numerical techniques will be reported for accurately simulating the transmission properties of strongly coupled arrayed waveguides and disordered CROWs in excellent agreement with experimental measurements on fabricated devices.

Experimental methods were developed for the accurate measurement of transmitted intensity and group delay of silicon nanophotonic waveguides and multi-resonator circuits including CROWs and side-coupled integrated spaced sequence of resonators (SCISSORS). The role of external amplification in reliably measuring waveguide transmission using the method of swept wavelength interferometry was studied in detail. Also, a technique of swept-wavelength infrared imaging was developed and applied for quantitative diagnostics of multi-resonator circuits which need not have accessible drop ports on every device.

1 Silicon Photonics

I believe there will be a world market for approximately five computers.
–Thomas Watson, President of IBM, 1943

Within the coming decade, the circuitry embodied by a rack of today's network servers will in theory fit onto a single silicon chip half the size of a postage stamp.
–Michal Lipson, Nature Photonics, 2007

1.1 Introduction to Silicon Photonics

Photonics is suitable for energy-efficient interconnects in large-scale computer systems, including future multi-processor chips. The past decade has seen considerable progress with regard to demonstrating most of the active and passive components necessary for a fully integrated silicon-on-insulator photonic network on a chip [1]. Such a network would require access to a suitable light source, an on-chip electrically driven modulator for encoding an electrical data stream onto optical packets of energy, a network of passive and active devices responsible for switching, buffering, routing and possibly regenerating photonic signals, and finally efficient and large gain-bandwidth product on-chip detectors to detect and convert the optical energy back into electrical data.

Research in silicon photonics is motivated by the fundamental limitations and performance costs imposed by the current method of using copper interconnects to transport information [2, 3, 4]. In modern computing, interconnects consume 80% of a microprocessor's power [5], and while both optical and electrical interconnects transport information on electromagnetic waves (using photons), electrical interconnections on

chips are currently limited in providing adequate speed and performance—determined by the resistance, inductance, and capacitance of the line [6, 7]. The bit rate for sending information in electrical transmission lines is thus being fundamentally limited by material constants, imposing a prohibitive scaling relationship determined by the aspect ratio and length of the wire, $B \approx B_0 A/l^2$, where $B_o \approx 10^{15}$, l corresponds to the length of the wire, and A the area [8]. As such, optical interconnects—which do not have an equivalent aspect ratio scaling—are poised to first replace longer interconnects for transporting larger bandwidths [5].

This isn't the first time in which an alternative interconnect has been needed to meet the demands of increased computing speeds. From the 1960s to the 1990s aluminum was considered the conductor of choice, even though it was well understood that copper provided lower resistance, higher current density, and increased scalability. It wasn't until the 1990s that many of the fabrication hurdles preventing copper from being used on a CMOS line were overcome [9, 10, 11]. And while research in ways to improve the transmission characteristics of copper interconnects is still very much an active field [12], researchers are again running into fundamental limitations as copper interconnects reach their maximum potential, again requiring the development of new methods of transporting data.

The use of high-index contrast silicon-on-insulator optical waveguides is particularly appealing in this role, as undoped silicon has very low intrinsic material losses at telecommunication wavelengths (0.004 dB/cm), and a silicon waveguide interconnect would have higher bandwidth, smaller interconnect delays, and better resistance to electromagnetic interference, than a copper interconnect. Also, the large index contrast between the core and the cladding allows for increased device density, strong confinement, and sharp bending radii, compared to other types of waveguides, e.g., doped glass, or polymeric waveguides. But perhaps the most appealing aspect of the silicon-on-insulator photonics platform is its compatibility with the CMOS process used for fabricating electrical devices, allowing optics and electronics to be realized on the same chip [13].

This dissertation focuses on novel forms of strongly coupled waveguides, however, operation of optical interconnects with these added benefits requires several other

mandatory additional optical components which will be breifly reviewed. Foremost, in order to transport optical signals from one location on a chip to another, they must first be generated via a coherent optical light source.

1.1.1 The Silicon Laser

By far the most illusive optical device to realize in silicon has been the laser [14]. The reason being that, unlike direct-bandgap semiconductors such as GaAs and InP where radiative recombination can occur as a two particle process, silicon's indirect bandgap only allows for emission to occur as a result of a three-particle process, requiring a third particle—usually a vibrational wave of the silicon's crystal lattice—to balance the conservation of momentum requirement. As such, only about one in a million excited electrons in bulk silicon will release a photon, compared with GaAs (used in DVD players), where the efficiency is approximately 10,000 times larger due to its direct-bandgap and steep upper bands [15]. While aggressive efforts have been made to demonstrate lasing in erbium-doped silicon and also silicon nanocrystals—where quantum confinement is used to relax momentum conversation requirements—the first demonstration showing lasing in silicon utilized the Raman effect, which is 10^4 times larger in silicon compared with optical fibers [16, 17, 18]. The Raman effect involves adding energy to the vibrational modes of the silicon lattice via an optical pump—which allows a weak beam at a frequency resonant with the Stokes transition, propagating through the silicon, to then become amplified.

In 2004, the first silicon Raman laser emitted light at 1675 nm with a 30 ps pulse width, a 25 MHz repetition rate, using a 9 W pump at 1540 nm [18]. The silicon laser consisted of a 2 cm long rib waveguide, where feedback was provided by an optical fiber. While the pump and lasing wavelength was insufficient to excite electrons into the conduction band—the bandgap of silicon is 1.1 eV—a few electrons do become excited from a process called two-photon absorption (TPA). TPA is a common source of loss in nonlinear silicon photonics and involves the combination of energies from two photons to excite electrons into the conduction band. Once excited, these electrons contribute to another deleterious effect common to silicon: free carrier absorption (FCA). FCA is a non-radiative process in which electrons in the conduction band may simply absorb

photons by being excited to a higher energy level within the conduction band [19, 20]. Avoiding this additional FCA loss term was the motivation behind using such a low repetition rate—requiring that the pulse period be larger then the recombination time—and a pulse width shorter then the carrier life time, so as to render FCA effects irrelevant. However, such a technique merely avoids the problem, which had to be adequately addressed for continuous wave operation.

In 2005 Intel demonstrated the first continuous wave Raman laser operating at 1686 nm and pumped at 1550 nm [21]. The laser cavity was formed by a 4.8 cm long waveguide, with a broadband back reflector with a reflection coefficient of 90%. The front reflector was a dielectric layered stack that provided 71% reflectivity for the lasing wavelength and 24% for the pump. In order to overcome losses associated with TPA induced FCA, a p-i-n diode was formed by implanting boron and phosphorous atoms on opposite sides of the silicon ridge waveguide, separated by 6 μm. Then, when a voltage is applied to aluminum contacts residing above these doped regions, an electric field is generated between the p- and n-doped regions, sweeping out the electron-hole pairs in the silicon waveguide created by TPA and effectively reducing the carrier lifetime from approximately 10 ns to 1 ns. While it was shown that this number can be reduced further by proper device design [22], it is fundamentally limited by the speed in which electrons can move (one thousandths of the speed of light). The first continuous wave silicon Raman laser had a threshold of 280 mW of pump power when a 5 V bias was applied, and 180 mW with a 25 V bias.

Both the pulsed and continuous-wave silicon Raman lasers constituted a significant advancements in the field of silicon photonics; however, they suffered from not being directly applicable to modern silicon-on-insulator photonic circuits. This is because both lasers require an external coherent optical pump to be coupled into the silicon waveguide, which resides off the chip.

The huge demand for compact electrically pumped lasers on a SOI chip, compounded with the incredible obstacles imposed by the silicon material platform, has led many researches to avoid the “silicon problem” altogether [23]. Perhaps the most promising and advanced device functionality has been demonstrated using “hybrid silicon lasers,” which consist of wafer bonding compound semiconductors to silicon-on-

insulator substrates [14]. The compound semiconductors provide the necessary gain medium, while the optical mode is guided in the silicon waveguide. Both Fabry-Perot and micro-resonator based hybrid lasers have been demonstrated [24, 25]. Recently, indium phosphide hybrid lasers provided the optical source for the first demonstration of a 50 Gb/s integrated link, which consisted of four lasers modulated at 12.5 Gb/s, where the individual wavelengths were determined by etching lithographically defined grating periods into the silicon waveguides [26]. Each hybrid laser measures about 1 μm wide and 800 μm long. Once a coherent light source is generated, it must then be transformed into discrete packets of energy for transporting information.

1.1.2 The Silicon Modulator

Perhaps the biggest power penalty for switching from electrical to optical interconnects is the need to perform electrical to optical conversion at both the transmitter and receiver. In order to compete with electrical interconnects, power consumption should reach levels comparable to 1 pJ per bit [5].

The most common commercial modulators for telecommunications rely on either the Pockles effect or the Franz-Keldysh effect. For the former, an applied electric field on a material induces a change in the real part of its refractive index, and for the latter, an applied electric field changes the band-gap energy. For photons near the band-edge this leads to an increase in the absorption coefficient (the applied electric field, however, does not usually excite carriers). Modulators based on the Pockles effect are usually incorporated in a Mach-Zehnder configuration, in which a refractive index change from an applied voltage induces a phase shift in one arm or both arms (push pull), causing the electric field in one arm to become in phase or out of phase with respect to the other arm. As such, when the two waves recombine, they will continue in the waveguide if they are in phase, and form a radiation mode—leaving the waveguide—if they are out of phase. Another common technique for achieving intensity modulation using the real part of the refractive index is by changing the resonant wavelength or the coupling coefficient of micro-cavities, thus allowing a fixed frequency to be switched on and off resonance, varying the optical intensity at the through and drop port of the resonator [27].

At telecommunication wavelengths, both of these effects in silicon are very weak, and have led researchers to look for alternative methods of electrically manipulating a waveguide's effective index. Silicon does provide a large thermo-optic coefficient, dn/dT = 1.86$\times 10^{-4}$ /K at 300 K, which has proven useful for many advanced active silicon devices [28]; however, its modulation rate is too slow for the data speed requirements of modern interconnects. In 1987 Richard Soref and Brian Bennett evaluated the change in both the real and imaginary parts of the refractive index in crystalline-silicon for different carrier concentrations [29]. This eventually led to the realization of many different devices that electrically manipulate the free carrier concentration within a silicon optical waveguide, known as the plasma dispersion effect. This effect enabled some of the first silicon modulators capable of realizing speeds in the GHz regime.

In 2007, IBM demonstrated an ultra-compact silicon modulator occupying a length of only 200 μm, capable of operating at 10 Gb/s and consuming only 5 pJ/bit [30]. The device consisted of 550 x 220 nm silicon nanowires which composed a Mach-Zehnder, allowing for broadband spectral operation, where one arm was doped on both sides to form a p^+-i-n^+ diode allowing for carrier injection. Compared with significantly larger predecessors [31], operation was realized for such a small device length by utilizing the high optical confinement provided by silicon nanowires, allowing for strong overlap between the optical mode and the injected free carriers.

While the device footprint size may still be aggressively scaled down further using ring resonators, there is a significant price to pay in terms of operational bandwidth [32], as the Lorentzian response of a typical micro-resonator is on the order of only a few hundred pico meters. Whereas Mach-Zehnder configurations usually allow for operations encompassing approximately 20 nm. Further, the resonant wavelength of a micro-resonator is incredibly sensitive to temperature fluctuations, requiring thermal stabilization or a tunable laser source to compensate. While state of the art silicon modulators using the plasma dispersion effect operating at 40 Gb/s have been demonstrated, using a traveling wave design [33], the need for higher and higher communication speeds will continue to drive researchers to find new and creative methods of modulating optical sources.

Once information has been encoded onto an optical stream of pulses, advanced

functionality responsible for routing and manipulating optical signals will be required to deliver the signal to its desired location, where it then must be converted back into an electrical data stream.

1.1.3 Detecting light

Like the silicon laser and the silicon modulator, silicon imposes prohibitive constraints when it comes to optical detection at telecommunication wavelengths. The reason being, that silicon absorbs very few photons in this region, which is also what allows it to perform so proficiently as an optical waveguide. In order to realize optical detection on a SOI chip, necessary for any transmission link, researches had to once again look towards hybrid solutions.

There is currently a significant amount of interest in graphene as a candidate for the next generation of photodetectors, and the first optical link using graphene was recently demonstrated operating at 1550 nm with a responsivity of 6.1 mA/W [34]. Graphene consists of only a single layer of carbon atoms arranged in a honeycomb lattice, and is expected to allow optical detection at speeds as high as 500 GHz [35]. However, research in photodetectors for silicon optical interconnects is currently being dominated by germanium photodetectors [36].

While germanium is significantly easier to integrate with silicon, compared with many other common detectors, numerous obstacles had to be overcome in order to compensate for germanium's 4.2% lattice miss-match with silicon. Progress in this area has allowed the development of many high quality films and devices free of dislocation defects [37, 38, 39]. Recently, significant advances in germanium avalanche photodetectors were made at IBM [40]. Using a rapid melting growth technique, a 140 nm germanium layer was grown on top of a thin layer of SiON, which resides on 100 nm of silicon. As germanium is one of the few materials with a refractive index higher then silicon ($n \approx 4$), light is pulled up into the thin gemanium layer allowing for high modal overlap. This thin layer thus allows for operational speeds greater then 30 Ghz, at a low bias voltage of 1.5 V. For this device, light is coupled into the detector directly from the routing waveguide, and an avalanch gain of 10 dB was obtained.

This past decade has indeed seen tremendous progress in developing the nec-

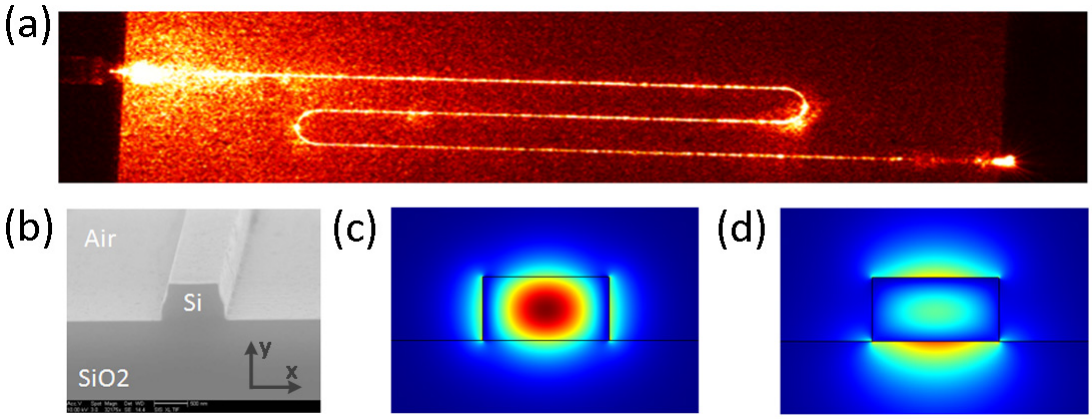

Figure 1.1: (a) Infrared image of light propagating through a silicon nanowire, coupled into the waveguide using lens-tipped fibers. (b) Scanning electron microscope image of the cross-section of a silicon nanowire, which consists of a silicon core (n = 3.47), a SiO_2 substrate (n = 1.46), and an air superstrate (n = 1). The height of the waveguide is 250 nm and the width 500 nm. (c) Finite element simulation of the transverse electric mode E_x, with an effective index of 2.49. (d) Finite element simulation of the transverse magnetic mode E_y, with an effective index of 1.83.

essary components for optical computing. The next section, and the majority of this dissertation, will be focused on novel forms of waveguides. Before embarking on a discussion of new strongly coupled waveguides, and deviations from previous theories, it is beneficial to first give a review of a few fundamental concepts.

1.2 Fundamentals of Optical Waveguiding

Once a coherent light source has been transformed into binary packets of energy, they must be guided and routed from one destination to another. The last sections laid out several prohibitive constraints imposed by the silicon material platform for active devices, however, guiding electromagnetic fields at telecommunication wavelengths is where silicon truly shines. The incredibly low material losses at telecommunication wavelengths, compounded with one of the highest index contrasts available, makes silicon an excellent material for guiding photonic signals, allowing for bending radiuses on the order of just a few microns [41].

Fig. 1.1(a) shows an infrared image of a 5.9 mm long silicon waveguide with a

500 x 250 nm cross-section, guiding light around two 180 degree bends with an 80 μm radius. Light is coupled into and out of the chip using lens-tipped fibers. A scanning electron microscope image of the cross-section of the silicon rib waveguide is shown in Fig. 1.1(b). For silicon nanowires, guiding light is achieved through total internal reflection.

In general form, optical waveguides and resonant structures are often characterized in the frequency domain, where the electromagnetic fields are described as sinusoidal functions of time at a single optical frequency ω, and that the structure is assumed invariant in the direction of propagation, z:

$$\vec{E} = \vec{E}(x,y)e^{i(\omega t - \beta z)}. \tag{1.1}$$

$\vec{E}(x,y)$ describes the confinement of the light for a given mode within the provided waveguide's refractive index profile. β is the propagation constant of the electromagnetic mode, defined as $\beta = \frac{2\pi n_{eff}}{\lambda}$, where λ is the free-space wavelength. The effective index, n_{eff}, represents the wavelength scaling of the propagating mode due to the waveguide, which is directly proportional to the mode's phase velocity, $v_p = c/n_{eff}$. To first order, one may think of the effective index as an average of the waveguide's refractive index profile, weighted by the concentration of light in each of the dielectric regions. For example, optical modes in which the light is mostly confined in the silicon waveguide will have a higher effective index, closer to that of silicon (n_{Si} = 3.47 at λ = 1550 nm), compared to a mode near cutoff, which will have an effective index close to that of oxide (n_{SiO_2} = 1.46). In general, for an optical mode to be guided it's effective index must reside in between that of the core and the cladding, $n_{SiO_2} < n_{eff} < n_{Si}$.

As will be detailed in Chapter 4, one obtains the dispersion relationship, $\beta(\omega)$, of an optical waveguide's mode by calculating the propagation constant as a function of the normalized frequency. For high-index contrast waveguides, calculation of an optical mode's electric field profile, $\vec{E}(x,y)$, and the corresponding propagation constants, β, is typically done by numerically solving the full or semi-vectorial wave equation (Helmholtz equation)—derived from Maxwell's equations (Section 4.1). Once the dispersion relationship is known, calculation of higher order terms such as the group delay–a measure of the transit time of a pulse, and the group velocity dispersion–a measure of

the tendency of a pulse to broaden, is straight forward (see Section 4.2).

Larger waveguides will support multiple higher order modes, however, a typical silicon nanowire will guide only a single quasi-transverse electric mode, and a single quasi-transverse magnetic mode (while the waveguide technically guides two modes, one for each polarization, it is typically referred to as a "single-mode waveguide"). Fig. 1.1(c) shows the quasi-TE mode, E_x, of the silicon nanowire with an effective index of 2.49; as can be seen, the light mostly resides within the silicon core. Fig. 1.1(d) shows the more weakly confined quasi-TM mode, E_y, with an effective index of 1.83. The dispersion properties of these modes strongly depend on the waveguide's aspect ratio [42, 43].

It is important note that when light goes around a bend, the mode shifts away from the radial center lowering its effective index [44]. This causes two deleterious effects to its propagation: firstly, it causes a mode mismatch between the plane joining the bending and straight waveguide regions, which results in optical losses. Methods of offsetting the straight regions and the bent regions to achieve higher modal overlap have shown reduced losses in lower index contrast structures, but require nanometer scale precision for SOI [45]. Secondly, as the mode peak has shifted towards the dielectric boundary, the mode will undergo higher scattering losses [46], and may be completely radiated if the effective index drops below the refractive index of the surrounding medium. In fact, it is quite common to use thinner silicon waveguides (height = 200 nm), to completely strip off the quasi-TM polarization as it propagates around a few bends [47].

1.3 Outline of the Dissertation

This dissertation is concerned with novel strongly coupled silicon-on-insulator waveguides that fall well outside the domain of coupled mode theory. The new functionality provided by these strongly coupled waveguides will be presented, along with the needed numerical mode solvers for accurate design. Chapter 2 and 3 present experimental results of strongly coupled arrayed waveguides and coupled resonator optical waveguides. It will be shown that for the former, numerous new device functionalities can be

realized, including a device with a giant birefringence of $n_g \approx 1.5$. For the latter, it will be demonstrated that Gaussian distributions of time delay statistics, indicating ballistic transport, can be obtained for CROWs consisting of as many as 235-rings. Chapter 4 is concerned with numerical methods of simulating the optical properties of such devices, including the effects of disorder on the eigenvectors and eigenvalues of periodic waveguide structures. In Chapter 5, a numerically assisted coupled mode theory is presented, and used to point out precisely where coupled mode theory fails in characterizing the supermodes of a strongly coupled arrayed waveguide. Finally, in Chapter 6 experimental methods of measuring propagation time will be outlined, and also a method of wavelength resolved infrared imaging, which allows the exact disordered eigenvectors of a coupled resonator optical waveguide to be observed.

References

[1] B. Jalali and S. Fathpour, "Silicon photonics," *J. Lightwave Technol.*, vol. 24, pp. 4600–4615, 2006.

[2] J. Goodman, F. I. Leonberger, S. Kung, and R. A. Athale, "Optical interconnections for vlsi systems," *Proc. IEEE*, vol. 72, pp. 850–866, 1984.

[3] F. A. P. Tooley, "Challenges in optically interconnecting electronics," *IEEE J. Sel. Top. Quantum Electron.*, vol. 2, pp. 3–13, 1996.

[4] D. A. Miller, "Optical interconnects to silicon," *IEEE J. Select. Topics Quantum Electron*, vol. 6, pp. 1312–1317, 2000.

[5] G. T. Reed, G. Mashanovich, F. Y. Gardes, and D. J. Thomson, "Silicon optical modulators," *Nature Photonics*, vol. 4, pp. 518–526, 2010.

[6] D. A. Miller, "Physical reasons for optical interconnections," *Int. J. Optoelectronics*, vol. 11, pp. 155–168, 1997.

[7] H. B. Bakoglu, *Circuits, interconnections, and packaging for VLSI*. New York: Addison-Wesley, 1990.

[8] D. A. Miller and H. M. Ozaktas, "Limit to the bit-rate capacity of electrical interconnects from the aspect ratio of the system architecture," *Journal of Parallel and Distributed Computing*, vol. 41, pp. 42–52, 1997.

[9] D. C. Edelstein, G. A. Sai-Halasz, and Y.-J. Mii, "On-chip interconnection performance simulations and measurements," *IBM J. Res. Develop.*, vol. 39, p. 383, 1995.

[10] D. Edelsteln, J. Heidenreich, R. Goldblatt, W. Cote, C. Uzoh, N. Lustig, P. Roper, T. McDevitt, W. Motsiff, A. Simon, J. Dukovic, R. Wachnik, H. Rathore, R. Schulz, L. Su, S. Luce, and J. Slattery, "Full copper wiring in a sub-0.25 ixm cmos ulsi technology," *Technical Digest, IEEE International Electron Devices Meeting*, vol. 42, p. 773, 1997.

[11] P. C. Andricacos, C. Uzoh, J. O. Dukovic, J. Horkans, and H. Deligianni, "Damascene copper electroplating for chip interconnections," *IBM J. Res. Develop.*, vol. 42, pp. 567–574, 1998.

[12] R. Mendis and D. Grischkowsky, "Undistorted guided-wave propagation of subpicosecond terahertz pulses," *Optics Letters*, vol. 26, pp. 846–848, 2001.

[13] A. Narasimha, B. Analui, E. Balmater, A. Clark, T. Gal, D. Guckenberger, S. Gutierrez, M. Harrison, R. Koumans, D. Kucharski, Y. Liang, A. Mekis, S. Mirsaidi, M. Peterson, T. Pham, T. Pinguet, V. Sadagopan, T. J. Sleboda, D. Song, Y. Wang, B. Welch, J. Witzens, S. Abdalla, and S. G. andP. De Dobbelaere, "A 40-gb/s qsfp optoelectronic transceiver in a 0.13 μm cmos silicon-on-insulator technology," *Optical Fiber Communication Conf. and Exposition*, vol. OMK7, 2008.

[14] D. Liang and J. Bowers, "Recent progress in lasers on silicon," *Nature Photonics*, vol. 4, pp. 511–517, 2010.

[15] B. Jalali, "Making silicon lase," *Scientific American*, vol. 2, p. 59, 2007.

[16] L. Pavesi, L. D. Negro, C. Mazzoleni, G. Franzo, and F. Priolo, "Optical gain in silicon nanocrystals," *Nature*, vol. 440, p. 59, 2000.

[17] G. Franzo, S. Coffa, F. Priolo, and C. Spinella, "Mechanism and performance of forward and reverse bias electroluminescence at 1.54 ČÊm from er-doped si diodes," *J. Appl. Phys.*, vol. 81, pp. 2784–2793, 1997.

[18] O. Boyraz and B. Jalali, "Demonstration of a silicon raman laser," *Opt. Express*, vol. 12, pp. 5269–5273, 2004.

[19] T. Liang and H. Tsang, "Role of free carriers from two-photon absorption in raman amplification in silicon-on-insulator waveguides," *Appl. Phys. Lett.*, vol. 84, pp. 2745–2747, 2004.

[20] R. Claps, V. Raghunathan, D. Dimitropoulos, and B. Jalali, "Influence of nonlinear absorption on raman amplification in silicon waveguides," *Opt. Express*, vol. 12, pp. 2774–2780, 2004.

[21] H. Rong, R. Jones, A. Liu, O. Cohen, D. Hak, A. Fang, and M. Paniccia1, "A continuous-wave raman silicon laser," *Nature*, vol. 433, pp. 725–728, 2005.

[22] H. Rong, S. Xu, Y. H. Kuo, V. Sih, O. Cohen, O. Rayday, and M. Paniccia, "Low-threshold continuous-wave raman silicon laser," *Nature Photonics*, vol. 1, pp. 232–237, 2007.

[23] G. Roelkens, D. V. Thourhout, R. Baets, R. Nötzel, and M. Smit, "Laser emission and photodetection in an inp/ingaasp layer integrated on and coupled to a silicon-on-insulator waveguide circuit," *Opt. Express*, vol. 14, pp. 8154–8159, 2006.

[24] A. W. Fang, H. Park, O. Cohen, R. Jones, M. J. Paniccia, and J. E. Bowers, "Electrically pumped hybrid algainas-silicon evanescent laser," *Opt. Express*, vol. 14, pp. 9203–9210, 2006.

[25] J. V. Campenhout, P. R. Romeo, P. Regreny, C. Seassal, D. V. Thourhout, S. Verstuyft, L. D. Cioccio, J. M. Fedeli, C. Lagahe, and R. Baets, "Electrically pumped inp-based microdisk lasers integrated with a nanophotonic silicon-on-insulator waveguide circuit," *Opt. Express*, vol. 15, pp. 6744–6749, 2007.

[26] M. Paniccia, "Integrating silicon photonics," *Nature Photonics*, vol. 4, pp. 498–499, 2010.

[27] W. D. Sacher and J. K. S. Poon, "Dynamics of microring resonator modulators," *Opt. Express*, vol. 16, pp. 15741–15753, 2008.

[28] M. H. Khan, H. Shen, Y. Xuan, L. Zhao, S. Xiao, D. E. Leaird, A. M. Weiner, and M. Qi, "Ultrabroad-bandwidth arbitrary radiofrequency waveform generation with a silicon photonic chip-based spectral shaper," *Nature Photonics*, vol. 4, pp. 117–122, 2010.

[29] R. A. Soref and B. R. Bennett, "Electrooptical effects in silicon," *IEEE Journal of Quantum Electronics*, vol. QE-23, pp. 123–129, 1987.

[30] W. M. Green, M. J. Rooks, L. Sekaric, and Y. A. Vlasov, "Ultra-compact, low rf power, 10 gb/s silicon mach-zehnder modulator," *Optics Express*, vol. 15, pp. 17106–17113, 2007.

[31] A. Liu, R. Jones, L. Liao, D. Samara-Rubio, D. Rubin, O. Cohen, R. Nicolaescu, and M. Paniccia, "A high-speed silicon optical modulator based on a metal oxide-semiconductor capacitor," *Nature*, vol. 427, pp. 615 –618, 2004.

[32] Q. Xu, B. Schmidt, S. Pradhan, and M. Lipson, "Micrometre-scale silicon electro-optic modulator," *Nature*, vol. 435, pp. 325–327, 2007.

[33] L. Liao, A. Liu, D. Rubin, J. Basak, Y. Chetrit, H. Nguyen, R. Cohen, N. Izhaky, and M. Paniccia, "40 gbit=s silicon optical modulator for highspeed applications," *Electronics Letters*, vol. 43, p. 22, 2007.

[34] T. Mueller, F. Xia, and P. Avouris, "Graphene photo-detectors for high-speed optical communications," *Nature Photonics*, vol. 4, pp. 297–301, 2010.

[35] F. Xia, T. Mueller, Y. Lin, A. Valdes-Garcia, and P. Avouris, "Ultrafast graphene photodetector," *Nature Nanotechnology*, vol. 4, pp. 839–843, 2009.

[36] L. Chen and M. Lipson, "Ultra-low capacitance and high speed germanium photodetectors on silicon," *Opt. Express*, vol. 17, pp. 7901–7906, 209.

[37] G. Dehlinger, S. J. Koester, J. D. Schaub, J. O. Chu, Q. C. Ouyang, and A. Grill, "High-speed germanium-on-soi lateral pin photodiodes," *IEEE Photon. Technol. Lett.*, vol. 16, pp. 2547–2549, 2004.

[38] D. Ahn, C. Hong, J. Liu, W. Giziewicz, M. Beals, L. C. Kimerling, J. Michel, J. Chen, and F. X. Kärtner, "High performance, waveguide integrated ge photodetectors," *Opt. Express*, vol. 15, pp. 3916–3921, 2007.

[39] L. Vivien, M. Rouvière, J. Fédéli, D. Marris-Morini, J. Damlencourt, J. Mangeney, P. Crozat, L. Melhaoui, E. Cassan, X. Roux, D. Pascal, and S. Laval, "High speed and high responsivity germanium photodetector integrated in a silicon-on-insulator microwaveguide," *Opt. Express*, vol. 15, pp. 9843–9848, 2007.

[40] S. Assefa, F. Xia, and Y. A. Vlasov, "Reinventing germanium avalanche photodetector for nanophotonic on-chip optical interconnects," *Nature*, vol. 464, pp. 80–84, 2010.

[41] Q. Xu, D. Fattal, and R. G. Beausoleil, "Silicon microring resonators with 1.5-ţm radius," *Opt. Express*, vol. 16, pp. 4309–4315, 2008.

[42] A. C. Turner, C. Manolatou, B. S. Schmidt, M. Lipson, M. A. Foster, J. E. Sharping, , and A. L. Gaeta, "Tailored anomalous group-velocity dispersion in silicon channel waveguides," *Optics Express*, vol. 14, p. 4357, 2006.

[43] E. Dulkeith, F. Xia, L. Schares, W. M. J. Green, , and Y. A. Vlasov, "Group index and group velocity dispersion in silicon-on-insulator photonic wires," *Opt. Express*, vol. 14, p. 3853, 2006.

[44] M. Heiblum and J. H. Harris, "Analysis of curved optical waveguides by conformal transformation," *J. Quantum. Elect.*, vol. 11, p. 186, 1975.

[45] E. G. Neumann and R. Nat, "Curved dielectric optical waveguides with reduced transition losses," *IEE Proc., Pt. H*, vol. 129, pp. 278–280, 1983.

[46] F. P. Payne and J. P. R. Lacey, "A theoretical analysis of scattering loss from planar optical waveguides," *Opt. Quantum Electron.*, vol. 26, pp. 977–986, 1994.

[47] S. J. McNab, N. Moll, and Y. A. Vlasov, "Ultra-low loss photonic integrated circuit with membrane-type photonic crystal waveguides," *Optics Express*, vol. 11, no. 22, pp. 2927–2939, 2003.

2 Coupled Resonator Optical Waveguides (CROWs)

Decades of research in the CMOS process has allowed silicon devices to be fabricated with sub-100 nanometer features. At such separation distances, the characteristics of an individual isolated waveguide does not provide sufficient information, using traditional theories, to accurately describe the functionality of a strongly coupled composite structure. In Chapter 5, methods to improve on existing analytical theories for describing the optical modes of such strongly coupled waveguides will be presented; however, for the most part, their modal properties must be characterized through robust numerical techniques. Despite the lack of time-efficient analytical tools for describing strongly coupled high-index contrast waveguides, such coupled waveguides have shown themselves to be indispensable in providing the necessary apodization of CROWs, and also allowing light to be guiding in a low index material, provided by a single-mode "slot" waveguide. In the next two chapters the incredible functionality of two strongly-coupled photonic devices in particular will be detailed: coupled resonator optical waveguides and strongly coupled arrayed waveguides.

Coupled resonator optical waveguides (CROWs) consist of long chains of resonators where light is guided by tunneling between adjacent resonators, which may be micro-rings, micro-disks, or photonic crystals [1, 2, 3, 4]. These devices have been proposed for applications in slow light, temperature insensitive high-order optical filters, dispersion compensation, etc. [5, 6, 7, 8, 9, 10].

For an infinite chain of equally spaced identical resonators, the fields will be periodic at twice the lattice constant, Λ. This formalism is identical to the tight-binding formalism, where the potential barriers are represented by the inter-resonator coupling

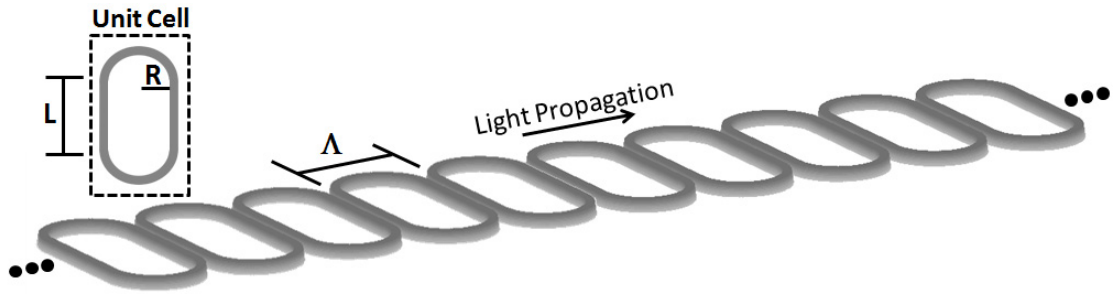

Figure 2.1: Coupled resonator optical waveguide (CROW), periodic chains of microresonators, with radius R, and track-length L, where light propagates through the structure by tunneling from resonator to resonator.

coefficient (numerical methods for calculating the wavelength dependence of this coupling coefficient will be presented in Chapter 4). Fig. 2.1 shows a CROW along with the corresponding unit-cell, composed of a single racetrack resonator with bending radius R and track length L. For finite, "large" number of resonators, a CROW may be regarded as a waveguide with its own dispersion characteristics [11], which strongly depends on the nanowires of which it is composed [12].

The dispersion relationship of a CROW has been derived elsewhere using the tight binding formalism and transfer matrix techniques [11],

$$\cos(\beta\pi R) = \pm\kappa\,\cos(K\Lambda) \tag{2.1}$$

where $\beta(\omega) = n_{\text{eff}}(\omega)\omega/c$, κ represents the magnitude of the dimensionless cross-coupling coefficient between two resonators, Λ and K represent the periodicity and propagation constant of the CROW respectively, and R is the "effective" radius, defined for racetrack resonators as the ring radius plus L/π.

2.1 Dependence on the Silicon Nanowire

In order to derive the effects of waveguide dispersion on the CROW, we recall that Eq. (2.1) is used to describe a relatively narrow band of radial frequencies ω in the vicinity of the single-resonator eigen-frequency, Ω. Therefore, writing $\omega = \Omega + \delta\omega$

where $|\delta\omega| \ll \Omega$, we approximate n_{eff} by the following,

$$n_{\text{eff}}(\omega) = n_{\text{eff}}(\Omega) + \delta\omega \left.\frac{dn_{\text{eff}}}{d\omega}\right|_{\omega=\Omega}, \tag{2.2}$$

and re-write the left-hand side of Eq. (2.1), discarding terms of higher order than $\delta\omega$,

$$\begin{aligned} &\sin(\beta\pi R) \\ &\approx \sin\left[\underbrace{\pi n_{\text{eff}}(\Omega)\frac{R}{c}\Omega}_{m} + \underbrace{\pi\left(n_{\text{eff}}(\Omega) + \Omega \left.\frac{dn_{\text{eff}}}{d\omega}\right|_{\omega=\Omega}\right)}_{n_{\text{g}}(\Omega)}\frac{R}{c}\delta\omega\right] \\ &= (-1)^m \sin\left[\pi m \frac{n_{\text{g}}(\Omega)}{n_{\text{eff}}(\Omega)}\frac{\delta\omega}{\Omega}\right], \end{aligned} \tag{2.3}$$

using the standard definitions of the mode number m and group index $n_{\text{g}}(\Omega)$. We can thus rewrite Eq. (2.1),

$$\sin\left[\pi m \frac{n_{\text{g}}(\Omega)}{n_{\text{eff}}(\Omega)}\frac{\delta\omega}{\Omega}\right] = \pm(-1)^m \kappa \cos(K\Lambda). \tag{2.4}$$

We see that the bandwidth $\delta\omega$ is scaled by the factor $n_{\text{eff}}/n_{\text{g}}$. For these SOI waveguides, this ratio represents a 42% reduction of the bandwidth.

The average group delay τ_{g} of an N-element CROW is defined by the length of the structure (ΛN) divided by the group velocity, $d\omega/dK$, evaluated at Ω,

$$\tau_{\text{g}} = \frac{\pi n_{\text{g}} R N}{|\kappa| c}. \tag{2.5}$$

Therefore, a high value of the waveguide group index actually causes increased delay in a CROW—the enhancement is about 73% for these SOI microring CROWs. In general, the delay can be precisely modified by adjusting the aspect ratio of the constituent waveguides in order to vary n_{g} [13, 14].

The dispersion relationship can also be used to estimate the coupling coefficient between adjacent microrings from a measurement of the full-width ($2\,\delta\lambda_{1/2}$) of a CROW transmission band. Since $\delta\omega/\Omega = -\delta\lambda/\lambda_0$, where Ω and λ_0 are the resonance radial frequency and wavelength of a single resonator, at the band edge, $\lambda = \lambda_0 \pm \delta\lambda_{1/2}$, and the cosine term on the right hand side of Eq. (2.4) takes on the value -1. Therefore,

$$|\kappa| = \sin\left[2\pi^2 n_{\text{g}}(\lambda_0)\frac{R}{\lambda_0}\frac{\delta\lambda_{1/2}}{\lambda_0}\right] \approx 2\pi^2 n_{\text{g}}(\lambda_0)\frac{R}{\lambda_0}\frac{\delta\lambda_{1/2}}{\lambda_0}, \tag{2.6}$$

the approximation being valid in the limit of small bandwidth, and shown by values of $|\kappa| \ll 1$.

As with most slow light structures, the increased delay in a CROW is achieved by allowing light to retrace a circuitous path. The loss of a CROW, α_{CROW}, is given by the product of the effective distance traveled (the product of the group delay of the CROW and group velocity of the constituent waveguide), and the loss per unit length. At band center, the loss is readily calculated as [1],

$$\alpha_{\mathrm{CROW}} = \frac{\alpha_{\mathrm{wg}} N \pi R}{|\kappa|} \tag{2.7}$$

where α_{wg} is the loss per unit length of the waveguides.

2.2 Experimental Results

A single CROW waveguide can readily achieve multiple bands of slow and filtered light in the same physical structure, unlike band-edge photonic crystal slow light waveguides [15, 16, 17]. This characteristic is particularly useful for on-chip wavelength division multiplexing, temperature-insensitive optical filters, and nonlinear optics, in which several wavelengths of light are often used simultaneously.

CROWs were fabricated at the IBM Microelectronics Research Laboratory on 200 mm SOI wafers wafers where the waveguide dimensions and gaps were varied from their nominal values as a result of dose-striping. Fig. 2.2 shows a schematic of a typical wafer, also shown is the effect dose-striping has on the CROW's composite directional couplers. High dose yields an increased gap, but the center-to-center separation distance remains the same compared with the low-dose regions. The wafers were post-processed with two different surface roughness reduction techniques: hydrogen annealing and double oxidation. A typical chip is shown in Fig. 2.3, which consists of five CROWs, with 35, 65, 95, 135 and 235 coupled microrings. Group delay measurements were carried out using a single-scan, Jones matrix-based, interferometric spectral measurement instrument (Luna Tech. Optical Vector Analyzer CTe [18]). Light was coupled into and out from the chip using polarization maintaining lensed tapered fibers (Oz Optics) that have been measured to achieve $\geq$20 dB polarization selectivity. The TE-polarized light

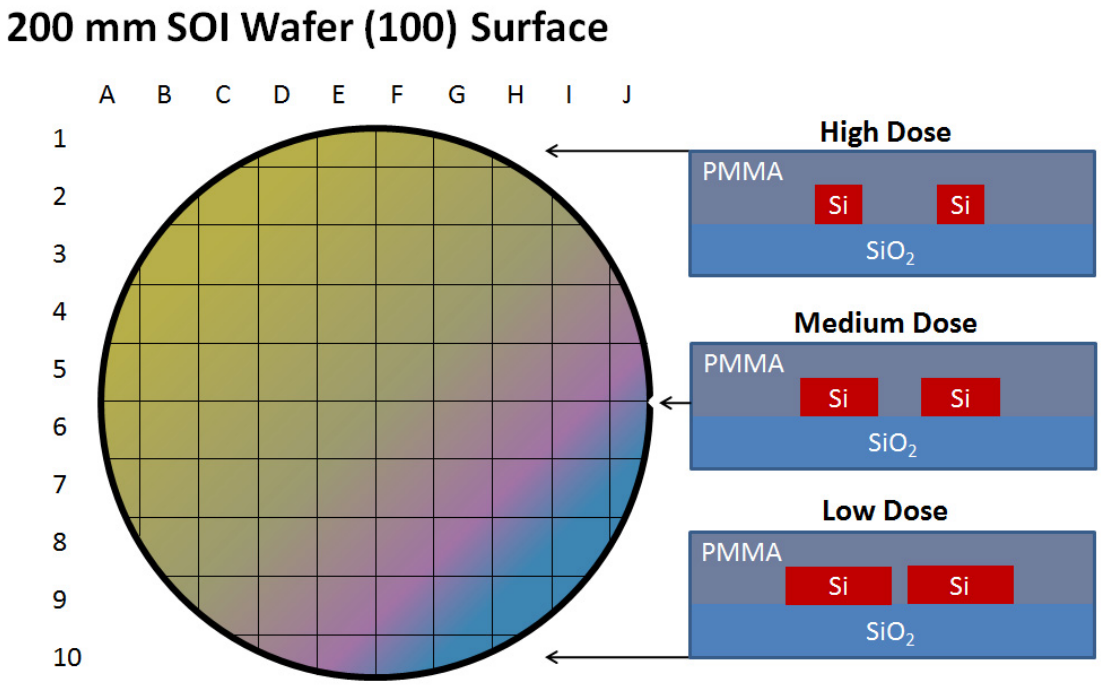

Figure 2.2: CROWs were fabricated at the IBM Microelectronics Research Laboratory on 200 mm SOI wafers wafers where the waveguide dimensions and gaps were varied from their nominal values as a result of dose-striping. High dose results in an increased gap between the directional couplers of the racetrack resonators, but the center-to-center separation distance remains the same compared with the low-dose regions.

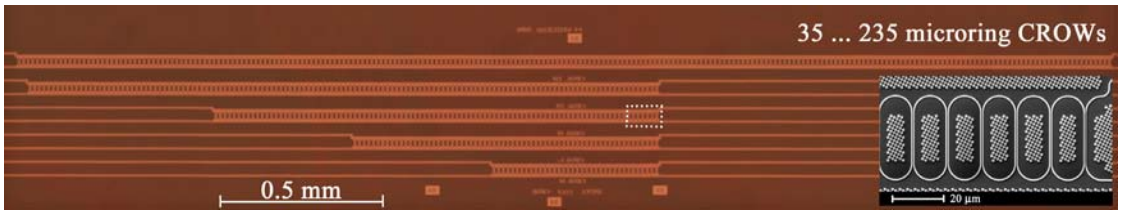

Figure 2.3: Silicon microring CROWs ranging from 35 to 235 microrings, fabricated on 200 mm wafers and cleaved into 4 mm-long chips. (*Inset*) Scanning electron microscope image of the region indicated by the dashed box.

(in the plane of the silicon) was used and the waveguide loss was measured to be about -3.2 dB/cm. For the CROWs considered here, a loss of 0.074 dB/ring was measured.

The (TE) group index of the composite silicon nanowires, n_g, was measured in two separate ways. First, n_g was measured from the relative group delay of a set of four waveguides (without resonators) on the same chip, ranging in length from 0.35 cm

to 4.15 cm. Second, n_{g} was determined from the free spectral range, Δf_{FSR}, of the CROW,

$$n_{\mathrm{g}} = \frac{c}{2\pi R \Delta f_{FSR}}, \tag{2.8}$$

where Δf_{FSR} was calculated from the center-to-center spacing of each CROW band. Fig. 2.4 shows the group index data obtained from each method. The figure illustrates that excellent mutual agreement with a value $n_{\mathrm{g}} = 4.25$ is obtained for both types of measurement. We expect the fluctuations around the average group delay to be due to the high index contrast and high confinement nature of these SOI waveguides.

Fig. 2.5(a) shows the experimentally measured transmission and group delay spectra for eleven bands of a 35-ring CROW, along with each band's center wavelength. Conventionally, the "usable" bandwidth of a CROW for purposes of spectrally-flat group delay is defined as the central half of the total bandwidth [19]. In Fig. 2.5(b), we plot the measured group delay averaged over the center half of each band for the 35, 65, 95, 135, and 235-ring CROWs. The solid black line is the prediction of Eq. (2.5), in which the value of κ is obtained from the bandwidth of the 35-ring CROW, using Eq. (2.6).

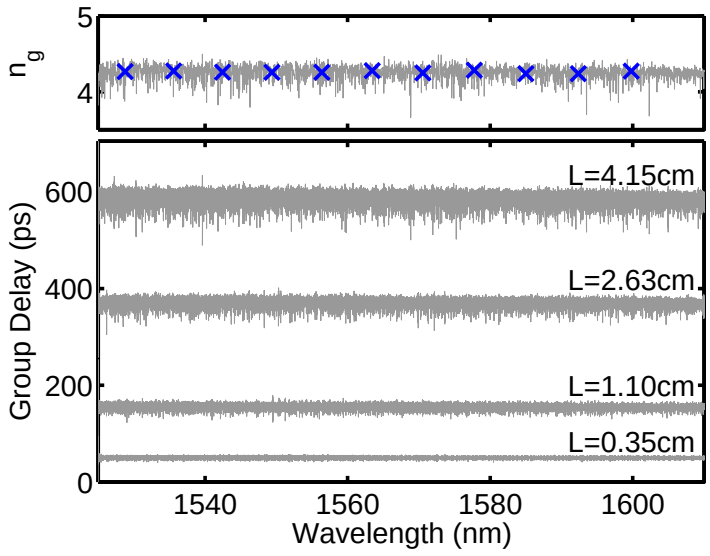

Figure 2.4: (*Top*) Group index (n_{g}) of the CROW's constituent waveguides, derived from the free spectral range of the CROW (*markers*) and (light-gray) group index data determined from (*Bottom*) the group delay of four straight waveguides of varying lengths, L.

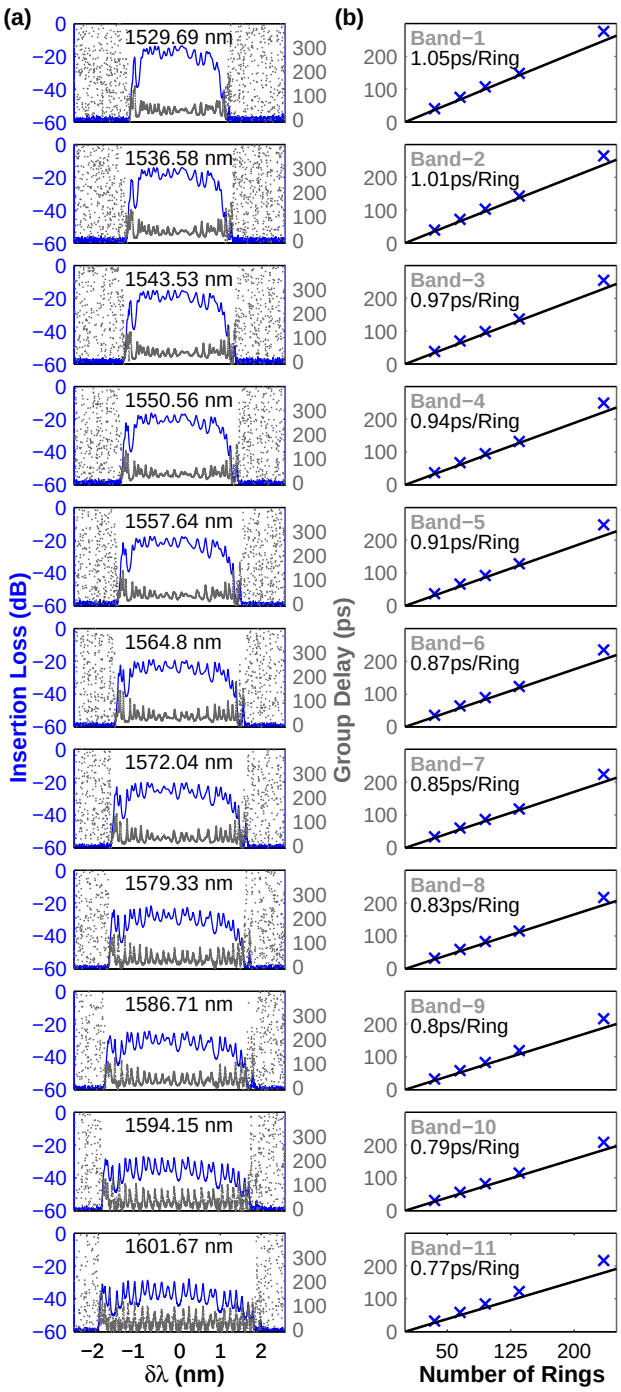

Figure 2.5: (a) Transmission and group delay spectra for eleven bands of a 35-ring CROW, along with each band's center wavelength. (b) (*Markers*) Band-center group delay for different length CROWs across the measured eleven bands. (*Solid-line*) Prediction of the group delay of a CROW using Eq. (2.5).

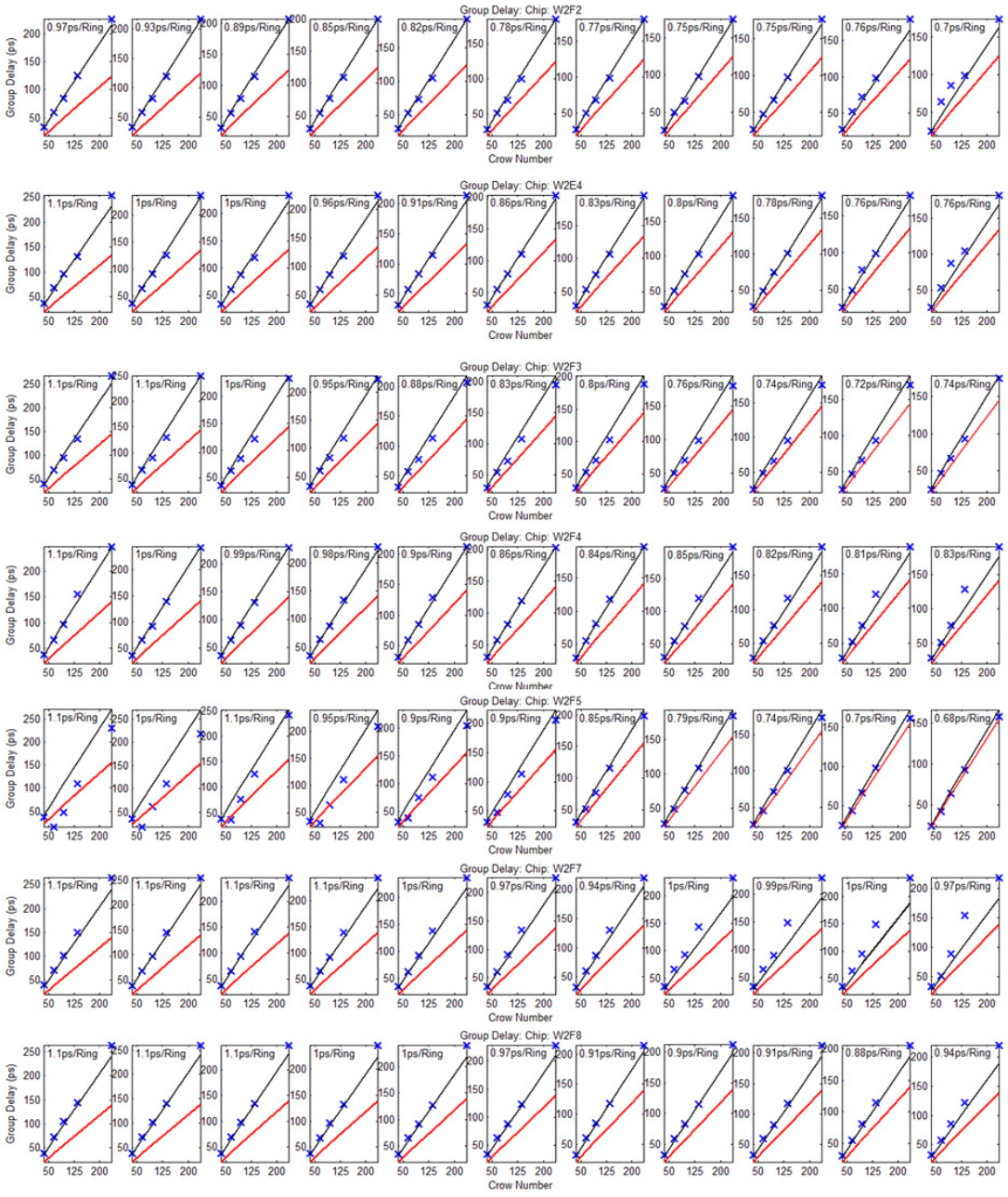

Figure 2.6: (*Blue Markers*) Band-center group delay measured for different length CROWs across the eleven bands, for seven different chips. (*black-line*) Prediction of the group delay of a CROW using Eq. (2.5). The (*red-line*) shows previously derived results, which did not account for the waveguide dispersion [1].

Since Fig. 2.4 shows that the group index n_{g} does not vary appreciably over the spectral range characterized, Eq. (2.5) indicates that any band-to-band variation in group delay is due to the wavelength dependence of the coupling coefficient. We see that there is an excellent fit to the measured data, from which we can infer a range of delays of about 0.77 to 1.05 ps per unit cell of length Λ = 14.3 μm. The slowing factor, c/v_{g}, where v_{g} is the group velocity, thus ranges from 16.0 to 22.1 over the measured bands.

With increasing center wavelength, as the delay per ring decreases, the bandwidth of the CROW increases. The linear scaling of group delay with N was confirmed for over eight chips, as shown in Fig. 2.6.

2.3 Band Dependence on the Composite Directional Couplers

As shown in Fig. 2.4, coupled resonator optical waveguides can be broken down into their composite directional couplers. By substituting into Eq. (2.6) the definition of free spectral range of a microring,

$$\Delta\lambda_{FSR} = \frac{\lambda^2}{2\pi n_g R}, \tag{2.9}$$

we obtain the dimensionless coupling coefficient, which can be measured from a single-scan of the transmission spectrum,

$$|\kappa| = \sin\left[\pi\frac{\delta\lambda_{1/2}}{\Delta\lambda_{FSR}}\right]. \tag{2.10}$$

By using Eq. 2.10 at each band of the CROW, one may extract the wavelength dependent coupling coefficient of the composite directional couplers using a CROW.

Fig. 2.8(a) and (b) shows sample bands each around 1550 nm of a 35-ring CROWs measured at the top, middle, and bottom of the double oxidized and hydrogen annealed wafers, respectively. It can be seen that the bandwidth varies from chip to chip due to the change in lithography exposure, and hence waveguide width. Fig. 2.8(c) shows the experimentally derived coupling coefficients using Eq. (2.10), for eight chips across each wafer, where the waveguide dimensions and gaps were varied from their

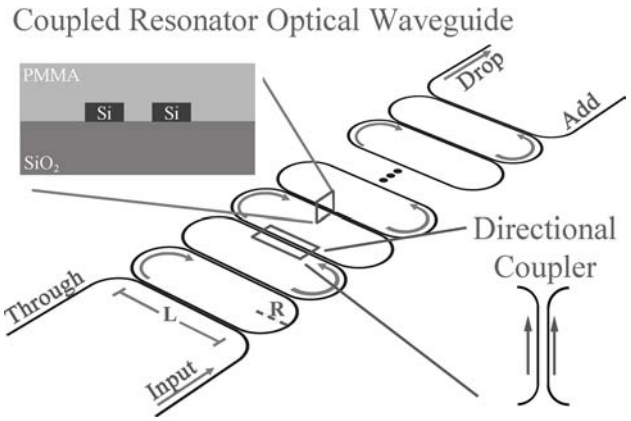

Figure 2.7: Coupled resonator optical waveguides may be broken down and characterized in terms of their composite directional couplers

nominal values as a result of dose-striping.

While it has been previously shown that disorder between the individual resonators may also have perturbative effects on the transmission spectrum of a CROW [20], Fig. 2.8(c) nevertheless shows a strong correspondence between the experimentally derived coupling coefficients using Eq. (2.10) as the waveguide widths and height were varied. Waveguides with smaller widths due to dose-striping resulted in an increased coupling coefficient, due to the mode being less confined. Compared with the

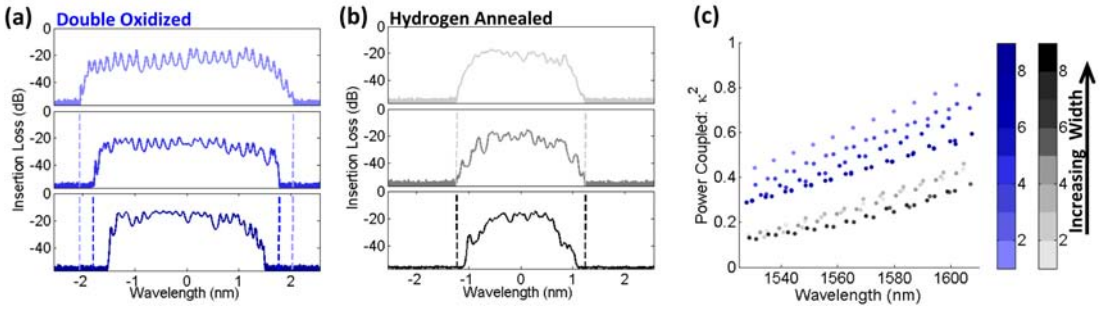

Figure 2.8: (a) Sample band around 1550 nm of a 35-ring CROW at the top, middle, and bottom of the double oxidized, and (b) hydrogen annealed wafers. Waveguide dimensions were varied from their nominal values as a result of dose-striping, demonstrated in Fig. 2.2, which results in thinner waveguides at the top of the wafer, and wider waveguides at the bottom. The double oxidation process further thinned the waveguide dimensions, height and width, by 20 nm. (c) Experimentally derived coupling coefficients using Eq. (2.10), for eight chips across each wafer, where the waveguide dimensions and gaps were varied from their nominal values as a result of dose-striping.

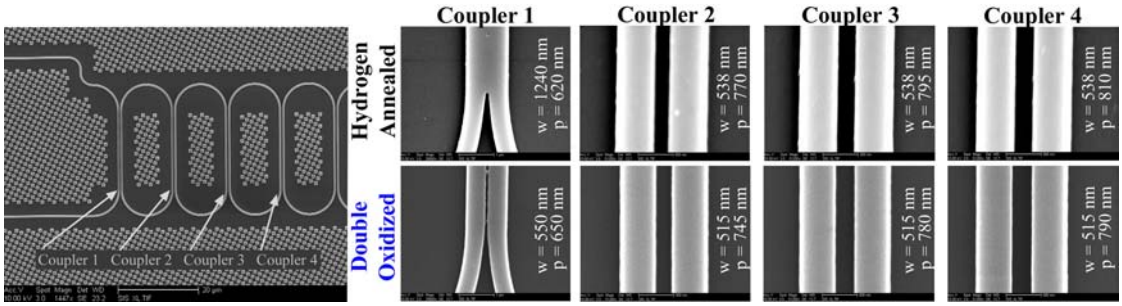

Figure 2.9: Scanning electron microscope (SEM) image of the waveguide cross-section and first four directional couplers for both the hydrogen annealed and double oxidized wafers.

hydrogen annealed wafer, it can be seen that the double oxidation processes resulted in a higher coupling coefficient between the resonators and increased sensitivity to variations in waveguide width due to dose-striping. We will confirm, through simulation in (Section 4.3), that this was due to the nature of the double oxidation process, in which approximately 20 nm of silicon (n_{Si} = 3.47) is replaced by oxide (n_{SiO_2}=1.44). This also results in less confinement, and thus increased overlap, of the waveguide modes.

2.4 Strongly Coupled Nanowires for Apodization

In order to reduce the group delay and insertion loss ripple of a CROW, apodization of the directional couplers is performed by tapering the spacing (coupling coefficients) of the first rings at the input and output of the CROW. Fig. 2.9 shows a scanning electron microscope image of the first four couplers of a 35-ring CROW, along with the waveguide widths and center-to-center spacing, p. These strongly coupled directional couplers allow for a high coupling coefficient leading into the CROW, and for it to be gradually ramped down to the value of the CROW where it remains constant (this is similar to impedance matching in electronics). However, as the separation distance between the directional couplers is reduced, the propagation constants of the even and odd supermodes will fan out [21]. As will be shown in Section 4.3, the coupling coefficient of these sub 100-nm directional couplers can become very dispersive, resulting in strong apodization variations with wavelength, as can be seen by analyzing the increased insertion loss ripple and group delay ripple for the higher bands shown in

Fig. 2.5. Further effects resulting from wavelength dependent apodization on the CROW will be discussed in Section 4.4.

2.5 Limitations Imposed by Disorder and the Motivation for Strong Coupling

Practical applications require relatively long CROWs, consisting of hundreds of coupled resonators [2, 3, 4, 22], while maintaining good performance. In spite of great theoretical interest in this novel form of waveguiding, the practical applications requirement that several hundreds of resonators must be chained together in a disorder-free manner has constituted a technological challenge [22, 2].

Disorder in CROWs has thus far been a severe practical problem, since in a multi-resonator ensemble, the resonance frequencies of the constituent resonators must be precisely aligned. Active resonance tuning mechanisms, e.g., thermal heaters placed over each ring [23, 24], are impractical for ensembles consisting of hundreds or thousands of rings. Moreover, although the benefit of microrings and CROWs increases for higher quality factors (lower coupling coefficient, increased resonator separation), such resonators are also harder to align. In fact, coupled-resonator and photonic crystal waveguides that are about a hundred lattice periods in length have shown disorder-induced localization of light [25, 26], which though fundamentally interesting and potentially useful for some applications [15], is generally considered problematic for most device applications. As such, a high coupling coefficient is needed to relax the constraints on the fabrication process, that the resonators be exactly identical, by broadening the Lorentzian response of the composite resonators.

Indeed, there have been few reports of long CROWs, in each case with transmission characteristics that show considerable ripple [4, 3, 23]. Moreover, the recently-demonstrated disorder-induced localization of slow light in CROWs and photonic crystal waveguides indicates serious challenges to making long structures, since all the eigenmodes of a one-dimensional waveguide are localized in theory for any value of disorder [27, 28]. Scaling up the number of resonators within a single CROW waveguide, while maintaining suitable “ballistic” [29, 30] propagation characteristics, poses a

significant technical challenge, as failure rates of such series-coupled structures may be thought to scale as a power law with the number of unit-cells in the exponent.

2.6 Statistics of Light Transport for Increasing Number of Resonators

To overcome the fiber-to-waveguide coupling losses and maintain a high signal to noise ratio at the detector for accurate statistical analysis, the output of the OVA (average power 200 μW) was then amplified (before the chip) by an L-band EDFA, which was used in the saturation regime (constant current mode, output power +18 dBm), followed by a programmable passive attenuator to reduce the power level incident on the silicon chip to a sufficiently low level to avoid nonlinearities. No amplification was performed after the chip. In this way, it was ensured that the amplifier noise contribution remained constant, regardless of the spectral variations in the CROW response. Calibration measurements showed that the EDFA and attenuator combination added only 0.14 ps RMS noise to the measured propagation delay data (Section 6.2).

Propagation delay measured data were corrected for the shorter "input" and "drop" straight waveguide sections in longer structures, as can be seen in Fig. 2.3. Based on the measured group index in the straight waveguides, Fig. 2.4, this length difference translated to 40.5 ps difference in the measured propagation time. Similar relative differences were calculated for the 65, 95 and 135 ring CROWs to be 6.1 ps, 12.2 ps, and 20.3 ps, respectively.

Transmission (insertion loss) spectra

Fig. 2.10 shows a typical set of transmission spectra from a group of 5 CROWs consisting of 35, 65, 95, 135, and 235 microrings on a single chip, showing well-aligned passbands over a wide range of wavelengths. The width of the passbands increased slightly with wavelength for all the chips measured because of the dispersion of the silicon waveguides [29]. However, the average level of transmission in the passband, as well as high on-off extinction, remained approximately the same for each CROW, thus showing the high level of ring-to-ring uniformity achieved in these CROW structures.

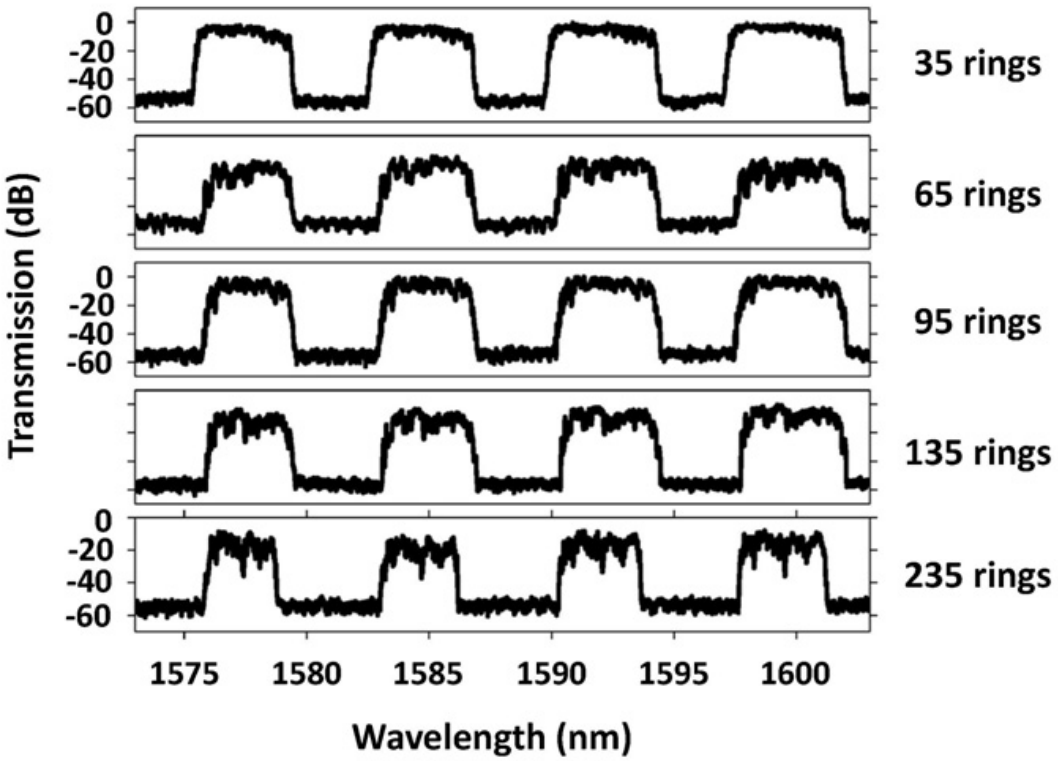

Figure 2.10: Transmission (insertion loss) spectra were measured with resolution 1.4 pm, for 35, 65, 95, 135, and 235 ring waveguides. Shown here are the averages of 128 measured traces. Relative to the 35-ring CROW, measurements for 65, 95, 135 and 235 ring CROWs were amplified by 7, 4, 3, and 7 dB, respectively in order to boost the power level detected at the photoreceiver.

Group delay spectra

Fig. 2.11 shows the group delay spectra for the CROWs over the same range of wavelengths as in Fig. 2.10. The band-edge and stop-band regions, clearly indicated by the significantly increased group delay ripple at those wavelengths, are excluded from the statistical analysis. Within the central region of the passband (approximately two-thirds of the edge-to-edge span), spectrally-dependent properties such as the density of states and the localization length should be approximately constant [25] and therefore, the variation of measured group delay with wavelength can be used as a statistical variable.

Group delay ripple (GDR) here is defined as the difference between the measured group delay $\tau(\lambda)$ and τ_{rms}, the root-mean-squared group delay over the central

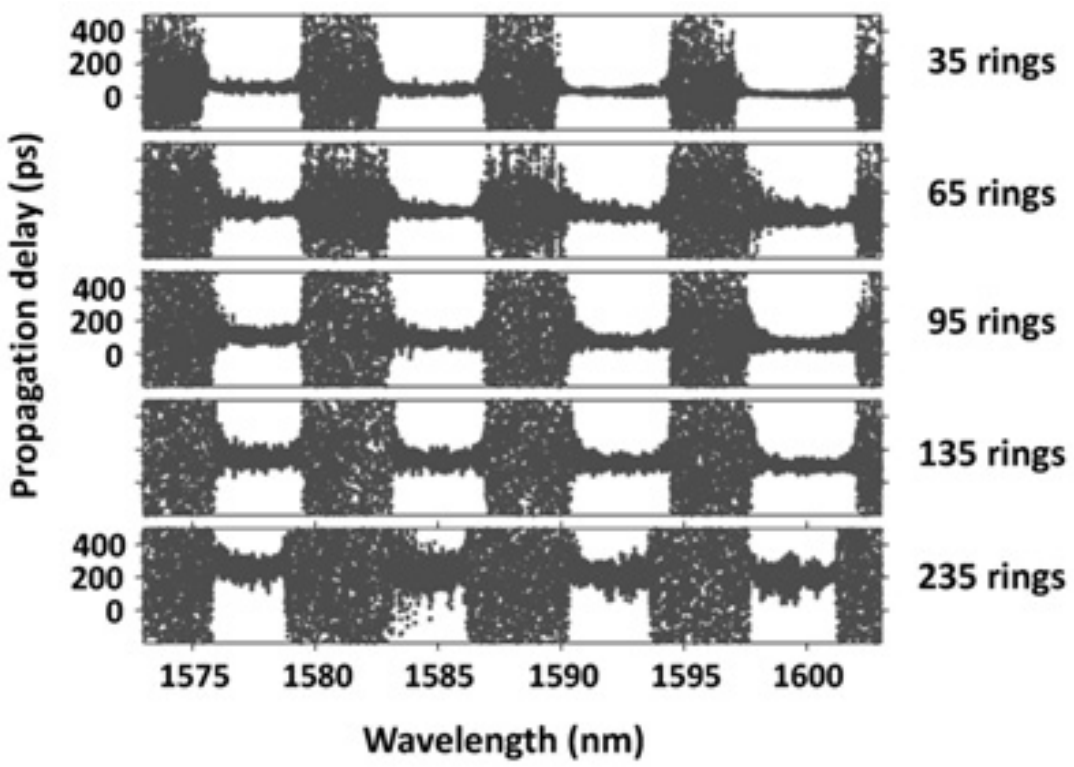

Figure 2.11: Group delay spectra were measured with resolution 1.4 pm, for 35, 65, 95, 135, and 235 ring waveguides, over the same range of wavelengths as in Fig. 2.10. Spectral regions of large variation in delay correspond exactly to the stopbands of the intensity spectrum shown in Fig. 2.10

portion of the passband. GDR is an important parameter in the study of devices for optical communications, since spectral components of GDR that are on the order of the signal bandwidth affect the signal spectrum by imposing an average chromatic dispersion, which can be compensated at the receiver. Therefore, in the study of fiber Bragg gratings, the average dispersion over the (narrow) band of interest is usually subtracted out from the phase variations, and the residual phase variation is used as the noise statistic which determines performance degradation [31]. The averaging bandwidth depends on the spectral width of the pulses used in data transmission. For example, 40 Gbps modulated optical data streams will average over ripple with spectral components less than 100 pm, effectively sensing them as a constant group delay [32].

In the next section, we use ripple statistics not to investigate the performance degradation of data transmission but the nature of light propagation in the CROWs. The

band-to-band variation in average group delay is less than 0.1 ps/Ring over 20 nm. As shown in Section 6.2, a linear slope imposed on the spectral variation of the measured group delay by the EDFA of -1.81 ps/nm is was subtracted from all the data. Calibration measurements showed that the EDFA added only 0.14 ps RMS noise to the measured propagation delay data, which is negligible in the context of approximately 30-200 ps of group delay ripple that characterizes the CROWs.

Statistical analysis

In a regime where disorder may play a significant role, it is very important to realize that measurement of only the average transmission properties of a long waveguide constitutes an incomplete story of transport. This is because: (a) absorption reduces the average transmission of light in a similar way as does localization (exponentially with length), [33, 34, 35] and (b) the average propagation time through the waveguide scales similarly in both the localized and non-localized regimes (linearly with length) [36, 37]. A distinction between the localized and non-localized transport regimes can be obtained only through an analysis of the statistical properties of the transmission intensity and propagation time and further, by directly imaging the light propagating through the structure.

IR imaging

Eigenmodes of light propagation in a 235-ring waveguide were imaged using an infrared camera diagnostic method developed for multi-ring waveguides, described in detail in Chapter 6. Selected wavelengths in the stop-band, band-edge, and at locations throughout the passband, as indicated in Fig. 2.12(a), were imaged under cw excitation from a narrow-linewidth tunable laser, using a microscope fitted with an infrared camera. Several image fields were stitched together laterally, but no data correction was made for the absorptive decay of intensity with length, thus showing clearly the low intrinsic loss of the propagating modes, quantified to be -0.08 dB/ring. Since the chip was imaged through a semi-transparent and scattering polymeric cladding layer, the camera did not resolve individual microrings, but nevertheless clearly showed the general trends of propagation. Although modes at only a few selected wavelengths are shown in

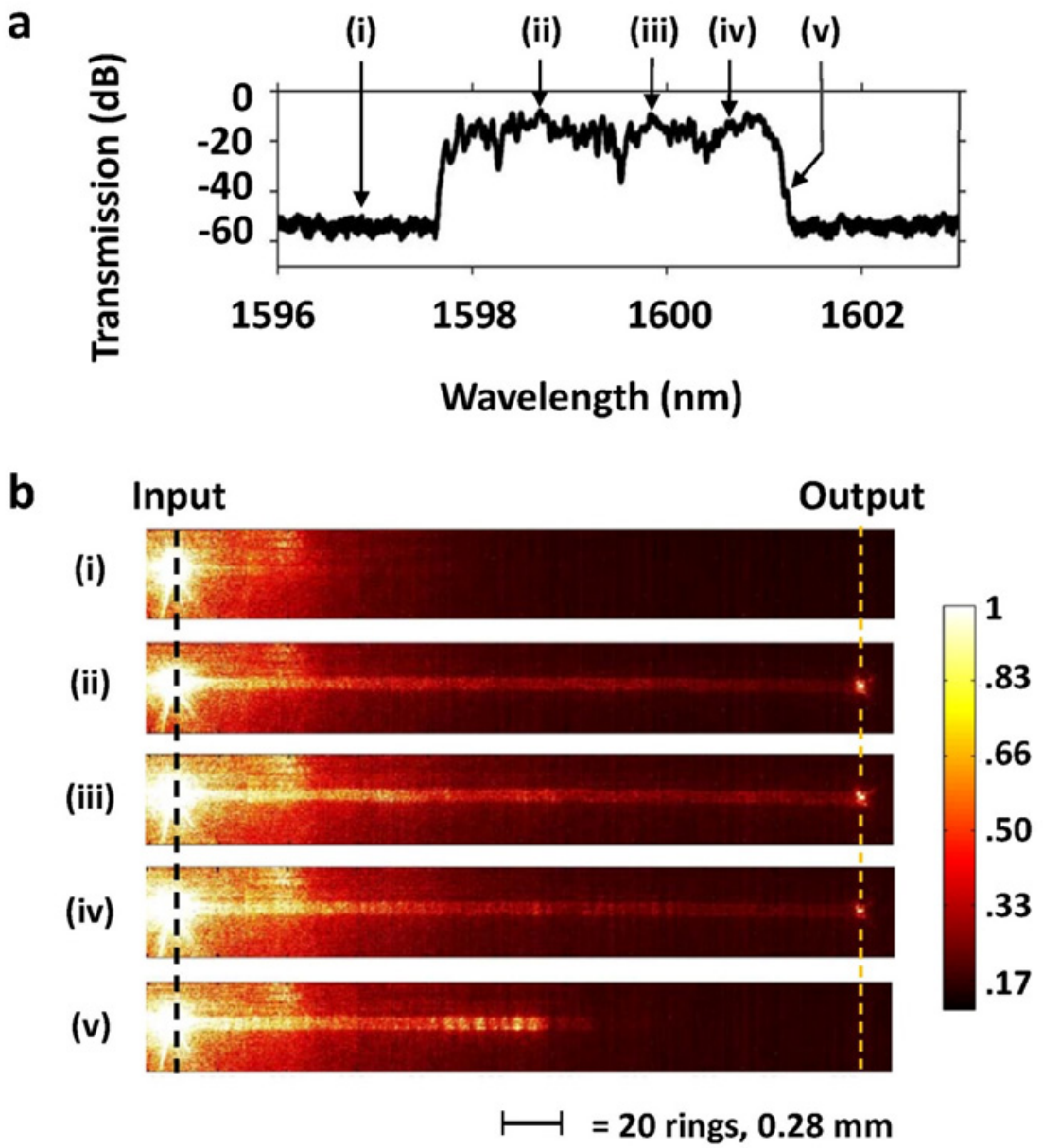

Figure 2.12: (a) Transmission (insertion loss) spectrum for a single passband of a 235 ring CROW, with measurements at selected wavelengths labeled (i)-(v). (b) Intensity profiles of the eigenmodes at the wavelengths (ii)-(iv) measured with an infrared camera, show that non-localized excitations (extended throughout the entire waveguide length) were observed throughout the passband, in contrast with out-of-band (i) and band-edge (v) wavelengths. No correction was made in these images for the absorptive decay of intensity with length of the propagating modes.

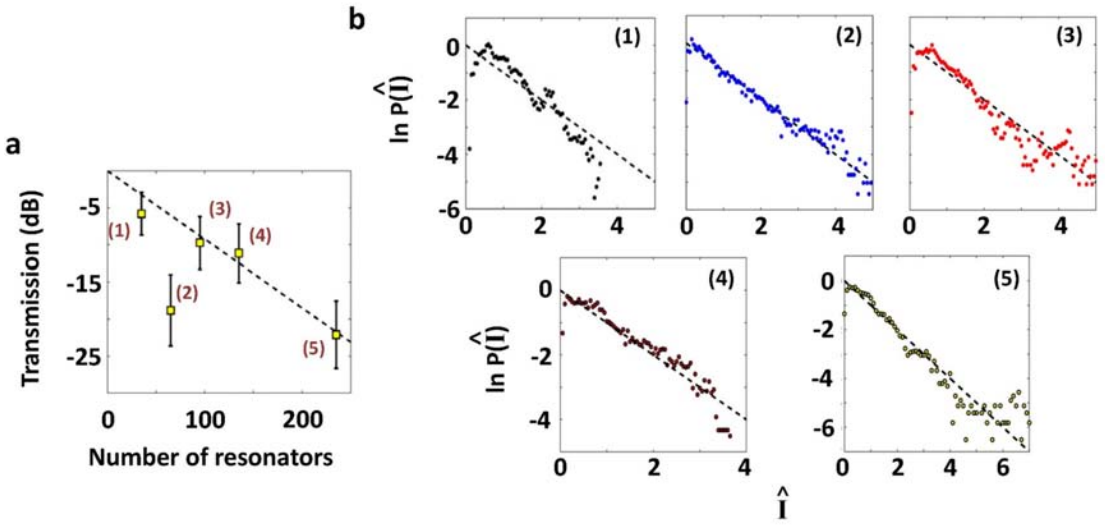

Figure 2.13: (a) The mid-band average of the transmitted intensity (in dB), measured without amplification, decreased linearly with length (-0.08 dB/resonator), except for one anomalous waveguide on the measured chip (65 rings) as discussed in the text. The errorbars represent the standard deviation, i.e., ripple, in the measured delay over the flat portion of the band. (b) The probability distribution function (PDFs) of the normalized intensity transmission ($\hat{I} \equiv \frac{I}{\langle I \rangle}$) for the all the CROWs show agreement with the Rayleigh distribution, shown by the dashed lines, indicating non-localized transport through the waveguide. In contrast, the localized regime would show considerably different (long-tailed) statistics [15, 33, 39].

Fig. 2.12(b) for clarity, the results for other wavelengths were very similar, except at two sharp disorder-induced notches in the passband. Based on Fig. 2.12(b), panels (i)-(v), it is clear that light can be transmitted throughout the entire length of a 235-ring CROW without localization.

It is also important to point out the increased intensity shown for the local resonators at the band-edge wavelengths in Fig. 2.12, where it is a well known property for coupled resonator optical waveguides that group delay increases at band-edge, caused by an increased number of circulations within the resonators before coupling to an adjacent resonator—thus higher intensity enhancement, and radiated intensity [38].

Transmission scaling

High-resolution spectral measurements (Fig. 2.10 and 2.11) reveal strong, well-resolved transmission passbands for CROWs composed of 35 to 235 coupled microrings. The high-frequency transmission "ripple" bears the signature of random disorder in the fabrication of CROWs, and can be seen to increase with the number of unit cells. Both disorder and loss contribute to a bandwidth narrowing with increasing length of only 0.2% per ring, i.e., 100 additional rings reduced the bandwidth by 20% compared to the bandwidth of the 35 ring structure. A wide passband exceeding 380 GHz (in each band) was therefore maintained even in the 235 ring structure, sufficient for many high-speed optical signal applications. As shown in Fig. 2.13(a), a linear fit to the spectrally-integrated power transmitted at mid-band for CROWs of different length indicated an average loss per ring of only -0.08 dB/ring, i.e., the insertion loss of a 35 ring CROW by itself was less than -3 dB. The 65 ring CROW may have had a defective input coupler or damaged cleaved facet, which lowered the overall transmission through the device, but did not affect the transmission statistics. As shown in Fig. 2.13(b), the measured probability distribution of the normalized intensity agreed with the Rayleigh distribution [dashed line, $P(\hat{I}) = \exp(\hat{I})$] which indicates transport occurred in the non-localized regime even in the longest CROW. This negative-exponential statistical signature of non-localized propagation is significantly distinct from the long-tailed log-normal distributions reported for diffusive and localized light [15, 33, 39].

Group delay scaling

Further evidence of non-localized transport was obtained from measurements of the transmission delay, which comprises the summed contributions from each of the rings encountered by photons traveling from input to output ports, and is therefore the sum of a large number of random variables. The average delay value $\langle\tau\rangle$ (units of picoseconds, ps), shown in Fig. 2.14(a), was obtained by the root-mean-squared average of the measured group delay data over the central one-half region of the transmission band. As expected [8, 2], the average delay increased linearly with the number of resonators, N, with a slope $\langle\tau\rangle$/N = 0.73 ps/ring. This linear scaling was confirmed by additional measurements on more than 800 CROW bands measured over 16 different chips. How-

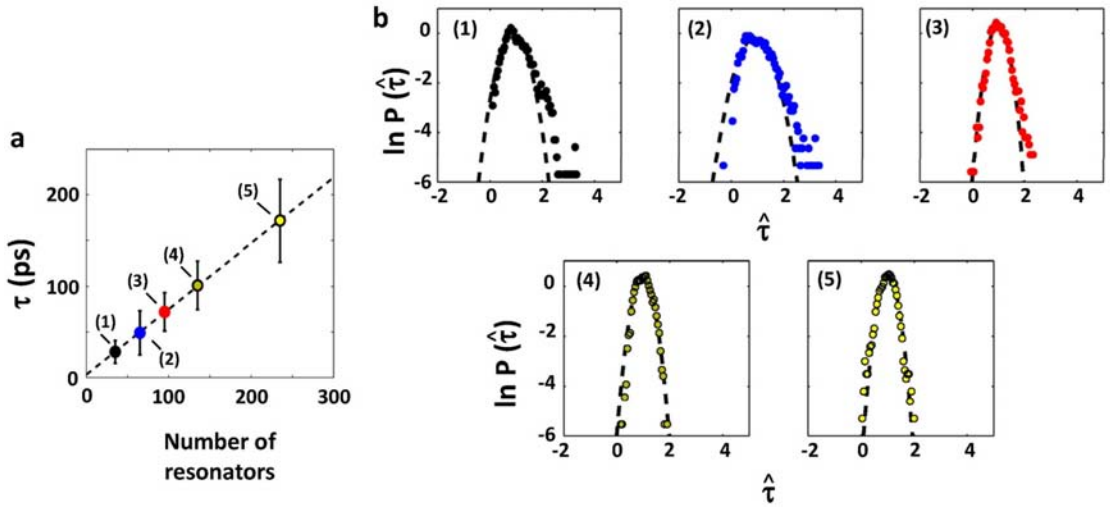

Figure 2.14: (a) The measured propagation delay averaged over the middle of a transmission band $\langle\tau\rangle$ (units of picoseconds) increased linearly with length (L = 35, 65, Ĕ, 235 rings). The errorbars represent the standard deviation, i.e., ripple, in the measured delay over the flat portion of the band. (b) The probability distributions of normalized delay $\hat{\tau} \equiv \frac{\tau}{\langle\tau\rangle}$ were peaked at unity (i.e., τ=$\langle\tau\rangle$). The dashed line is a Gaussian (normal distribution) fit to the data, which indicates ballistic propagation statistics and the absence of localization, previously estimated to be a severe constraint on achieving $>$ 100 resonator lengths of CROWs. In fact, the self-averaging properties of longer chains of resonators yielded better fits to normal statistics than for the shorter waveguides, where finite-size effects caused an asymmetric lineshape in the tails of the distributions.

ever, as mentioned before, the average propagation time through the waveguide does not by itself provide conclusive evidence that transmission occurs in the non-localized regime; the average delay is indeed expected to scale linearly with length in both the localized and non-localized regimes [34]. Therefore, we examined the distributions of the normalized time delay of propagation ($\hat{\tau} \equiv \tau/\langle\tau\rangle$, where τ represents the raw group delay data, and the denominator $\langle\tau\rangle$ is linearly proportional to N as discussed in the earlier paragraph), which are plotted in Fig. 2.14(b), using a logarithmic scale on the vertical axis for clarity. As shown by the dashed lines in Fig. 2.14(b), the delay time distributions were well described by Gaussian statistics, characteristic of the ballistic, i.e., non-localized , propagation regime only [36]. In contrast, diffusive or localized propagation would result in much wider (polynomial) tails to the distribution, as has been previously demonstrated for disordered microwave waveguides [35, 40].

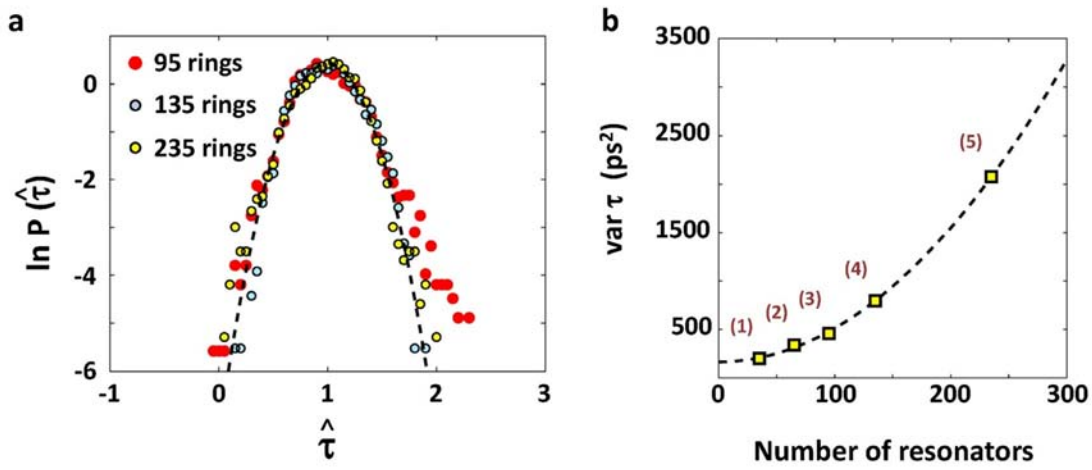

Figure 2.15: (a) The measured probability distribution functions (PDFs) of the normalized group delay $\hat{\tau} \equiv \tau/\langle\tau\rangle$ are shown, using a logarithmic scale on the vertical axis for clarity, for the waveguides labeled (3)-(5) in Fig. 2.10(a). With increasing length, the distributions converged to a single-parameter Gaussian distribution, shown by the dashed black line. (b) The variance of the measured delay (ps2) increased with the square of the number of resonators (N), as shown by the dashed fit, var(τ) = 0.0346 N^2+(12.9 ps)^2 where the second term was the typically measured group delay ripple of the measurement apparatus. This scaling behavior was different from that of conventional waveguides or cascaded fiber Bragg gratings, and as discussed in the text, demonstrated that the individual resonator excitations are mutually correlated.

Ballistic transport

In fact, the self-averaging properties of longer chains of resonators yielded better fits to normal statistics (i.e. Fig. 2.14(b), panels 3-5) than for the shorter waveguides (i.e. Fig. 2.14(b), panels 1-2), where finite-size effects caused an asymmetric lineshape [1]. As shown in Fig. 2.15(a), in the case of the three longest waveguides with 95, 135, and 235 coupled microrings, the normalized delay distributions converged to a single-parameter distribution [36] whose width describes the average level of group delay ripple per ring, equal to 0.19 ps/ring. This value can potentially be reduced with further improvements in fabrication, or by post-fabrication trimming [41]. Moreover, since Fig. 2.15(a) shows that the width of the distribution of normalized delay was a constant, i.e., independent of N, it follows that the variance of the delay itself, var(τ), scaled as N^2, as shown by the dotted line in Fig. 2.15(b). This prediction was in excellent agreement with var(τ) extracted directly from the measured data, shown by the squares

in Fig. 2.15(b), and moreover agrees with numerical simulations. This behavior was in contrast to what is expected from conventional photonic waveguides, or a sequence of cascaded fiber Bragg gratings, in which cases var(τ) scales linearly with N [42, 32, 43].

To explain this behavior, we recall that according to statistical theory, the variance of the mean of an ensemble of uncorrelated random variables of sample size N decreases as N^{-1}, which is commonly called the law of large numbers [44]. For an ensemble of correlated random variables, however, theory dictates that the variance of the sample mean (i.e., average delay per ring) reaches a constant value, independent of N, and is equal to the degree of correlation [44], so that the total delay variance of an N-ring waveguide thus scales as N^2. This latter case is indeed the behavior shown in Fig. 2.15(b), and can be explained by the physical nature of light propagation in a CROW, in which coherent oscillations of all N coupled resonators constitute each of the propagating eigenmodes. The delay values measured across the passband are therefore shown to be correlated random variables, with a sample space increasing linearly with the length of the waveguide. Therefore, Fig. 2.15 provides experimental evidence of the mutually-correlated physical mechanism by which light propagates in a CROW. Understanding the statistical scaling behavior with length is particularly relevant for phase-sensitive applications e.g., in coherent optics, power combining, waveguide quantum light circuits and slow light.

Moreover, the fact that only nearest neighbors are directly coupled fulfills the criterion for applicability of the generalized Central Limit Theorem [45] and thus, the distribution of total delay will tend to a Gaussian probability distribution as N becomes large, exactly as shown by Fig. 2.15(a). The Gaussian fit is characteristic of only the ballistic propagation regime [37]; the statistics in the near-localization (diffusive) regime would show distributions with wider polynomially-decaying tails [46], becoming even wider in the localized regime, in fact, with exponential divergence of the higher moments [36]. Furthermore, localization would destroy any long-range phase correlation across the 235-ring length of the structure. Therefore, increasing the length of a waveguide structure wherein transport occurs in the localized regime would decrease the number of resonators that are mutually coupled [25, 47], leading to an entirely different scaling behavior (exponentially growing with N) from Fig. 2.15(b) [36].

2.7 Summary

The directional couplers which constitute microring resonators of a CROW can considerably affect the dispersion characteristics of coupled-resonator optical waveguides (CROWs). Strongly coupled waveguides, on the order of a 100 nm, are necessary for properly apodizing the CROW, achieving the desired bandwidth and group delay of the pass band, and allowing for ballistic transport through a 235-ring structure.

References

[1] J. K. S. Poon, L. Zhu, G. A. DeRose, and A. Yariv, "Polymer microring coupled-resonator optical waveguides," *J. Lightwave Technol.*, vol. 24, p. 1843, 2006.

[2] F. Xia, L. Sekaric, and Y. Vlasov, "Ultracompact optical buffers on a silicon chip," *Nature Photonics*, vol. 1, pp. 65 –71, 2007.

[3] X. Luo and A. W. Poon, "Many-element coupled-resonator optical waveguides using gapless-coupled microdisk resonators," *Opt. Express*, vol. 17, pp. 23617–23628, 2009.

[4] M. Notomi, E. Kuramochi, and T. Tanabe, "Large-scale arrays of ultrahigh-q coupled nanocavities," *Nature Photonics*, vol. 2, pp. 741–747, 2008.

[5] A. Yariv, Y. Xu, R. K. Lee, and A. Scherer, "Coupled-resonator optical waveguide: a proposal and analysis," *Optics Letters*, vol. 24, pp. 711–713, 1999.

[6] J. E. Heebner, P. Chak, S. Pereira, J. E. Sipe, and R. W. Boyd, "Distributed and localized feedback in microresonator sequences for linear and nonlinear optics," *Journal of the Optical Society of America B*, vol. 21, no. 10, pp. 1818–1832, 2004.

[7] P. Sanchis, J. Marti, W. Bogaerts, P. Dumon, D. V. Thourhout, and R. Baets, "Experimental results on adiabatic coupling into soi photonic crystal coupled-cavity waveguides," *IEEE Photonics Technology Letters*, vol. 17, pp. 1199–1201, 2005.

[8] J. K. S. Poon, L. Zhu, G. A. DeRose, and A. Yariv, "Transmission and group delay of microring coupled-resonator optical waveguides," *Optics Letters*, vol. 456-458, pp. 456–458, 2006.

[9] Y. A. Vlasov, W. M. J. Green, and F. Xia, "High-throughput silicon nanophotonic wavelength-insensitive switch for on-chip optical networks," *Nature Photonics*, vol. 2, pp. 242–246, 2008.

[10] A. Melloni, F. Morichetti, C. Ferrari, and M. Martinelli, "Continuously tunable 1 byte delay in coupled-resonator optical waveguides," *Optics Letters*, vol. 33, pp. 2389–2391, 2008.

[11] J. K. S. Poon, J. Scheuer, S. Mookherjea, G. T. Paloczi, Y. Y. Huang, and A. Yariv, "Matrix analysis of microring coupled-resonator optical waveguides," *Opt. Express*, vol. 12, no. 1, pp. 90–103, 2004.

[12] M. L. Cooper, G. Gupta, M. A. Schneider, W. M. J. Green, S. Assefa, F. Xia, D. K. Gifford, and S. Mookherjea, "Waveguide dispersion effects in silicon-on-insulator coupled-resonator optical waveguides," *Optics Letters*, vol. 35, pp. 3030–3032, 2010.

[13] A. C. Turner, C. Manolatou, B. S. Schmidt, M. Lipson, M. A. Foster, J. E. Sharping, , and A. L. Gaeta, "Tailored anomalous group-velocity dispersion in silicon channel waveguides," *Optics Express*, vol. 14, p. 4357, 2006.

[14] E. Dulkeith, F. Xia, L. Schares, W. M. J. Green, , and Y. A. Vlasov, "Group index and group velocity dispersion in silicon-on-insulator photonic wires," *Opt. Express*, vol. 14, p. 3853, 2006.

[15] L. Sapienza, H. Thyrrestrup, S. Stobbe, P. D. Garcia, S. Smolka, and P. Lodahl, "Cavity quantum electrodynamics with anderson-localized modes," *Science*, vol. 327, pp. 1352–1355, 2010.

[16] S. Mazoyer, P. Lalanne, J. Rodier, J. Hugonin, M. Spasenović, L. Kuipers, D. Beggs, and T. Krauss, "Statistical fluctuations of transmission in slow light photonic-crystal waveguides," *Opt. Express*, vol. 18, no. 14, pp. 14654–14663, 2010.

[17] T. Baba, "Slow light in photonic crystals," *Nat. Photon.*, vol. 2, no. 8, pp. 465–473, 2008.

[18] D. K. Gifford, B. J. Soller, M. S. Wolfe, and M. E. Froggatt, "Optical vector network analyzer for single-scan measurements of loss, group delay, and polarization mode dispersion," *Appl. Opt.*, vol. 44, no. 34, pp. 7282–7286, 2005.

[19] J. K. S. Poon, J. Scheuer, Y. Xu, and A. Yariv, "Designing coupled-resonator optical waveguide delay lines," *J. Opt. Soc. Am. B*, vol. 21, p. 1665, 2004.

[20] C. Ferrari, F. Morichetti, and A. Melloni, "Disorder in coupled-resonator optical waveguides," *Journal of the Optical Society of America B*, vol. 26, pp. 858–866, 2009.

[21] M. L. Cooper and S. Mookherjea, "Numerically-assisted coupled-mode theory for silicon waveguide couplers and arrayed waveguides," *Optics Express*, vol. 17, pp. 1583 –1599, 2009.

[22] J. B. Khurgin, "Optical buffers based on slow light in electromagnetically induced transparent media and coupled resonator structures: comparative analysis," *Journal of the Optical Society of America B*, vol. 22, pp. 1062–1074, 2005.

[23] H. Shen, M. H. Khan, L. Fan, L. Zhao, Y. Xuan, J. Ouyang, L. T. Varghese, and M. Qi, "Eight-channel reconfigurable microring filters with tunable frequency, extinction ratio and bandwidth," *Optics Express*, vol. 18, pp. 18067–18076, 2010.

[24] D. Dai, L. Yang, and S. He, "Ultrasmall thermally tunable microring resonator with a submicrometer heater on si nanowires," *Journal of Lightwave Technol.*, vol. 26, pp. 704–709, 2008.

[25] S. Mookherjea, J. S. Park, S. H. Yang, and P. R. Bandaru, "Localization in silicon nanophotonic slow-light waveguides," *Nature Photonics*, vol. 2, p. 90, 2008.

[26] J. Topolancik, B. Ilic, and F. Vollmer, "Experimental observation of strong photon localization in disordered photonic crystal waveguides," *Phys. Rev. Lett.*, vol. 99, no. 25, p. 253901, 2007.

[27] D. C. Herbert and R. Jones, "Localized states in disordered systems," *Journal of Physics Part C Solid State Physics*, vol. 4, p. 1145, 1971.

[28] D. J. Thouless, "Relation between density of states and range of localization for one dimensional random systems," *Journal of Physics Part C Solid State Physics*, vol. 5, p. 77, 1972.

[29] D. K. Ferry, *Semiconductor transport*. New York: Taylor and Francis, London, 1st ed., 2000.

[30] E. Akkermans and G. Montambaux, *Mesoscopic physics of electrons and photons*. Cambridge: Cambridge University Press, 1st ed., 2007.

[31] M. H. Eiselt, C. B. Clausen, and R. W. Tkach, "Performance characterization of components with group delay fluctuations," *IEEE Photon. Tech. Lett.*, vol. 15, no. 8, pp. 1076–1078, 2003.

[32] H. Chotard, Y. Painchaud, A. Mailloux, M. Morin, F. Trepanier, and M. Guy, "Group delay ripple of cascaded bragg grating gain flattening filters," *IEEE Photonics Technology Letters*, vol. 14, pp. 1130–1132, 2002.

[33] E. Kogan and M. Kaveh, "Random-matrix-theory approach to the intensity distributions of waves propagating in a random medium," *Phys. Rev. B.*, vol. 52, no. 6, p. R3813, 1995.

[34] P. Markos and C. M. Soukoulis, "Intensity distribution of scalar waves propagating in random media," *Phys. Rev. B.*, vol. 71, no. 5, p. 054201, 2005.

[35] J. A. Sanchez-Gil, V. Freilikher, I. Yurkevich, and A. A. Maradudin, "Coexistence of ballistic transport, diffusion, and localization in surface disordered waveguides," *Phys. Rev. Lett.*, vol. 80, no. 5, p. 948, 1998.

[36] C. Texier and A. Comtet, "Universality of the wigner time delay distribution for one-dimensional random potentials," *Phys. Rev. Lett.*, vol. 82, no. 21, pp. 4220–4223, 1999.

[37] A. Z. Genack, P. Sebbah, M. Stoytchev, and B. A. van Tiggelen, "Statistics of wave dynamics in random media," *Phys. Rev. Lett*, vol. 82, no. 4, p. 715, 1999.

[38] J. P. R. L. F. P. Payne, "A theoretical analysis of scattering loss from planar optical waveguides," *Opt. Quantum Electron.*, vol. 26, pp. 977–986, 1994.

[39] M. Stoytchev and A. Z. Genack, "Observations of non-rayleigh statistics in the approach to photon localization," *Optics Letters*, vol. 24, no. 4, pp. 262–264, 1999.

[40] A. A. Chabanov and A. Z. Genack, "Statistics of dynamics of localized waves," *Phys. Rev. Lett.*, vol. 87, no. 23, p. 233903, 2001.

[41] C. K. Madsen and J. H. Zhao, "Postfabrication optimization of an autoregressive planar waveguide lattice filter," *Applied Optics*, vol. 36, pp. 642–647, 1997.

[42] R. Adar, C. H. Henry, M. A. Milbrodt, and R. C. Kistler, "Phase coherence of optical waveguides," *J. Lightwave Technol.*, vol. 12, no. 4, pp. 603–606, 1994.

[43] T. Goh, S. Suzuki, and A. Sugita, "Estimation of waveguide phase error in silica-based waveguides," *J. Lightwave Technol.*, vol. 15, no. 11, pp. 2107–2113, 1997.

[44] W. B. Davenport and W. L. Root, *An Introduction to the Theory of Random Signals and Noise*. New York: McGraw-Hill, 1st ed., 1958.

[45] B. Rosén, "On the central limit theorem for sums of dependent random variables," *Probability Theory and Related Fields*, vol. 7, pp. 48–82, 1967.

[46] B. A. van Tiggelen, P. Sebbah, M. Stoytchev, and A. Z. Genack, "Delay-time statistics for diffuse waves," *Phys. Rev. E*, vol. 59, no. 6, p. 7166, 1999.

[47] Y. Lahini, A. Avidan, F. Pozzi, M. Sorel, R. Morandotti, D. N. Christodoulides, and Y. Silberberg, "Anderson localization and nonlinearity in one-dimensional disordered photonic lattices," *Phys. Rev. E*, vol. 100, p. 013906, 2008.

1. Chapter 2 contains material published in:

   M. L. Cooper, G. Gupta, M. A. Schneider, W. M. J. Green, S. Assefa, F. Xia, D. Gifford, and S. Mookherjea, “Waveguide dispersion effects in silicon-on-insulator coupled-resonator optical waveguides,” *Optics Letters*, 35, 2010.

   The dissertation author was the primary author of this paper.

2. Chapter 2 contains material that was submitted to *Optics Express*:

   M. L. Cooper, G. Gupta, M. A. Schneider, W. M. J. Green, S. Assefa, F. Xia, D. Gifford, Yurii A. Vlasov, and S. Mookherjea, “Statistics of light transport in 235-ring silicon coupled-resonator optical waveguides,” submitted to *Optics Express*.

   The dissertation author was the primary author of this paper.

3 Strongly-Coupled Arrayed Waveguides

The difference between a directional coupler and an N = 2 arrayed waveguide comes down to excitation. For a directional coupler, such as those discussed in the previous sections, light begins by entering one arm of the directional coupler where it then begins to couple to the adjacent arm. Arrayed waveguides, however, are characterized by their supermodes (eigenvectors), which propagate down the waveguide with only sinusoidal variations in amplitude. It will be detailed in Chapter 4, that these two phenomena are one in the same. When light enters one arm of a directional coupler it splits (not necessarily equally), into the even and odd supermodes of the N = 2 arrayed waveguide. These supermodes then propagate down the coupler shifting in and out of phase with one another; causing the concentration of light in the directional coupler to oscillate back and forth between the separated waveguides. Here, we are concerned with the shape of these modes as the separation distance between the waveguides is varied. At sub-100 nanometer separation distances, it will be shown that these waveguides have unique properties, such as the ability to guide light in a low index medium.

3.1 Supermodes and their Probability of Excitation

Coupled mode theory predicts that when N single-mode waveguides are weakly coupled together, the modes of the cascaded waveguide structure will split into N supermodes. Fig. 3.1 and Fig. 3.2 show finite difference frequency domain simulations (Section 4.1) of the supermodes of five coupled rib waveguides surrounded by oxide, for the transverse electric and transverse magnetic polarization respectively. Each indi-

vidual single-mode waveguide measures 500 nm x 200 nm.

Boundary conditions require the continuity of the dielectric displacement. As can be seen for the TE polarization, this results in a jump discontinuity of the electric field at the top and bottom of each of the silicon rib waveguides, where the mode then decays into the cladding. For the TM polarization light undergoes the jump discontinuity at the waveguide edge within the coupling region. The magnitude of this jump discontinuity at the waveguide boundary is determined by the dielectric permittivity, ϵ, i.e., $E_{\mathrm{Clad}\perp} = \frac{\epsilon_{\mathrm{Si}}}{\epsilon_{\mathrm{SiO_2}}} E_{\mathrm{Core}\perp}$ and $E_{\mathrm{Clad}\parallel} = E_{\mathrm{Core}\parallel}$. For a silicon/air interface this discontinuity is a factor of 12, and for silicon/oxide, 5.6. The premise behind slot waveguides is that for the TM polarization if the waveguide separation is sufficiently close the electric field will not have ample room to decay, and will thus remain high in the slot. As the magnetic field is continuous in the coupling region, this results in a higher optical intensity in the low index material between the waveguides.

Light is typically coupled into the multi-slot waveguide by a waveguide (without slots) of equal width, as shown in Fig. 3.3. There can be a significant difference between the shape of the feeder mode with that of each supermode of the arrayed waveguide. The percent of power, a^2, that couples into each of the supermodes by the feeder waveguide can be determined from the overlap integral of the corresponding supermode, $\hat{E}^{s.m.}$, with the mode of the feeder waveguide, $\hat{E}^{Feeder}$:

$$a^2 = \frac{\left| \left\langle \hat{E}^{Feeder} \hat{E}^{s.m.} \right\rangle \right|^2}{\left\langle \hat{E}^{Feeder} \hat{E}^{Feeder} \right\rangle \left\langle \hat{E}^{s.m.} \hat{E}^{s.m.} \right\rangle}. \tag{3.1}$$

3.2 Giant Birefringence in Multislot Waveguides

The guided modes of the multi-slot waveguide in Fig. 3.3 are shown in Fig. 3.4; also shown, is the fundamental mode for each polarization for the multimode feeder waveguide. This multi-slot waveguide consist of five silicon nanowires of 500 nm height, 150 nm width, and separated by 100 nm, with an air cladding that allows for an ultra-high birefringence [1]. For the TM-polarization, the multi-slot waveguide is single-mode. Numerically solving Eq. (3.1) we note a mode mismatch of 42%, result-

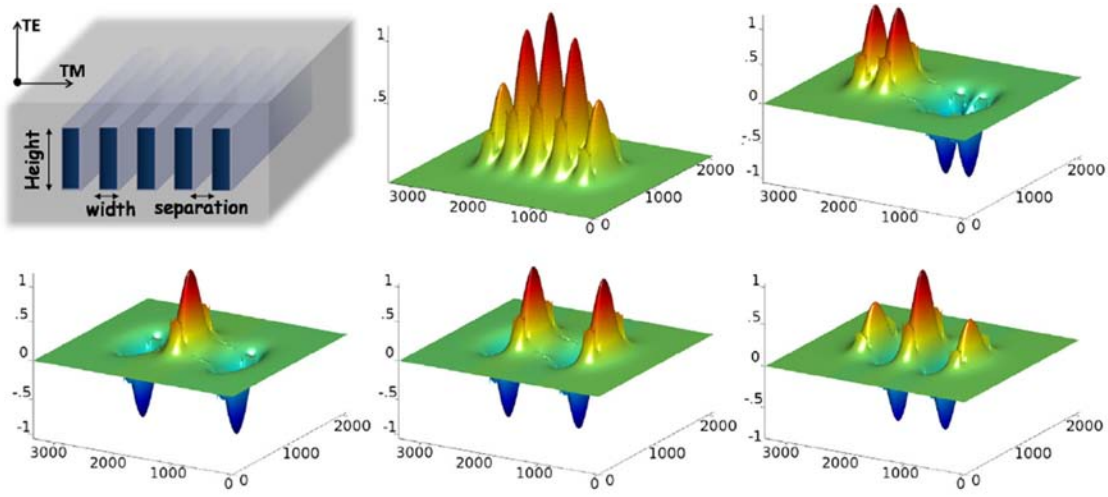

Figure 3.1: *Transverse Electric Polarization*: Supermodes of five silicon-on-insulator arrayed waveguides of 500 nm height, 200 nm width, at a separation distance of 200 nm.

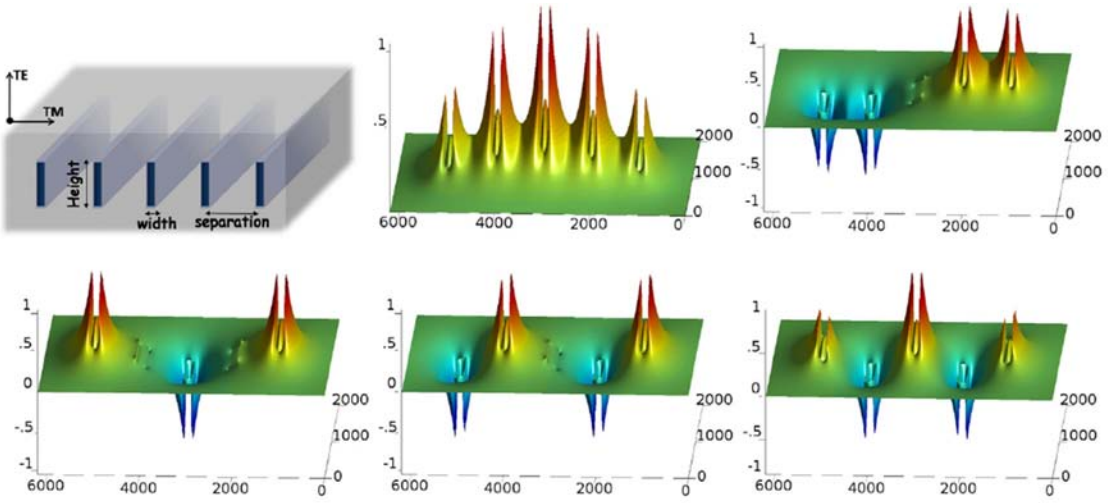

Figure 3.2: *Transverse Magnetic Polarization*: Supermodes of five silicon-on-insulator arrayed waveguides of 500 nm height, 200 nm width, at a separation distance of 500 nm.

ing in a loss of ≈ 3.75 dB—which is coupled to radiation modes (this doesn't include the additional losses due to the silicon/air reflections caused by the Fabry-Perot gap shown in Fig. 3.3). For the TE Polarization, one can readily calculate that the multi-slot waveguide supports three guided modes, where 95% of the light from the feeder waveguide will couple into the fundamental mode, $\approx$0% for TE_1 and 1.6% for TE_2.

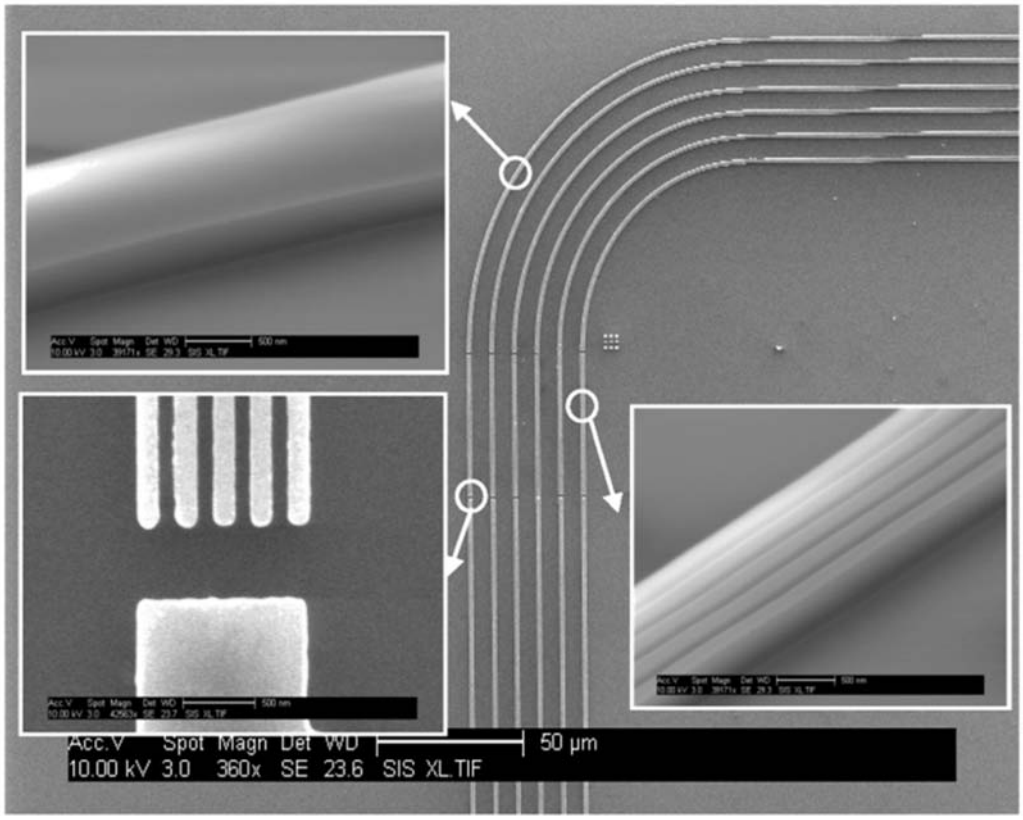

Figure 3.3: An arrayed waveguide consisting of an SiO_2 substrate and an air superstrate, with 500 nm high silicon rib waveguides, each 150 nm wide, and separated by 100 nm "slots". Both the effective index and group index of this structure is very different for each polarization.

As shown in Fig. 3.4, for the TM polarization of the multi-slot waveguide most of the light is being guided in air, while, for the TE polarization most of the light is being guided in the silicon. Recalling the discussion of the effective index from Section 1.2, this will result in a very high effective index for the TE polarization—guided in silicon, and a very low effective index for the TM polarization—guided in air.

This type of birefringence is referred to as "form birefringence", and is used to describe periodic layered media where the periodicity is smaller then the wavelength of the light. The ability to engineer birefringence is useful in nonlinear optics, which requires phase matching between different optical waves. In contrast to earlier studies where light is incident in a surface normal configuration, for the device shown in Fig. 3.3 light propagates axially along the length of the etched ribs. Previous values of birefrin-

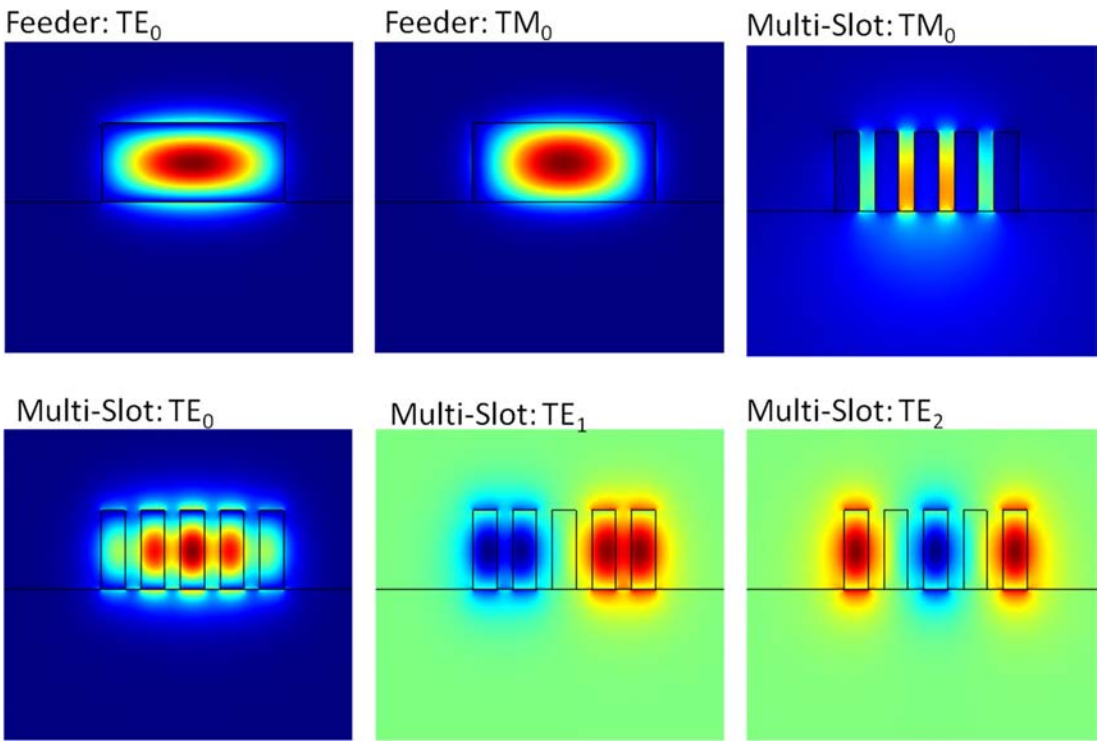

Figure 3.4: The modes of the multi-slot waveguide shown in Fig. 3.3 for each polarization, as well as the modes of the feeder waveguide. Note that for the TM_0 polarization the light is mostly guided in the slot region, allowing for a high birefringence between the two polarizations. By numerically solving Eq. (3.1), one can see that there will be a modal mismatch loss of 3.75 dB with the feeder waveguide. As no other modes are supported for this structure for the transverse magnetic polarization, this "lost" light is radiated into free space.

gence have been on the order of $\Delta n \approx 0.04$ [2]. The structure shown in Fig. 3.3 was optimized to achieve a record birefringence of $\Delta n_{group} \approx 1.5$ and $\Delta n_{eff} \approx 1$.

The fraction of the slot-to-slot width (period) occupied by the low-index cladding defines the filling fraction, q, of an arrayed waveguide. A schematic of the transverse cross-section of the multi-slot waveguide is shown in Fig. 3.5(a). Using a finite difference frequency domain algorithm (Section 4.1), the effective index is calculated for each polarization as the filling fraction is varied. Fig. 3.5(b) shows the difference between these two effective indices as a functions of q. The shape of the curve is similar to that derived using effective medium theories for plane waves incident on an infinitely-wide periodically stratified grating [2]. As shown, a maximum birefringence occurs at

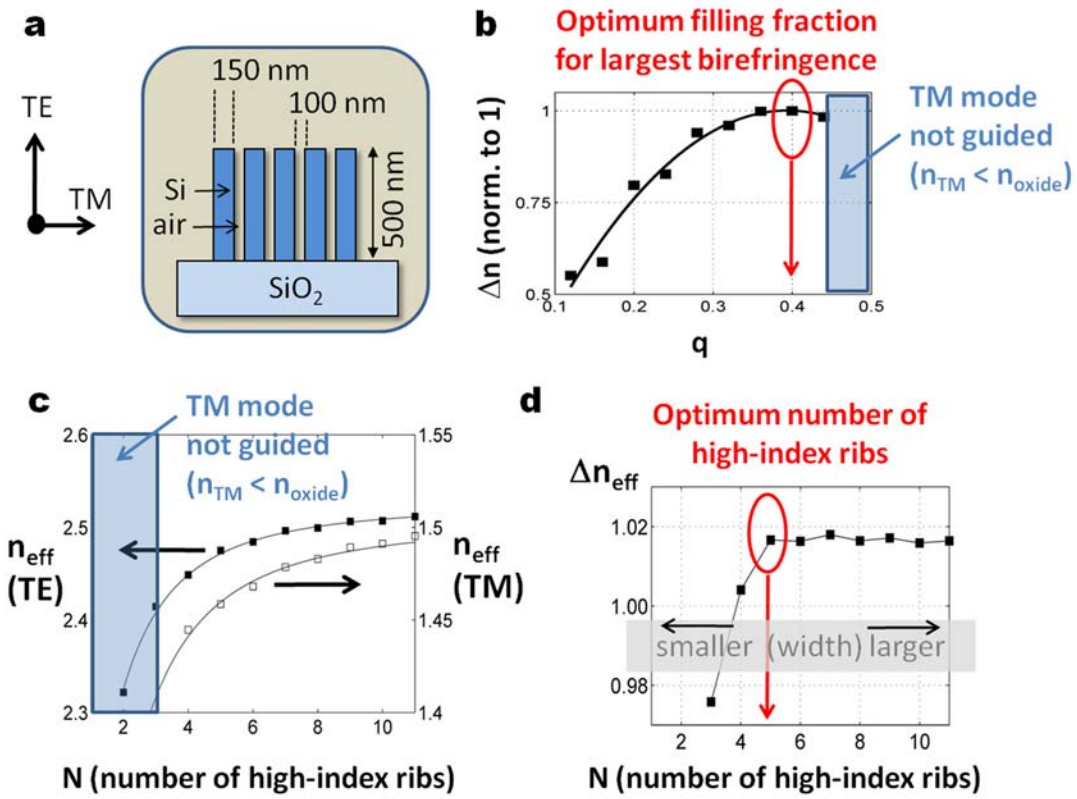

Figure 3.5: (a) Schematic of the cross-section of the giant birefringence multi-slot waveguide. (b) Using a finite difference frequency domain algorithm, the maximum filling fraction was calculated to be q = 0.38. For filling fractions larger then q = 0.43, the effective index of the transverse magnetic mode drops below that of the oxide substrate. (c) Plot of the effective indices for both polarization for different values of N. (d) Calculation of the birefringence, showing that it asymptotes to a constant value for increasing N, and that N = 5, as fabricated, is the smallest value of N for which the birefringence saturates. The physical reason behind the saturation is that for N $<$ 5, the mode mostly resides in the oxide. By continuously adding more high-index regions light is pulled out of the substrate. Once N = 5, light has been pulled out of the substrate, and adding additional waveguides has no effect on the structure's birefringence.

$q = 0.38$, also, there exists a value of q beyond which no transverse magnetic modes are supported. The physical reason behind this cut-off is that large filling fractions have very little silicon. As such the potential-well defined by the silicon waveguide thus has a higher energy compared to the ocean of oxide below it, forcing the mode to dive into the substrate. Fig. 3.5(c) plots the effective indices for the two polarizations for an increasing number, N, of silicon ribs. From this figure, one may readily calculate the

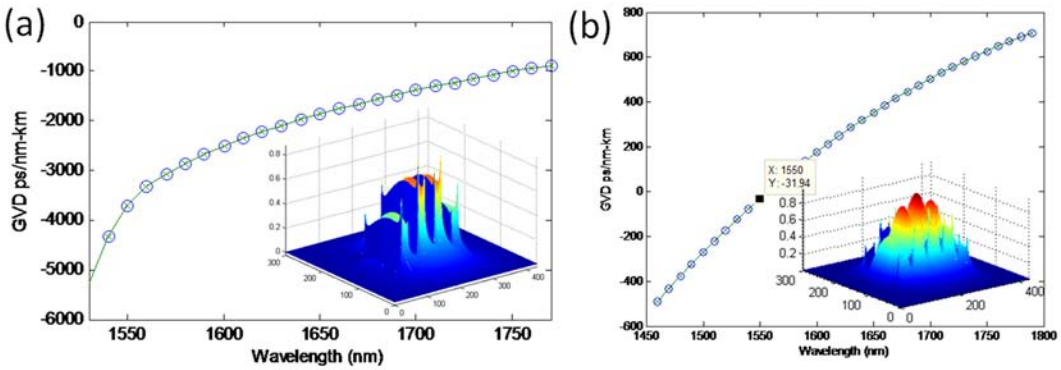

Figure 3.6: Group velocity dispersion for the (a) transverse magnetic and (b) transverse electric polarization.

corresponding birefringence shown in Fig. 3.5(d). It can be seen that the birefringence asymptotes to a constant value for increasing N, and that N = 5, as fabricated, is the smallest value of N for which the birefringence saturates. The physical reason behind this saturation is that N $<$ 5, the mode mostly resides in the oxide. By continuously adding more high-index regions light is pulled out of the substrate. Once N = 5, light has been fully pulled out of the substrate, and adding additional waveguides has no effect on the structure's birefringence.

The finite difference frequency domain algorithm may be further used to give an estimate of the dispersive nature of these corresponding modes. As shown in Fig. 3.6, the slot-mode has significantly higher dispersion compared with the transverse electric polarization—which has a wavelength crossing the telecommunications band of 0 GVD. This will result in more broadening of a pulse as it propagates through this device for the TM polarization compared with the TE polarization.

As shown in Fig. 3.3, in order to measure the group indices the multi-slot waveguide was separated by the feeder and output waveguide (that have no slots) by 50 nm air gaps. A C+L band narrow-spectrum mode-hop free turnable laser source was coupled into the chip using tapered and lensed polarization maintaining fibers. The air gaps form a Fabry-Perot resonator of precisely known length. By bandpass-filtering the measured transmission spectrum, one may extract the frequency component which corresponds to the Fabry-Perot resonances of length L, shown in Fig. 3.7. Using the definition of the free spectral range, one may then determine the group index for both polarizations. The

experimental values shown in Fig. 3.7 agree very well with simulation.

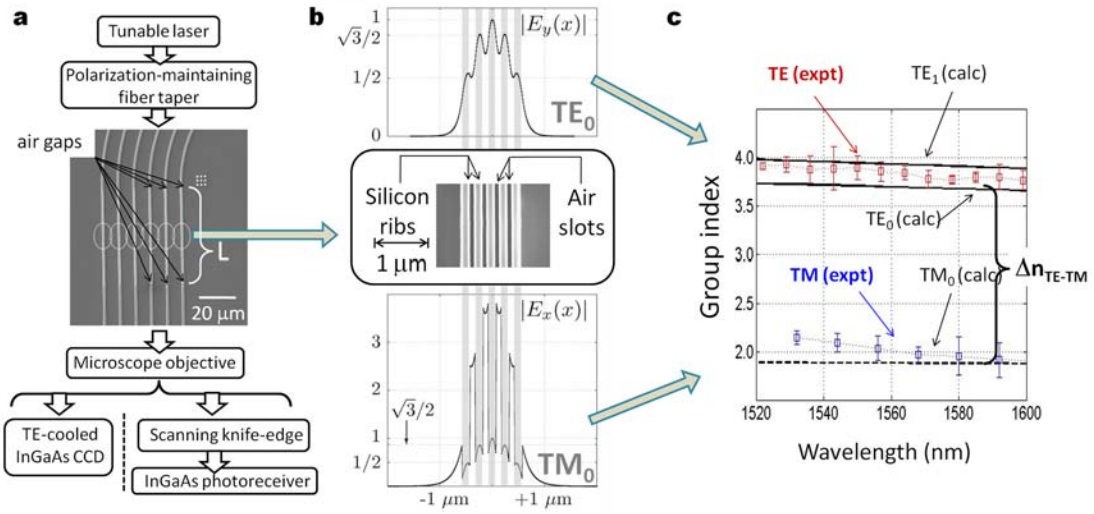

Figure 3.7: (a) Measurement setup for experimentally determining the group indicies of the multi-slot waveguide. A C+L band narrow-spectrum mode-hop free turnable laser source was coupled into the chip using tapered and lensed polarization maintaining fibers. The air gaps form a Fabry-Perot resonator of precisely known length. By bandpass-filtering the measured transmission spectrum, one may extract the frequency component which corresponds to the Fabry-Perot resonances of length L. (b) Cross-section of the transverse magnetic and transverse electric modes of the multi-slot waveguide. (c) Using the definition of the free spectral range, the group index was obtained. The experimental values shown are in good agreement with the predicted values.

3.3 Horizontal vs. Vertical Slots

By way of comparison, simulations were done to optimize a similar structure composed of horizontal slot waveguides. The horizontal multi-slot waveguide would be expected to have reduced losses, as the dominant source of scattering losses for the vertical-slot waveguide is due to the surface roughness created by the etching process. It was shown in the previous section that a vertical slot waveguide could obtain a giant birefringence as high as $\Delta n_{group} \approx 1.5$ and $\Delta n_{eff} \approx 1$. This was achieved by guiding light in the air-slot for one polarization, and silicon for the other. This is not practical for the horizontal slot-waveguide shown in Fig. 3.8, where a supporting medium is required to keep the device from collapsing. Fig. 3.8 shows similar calculations for the horizontal

slot waveguide, where the slot material was filled with SiO_2. Similar to the vertical multi-slot waveguide, the birefringence peaks for a given filling fraction, and for high filling fractions the modes are no longer guided. However, as the slot-mode is now located in a higher index, n_{SiO_2} = 1.46, the maximum birefringence that can be obtained is Δn_{eff} = 0.64, significantly less then the vertical multi-slot waveguide.

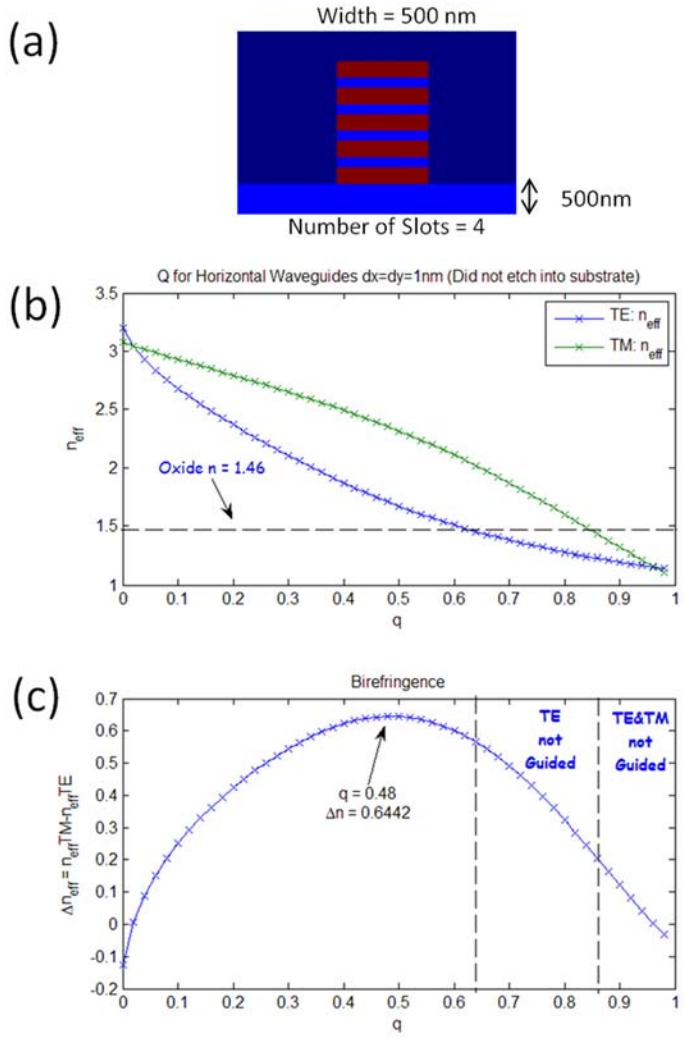

Figure 3.8: (a) Schematic of the horizontal multi-slot waveguide consisting of 500 nm wide and 150 nm tall silicon waveguides stacked vertically and separated by 100 nm of SiO_2. (b) Using a finite difference frequency domain, the effective index of both modes are calculated as the filling fraction, q, is varied. (c) The birefringence of the horizontal multi-slot waveguide. The maximum value that can be obtained is considerably less then for the vertical multi-slot waveguide.

3.4 The “Slot” Waveguide and its Applications

In addition to giant birefringence, slot waveguides have proven useful for a number of additional applications:

Modulators

Most modulators on the market today require voltage shifts on the order of one volt to achieve full extinction. In order to maximize the shift in effective index of an electro-optic waveguide, M. Hochberg et al. [3] proposed a modulator that uses the two silicon ridges of a slot waveguide as a pair of very closely spaced but electrically isolated electrodes. These closely spaced electrodes allow for a strong interaction between the electric field and the non-linear polymer. They found that the modulation strength was inversely proportional to the width of the slot; and with a nonlinear polymer of r_{33} = 500 pm/V, a Mach-Zehnder modulator with a V_{π}-L of 4 mV-cm may be realized.

Detectors

T. Baehr-Jones et al. [4], demonstrated a slot waveguide filled with nonlinear electro optic polymers that could detect low power optical signals. Due to the nanoscale high intensity confinement of light in the slot waveguide a standing DC field is created. This field induces a potential difference between the silicon electrodes resulting in current flow which allows for optical to electrical conversion. They were able to measure conversion with less than 1mW of non-pulsed input.

Polarization independent couplers

Making use of the distinctiveness of the TE and TM mode profiles of the slot waveguide, Fujisawa et al. [5] were able to overcome the high polarization dependence known to exist for SOI optical waveguide directional couplers. For two slot waveguides, they observed that the coupling length of the TM mode shows a greater dependence on the slot material compared to the TE mode. This is because in the TM mode the light is guided in the slot material. By choosing a material for the slot that corresponds to identical coupling lengths of the two polarizations, a polarization independent optical

waveguide direction coupler is realized. Coupling lengths on the order of tens of microns can be achieved. Polarization independent operation can also be obtained for a given slot material by tuning the separation of the two slot waveguides.

All-optical logic gates

Extending on their slot waveguide polarization independent coupler Fujisawa et al. [6] proposed an all-optical logic gate based on nonlinear slot-waveguide couplers. By filling the slot with a material that has Kerr type nonlinearity, a slot waveguide is realized that operates as a polarization independent coupler in the linear regime, and becomes polarization dependent in the nonlinear regime. In the nonlinear regime the TE mode no longer couples to the adjacent waveguide, while the TM shows almost no change in the transmission characteristic compared to the linear regime. With the use of silicon nanocrystals switching powers on the order of tens of watts is achieved. With this device NOT, OR and AND logic gates can be realized.

Slow light

By embedding one-dimensional photonic crystals into slot waveguides Riboli et al. [7] were able to achieve a coupled resonator optical waveguide (CROW) device that shows a group velocity of more than c/10 at 1.55 m. The embedded photonic crystal was obtained by defining trenches, or air slits, perpendicular to the propagation direction of a slot waveguide.

Polarization independent multimode interference (MMI) slot waveguide

Continuing on the idea that the optical characteristics of the TM mode of a slot waveguide are more sensitive to the slot material then the TE mode, Fujisawa et al. proposed a polarization insensitive multimode interference waveguide [8]. The beat length L which characterizes MMI waveguides, shows a greater dependence on the slot material for the TM mode then the TE. If the width of the MMI slot waveguide is not too thick, then one can find an index in which the beat length for the two polarizations are

identical. At this beat length the MMI slot waveguide achieves polarization independence. Fujisawa et al. also note that having more than 2 output ports may be difficult for their geometry as there are no crossing points in the L curves for the two polarizations with widths greater than 10 m.

Optical resonators

In silicon nanowires light is strongly confined to the core of the waveguide. These waveguides can be fabricated with very low loss enabling high Q resonators. However at high intensities two photon absorption (TPA) in silicon becomes a significant phenomenon and can lead to high optical losses. The slot waveguide maybe be able to overcome this problem as it allows light to still be tightly confined while concentrating it in between the silicon ribs reducing the losses associated with TPA. Baehr-Jones et al., achieved a quality factor of 27,000 using the slot waveguide geometry with losses of -10 dB/cm [9].

Hybrid slot waveguides

Using silicon hybrid solutions [10], researchers were able to overcome the slow dynamics resulting from two photon absorption generated free carriers. Using molecular beam deposition to cover the slot waveguide with organic materials, all-optical interactions were significantly enhanced. Researchers were able to demonstrate record nonlinear coefficient as high as $\gamma = 10^{-5}$ 1/W-km without introducing significant absorption. This allowed for the demonstration of all optical demultiplexing at speeds of all-optical 170.8 Gb/s.

3.5 Summary

In this Chapter 2 and 3, it was shown that new device functionality can be achieved in silicon photonics through strongly coupled devices. For coupled resonator optical waveguides, directional couplers spaced on the order of 100 nm are needed for proper apodization. Further, it was demonstrated that by utilizing a higher coupling coefficient, “ballistic” propagation may be achieved for a coupled-resonator structure con-

sisting of 235-rings. For slot-waveguides, it was shown that an ultra-high birefringence can be achieved if the coupler is separated by sub-100 nm; numerous other device functionalities were also outlined. However despite their prominence in photonic research, most of the well developed formalism for analytically calculating the modal properties of optical waveguides are simply not accurate for high-index contrast strongly coupled devices, requiring one to rely on numerical techniques. In the next chapter, methods of numerically characterizing these structures will be detailed.

References

[1] S. H. Yang, M. L. Cooper, P. R. Bandaru, and S. Mookherjea, "Giant birefringence in multi-slotted silicon nanophotonic waveguides," *Optics Express*, vol. 16, p. 8306, 2008.

[2] P. Yeh, *Optical Waves in Layered Media*. New York: John Wiley & Sons, Inc., 2005.

[3] M. Hochberg, T. Baehr-Jones, G. Wang, J. Huang, P. Sullivan, L. Dalton, and A. Scherer, "Towards a millivolt optical modulator with nano-slot waveguides," *Optics Express*, vol. 15, p. 8401, 2007.

[4] T.Baehr-Jones and M. Hochberg, "Optical modulation and detection in slotted silicon waveguides," *Optics Express*, vol. 13, p. 5216, 2005.

[5] T. Fujisawa and M. Koshiba, "Polarization-independent optical directional coupler based on slot waveguides," *Optics Letters*, vol. 31, p. 56, 2007.

[6] T. Fujisawa and M. Koshiba, "All-optical logic gates based on nonlinear slot-waveguide couplers," *J. Opt. Soc. Am. B*, vol. 23, pp. 684–690, 2006.

[7] F. Riboli, P. Bettotti, and L. Pavesi, "Band gap characterization and slot light effects in one dimensional crystals based on silicon slot-waveguides," *Opt. Express*, vol. 12, p. 11769, 2007.

[8] T. Fujisawa and M. Koshiba, "Theoretical investigation of ultra small polarization-insensitive 1 x 2 multimode interference waveguides based on sandwiched structures," *Phot. Tech. Lett.*, vol. 18, pp. 1246 – 1248, 2006.

[9] T. Baehr-Jones, M. Hochberg, C. Walker, , and A. Scherer, "High-q optical resonators in silicon-on-insulator-based waveguides," *Applied Physics Letters*, vol. 86, p. 081101, 2005.

[10] C. Koos, P. Vorreaul, T. Vallaitis, P. Dumon, W. Bogaerts, R. Baets, B. Esembeson, I. Biaggio, T. Michinobu, F. Diederich, W. Freude, and J. Leuthold, "All-optical high-speed signal processing with siliconŰorganic hybrid slot waveguides," *Nature Photonics*, vol. 3, pp. 216–219, 2009.

1. Chapter 3 contains material published in:

   S. H. Yang, M. L. Cooper, P. R. Bandaru and S. Mookherjea, “Giant birefringence in multi-slotted silicon nanophotonic waveguides,” *Optics Express*, 16, 2008.

   The dissertation author is the secondary author of this paper.

4 Modeling Techniques for Nano-photonic Devices

If you don't know where you are going, any road will take you there.
—Lewis Carroll, Alice in Wonderland, 1865

One of the biggest expenses for research on photonic devices is fabrication. In a recent commentary article for *Nature Photonics*, Michael Hochberg and Tom Baehr-Jones point out that, "A single high-resolution photomask can cost over US $100,000, and an advanced electronics chip can require a set of 40 masks or more with varying resolutions" [1]. The ability to accurately design and simulate device functionality before fabrication is therefore crucial in reducing company costs. In this chapter numerical methods for simulating the dispersive effects of waveguides, directional couplers, and coupled resonator optical waveguides will be reviewed. It will be shown how device parameters can be varied from their nominal values to determine fabrication tolerances, necessary for evaluating and predicting device yield. This chapter almost entirely focuses on frequency domain simulation methods, however, a technique for simulating the eye-diagrams for a 40 Gb/s data stream propagating through a disordered CROW will also be highlighted.

4.1 Numerical Solutions to Maxwell's equations

The fundamental equations that govern electromagnetism are Maxwell's equations. The electromagnetic modes of an isolated single waveguide, the supermodes of an arrayed waveguide, or (equivalently) the even and odd modes of a directional cou-

pler, are all solutions to these fundamental equations. These equations, named after the Scottish physicist James Clerk Maxwell, consist of a compilation of equations:

$$\nabla \times \mathbf{E} = \frac{-\partial \mathbf{B}}{\partial t} \qquad \text{(Faraday's law)} \tag{4.1a}$$

$$\nabla \times \mathbf{H} = \mathbf{J} + \frac{\partial \mathbf{D}}{\partial t} \qquad \text{(Ampere's law)} \tag{4.1b}$$

$$\nabla \cdot \mathbf{D} = \rho \qquad \text{(Gauss's law)} \tag{4.1c}$$

$$\nabla \cdot \mathbf{B} = 0 \qquad \text{(Gauss's law for magnetism)} \tag{4.1d}$$

where **E** is the electric field vector, **B** the magnetic flux density vector, **D** the electric displacement vector, and **H** the magnetic field vector. ρ and **J** represent the volume density of free charges, and the density vector of free currents, respectively, and are set to zero when finding the eigenvectors (modes) of a dielectric waveguide. Incidentally, Maxwell's contribution was an additional term in Ampere's law. Assuming a time dependence of $e^{j\omega t}$, with $\mathbf{J} = \rho = 0$, and substituting in the constitutive equations for linear dielectric materials, $\mathbf{D} = \epsilon\mathbf{E}$ and $\mathbf{B} = \mu\mathbf{H}$, Faraday's law and Ampere's law may be further reduced:

$$\nabla \times \mathbf{E} = -i\omega\mu_0\mathbf{H} \tag{4.2a}$$

$$\nabla \times \mathbf{H} = j\omega n^2\epsilon_0\mathbf{E} \tag{4.2b}$$

where ϵ and μ for a given dielectric material are related to their respective values in vacuum ($\epsilon_0 = 8.854 \times 10^{-12}$ F/m and $\mu_0 = 4\pi \times 10^{-7}$) by $\epsilon = \epsilon_0 n^2$, and $\mu = \mu_0$, where n is the refractive index of the dielectric material. In similar form as [2], taking the curl of Eq. (4.2a) and using Eq. (4.2b), along with the vector identity $\nabla \times \nabla = \nabla\left(\nabla\cdot\right) - \nabla^2$, one obtains:

$$\nabla^2\mathbf{E} + n^2k^2\mathbf{E} = \nabla\left(\nabla \cdot \mathbf{E}\right), \tag{4.3}$$

note that all of the vectorial components are contained on the right hand side.

Countless numerical and analytical techniques have been developed for reducing and then solving Eq. (4.3) for rectangular waveguides. Among the most prevalent analytical solutions, which rely on perturbative approaches, are Marcatili's method [3]—which solves the rectangular waveguide as two independent slab waveguides, Kumar's method [4]—which improved on Marcatili's method by analyzing the diagonal components of the waveguide's refractive index profile, and perhaps the most well known due to its applicability to ridge waveguides: the effective index method [5]. While these analytical techniques give fairly accurate solutions to the waveguide's electric field profiles for high-index contrast silicon-on-insulator nanowires, they often lead to erroneous results in predicting the propagation constants: used to determine group delay, group velocity dispersion, coupling lengths, etc. Accurate design of high-index contrast strongly coupled devices thus requires analysis using robust numerical techniques to solve Eq. (4.3). In the following section, we outline one method specifically: the finite difference frequency domain algorithm.

Finite difference frequency domain

In the finite-difference frequency-domain (FDFD) algorithm, developed by C. L. Xu *et al*. [2], the dielectric profile of the waveguide's cross section is discretized on a rectangular grid as shown in Fig. 4.1(a,b). We note from Eq. (4.1c) that the three vectorial components of the electric field are directly related such that once two components are solved for, determination of the final component is straight forward.

In similar fashion as [2], we begin by expanding Gauss's law into its transverse and axial components:

$$\nabla_\perp \cdot \left(n^2 E_\perp\right) + \frac{\partial n^2}{\partial z} E_z + n^2 \frac{\partial E_z}{\partial z} = 0. \tag{4.4}$$

As we are solving for the modes of a waveguide assumed to be invariant in the direction of propagation, z, the middle term on the LHS may be set to zero. Similarly we expand the RHS of Eq. (4.3),

$$\nabla^2 \mathbf{E} + n^2 k^2 \mathbf{E} = \nabla \left(\nabla_\perp \cdot E_\perp + \frac{\partial E_z}{\partial z} \right). \tag{4.5}$$

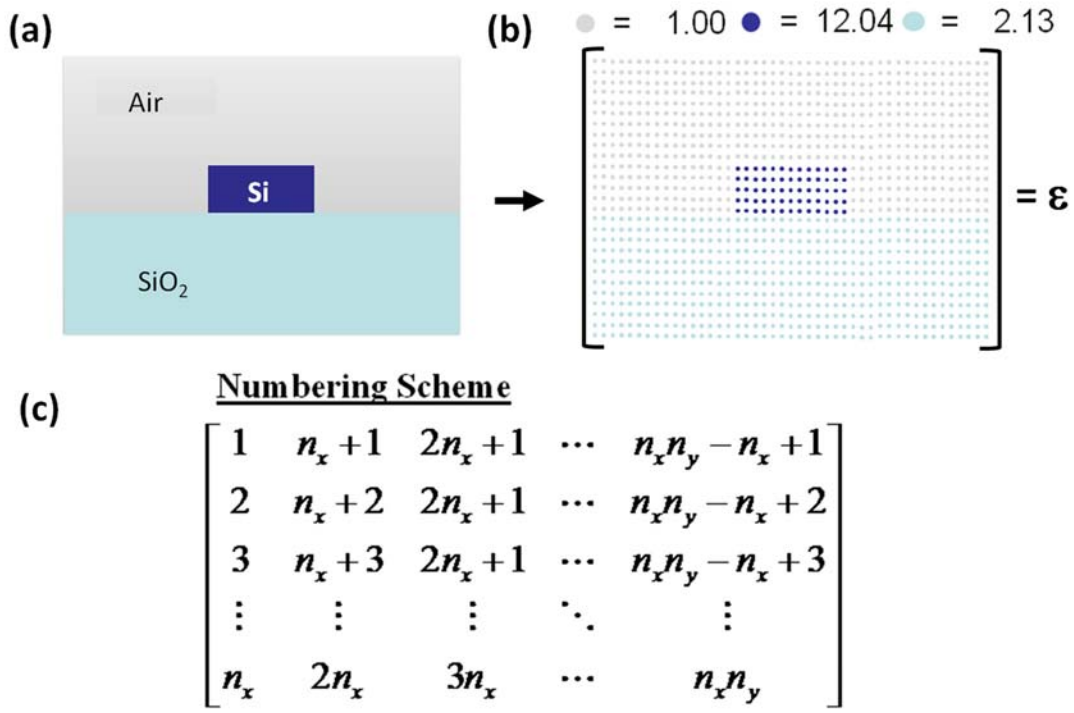

Figure 4.1: (a) Typical silicon-on-insulator waveguide (b) In the finite difference frequency domain algorithm the dielectric permittivity, ϵ, of the piecewise homogeneous layers of the waveguide are discretized into a matrix. Note that the refractive index matrix is readily calculated as $n = \epsilon^{1/2}$. (c) Numbering scheme used to label the individual elements of the matrix shown in (b).

Solving Eq. (4.4) for $\frac{\partial E_z}{\partial z}$, substituting into Eq. (4.5), and assuming a modal profile of the form, $\mathbf{E}(x, y, z) = \mathbf{E}_\perp(x, y)e^{-i\beta z}$, one obtains the transverse vectorial wave equation:

$$\nabla_\perp^2 \mathbf{E}_\perp + \left(n^2 k^2 - \beta^2\right) \mathbf{E}_\perp = \nabla_\perp \left[\nabla_\perp \cdot \mathbf{E}_\perp - \frac{1}{n^2} \nabla \cdot (n^2 \mathbf{E}_\perp)\right], \tag{4.6}$$

where $\mathbf{E}_\perp(x, y)$ is the transverse electric field vector. Decomposing Eq. (4.6) into its individual transverse components, $\hat{\mathbf{x}}$ and $\hat{\mathbf{y}}$, one obtains two equations written in matrix form as

$$\begin{pmatrix} P_{xx} & P_{xy} \\ P_{yx} & P_{yy} \end{pmatrix} \begin{pmatrix} E_x \\ E_y \end{pmatrix} = \beta^2 \begin{pmatrix} E_x \\ E_y \end{pmatrix} \tag{4.7}$$

where,

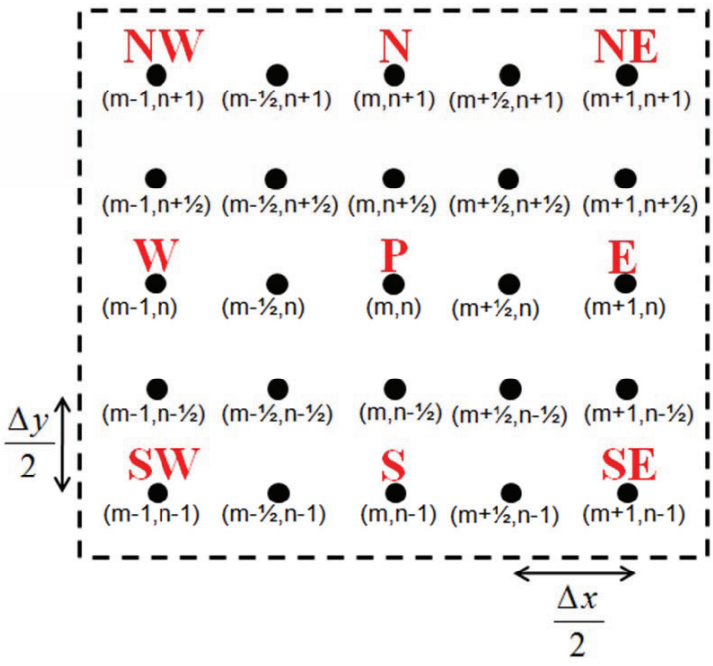

Figure 4.2: A single point shown in Fig. 4.1, labeled here as **P**, is characterized and differentiated using its cardinal and inter-cardinal terms.

$$P_{xx}E_x = \frac{\partial}{\partial x}\left[\frac{1}{n^2}\frac{\partial\left(n^2E_x\right)}{\partial x}\right]+\frac{\partial^2 E_x}{\partial y^2}+n^2k^2E_x\,,\; P_{xy}E_y = \frac{\partial}{\partial x}\left[\frac{1}{n^2}\frac{\partial(n^2E_y)}{\partial y}\right]+\frac{\partial^2 E_y}{\partial x\,\partial y},$$

$$P_{yx}E_x = \frac{\partial}{\partial y}\left[\frac{1}{n^2}\frac{\partial(n^2E_x)}{\partial x}\right]+\frac{\partial^2 E_x}{\partial y\,\partial x}\,,\; P_{yy}E_y = \frac{\partial}{\partial y}\left[\frac{1}{n^2}\frac{\partial(n^2E_y)}{\partial y}\right]+\frac{\partial^2 E_y}{\partial x^2}+n^2k^2E_y.$$

Eq. (4.7) is an eigenvalue problem that may be solved using various numerical techniques. For the results presented in this dissertation, Matlab's subroutine "eigs" was used, which is optimized for solving the eigenvalues of sparse matrices (a matrix primarily populated with zeros). It will be shown later that Eq. (4.7) is indeed a sparse matrix.

Operator discritisation

When a continuous function $u(x)$ is discretized at equal intervals separated by Δx, its first order and second order derivatives at a point u_m are readily calculated using central difference formulas:

$$\frac{\partial u_m}{\partial x} = \frac{u_{m+1} - u_{m-1}}{2\Delta x} \tag{4.8a}$$

$$\frac{\partial^2 u_m}{\partial x^2} = \frac{u_{m+1} - 2u_m + u_{m-1}}{\Delta x^2}. \tag{4.8b}$$

In this section discretization of P_{xx} will be presented, the derivation for the other operators is similar [6]. In FDFD *each* data point shown in Fig. 4.1(b) is characterized and labeled by a grid such as the one shown in Fig. 4.2. For clarity of derivation, $P_{xx}E_x$ is broken up into three subsections.

$$P_{xx}E_x = \underbrace{\frac{\partial}{\partial x}\left[\frac{1}{n^2}\frac{\partial(n^2 E_x)}{\partial x}\right]}_{(1)} + \underbrace{\frac{\partial^2 E_x}{\partial y^2}}_{(2)} + \underbrace{n^2 k^2 E_x}_{(3)} \tag{4.9}$$

Using Fig. 4.2, (3) can readily be discretized by inspection:

$$(3) = n^2_{(m,n)} k^2 E_{x|(m,n)}. \tag{4.10}$$

In words, the number for this term in the matrix element is simply the refractive index at that location squared times the wavenumber squared. Eq. (4.8b) may be used directly to solve for (2):

$$(2) = \frac{E_{x|(m,n+1)} - 2E_{x|(m,n)} + E_{x|(m,n-1)}}{\Delta y^2}. \tag{4.11}$$

To solve for (1), Eq. (4.8a) is used once for the inner partial derivative:

$$(1) = \frac{\partial}{\partial x}\left[\frac{1}{n^2}\left(\frac{n^2_{(m+1/2,n)} E_{x|(m+1/2,n)} - n^2_{(m-1/2,n)} E_{x|(m-1/2,n)}}{\Delta x}\right)\right], \tag{4.12}$$

and once again for the outer partial derivative:

$$\begin{aligned}(1) \;=\; & \frac{1}{n^2_{(m+1/2,n)}}\left[\frac{n^2_{(m+1,n)} E_{x|(m+1,n)} - n^2_{(m,n)} E_{x|(m,n)}}{\Delta x^2}\right] - \\ & \frac{1}{n^2_{(m-1/2,n)}}\left[\frac{n^2_{(m,n)} E_{x|(m,n)} - n^2_{(m-1,n)} E_{x|(m-1,n)}}{\Delta x^2}\right].\end{aligned} \tag{4.13}$$

In order to obtain an expression in terms of the cardinal points as shown in Fig. 4.2, the refractive index at an intermediate data point is taken as an average of the nearest-neighbor cardinal points, known as the "graded index approximation" [7]:

$$n^2_{(m+1/2,n)} \approx \frac{1}{2}\left(n^2_{(m+1,n)} + n^2_{(m,n)}\right) \tag{4.14a}$$

$$n^2_{(m-1/2,n)} \approx \frac{1}{2}\left(n^2_{(m-1,n)} + n^2_{(m,n)}\right). \tag{4.14b}$$

Substituting the graded index approximation into Eq. (4.13), and after a few algebraic steps and grouping of like terms, P_{xx} may be expressed as:

$$\begin{aligned} P_{xx}E_x &= P_{xxW}E_{x|(m-1,n)} + P_{xxP}E_{x|(m,n)} + \\ &\quad P_{xxE}E_{x|(m+1,n)} + P_{xxN}E_{x|(m,n+1)} + P_{xxS}E_{x|(m,n-1)}, \end{aligned} \tag{4.15}$$

where,

$$P_{xxW} = \frac{T_{m-1}}{\Delta x^2}, \qquad P_{xxE} = \frac{T_{m+1}}{\Delta x^2}, \qquad P_{xxN} = P_{xxS} = \frac{1}{\Delta y^2},$$

$$P_{xxP} = \frac{-\left(2 - R_{m+1} - R_{m-1}\right)}{\Delta x^2} - \frac{2}{\Delta y^2} + n^2_{(m,n)}k^2,$$

and,

$$T_{m\pm1} = \frac{2n^2_{(m\pm1,n)}}{n^2_{(m\pm1,n)} + n^2_{(m,n)}}, \qquad R_{m\pm1} = T_{m\pm1} - 1.$$

Eq. (4.15) is the final result: the operator P_{xx} is thus expressed entirely in terms of the of the waveguide's discretized refractive index profile, shown in Fig. 4.1(b), and the wavenumber $k = 2\pi/\lambda$, where λ is the free space wavelength.

Assembling P_{xx}

P_{xx} so far has been written in terms of a single data point. This section will demonstrate how to extend P_{xx} for the entire refractive index profile using the numbering scheme shown in Fig. 4.1(c). If it can be assumed that within the waveguide the polarizations are weakly coupled, the simplified semi-vectorial version of Eq. (4.7) may be solved instead for each polarization separately: $P_{xx}E_x = \beta^2 E_x$ and $P_{yy}E_y = \beta^2 E_y$.

Figure 4.3: Numbering scheme for a 12 point matrix. The numerical values of this matrix would represent a discretized refractive index profile of a waveguide, such as the one shown in Fig. 4.1(a)

For the purposes of demonstration, we will set up a matrix P_{xx} assuming the "waveguide," such as the one shown in Fig. 4.1(b), contains only twelve points. The numbering scheme for this twelve point waveguide is shown in Fig. 4.3.

Eq. (4.16) shows the fully assembled eigenvalue equation $P_{xx}E_x = \beta^2 E_x$. Reading off the top row, which represents point (1) in Fig. 4.3, the matrix reads that the east element of point (1) is point (2), and is thus multiplied by $E_x(2)$. The north element is point (1) is point (4), and is thus multiplied $E_x(4)$. Note that point (1) has no south or west point, and are inherently set to zero (Dirichlet boundary conditions).

Similarly reading off the second row, which represents point (2) in Fig. 4.3, the matrix reads that the west element of point (2) is point (1), and so it is multiplied by $E_x(1)$. The east element of point (2) is point (3), and so it is multiplied by $E_x(3)$, and the north element of point (2) is point (5), and so it is multiplied by $E_x(5)$. Point (2) has no southern element, and is inherently set to zero. This process is repeated to construct rows three through twelve, shown in Eq. (4.16), which directly correspond to points three through twelve in Fig. 4.3.

It should be noted that the operators, P_{xxP}, P_{xxN}, P_{xxS}, P_{xxE}, P_{xxW} in row one refer to point (1) in Fig. 4.3, and should be calculated using the definitions for these operators in Eq. (4.15) at the location of point (1). Similarly, these five operators may or may not be the same for point (2), where these operators in Eq. (4.15) are now evaluated

at point (2).

As each row in Eq. (4.16) can have at most four non-zero elements (eight non-zero elements for each row in Eq. (4.7) as the inter-cardinal elements must be considered), P_{xx} becomes very sparse as the number of data points increases. The non-zero elements consist of numbers solely calculated from the discretized refractive index matrix, such as the one shown in Fig. 4.1(b), and the wavenumber. The implicit assumption of Dirichlet boundary conditions is that the electric field of any guided mode of the waveguide has sufficiently decayed before reaching the numerical boundary—where it is pinned down to a value of 0. As the modes of dielectric waveguides decay into their cladding exponentially, this assumption is usually valid provided a sufficiently large computational window is used. Derivation of P_{xy}, P_{yy}, P_{yx} is straight forward. Once the elements of Eq. (4.7) are assembled, the eigenvalues (propagation constants) and eigenvectors (modes) for the full-vectorial wave-equation may be solved using any matrix eigenvalue solver subroutine, preferably one optimized to handle sparse matrices.

$$\begin{pmatrix} P_{xxP} & P_{xxE} & 0 & P_{xxN} & 0 & 0 & 0 & 0 & 0 & 0 & 0 & 0 \\ P_{xxW} & P_{xxP} & P_{xxE} & 0 & P_{xxN} & 0 & 0 & 0 & 0 & 0 & 0 & 0 \\ 0 & P_{xxW} & P_{xxP} & 0 & 0 & P_{xxN} & 0 & 0 & 0 & 0 & 0 & 0 \\ P_{xxS} & 0 & 0 & P_{xxP} & P_{xxE} & 0 & P_{xxN} & 0 & 0 & 0 & 0 & 0 \\ 0 & P_{xxS} & 0 & P_{xxW} & P_{xxP} & P_{xxE} & 0 & P_{xxN} & 0 & 0 & 0 & 0 \\ 0 & 0 & P_{xxS} & 0 & P_{xxW} & P_{xxP} & 0 & 0 & P_{xxN} & 0 & 0 & 0 \\ 0 & 0 & 0 & P_{xxS} & 0 & 0 & P_{xxP} & P_{xxE} & 0 & P_{xxN} & 0 & 0 \\ 0 & 0 & 0 & 0 & P_{xxS} & 0 & P_{xxW} & P_{xxP}(8) & P_{xxE} & 0 & P_{xxN} & 0 \\ 0 & 0 & 0 & 0 & 0 & P_{xxS} & 0 & P_{xxW} & P_{xxP} & 0 & 0 & P_{xxN} \\ 0 & 0 & 0 & 0 & 0 & 0 & P_{xxS} & 0 & 0 & P_{xxP} & P_{xxE} & 0 \\ 0 & 0 & 0 & 0 & 0 & 0 & 0 & P_{xxS} & 0 & P_{xxW} & P_{xxP} & P_{xxE} \\ 0 & 0 & 0 & 0 & 0 & 0 & 0 & 0 & P_{xxS} & 0 & P_{xxW} & P_{xxP} \end{pmatrix} \cdot \begin{pmatrix} E_x(1) \\ E_x(2) \\ E_x(3) \\ E_x(4) \\ E_x(5) \\ E_x(6) \\ E_x(7) \\ E_x(8) \\ E_x(9) \\ E_x(10) \\ E_x(11) \\ E_x(12) \end{pmatrix} = \beta^2 \begin{pmatrix} E_x(1) \\ E_x(2) \\ E_x(3) \\ E_x(4) \\ E_x(5) \\ E_x(6) \\ E_x(7) \\ E_x(8) \\ E_x(9) \\ E_x(10) \\ E_x(11) \\ E_x(12) \end{pmatrix} \tag{4.16}$$

4.2 Dispersion Engineering of SOI Waveguides

The previous section described a numerical method suitable for solving for the exact eigenvectors (modes) and eigenvalues (propagation constants) of high-index contrast waveguides. Similarly, there exists numerous commercial programs that may be used such as COMSOL, HFSS, and RSOFT, where the mode solvers are based on the finite element method. For these commercial programs—identical to the FDFD algorithm—one describes a waveguide geometry with the corresponding dielectric constants and a free space wavelength; these numerical solvers then return the modes (electric field patterns), and the corresponding propagation constants, of the waveguide.

When the excitation wavelength is changed, not only does the waveguide respond differently (waveguide dispersion), so does the materials of which the waveguide is composed (material dispersion). In order to calculate the dispersion relationship of a waveguide, $\beta(\omega)$, one must iteratively run the mode solver not only updating the freespace wavelength λ ($\omega = 2\pi c/\lambda$), but also the dielectric constants of the waveguide's constituent materials using each material's Sellmeier equation [8]. Once one obtains the propagation constant, the waveguide's effective index is readily calculated through $\beta = \frac{2\pi n_{eff}}{\lambda}$. The speed of light traveling at this frequency (phase velocity) through the waveguide is readily calculated as $v_p = c/n_{eff}$.

As outlined in Chapter 1, optical information is carried on pulses, which are composed of a narrow band of frequencies around a carrier frequency ω. As such, each of the frequency components within the pulse will travel at slightly different speeds, giving way to pulse broadening as it propagates down the transmission line. The speed at which the pulse travels is determined by its group velocity $v_g = c/n_g$, where n_g is defined as:

$$n_g = n_{eff} - \lambda \frac{dn_{eff}}{d\lambda}. \tag{4.17}$$

A measure of a pulse's tendency to spread is determined by its group velocity dispersion, GVD,

$$\mathrm{GVD} = -\frac{\lambda}{c}\frac{d^2 n_{eff}}{d\lambda^2}, \tag{4.18}$$

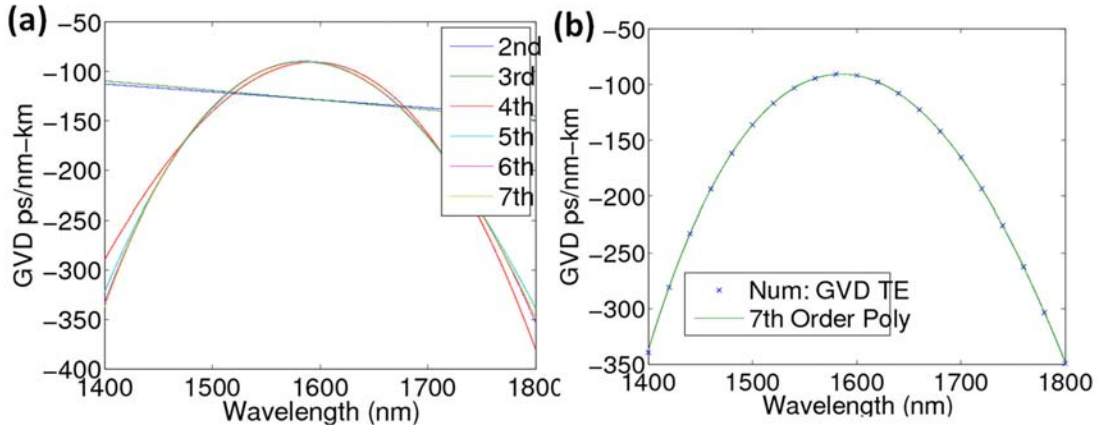

Figure 4.4: (a) Comparison between solving for the group velocity dispersion using numerical derivatives, and increasing order of polynomial fits. (b) For higher order polynomials the two methods produce identical results.

where GVD is usually given in units of ps/nm-km. The following Matlab code is re-posted below due to its frequent re-usability, where the wavelength is assumed initially to be in nanometers. Using the central difference equations, Eq. (4.8a) and Eq. (4.8b), one may obtain the group index "ng" and group velocity dispersion "GVD", of a waveguide from an array of equally spaced wavelengths "wave" and the corresponding array of numerically evaluated effective indexes, "neff."

```
% Calculate Group Index
wave = wave*10^-9;  % Wavelength in meters
d_lambda = wave(2)-wave(1);
d_neff = neff(3:end)-neff(1:end-2);
dndl = d_neff/(2*d_lambda); % Central Difference (CD)
dwave = wave(2:end-1);  % Lose two points from CD.
ng = neff(2:end-1)-dwave.*dndl;  %Group Index

% Calculate GVD
dwave = dwave*10^9; % units are /nm
d_lambda = d_lambda*10^9;
c = 3*10^8/1000*1e-12; % Speed of Light in km/ps

GVD = -dwave/(c*d_lambda^2).*(neff(3:end)- ...
2*neff(2:end-1)+neff(1:end-2));
```

From the central difference formula, if an array of ten effective indices are solved for,

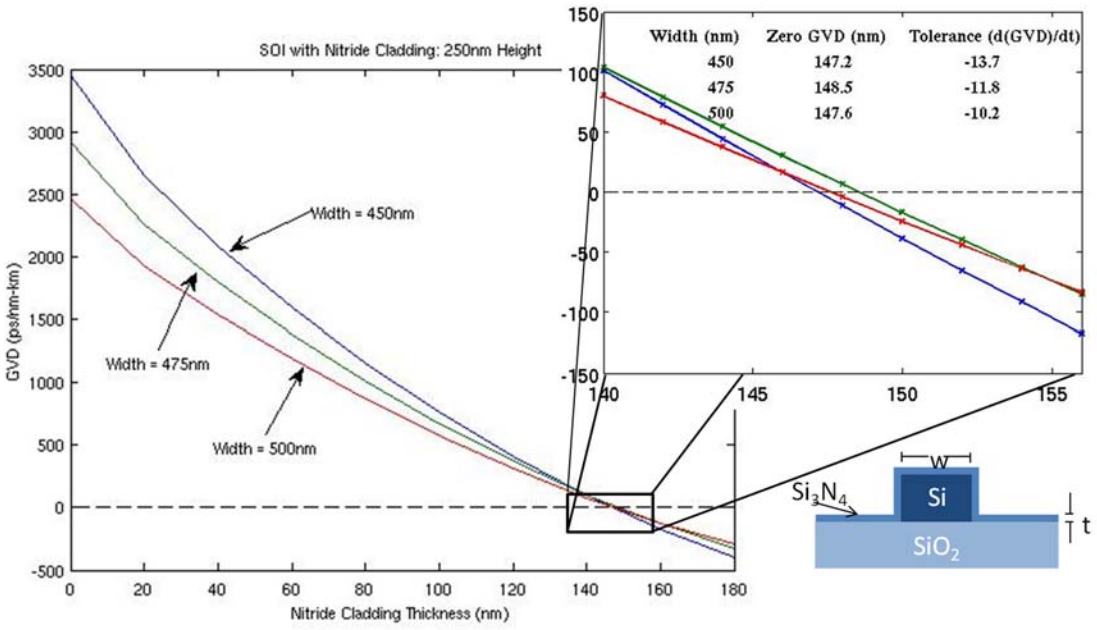

Figure 4.5: Change in group velocity dispersion (GVD) of three silicon nanowires of different width, w, as the thickness, t, of a thin film of Si_3N_4 residing on top of the waveguide is varied. The height of each of the silicon nanowires is 250 nm, and the wavelength is 1550 nm. The slope of the GVD vs thin film thickness in a local region describes the device sensitivity to fabrication irregularities.

equally spaced in wavelength, one may only calculate the group index and group velocity dispersion for the central eight data points.

The other common numerical technique for calculating the group index and group velocity dispersion is by fitting the effective index data to a polynomial, and then analytically differentiating the polynomial. Fig. 4.4 shows a comparison between the two methods. For higher order polynomials the two methods produce identical results.

As an example of how iterative solutions of a waveguide's propagation constant can be used to describe device tolerances, we examine the sensitivity of GVD to the thickness of a thin film cladding deposited on top of a silicon nanowire, as shown in Fig. 4.5. Dispersion in silicon nanowires is dominated by waveguide dispersion, not material dispersion. The ability to design waveguides that operate around zero GVD will become necessary for reducing signal distortion at high data speeds over long distances [9]. Being able to engineer GVD is also useful for wavelength conversion based on four-wave mixing [10]. By depositing a thin layer of Si_3N_4 on top of a silicon rib waveguide,

its dispersion characteristics can be precisely tailored [11]. Fig. 4.5 shows the group velocity dispersion of a typical silicon-on-insulator nanowire for three different widths, 250 nm height, λ = 1550 nm, as the thickness of a thin film of Si_3N_4 residing on top of the nanowire is varied. Note that at a zero-thickness the silicon nanowire has a relatively high dispersion of around 3000 ps/nm-km. By increasing the thickness of the thin film cladding the GVD is reduced, and at a certain value, it crosses zero. Shown in the inset of Fig. 4.5 is the waveguide width, along with the thickness required for zero GVD. Also shown is the rate of change, calculated from Eq. (4.8a), of the GVD with changing thickness. At a waveguide thickness of 450 nm, a thin film of Si_3N_4 at a thickness of 147.2 nm will bring the waveguide to zero GVD. If the fabrication steps are off by 1 nm in the thickness of the Si_3N_4 cladding, then the GVD will increase, or decrease, by 13.7 ps/nm-km.

The above example is perhaps the most useful capability of mode solvers. In practice, a fabricated waveguide will often have slightly different Sellmeier equations and a slightly different geometry due to fabrication irregularities resulting in waveguide surface roughness. By iterating device dimensions within a mode solver, one can determine the tolerance required by the fabrication process.

4.3 Dispersion of Directional Couplers

Thus far we have been concerned with the propagation constants and field patterns of single isolated waveguides. It was shown that by iterating a mode solver one may obtain the dispersion relationship, $\beta(\omega)$, for a given waveguide mode. As will be detailed in the next chapter, when N single-mode waveguides are weakly coupled together, the arrayed structure will contain N supermodes (technically 2N supermodes, N for each polarization). Each of these supermodes has its own dispersion characteristics. An N = 2 arrayed waveguide is a directional coupler, which contains two "supermodes," typically labeled as symmetric and antisymmetric. When light enters one arm of a directional coupler, called the feeder waveguide, it splits—not necessarily equally—into the even and odd supermodes of the N = 2 arrayed waveguide. Fig. 4.6 shows the feeder waveguide and its corresponding mode, as well as the superposition of the symmetric

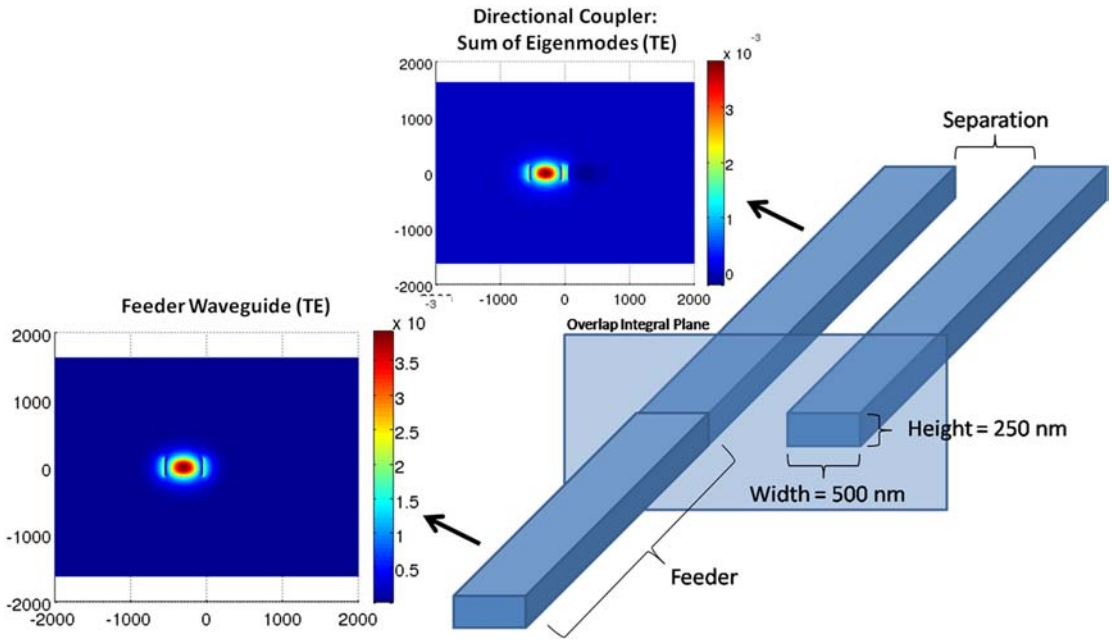

Figure 4.6: Schematic of a butt-coupled directional coupler. When light enters the directional coupler it splits into the even and odd supermodes, which then propagate down the waveguide shifting in and out of phase with one another. At the transition plane, the superposition of the symmetric and antisymmetric supermodes of the directional coupler have a high degree of overlap with the feeder mode.

and antisymmetric modes of the directional coupler. Note the high degree of overlap between these two profiles at the transition region, which will hold so long as the fields are not skewed from strong coupling (Section 5.3). However, when the supermodes propagate down the coupler, they will shift in and out of phase with one another due to their different dispersion characteristics; causing the concentration of light in the directional coupler to oscillate back and forth between the separated waveguides.

To analytically describe this phenomena we proceed in a manner similar as Hermann A. Haus in Ref. 14, only using the modes obtained from a numerical mode solver. We describe the coupling of modes in space for a four-port co-directional coupler. We begin by describing the evolution of the modes where the feeder waveguide is butt coupled to one of the two arms of the directional coupler, as shown in Fig. 4.6. We then describe the effects of adiabatic coupling, as would be the case for the racetrack resonators of a CROW, which were described in detail in Chapter 2.

When light from either of the uncoupled waveguides enters the coupling re-

gion of a directional coupler, the symmetric and anti-symmetric supermodes for the transverse-electric polarization are excited as:

$$\hat{E}^c(x,y,0)\hat{\mathbf{x}} = a_s\mathcal{E}^s(x,y)\hat{\mathbf{x}} + a_a\mathcal{E}^a(x,y)\hat{\mathbf{x}}, \tag{4.19}$$

where z = 0 represents the input coupling plane, $\hat{E}^c(x,y,0)$ represents the total electric field in the coupling region, and $\mathcal{E}^s(x,y)$ and $\mathcal{E}^a(x,y)$ represent the exact symmetric and antisymmetric supermodes of the directional coupler, obtained from a numerical mode solver such as FDFD, with

$$a_s^2 = \frac{\left|\left\langle \hat{E}^{w.g.1}(x,y,0)\mathcal{E}^s(x,y)\right\rangle\right|^2}{\left\langle \hat{E}^{w.g.1}(x,y,0)\hat{E}^{w.g.1}(x,y,0)\right\rangle\left\langle \mathcal{E}^s(x,y)\mathcal{E}^s(x,y)\right\rangle} \tag{4.20}$$

and

$$a_a^2 = \frac{\left|\left\langle \hat{E}^{w.g.1}(x,y,0)\mathcal{E}^a(x,y)\right\rangle\right|^2}{\left\langle \hat{E}^{w.g.1}(x,y,0)\hat{E}^{w.g.1}(x,y,0)\right\rangle\left\langle \mathcal{E}^a(x,y)\mathcal{E}^a(x,y)\right\rangle}, \tag{4.21}$$

which define the degree of mismatch between the feeder waveguide, assumed in this case to be waveguide 1, and the excited supermodes. As demonstrated in Fig. 4, the supermodes then propagate down the coupler beating against each other as,

$$\hat{E}^c(x,y,z)\hat{\mathbf{x}} = a_s\mathcal{E}^s(x,y)e^{i\beta^s z}\hat{\mathbf{x}} + a_a\mathcal{E}^a(x,y)e^{i\beta^a z}\hat{\mathbf{x}}, \tag{4.22}$$

where β^s and β^a are the propagation constants of the respective supermodes. After the waveguides have decoupled at a distance l_c, we obtain our dimensionless coupling coefficient as the overlap integral between the superposition of the propagated supermodes and the second waveguide of the directional coupler:

$$\kappa^2 = \frac{\left|\left\langle \hat{E}^{w.g.2}(x,y,l_c)\hat{E}^c(x,y,l_c)\right\rangle\right|^2}{\left\langle \hat{E}^{w.g.2}(x,y,l_c)\hat{E}^{w.g.2}(x,y,l_c)\right\rangle\left\langle \hat{E}^c(x,y,l_c)\hat{E}^c(x,y,l_c)\right\rangle}. \tag{4.23}$$

In order to obtain a more straightforward expression, we follow the methodology of coupled mode theory (CMT) and approximate the electric field of the supermodes as an expansion of the individual isolated waveguide modes,

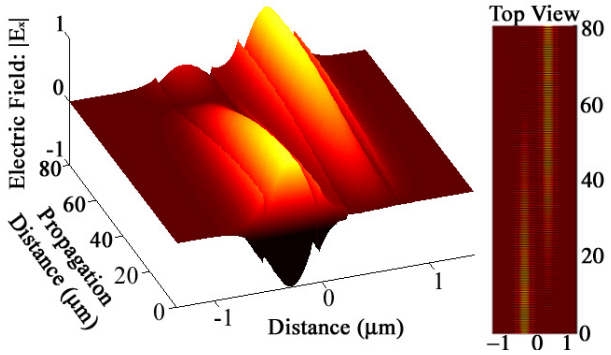

Figure 4.7: Superposition of the exact even and odd supermode obtained from a finite element mode solver and propagated as Eq. (4.22) at a waveguide height of 100 nm.

$$\mathcal{E}^s(x,y) = \frac{1}{\sqrt{2}}\left(\hat{E}^{w.g.1}(x,y) + \hat{E}^{w.g.2}(x,y)\right) \tag{4.24a}$$

$$\mathcal{E}^a(x,y) = \frac{1}{\sqrt{2}}\left(\hat{E}^{w.g.1}(x,y) - \hat{E}^{w.g.2}(x,y)\right). \tag{4.24b}$$

Substituting Eq. (4.22) and Eq. (4.24) into Eq. (4.23), and utilizing the orthogonality of the individual waveguide modes, the dimensionless coupling coefficient is reduced to:

$$\kappa^2 = \sin^2\left(\frac{\pi}{2}\frac{l_c}{L_c}\right) + A^2\cos^2\left(\frac{\pi}{2}\frac{l_c}{L_c}\right) \tag{4.25}$$

where,

$$A \equiv \left\langle \hat{E}^{w.g.2}(x,y)\hat{E}^{w.g.1}(x,y)\right\rangle \ll 1 \tag{4.26}$$

and the coupling length is defined as $L_c = \frac{\lambda}{2(n_s - n_a)}$, which physically represents the length where all of the light has transfered into the second waveguide. n_a and n_s are obtained from the propagation constants returned from a numerical mode solver.

In Fig. 4.8 we compare the first term of Eq. (4.25) with Eq. (4.23). Eq. (4.23) was solved by calculating the exact supermodes of the directional coupler and the mode of the feeder waveguide using a finite element mode solver (COMSOL). Overlap integrals are performed to determine a_s and a_a, where the mode in the coupling region is then propagated down the directional coupler using Eq. (4.22), where Eq. (4.23) may then be

directly evaluated using the mode of the second waveguide (also solved using the FEM). Sellmeier equations were used to account for the material dispersion for the silicon core, the SiO_2 substrate [8], and the PMMA superstrate [12]. The dominant variation between

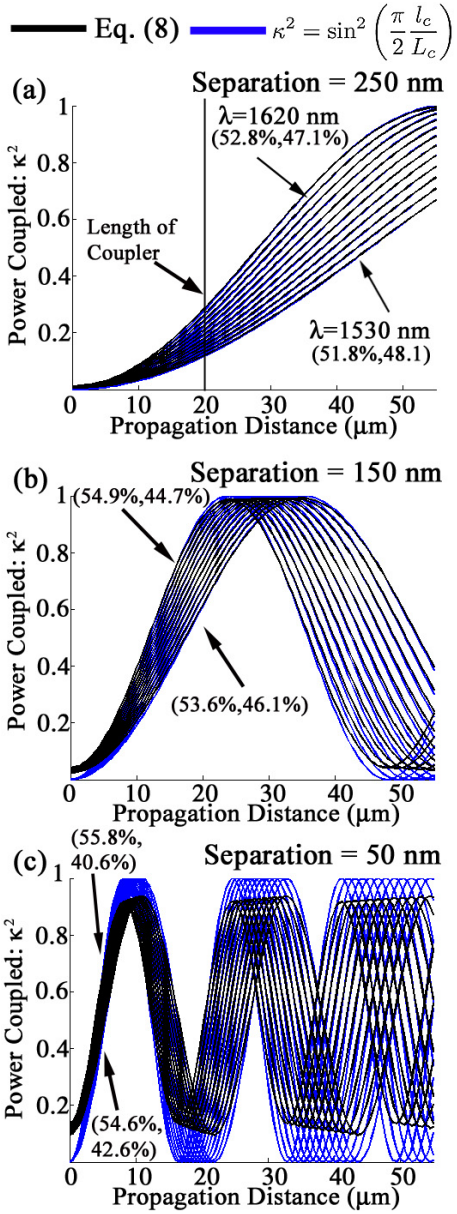

Figure 4.8: Dispersion of the coupling coefficient equi-spaced from 1530 nm to 1610 nm, calculated with Eq. (4.23) and the first term of Eq. (4.25), for a waveguide of dimensions 538 $\times$ 236 nm and separation distance of (a) 250 nm, (b) 150 nm, and (c) 50 nm. Also included is the percentage of the power coupled into each mode, (a_s^2, a_a^2), for λ = 1530 nm and λ = 1610 nm.

the two coupling coefficient expressions comes from assuming that the power is equally split into the two supermodes, which is not the case for butt-coupled directional couplers at short separation distance due to the dislocation of the field peaks from the waveguide centers within the coupling region, which is also predicted by CMT [13], compared with the feeder waveguide whose mode is centered within its dielectric boundaries.

In the case of racetrack microring resonators, the waveguides are parallel in the coupling region and bend away at both ends. The net result is that within the bending regions the propagation constants of the supermodes, and hence the coupling coefficient, becomes a function of position [14]. In a similar fashion as Ref. 15, we use coupled mode theory to describe the contributions to the couping coefficient due to the waveguide bends. We will start by describing the evolution of the supermodes as they bend away from the coupling region, and, by symmetry, this will be the same equivalent length contributed by input taper. As the waveguides bend away from one another, the effective index of the two supermodes both approach that of the single uncoupled waveguide, causing the coupling length to go to infinity. We ignore the spatial dependence of the supermodes, $A = 0$, which become less significant as the waveguides taper away from each other, and write the evolution of their phases as,

$$\begin{aligned} \hat{E}^c(x, y, z' > 0) &= \frac{1}{2} e^{i\left(\beta^s l_c + \int_0^{z'} \beta^s_{bends}(z')dz'\right)} \\ &+ \frac{1}{2} e^{i\left(\beta^a l_c + \int_0^{z'} \beta^a_{bends}(z')dz'\right)}, \end{aligned} \tag{4.27}$$

where $z' = z - l_c$. Substituting into Eq. (8), and evaluating over the entire bend, we have,

$$\kappa^2 = \sin^2\left(\frac{\pi}{2}\frac{l_c}{L_c} + \int_0^{\infty} \frac{\pi}{2L_c^{bends}(z)} dz'\right). \tag{4.28}$$

We assume an exponential form of the coupling length,

$$L_c^{bends}(z') = ae^{bg(z')}, \tag{4.29}$$

and approximate the spacing between the two waveguides, $g(z) \cong g_0 + \frac{z'^2}{R}$ [15], where g_0 is the minimum separation distance of the directional coupler and R is the bending

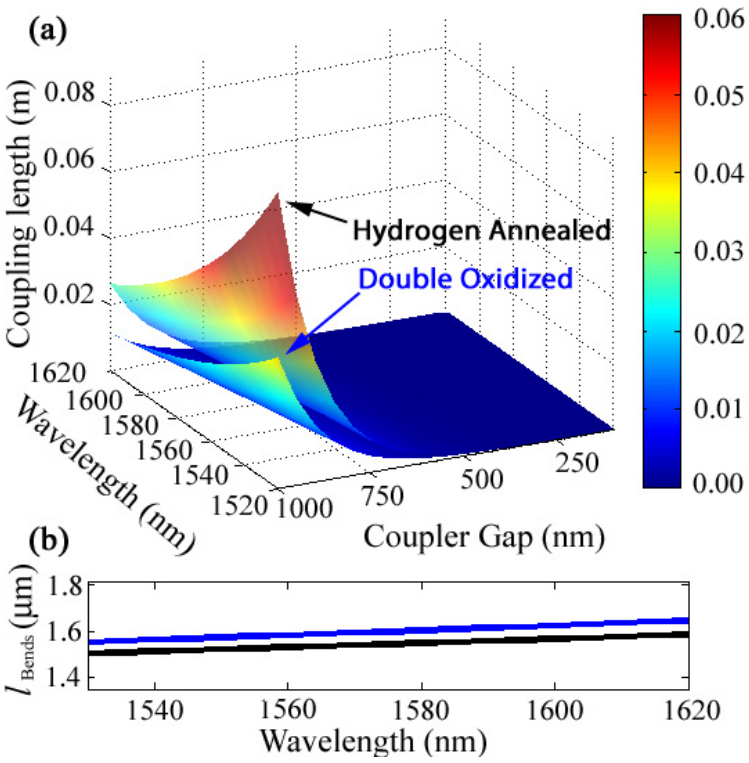

Figure 4.9: (a) Dependence of coupling length on the waveguide separation and wavelength. (b) The additional coupling length due to the contribution of the waveguide bends.

radius of the microring. Recognizing that $L_c = ae^{bg_0}$, the additional phase contribution due to both bends is readily calculated, and we obtain our coupling coefficient as,

$$\kappa^2 = \sin^2\left(\frac{\pi}{2L_c}\left(l_c + \sqrt{\frac{\pi R}{b}}\right)\right). \tag{4.30}$$

The effect of the waveguide bends is thus to increase the effective length of the directional coupler by $l_{bends} = \sqrt{\frac{\pi R}{b}}$.

4.3.1 The Directional Couplers of the CROWs

To proceed in evaluating Eq. (4.30) a test structure is needed: we use the directional couplers of the CROWs reported on in Section 2.1. Recall that the CROWs were fabricated on two different wafers, which underwent different sidewall roughness reduction techniques, hydrogen annealing and double oxidation. It was pointed out that in the

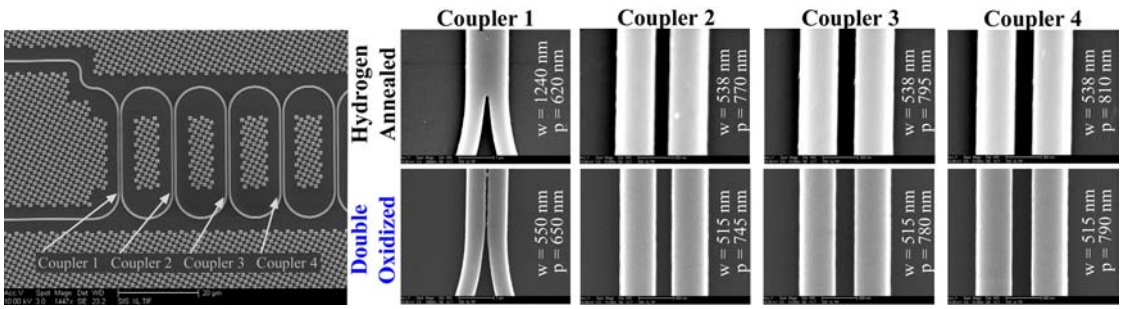

Figure 4.10: Scanning electron microscope (SEM) image of the waveguide cross-section and first four directional couplers for both the hydrogen annealed and double oxidized wafers.

process of oxidation, 10 nm of silicon is sacrificed at the waveguide boundary where it is replaced by 20 nm of oxide. Fig. 4.9(a) shows the dependence of the coupling length on the coupler gap and wavelength for both the hydrogen annealed and double oxidized directional couplers of which the CROW is composed; solved using Eq. (4.25) where both the wavelength and waveguide spacing was varied. These graphs are fitted to Eq. (4.29) to obtain $b(\lambda)$. Fig. 4.9(b) shows the contribution of the waveguide bends to the coupling length for both the double oxidized and hydrogen annealed wafers. Due to the reduction in height, the modes affect each other sooner coming around the bend for the double oxidized wafer and at longer wavelengths, which is a result of less confinement, thus increased overlap, of the waveguide modes.

In addition to the two wafers undergoing different post-fabrication surface roughness reduction processes, the lithography dosage on the wafers themselves was varied (Section 2.1). Fig. 4.10 shows a SEM image of the first four rings of a 35-ring CROW. In order to reduce the group delay and insertion loss ripple, apodization of the directional couplers is performed by tapering the spacing (coupling coefficients) of the first four rings [16]. We define the pitch of the coupler as $p = w_{si} + w_{gap}$. To determine the effects of dose-striping on the coupling coefficients, we solve for the coupling coefficient using Eq. (4.25) as the silicon filling fraction of the directional couplers, $q = \frac{w_{si}}{p}$ is varied, keeping the pitch constant. The initial filling fraction is determined from the SEM images of the first four couplers shown in Fig. 4.10, for both the hydrogen annealed and double oxidized wafer.

Fig. 4.11 shows the effects of varying the waveguide width by $\pm$ 50 nm for the

hydrogen annealed wafer in steps of 10 nm over the wavelength range that was measured experimentally. We note that the coupling coefficient of the microring directional coupler remains relatively insensitive to variation in the filling fraction as was reported in Section 2.1. As shown in Fig. 4.12, this is not the case for the more weakly confined double oxidized waveguide, which is 20 nm thinner. These simulations indicate that when the height of the silicon waveguide was reduced from the double oxidation process, the composite directional couplers of the CROW became more strongly coupled. This is in excellent agreement with the analysis presented in Section 2.1. The most dominant post-fabrication process was thus the reduction of the height of the silicon layer due to the double oxidization process. This led to an increase in the coupling coefficient and less tolerance to variations in waveguide width for the directional coupler.

4.3.2 Dispersion of Fused Waveguides

If the lithography dose is too low, and the desired waveguide separation is small, the two patterns can overlap resulting in a fused multimode waveguide, as shown for the first hydrogen annealed *Coupler 1* in Fig. 4.10. The feeder waveguide couples into all available modes of the multimode waveguide, in this case three, which are spatially different from that of the directional coupler. For example, the first mode for a directional

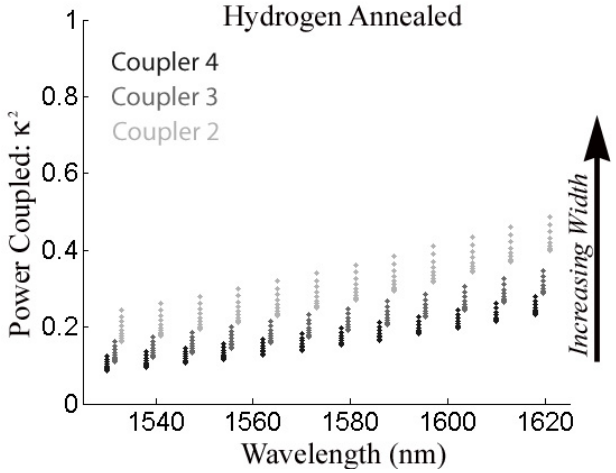

Figure 4.11: Wavelength dependent coupling coefficient for the hydrogen annealed for the first three couplers as the coupler pitch is held constant and the waveguide width is varied by $\pm$ 50 nm.

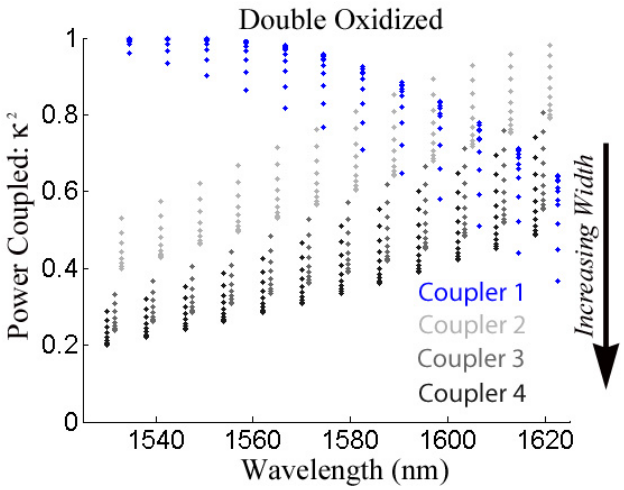

Figure 4.12: Wavelength dependent coupling coefficient for the double oxidized wafer for the first three couplers as the coupler pitch is held constant and the waveguide width is varied by $\pm$ 50 nm.

coupler contains two peaks, whereas the first mode for a fused waveguide only contains one. Also, for the directional coupler, we expect that varying the filling fraction will change where the modes begin to decay but not the location of the field peaks. This will not be the case when changing the width of the fused waveguide for the two higher order modes. From SEM images we notice an abrupt transition from the feeder waveguide and follow the methodology used for the butt-coupled waveguide described earlier. We write the electric field in the multimode coupler, $E^{m.m.c}(x,y,z)$, as superposition of the modes,

$$\begin{aligned}\hat{E}^{m.m.c}(x,y,z)\hat{\mathbf{x}} &= a_{TE_1}\mathcal{E}^{TE_1}(x,y)e^{i\beta^{TE_1}z}\hat{\mathbf{x}} \\ &+ a_{TE_2}\mathcal{E}^{TE_2}(x,y)e^{i\beta^{TE_2}z}\hat{\mathbf{x}} \\ &+ a_{TE_3}\mathcal{E}^{TE_3}(x,y)e^{i\beta^{TE_3}z}\hat{\mathbf{x}}, \end{aligned} \tag{4.31}$$

where again, a_i^2 represent the percentage of power coupled into the i^{th} mode, and is calculated as the overlap integral of that mode with the feeder waveguide. Fig. 4.13 shows the superposition of the three modes of the multimode waveguide and propagated as Eq. (4.31). In Fig. 4.14 we show the coupling coefficient, determined from the overlap integral of the propagated mode with the second waveguide. Also shown is the percent-

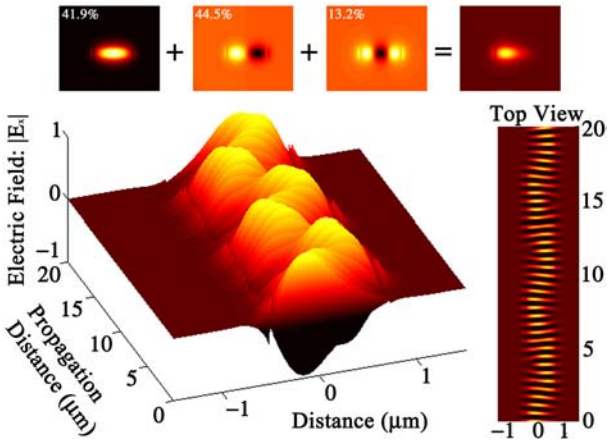

Figure 4.13: Superposition of the first three modes of a multimode waveguide, obtained from a finite element mode solver and propagated as Eq. (4.31) at a waveguide height of 100 nm.

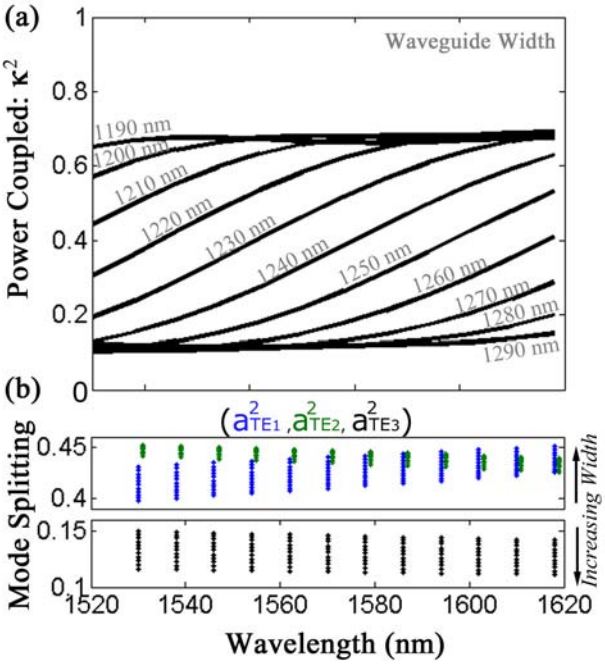

Figure 4.14: (a) Dispersion of the coupling coefficient of the fused waveguide for different widths. (b) The percentage of overlap between the feeder waveguide and each of the modes of the multimode waveguide for different widths.

age of power coupled into each of the three modes of the multimode waveguide. For the fused waveguide there is very strong dependence of the coupling coefficient with both wavelength and waveguide width as the three modes, each with their own dispersion

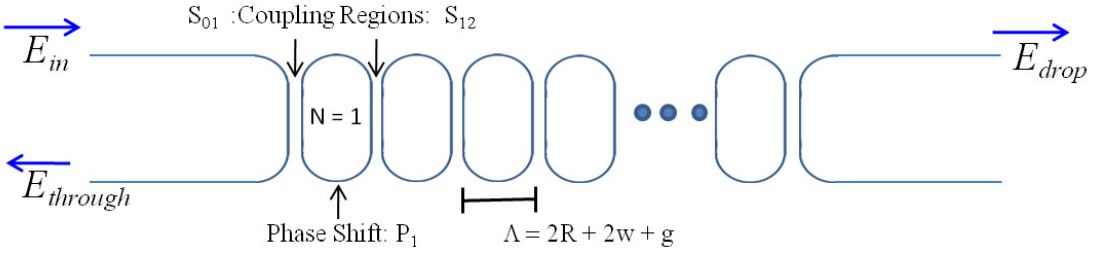

Figure 4.15: In the transfer matrix technique a CROW is decomposed into sub-matrices which characterize the coupling regions S_{mn} and phase regions P_{mn}. The periodicity of the CROW, Λ, is defined in terms of the ring radius, R, the waveguide width, w, and the separation distance g.

characteristics, beat against each other.

4.4 Simulation of a Disordered CROW

In the previous section it was shown that the composite directional couplers of a CROW may become highly dispersive as the resonator separation distance is reduced—required for proper apodization. Because of this dispersion the apodization of a CROW may vary significantly from band to band. In this section we will outline a technique for simulating the transmission spectrum of a CROW which will account for not only the wavelength dependence of the composite directional couplers, but also the dispersion of the silicon nanowires of which the CROW is composed. Further, with perturbations in ring size and track length the effects of disorder may be simulated.

4.4.1 Transfer Matrices

Methods for calculating the transmission spectrum of a CROW using transfer matrices have been developed and detailed elsewhere, and their results briefly summarized here [17, 18]. In this section we highlight the necessary adaptations that must be made to simulate a CROW composed of high-index contrast silicon-on-insulator waveguides, where the resonators may be individually misaligned.

As shown in Fig. 4.15, the input waveguide's electric field is related to that of

the drop port waveguide through a cascade of scattering matrices, S, and propagation matrices, P, as:

$$\begin{bmatrix} E_{in} \\ E_{through} \end{bmatrix} = \underbrace{S_{01}P_1S_{12}P_2\cdots P_NS_{N,N+1}}_{(M)} \begin{bmatrix} E_{drop,\text{ if } N_{odd}} \\ 0 \end{bmatrix} \tag{4.32}$$

where,

$$S_{n-1,n} = \frac{1}{\kappa_{n-1,n}} \begin{bmatrix} 1 & t_n^* \\ t_n & 1 \end{bmatrix}, P_n = \begin{bmatrix} e^{i\frac{\phi_n}{2}} & 0 \\ 0 & e^{-i\frac{\phi_n}{2}} \end{bmatrix}, M = \begin{bmatrix} m_{11} & m_{12} \\ m_{21} & m_{22} \end{bmatrix}, \tag{4.33}$$

and n indexes the total N resonators, $\phi_n = 2\pi n_{eff}(\lambda)C_n/\lambda$ represents the round trip phase shift of a single ring of circumference C_n, and $\kappa(\lambda)$ and $t(\lambda)$ represent the magnitude of the dimensionless cross-coupling and through-coupling coefficients between two resonators.

Section 4.2 detailed how one may obtain the dispersion of the silicon nanowires of which the CROW is composed, $n_{eff}(\lambda)$. Section 4.3 outlined how to simulate the wavelength dependence of the coupled silicon nanowires, $\kappa(\lambda)$, for different resonator separation distances. Eq. (4.32) contains 2N+1, 2x2 matrices: to accurately solve the transmission properties of a CROW, each of these matrices must be updated at each wavelength to account for the dispersion of the coupling coefficients, $\kappa(\lambda)$, and the dispersion of the silicon nanowire of which the CROW is composed, $n_{eff}(\lambda)$. Finite element simulations should be done first to fully characterize these two terms, and then these results substituted into Eq. (4.32). One may simulate an apodized CROW by tapering the first four and last four scattering matrices, by solving for and substituting in the corresponding $\kappa_n(\lambda)$. Once the matrix M(λ) is determined, the drop port response is readily calculated as $E_{drop}(\lambda) = 1/m_{11}(\lambda)$.

4.4.2 Reconstructing Field Patterns

As will be discussed in detail in Chapter 6, within a microring resonator the intensity becomes enhanced. Once the drop port response is determined, one may calculate the enhancement of energy, I_N, in the Nth ring as,

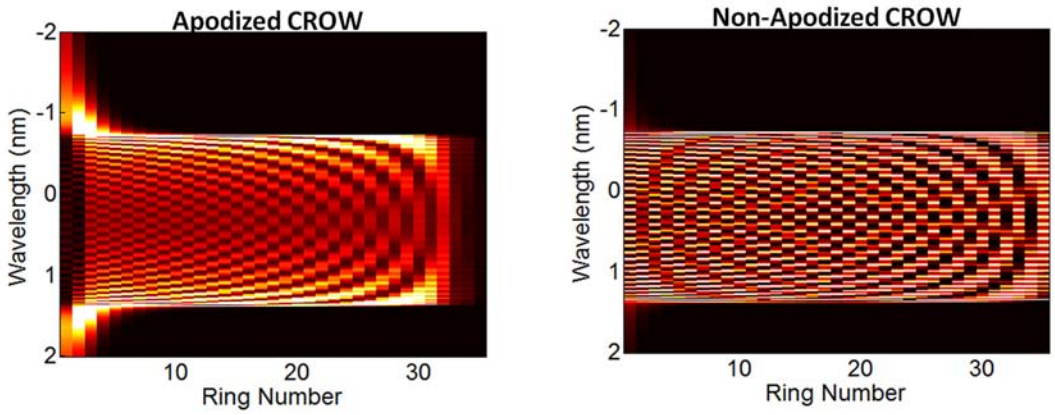

Figure 4.16: Intensity maps for both an apodized and a non-apodized 35-ring CROW. Note that for the individual rings, the resonators may undergo significantly different enhancements

$$I_N = S_{N,N+1} \begin{bmatrix} E_{drop} \\ 0 \end{bmatrix}. \tag{4.34}$$

Similarly, the intensity enhancement for the second to last ring, I_{N-1}, is,

$$I_{N-1} = S_{N-1,N} P_N S_{N,N+1} \begin{bmatrix} E_{drop} \\ 0 \end{bmatrix}. \tag{4.35}$$

Continuing this process for each ring at each wavelength one obtains the entire response of the individual rings of a CROW. Fig. 4.16 shows this response for a single band of a disorder-free apodized and non-apodized CROW. Within the CROW's transmission band, the individual resonators become enhanced forming the eigenmode of the CROW. Note that the individual coupled resonators of a non-apodized CROW have a much sharper linewidth, which leads to significant group delay and insertion loss ripple across the CROW's band. In Chapter 6, a method of directly imaging the response of these resonators will be outlined.

In practice, disorder in CROWs has thus far been a severe practical problem, since in a multi-resonator ensemble, the resonance frequencies of the constituent resonators must be precisely aligned. As the benefit of microrings and CROWs increases for higher quality factors (lower coupling coefficient, increased resonator separation), such resonators are also harder to align. In fact, CROWs over a hundred lattice peri-

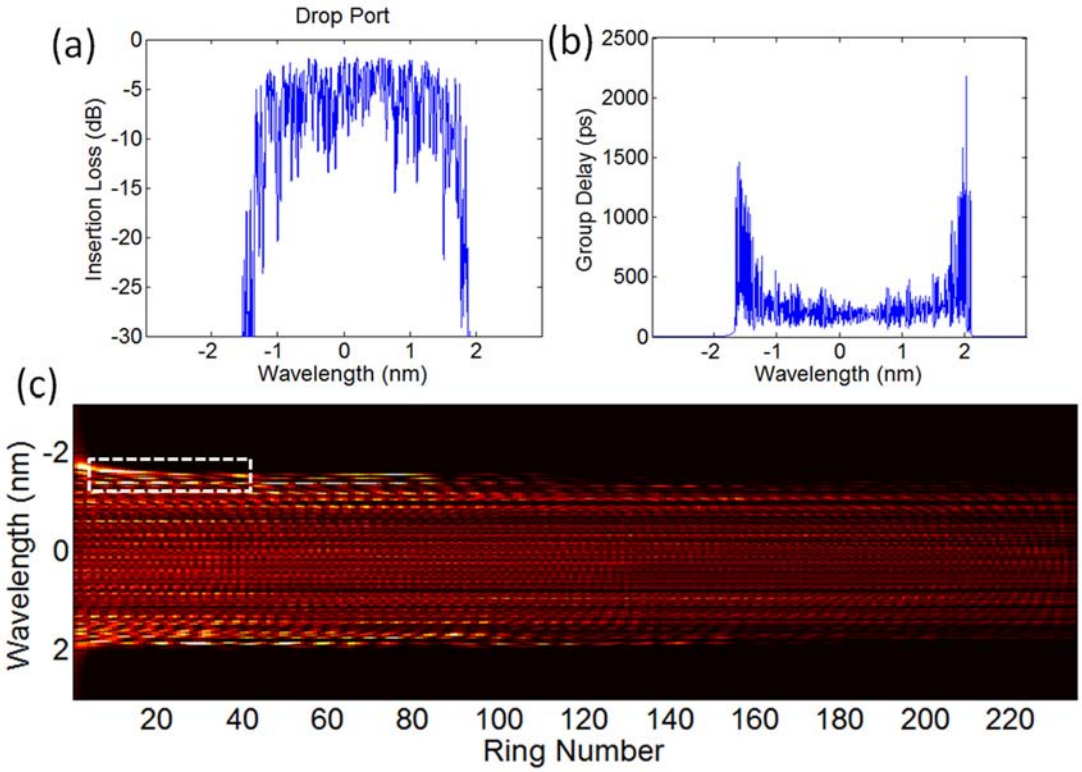

Figure 4.17: (a) Simulation of the transmission spectrum of a disordered 235-ring CROW composed of silicon nanowires of 200 nm height at 500 nm width, with 3 dB/cm propagation losses. The disorder was simulated by adding random Gaussian noise to the inter-resonator couping coefficients of Eq. (4.32) such that their standard deviation (STD) was defined by, $\delta\kappa$ = 0.02. Similarly the resonator size was perturbed such that the STD in the phase was $\delta\phi = 0.01$. (b) The simulated group delay of the disordered CROW. (c) Intensity variations of the individual micro-resonators. For a given wavelength, neighboring resonators in a CROW may undergo significantly different responses. The section outlined by the dashed-white box is shown in Fig. 4.18. In Chapter 6, using infrared imaging, the intensity map of a 235-ring CROW is directly measured.

ods in length have shown disorder-induced localization of light [19, 20], which though fundamentally interesting and potentially useful for some applications [21], is generally considered problematic for most device applications.

Eq. (4.32) may be used to simulate the effects of disorder on the passband of a CROW, and predict whether or not a given tolerance defined by the fabrication process will prohibit device operation. Fig. 4.17(a,b) show the transmission and group delay spectra of a disordered 235 ring CROW composed of silicon nanowires with 3 dB/cm propagation loss. In the simulation, random Gaussian noise was added to the

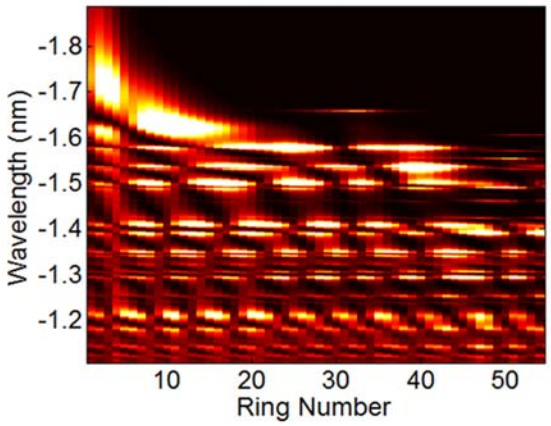

Figure 4.18: Zoomed in region of the white-dashed box in Fig. 4.18(c), showing the high spectral dependence of the individual resonators.

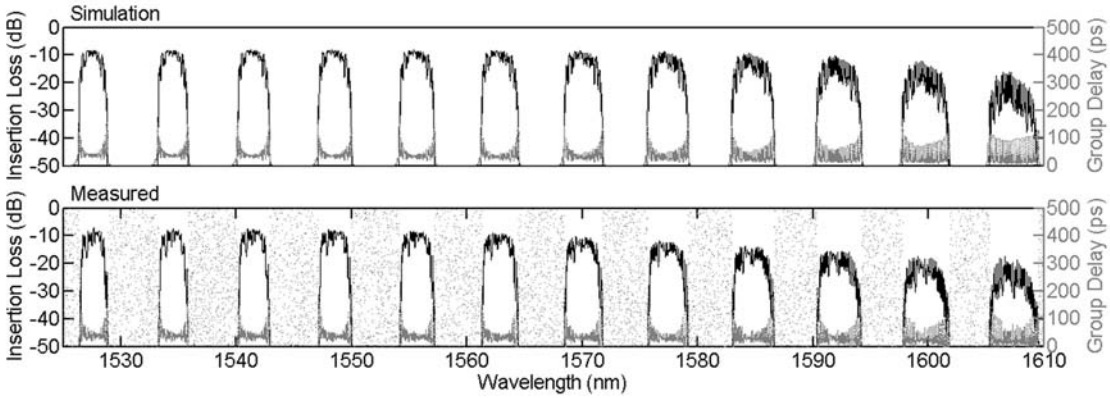

Figure 4.19: Comparison of simulated and measured, transmission and group delay, spectra of a 35-ring CROW

inter-resonator couping coefficients such that the standard deviation (STD) across the N rings was, $\delta\kappa$ = 0.02. Similarly, the resonator size was perturbed such that the STD in the phase across the N rings was, $\delta\phi = 0.01$. As shown in Fig. 4.17(c), for a given wavelength, neighboring resonators in a disordered CROW may undergo significantly different responses. The section outlined by the dashed-white box in Fig. 4.17(c) is expanded in Fig. 4.18.

It was demonstrated in Chapter 2 that from the transmission spectrum of a CROW, one may extrapolate the wavelength dependent coupling coefficient of the constituent directional couplers. Fig. 4.19 shows a comparison of a simulated spectrum of

a 35-ring CROW, along with a measured spectrum. The high degree of uniformity between these two traces is clearly evident. For this simulation, the wavelength dependent coupling coefficient of the inner micro-resonators was determined from the measured CROW's bandwidth. The dispersion properties of the composite silicon nanowires were solved using a finite element mode solver, as detailed in Section 4.2. The loss of the silicon nanowires was measured, and used in the simulation, to be -3.8 dB/cm; determined from the measurement of four straight waveguides of varying lengths on a nearby test site. The spectrum was further offset by 8 dB to account for the input and output couplers. The wavelength dependent coupling coefficient used in this simulation for the first directional coupler is similar to the one shown for the first directional coupler in Fig. 4.12. Because of the dispersion of the coupling coefficient in this first resonator, the CROW is properly apodized only at shorter wavelengths, and un-apodized for longer wavelengths. This results in higher group delay ripple, and insertion loss ripple, at higher wavelengths. Fig. 4.19 shows the high degree of accuracy provided by the transfer matrix method when the dispersion characteristics of all of the CROWs constituent parts are taken into consideration.

4.4.3 Sending Numerical Data Through a Numerical CROW

The previous section detailed a transfer matrix method for simulating the response of a multi-resonator apodized and disordered CROW in the frequency domain. The impulse response of this device is readily calculated in the time domain through the Fourier transform [15]. This representation is useful for analyzing certain group delay measurement techniques, such as swept wavelength interferometry (described in Chapter 6), where many of the data post-processing routines are performed in the time domain. Fig. 4.20 shows the impulse response of a 35-ring CROW as the attenuation of the constituent nanowires is ramped up. Note that for each of these simulations the peak of the response is located at the same location in time, and is a direct measure of the "band-center" delay of a CROW. "Band-edge" characteristics can also be analyzed by looking for spikes at later times. Through the convolution operation, one may thus simulate the response of a data-stream being sent through each of these CROWs. Similarly,

which is done here, one may stay in the frequency domain and transform the incoming data stream.

Information is transported in photonic integrated networks using pulses. Digital encoding interprets the presence of an optical pulse as a “1,” and the absence of a pulse as a “0’. In this section we highlight a method for simulating the eye-diagrams for high speed data propagating through a disordered CROW. The two most common methods of transmitting data are the return-to-zero (RZ) and nonreturn-to-zero (NRZ) formats. In this section we will focus on the transmission of a RZ data stream, where within each active bit duration a pulse will rise from, and return back to, zero. Modification for the NRZ data stream is straight forward.

The electric field of an incoming data stream, encoded onto an optical carrier at frequency ω_0, may be expressed as [22],

$$E^{data}(t) = Re\left[A_0(t)e^{i\phi_0}\exp\left(-i\omega_0 t\right)\right], \tag{4.36}$$

where the amplitude $A_0(t)$ is defined by,

$$A_0(t) = P_0^{1/2}\sum_n b_n f_p\left(t - nT_b\right), \tag{4.37}$$

where P_0 is the peak power, b_n represents a “1” if a pulse is present, and a “0” if there

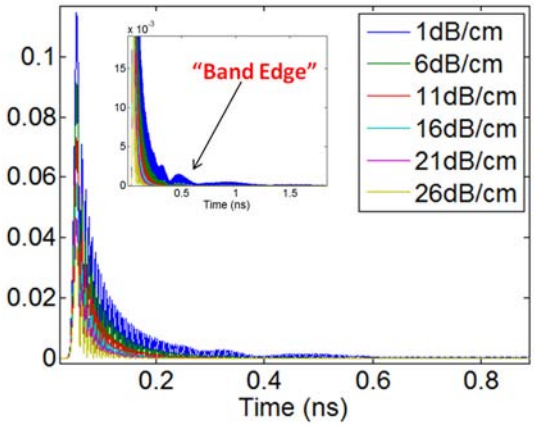

Figure 4.20: Simulation of the impulse response of a disorder free CROW as the attenuation of the constituent silicon nanowires was ramped up. The location in time of the peak response is a measure of the CROW’s “band-center” delay.

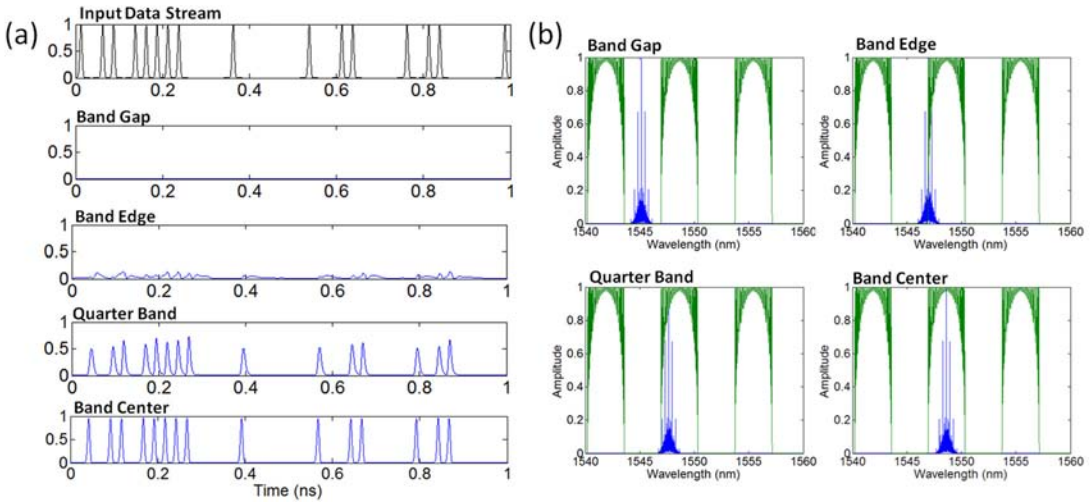

Figure 4.21: Simulation of the response of a 35-ring CROW on an incoming data stream as the carrier wavelength is tunned throughout the CROW's passband. (a) (Black) Initial data stream to be sent through the CROW. (Blue) The data stream after it has propagated through the CROW, where the carrier frequency is tuned to different locations in the band of the CROW. (b) The frequency domain response of the CROW (green), along with the frequency domain representation of the data stream (blue) at different carrier locations.

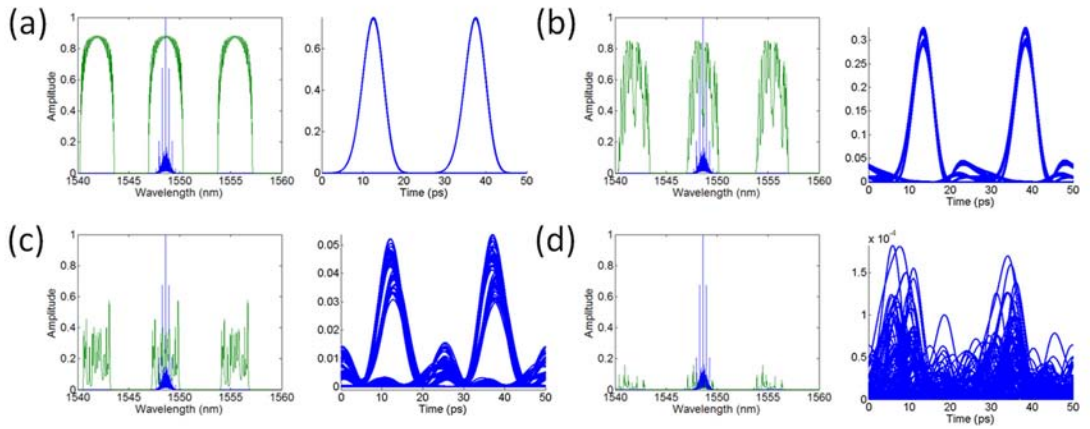

Figure 4.22: Simulation of the eye diagram for a RZ data stream propagating through a 35-ring CROW, tuned to band center. The data stream is shown in blue, and the CROW in green. Disorder was increased in the CROW by increasing the STD between the inter-resonators coupling coefficients and propagation lengths by: (a) $\delta\kappa$ = 0, $\delta\phi$ = 0,(b) $\delta\kappa$ = 0.02, $\delta\phi$ = 0.008,(c) $\delta\kappa$ = 0.06, $\delta\phi$ = 0.02,(d) $\delta\kappa$ = 0.1, $\delta\phi$ = 0.04.

is no pulse, $f_p(t)$ defines the shape of the pulse—assumed here to be Gaussian—and

$T_b = 1/B$, is the bit slot at the bit rate B. The top row of Fig. 4.36(a) shows a simulated 40 Gb/s data stream composed of 5 ps Gaussian pulses with a 25 ps bit slot. While only the initial few bits are shown, 200 bits were used for all of the simulations in this section. The frequency domain representation of this data stream may be calculated through the Fourier transform, $\mathscr{F}$, numerically this is done using FFT operations. Fig. 4.36(b) shows the frequency domain response of the 35-ring CROW (blue), along with the frequency domain representation of the data stream (green), while the carrier frequency of the data stream is being tuned throughout the passband. The corresponding output data streams, $E^{data,out}$, are shown in Fig. 4.36(a), and were numerically calculated from,

$$E^{data,out} = \mathscr{F}^{-1}\left(\mathscr{F}\left(E^{data}(t)\right) \cdot E^{CROW}(f)\right). \tag{4.38}$$

It can be seen that when the data stream's carrier wavelength is turned to the band-gap of the CROW, no signal is recovered at the output. As the carrier wavelength progresses throughout the band of the CROW the signal begins to be recovered. At band center, the data is simply attenuated and shifted in time by 30 ps. In Fig. 4.37 the eye diagrams are shown for an incoming data stream tuned to the center of the CROW band, as the disorder in the CROW is ramped up. Information can thus be recovered for weak variations between the individual resonators, but for a significant amount of disorder the information will not recovered.

4.5 Summary

In this Chapter numerical techniques were outlined to accurately simulate the dispersive properties of high-index contrast silicon-on-insulator nanowires. It was demonstrated that using iterative techniques, one may define fabrication tolerances required for device operation. By calculating the dispersion of the individual supermodes of coupled nanowires, one may obtain the wavelength dependent coupling coefficient $\kappa(\lambda)$. Further, it was demonstrated that by using both of these terms as sub-elements in transfer matrices, one may accurately simulate the multi-band transmission response of a CROW. Such simulations were compared with measured data, showing excellent agreement.

References

[1] M. Hochberg and T. Baehr-Jones, “Towards fabless silicon photonics,” *Nature Photonics*, vol. 4, p. 492Ű702, 2010.

[2] C. L. Xu, W. P. Huang, M. Stern, and S. K. Chaudhuri, “Full-vectorial mode calculations by finite difference method,” *IEE Proc.-Optoelectron.*, vol. 141, pp. 281 –286, 1994.

[3] E. A. J. Marcatili, “Dielectric rectangular waveguide and directional coupler for integrated optics,” *Bell Syst. Tech. J.*, vol. 48, pp. 2071–2102, 1969.

[4] A. Kumar, K. Thyagarajan, and A. K. Ghatak, “Analysis of rectangular-core dielectric waveguides—an accurate perturbation approach.,” *Optics Letters*, vol. 8, pp. 63–65, 1983.

[5] K. Okamoto, *Fundamentals of Optical Waveguides*. Academic Press, 2nd ed., 2006.

[6] W. P. Huang and C. L. Xu, “Simulation of three-dimensional optical waveguides by a full-vector beam propagation method,” *IEEE J. Quantum Electron.*, vol. 29, pp. 2639 –2649, 1993.

[7] W. C. Chew, *Waves and Fields in Inhomogeneous Media*. IEEE Press, 1995.

[8] M. J. Weber, *Handbook of Optical Materials*. CRC Press, 2003.

[9] E. Dulkeith, F. Xia, L. Schares, W. M. J. Green, , and Y. A. Vlasov, “Group index and group velocity dispersion in silicon-on-insulator photonic wires,” *Opt. Express*, vol. 14, p. 3853, 2006.

[10] J. S. Park, S. Zlatanovic, M. L. Cooper, J. M. Chavez-Boggio, I. B. Divliansky, N. Alic, S. Mookherjea, and S. Radic, “Two-pump four-wave mixing in silicon waveguides,” in *FiO 2009 OSA Annual Meeting, Frontiers in Optics*, p. FML2, 2009.

[11] X. Liu, W. M. J. Green, I.-W. Hsieh, J. I. Dadap, Y. A. Vlasov, and R. M. Osgood, "Dispersion engineering in silicon photonic wires using thin si3n4 conformal dielectric coating," in *Lasers and Electro-Optics (CLEO) and Quantum Electronics and Laser Science Conference (QELS), 2010 Conference on*, p. IMC7, 2008.

[12] T. Ishigure, E. Nihei, and Y. Koike, "Optimum refractive-index profile of the graded-index polymer optical fiber, toward gigabit data links," *Appl. Opt.*, vol. 35, p. 2048, 1996.

[13] M. L. Cooper and S. Mookherjea, "Numerically-assisted coupled-mode theory for silicon waveguide couplers and arrayed waveguides," *Optics Express*, vol. 17, pp. 1583 –1599, 2009.

[14] H. A. Haus and N. A. W. Jr., "Elimination of cross talk in optical directional couplers," *Applied Physics Letters*, vol. 46, p. 1, 1985.

[15] C. K. Madsen and J. H. Zhao, *Optical Filter Design and Analysis*. John Wiley & Sons, Inc., 1999.

[16] F. Xia, L. Sekaric, and Y. Vlasov, "Ultracompact optical buffers on a silicon chip," *Nature Photonics*, vol. 1, pp. 65 –71, 2007.

[17] J. K. S. Poon, J. Scheuer, S. Mookherjea, G. T. Paloczi, Y. Y. Huang, and A. Yariv, "Matrix analysis of microring coupled-resonator optical waveguides," *Opt. Express*, vol. 12, no. 1, pp. 90–103, 2004.

[18] A. Yariv, *Optical Electronics in Modern Communications*. New York: Oxford, fifth ed., 1997.

[19] S. Mookherjea, J. S. Park, S. H. Yang, and P. R. Bandaru, "Localization in silicon nanophotonic slow-light waveguides," *Nature Photonics*, vol. 2, p. 90, 2008.

[20] J. Topolancik, B. Ilic, and F. Vollmer, "Experimental observation of strong photon localization in disordered photonic crystal waveguides," *Phys. Rev. Lett.*, vol. 99, no. 25, p. 253901, 2007.

[21] L. Sapienza, H. Thyrrestrup, S. Stobbe, P. D. Garcia, S. Smolka, and P. Lodahl, "Cavity quantum electrodynamics with anderson-localized modes," *Science*, vol. 327, pp. 1352–1355, 2010.

[22] G. P. Agrawal, *Lightwave Technology: Telecommunication Systems*. New Jersey: John Wiley and Sons, 2005.

5 Breakdown of CMT: Strong Coupling Perturbations

Before I came here I was confused about this subject.
Having listened to your lecture I am still confused.
But on a higher level. —Enrico Fermi

Silicon-on-insulator (SOI) waveguides and optical on-chip circuitry rely on the high refractive index contrast between core (silicon, n = 3.5) and cladding (silicon dioxide, n = 1.45) materials to guide light in very compact structures and with small bending radii [1, 2]. SOI photonics is one of the most active areas of ongoing research and large-scale integrated circuits are being designed and fabricated. In many of these proposed circuits, one of the most critical waveguide components is the directional coupler between two parallel waveguides, which is used in microring-based filters [3], Mach-Zehnder interferometers and modulators [4, 5, 6], arrayed waveguide structures [7, 8, 9, 10] etc.

In Chapter 2 and 3 devices were outlined that rely on strongly coupled nanowires. Further, in Chapter 4, numerical techniques for calculating various properties of these waveguides were described; such as methods of calculating the eigenmodes and dispersion characteristics for both coupled and isolated structures. Here, we investigate and quantify the limitations of perhaps one of the most established analytical methods for coupled waveguide analysis, coupled-mode theory (CMT), in designing high index contrast SOI couplers and arrayed waveguides. CMT is a simple and often reliable approach for the design of such structures, formally applicable to low-index and weakly coupled structures, in which the coupling coefficient can be written down in terms of overlap

integrals of the individual waveguide modes and the refractive index distribution $n(x, y)$ in the cross-sectional plane [11, 12, 13]. More accurate corrections to CMT for slab waveguides have been investigated by Chiang [14], and Payne [15], among others (see references therein).

In this Chapter, "exact" results of the coupling coefficients of directional couplers, calculated using a fully-vectorial finite difference frequency-domain (FDFD) method (Section 4.1), are compared with predictions of CMT. We demonstrate how to solve the inverse problem of reconstructing the coupling matrix from the solutions of the FDFD program. As a test structure which highlights both the applicability and shortcomings of CMT, we will consider the multi-waveguide coupled-array structure [16] which consists of a number of directional couplers parallel to one another, as is often used in arrayed waveguide gratings and multi-element lasers and amplifiers, and which require an accurate estimate of the coupling coefficients to prevent imaging and phase errors [17]. We show that, because of the narrow waveguide widths allowed by the high index contrast, multi-waveguide structures can reveal significant next-to-nearest-neighbor coupling and other deviations from the conventional picture of modal coupling, and we find the "critical" waveguide-to-waveguide separation distance at which such terms become significant.

5.1 Coupled-Mode Theory (CMT) of the Modes of Multi-slot Waveguides

If many slot waveguides are arranged in a parallel array, as would be encountered in the cross-section of an arrayed waveguide grating or coupler, or coupled-waveguide laser, then their modes can often be adequately described by supermode theory [16], which is one of the fundamental predictions of coupled-mode theory (CMT), and hence can be a test of the applicability of CMT to SOI photonics. The next section presents the analysis of the modes based on supermode theory, which we will then allow us to compare the predictions of CMT with the FDFD calculations.

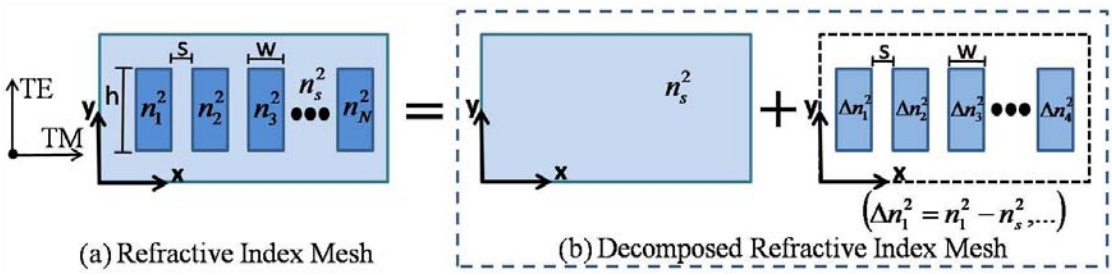

Figure 5.1: (a) Refractive index profile in the transverse plane n(x,y) for an N arrayed-waveguide structure. (b) The same refractive index profile may be decomposed, mathematically, into the sum of parts, $\Delta \mathrm{n}_i^2 = \mathrm{n}_i^2 - \mathrm{n}_s^2$, each of which appears in integrals equation for the coupling coefficients. For the structures considered in here, h = 500 nm, w = 200 nm, and s varies over the range 50 nm to 1μm. For these waveguide widths and heights (similar to those in Ref. [19]), the polarization direction of the principal transverse component of the electric field is indicated for the (quasi) TE and TM modes.

Coupled mode theory and its predictions

To describe the modes of multislot waveguides, we begin with the wave equation [18],

$$\nabla^2 \mathbf{E} + \frac{\omega^2}{c^2} n^2(x,y)\,\mathbf{E} = 0, \tag{5.1}$$

and consider each polarization in turn. (TE and TM polarization are defined in terms of as the major component of the electric field, which for the structure in question, are polarized vertically and horizontally as shown in Fig. 5.1.)

TE polarization

Consider an array of N single mode waveguides, whose refractive index profile is shown schematically in Fig. 5.1a. As long as the waveguides are not too close to each other (i.e., greater than a separation distance which we will investigate and quantify in a subsequent section), the transverse mode profile of the multislot waveguide structure can be approximated by an expansion of the individual high index waveguide modes

$$\hat{E} = \hat{\mathbf{y}} E(x,y)\, e^{-i\beta z} = \hat{\mathbf{y}} \left[\sum_{l=1}^{N} A_l \mathcal{E}_l(x,y) \right] e^{-i\beta z}. \tag{5.2}$$

As shown by Fig. 5.1, the relative dielectric coefficient distribution of the entire N waveguide structure $n^2(x,y)$ can be written as a sum of individual waveguide

contributions, so that

$$n^2(x,y) = n_s^2(x,y) + \sum_{l=1}^{N} \Delta n_l^2(x,y) \tag{5.3}$$

where $n_s^2(x,y)$ corresponds to the cladding. Thus, $n_s^2(x,y)$ + $\Delta n_l^2(x,y)$ would yield the dielectric coefficient profile of the l th waveguide in the absence of the others. Substituting the above two equations into the wave equation, we have,

$$\left(\nabla_\perp{}^2 + \frac{\omega^2}{c^2}\left[n_s^2(x,y) + \sum_{l=1}^{N} \Delta n_l^2(x,y)\right] - \beta^2\right)\left[\sum_{l=1}^{N} A_l \mathcal{E}_l(x,y)\right] = 0. \tag{5.4}$$

The modes of the individual waveguides satisfy their respective eigenvalue equations,

$$\left(\nabla_\perp^2 + \frac{\omega^2}{\mathrm{c}^2}\left[n_s^2(\mathrm{x},\mathrm{y}) + \Delta n_l{}^2(\mathrm{x},\mathrm{y})\right] - \beta_l{}^2\right)\mathcal{E}_l(x,y) = 0 \tag{5.5}$$

and therefore, using Eq. (5.5), Eq. (5.4) can be written as,

$$\sum_{l=1}^{N} A_l \left(\Delta_l + \frac{\omega^2}{c^2}\sum_{\substack{m=1 \\ m\neq l}}^{N} \Delta n_m^2(x,y)\right)\mathcal{E}_l(x,y) = 0 \tag{5.6}$$

where,

$$\Delta_l \equiv \beta_l^2 - \beta^2.$$

N equations are formed by multiplying Eq. (5.6) by $\mathcal{E}_j{}^*$ ($j = 1, 2, \ldots, N$), and integrating each of these equations over x and y,

$$\sum_{l=1}^{N} A_l \left(\Delta_l \iint \mathcal{E}_j^* \mathcal{E}_l \, dxdy + \frac{\omega^2}{c^2}\sum_{\substack{m=1 \\ m\neq l}}^{N} \iint \mathcal{E}_j^* \Delta n_m{}^2(x,y)\, \mathcal{E}_l \, dxdy\right) = 0 \; j = 1, 2, \ldots, N. \tag{5.7}$$

We define the modal overlap integrals as follows:

$$I_{jl} = \iint \mathcal{E}_j^* \mathcal{E}_l \, dxdy, \tag{5.8a}$$

$$\kappa_{jl} = \frac{\omega^2}{c^2}\sum_{\substack{m=1 \\ m\neq l}}^{N} \iint \mathcal{E}_j^* \Delta n_m^2(x,y) \mathcal{E}_l \, dxdy, \tag{5.8b}$$

with the normalization

$$\iint \mathcal{E}_l^* \mathcal{E}_l \, dxdy = 1. \tag{5.8c}$$

I_{jl} is the overlap integral of the modes of two waveguides which are not orthogonal to each other (particularly in the case of small waveguide separation), and κ are the self-coupling and cross-coupling (exchange coupling) coefficients familiar from coupled-mode theory [18, p. 362].

Eq. (9) can then be written in matrix form as an eigenvalue problem,

$$\begin{pmatrix} {\beta_1}^2 + \kappa_{11} & \Delta_2 I_{12} + \kappa_{12} & \dots & \Delta_{N-1} I_{1,N-1} + \kappa_{1,N-1} & \Delta_N I_{1N} + \kappa_{1N} \\ \Delta_1 I_{21} + \kappa_{21} & {\beta_2}^2 + \kappa_{22} & \dots & \Delta_{N-1} I_{2,N-1} + \kappa_{2,N-1} & \Delta_N I_{2N} + \kappa_{2N} \\ \Delta_1 I_{31} + \kappa_{31} & \Delta_2 I_{32} + \kappa_{32} & \dots & \Delta_{N-1} I_{3,N-1} + \kappa_{3,N-1} & \Delta_N I_{3N} + \kappa_{3N} \\ \vdots & \vdots & \vdots & \ddots & \vdots \\ \Delta_1 I_{N1} + \kappa_{N1} & \Delta_2 I_{N2} + \kappa_{N2} & \dots & \Delta_{N-1} I_{N,N-1} + \kappa_{N,N-1} & {\beta_N}^2 + \kappa_{NN} \end{pmatrix} \times$$

$$\begin{pmatrix} A_1 \\ A_2 \\ A_3 \\ \vdots \\ A_N \end{pmatrix} = \begin{pmatrix} \beta^2 & 0 & 0 & \dots & 0 \\ 0 & \beta^2 & 0 & \dots & 0 \\ 0 & 0 & \beta^2 & \dots & 0 \\ \vdots & \vdots & \vdots & \ddots & \vdots \\ 0 & 0 & 0 & \dots & \beta^2 \end{pmatrix} \begin{pmatrix} A_1 \\ A_2 \\ A_3 \\ \vdots \\ A_N \end{pmatrix}. \tag{5.9}$$

(The matrix on the left-hand side of the above equation will be referred to as M.)

If we assume that only nearest neighbor coupling is significant, then the integrals in Eq. (10) are nonzero only when $l = j-1,\ j,\ j+1$. M takes the tridiagonal form,

$$M = \begin{pmatrix} {\beta_1}^2 + \kappa_{11} & \Delta_2 I_{12} + \kappa_{12} & \dots & 0 & 0 \\ \Delta_1 I_{21} + \kappa_{21} & {\beta_2}^2 + \kappa_{22} & \dots & 0 & 0 \\ 0 & \Delta_2 I_{32} + \kappa_{32} & & \dots & 0 \\ \vdots & \vdots & \vdots & \ddots & \vdots \\ 0 & 0 & \dots & \Delta_{N-1} I_{N,N-1} + \kappa_{N,N-1} & {\beta_N}^2 + \kappa_{NN} \end{pmatrix}. \tag{5.10}$$

If the waveguides are identical and equally spaced, M can be further simplified by setting ${\beta_1}^2 = {\beta_2}^2 \ldots = {\beta_N}^2 \equiv {\beta_0}^2$ and also, $I_{l,l+1} = I_{l-1,l} \equiv I, \kappa_{l,l+1} = \kappa_{l-1,l} \equiv \kappa$. However, even if the waveguides are identical and equally spaced, κ_{11} and κ_{NN} are not equal to $\kappa_{22}, \kappa_{33}, \ldots, \kappa_{N-1\,N-1}$. In fact, Eq. (5.8b) shows that for those waveguides at

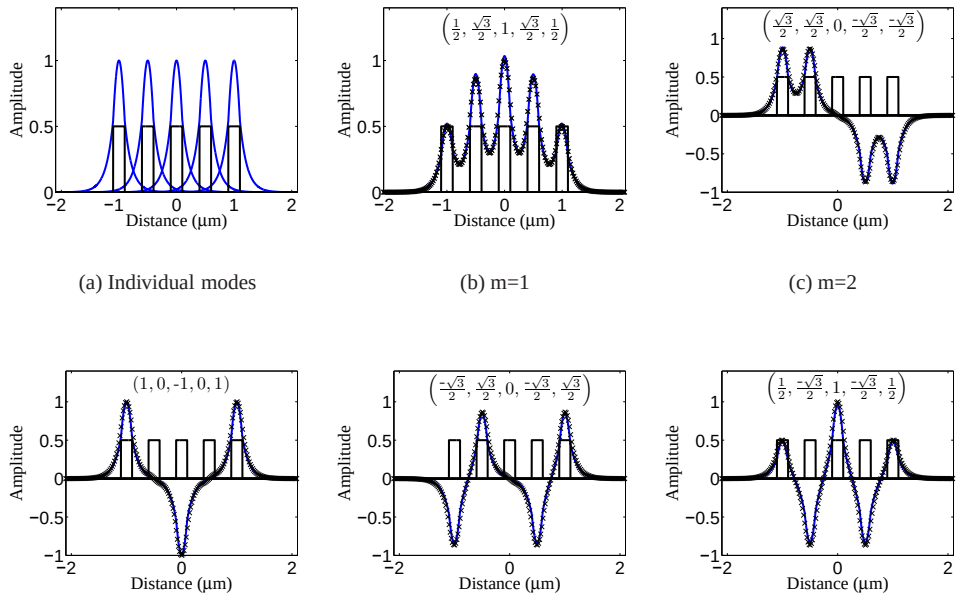

(a) Individual modes (b) m=1 (c) m=2

(d) m=3 (e) m=4 (f) m=5

Figure 5.2: *TE Polarization* E_y: The modes of an $N = 5$ coupled waveguide array for λ = 1550 nm, calculated using coupled-mode theory (blue solid lines), and a finite-difference frequency-domain algorithm (black crosses). The coupled-mode theory calculations were done by using the effective index method, calculating the overlap integrals, solving Eq. (5.9), and reassembling the field. Waveguide height = 500 nm, width = 200 nm, separation = 200 nm, $\mathrm{n_{core}}$ = 3.47, and $\mathrm{n_{clad}}$ =1.46. Under nearest neighbor coupling, the scaling relationship predicted by Eq. (5.11) adequately predicts the field amplitudes within each waveguide.

the edges ($l = 1$ and $l = N$) there are approximately only half as many contributing terms as the other waveguides: there are no waveguides to the left of the $l = 1$ waveguide, and there are no waveguides to the right of the $l = N$ waveguide, whereas all the other waveguides have contribution terms from both the left and right halves of their modal profiles.

We define $\kappa_{\text{self}} \equiv \kappa_{22}, \kappa_{33}, \ldots, \kappa_{N-1\,N-1}$, $\kappa_{\text{self,edge}} \equiv \kappa_{11}$ and κ_{NN}, and $\delta\kappa_{\text{self}} =$

$\kappa_{\text{self}} - \kappa_{\text{self,edge}}$. To first order in the perturbation $\delta\kappa_{\text{self}}$, the eigenvectors are

$$A_l^{(m)} = \left(\frac{2}{N+1}\right)^{1/2} \sin\frac{lm\pi}{N+1} - \delta\kappa_{\text{self}}\left(\frac{2}{N+1}\right)^{3/2} \times \sum_{\substack{n=1 \\ n\neq m}}^{N} \frac{1}{\beta^{2(m)} - \beta^{2(n)}} \left[\sin\frac{m\pi}{N+1}\sin\frac{n\pi}{N+1} + \sin\frac{mN\pi}{N+1}\sin\frac{nN\pi}{N+1}\right]\sin\frac{ln\pi}{N+1} \tag{5.11}$$

where m is the modal number and l indicates which high-index rib waveguide (or low-index slot) is being described. [The expression for the eigenvalues is written later, Eq. (5.20).]

For large N, the second term in the above expression, is smaller than the first by $(N+1)^{-1}$ and can be ignored, yielding a simpler expression. The progression of peak-amplitude values (in the high index regions) $\{A_l^{(m)}\}, l = 1, \ldots, N$ matches with the numerical calculations shown in Fig. 5.2. However, it will be shown that the agreement is good only at large separation distances between the individual waveguides.

TM polarization

For the TM polarization (in which the electric field is normal to the waveguide/slot boundary) the wave equation is now defined in terms of the magnetic field, which is expanded in terms of the individual waveguide modes,

$$\mathbf{H} = \hat{\mathbf{y}}\, H(x,y)\, e^{-i\beta z} = \hat{\mathbf{y}} \left[\sum_{l=1}^{N} A_l H_l(x,y)\right] e^{-i\beta z}. \tag{5.12}$$

Under nearest neighbor coupling, the magnetic field will also obey the scaling relationship of Eq. (5.11). If it can be assumed that $|\partial H_z/\partial y| \ll |\partial H_y/\partial z|$, then H_y and E_x are related by

$$E_x = \frac{\beta}{\varepsilon(x,y)\omega} H_y, \tag{5.13}$$

so that, within the high index ribs, it is expected that Eq. (5.11) describes the scaling relationship of the peak electric field amplitudes. Although the peak electric field amplitudes of the entire modal profile are found not in the high-index regions, but in the low-index regions (just inside the core-cladding boundary), they obviously satisfy the same scaling law, as can be seen in Fig. 5.3.

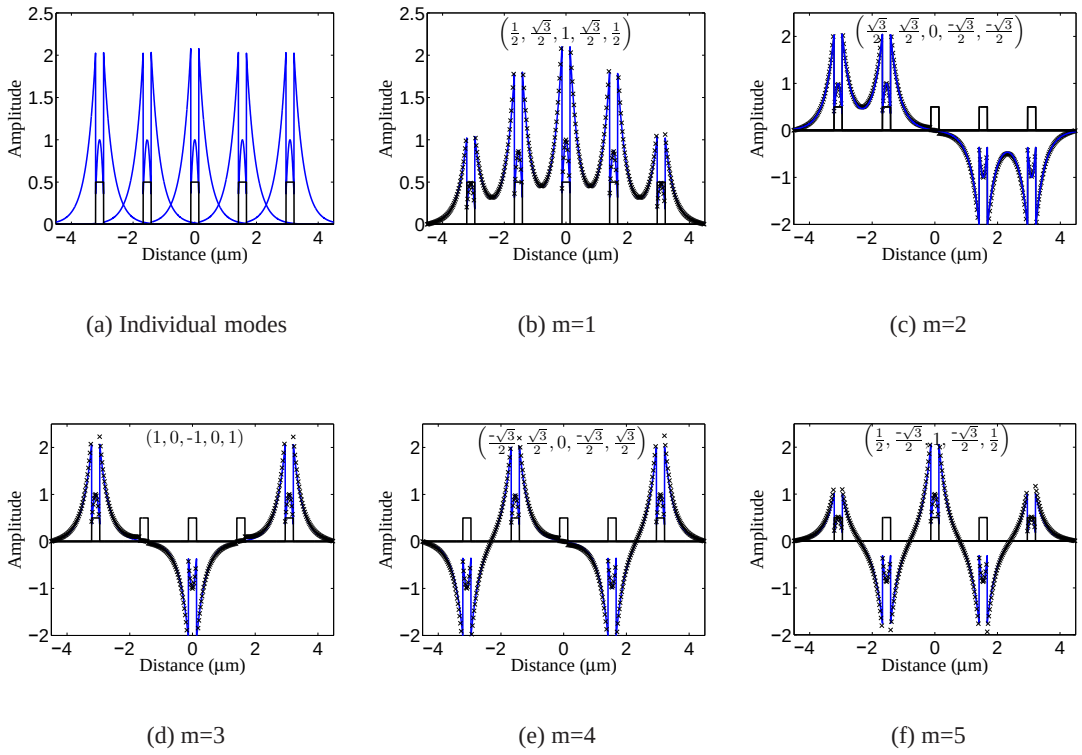

(a) Individual modes (b) m=1 (c) m=2

(d) m=3 (e) m=4 (f) m=5

Figure 5.3: *TM Polarization* E_x: The modes of an $N = 5$ coupled waveguide array, calculated using coupled-mode theory (blue solid lines), and a finite-difference frequency-domain algorithm (black crosses). The coupled-mode theory calculations were done by using the effective index method, calculating the overlap integrals, solving Eq. (5.9), and reassembling the field. Waveguide height = 500 nm, width = 200 nm, separation = 1μm, $\mathrm{n_{core}}$ = 3.47, and $\mathrm{n_{clad}}$ =1.46. Under nearest neighbor coupling, the scaling relationship predicted by Eq. (5.11) adequately predicts the field amplitudes within each waveguide.

5.2 Numerically-assisted CMT: the "Inverse Problem"

CMT offers valuable physical insight into how waveguides couple—in particular, the structure of matrix M in Eq. (11) is revealing—but the quantitative predictions of CMT are in error in high-index-contrast SOI structures at short separation distances. To obtain a numerically-accurate picture of modal coupling, a new extension of CMT is proposed, called "numerically assisted" CMT, to use the simulation results of the FDFD algorithm to back-calculate the elements of the coupling matrix M. One can thereby

check if the assumption of nearest-neighbor coupling is valid at short separation distances, and identify various other interesting coupling phenomena (e.g., non-Hermiticity of M) which have not been pointed out earlier.

To develop NA-CMT, the following mathematical procedure is used, based on a matrix theorem previously developed for coupled-resonator structures [20].

1. First, the supermodes are solved for using FDFD, which does not contain any of the limitations of nearest-neighbor CMT under investigation. The propagation constants of the supermodes are also obtained by this algorithm.

2. Having obtained both the eigenvectors (peak amplitudes) and eigenvalues (propagation constants), one may construct the (non-singular) matrix of eigenvectors A_{mn} (whose columns are the linearly-independent supermodes), and the diagonal matrix of eigenvalues, $\Lambda \equiv \text{diag}\{\beta_m^2\}$.

3. Next, M [see Eq. (5.9)] is reassembled by using the matrix theorem cited in Ref. [20, Eq. (7), Lem. 1–2]: if the eigenvalues are distinct (which they are in this case), M can be reconstructed as follows: $M = A\Lambda A^{-1}$. The matrix is unique to within a similarity transformation, which does not affect the following step. An example is shown in Table 1. (Notice that κ_{11} and κ_{55} are approximately one-half of κ_{22}, κ_{33}, or κ_{44}, as discussed earlier.) The values of the reconstructed M matrix may be useful to design couplers in the strongly-coupled regime from the output of the FDFD mode-solver algorithm itself.

5.2.1 Asymptotic Accuracy of Numerically-assisted CMT

Here, the eigenvalues (λ_k) and eigenvectors ($A^{(k)}$) are obtained from a computer simulation. However, they may be obtained from measurements on fabricated structures, in order to test whether the intended coupling matrix was successfully obtained in practice. The experimental procedure to measure eigenvalues and eigenvectors could be similar to that used to image the modes of laser resonators.

It is assumed that the measurements result in some small, uncorrelated errors in the eigenvalues ($\Delta\lambda_k$) and eigenvectors (Δu_k). The inversion algorithm presented in the

previous section can also be used with measured data. In this section the accuracy of the nearest-neighbor coupling and next-to-nearest-neighbor coupling coefficients in terms of $\Delta\lambda_k$ and Δu_k is studied.

First, a simple theoretical estimation is carried out. It will be assumed that the coupling matrix is Hermitian. After some algebra, the error in any element of M can be written to first order as

$$\Delta M_{ij} = \sum_{k=1}^{N} \left[(u_{ik} + u_{jk})\, \Delta u_k \lambda_k + u_{ik} u_{jk}\, \Delta\lambda_k \right]. \tag{5.14}$$

For simplicity, here, it is assumed that Δu_k is zero, i.e., the errors are only in the measured eigenvalues, since for identical arrayed waveguide structures, successive eigenvectors look quite different from each other and are easily distinguished [20]. The simpler form of the eigenvectors is used, retaining only the first term of Eq. (5.11), so that the errors in the reconstructed nearest-neighbor coupling and next-to-nearest-neighbor coupling coefficients are

$$\begin{aligned} \Delta M_{j\,j+1} &= \sum_{k=1}^{N} \frac{2}{N+1} \sin\frac{jk\pi}{N+1} \sin\frac{(j+1)k\pi}{N+1}\, \Delta\lambda_k, \\ \Delta M_{j-1\,j+1} &= \sum_{k=1}^{N} \frac{2}{N+1} \sin\frac{(j-1)k\pi}{N+1} \sin\frac{(j+1)k\pi}{N+1}\, \Delta\lambda_k. \end{aligned} \tag{5.15}$$

Assuming that $\Delta\lambda_k$ are uncorrelated identically-distributed random variables with mean $E[\Delta\lambda]$ and variance Var$[\Delta\lambda]$, the mean and variance of the nearest-neighbor coupling and next-to-nearest-neighbor coupling coefficients can be calculated. Both $\Delta M_{j\,j+1}$ and $\Delta M_{j-1\,j+1}$ are zero-mean, since, for example,

$$E[\Delta M_{j\,j+1}] = E[\Delta\lambda] \sum_{k=1}^{N} \frac{2}{N+1} \sin\frac{jk\pi}{N+1} \sin\frac{(j+1)k\pi}{N+1} = 0 \tag{5.16}$$

because the summation vanishes as a consequence of the orthogonality of the eigenvectors (the sum is equal to $\mathbf{u}^{(j)}.\mathbf{u}^{(j+1)} = 0$).

To calculate the variance, it can be shown that

$$\begin{aligned} \text{Var}[\Delta M_{j\,j+1}] &= \text{Var}[\Delta\lambda] \left(\frac{1}{N+1}\right)^2 \sum_{k=1}^{N} \left(\cos\frac{2k\pi}{N+1} - \cos\frac{2jk\pi}{N+1} \right)^2 \\ &= \text{Var}[\Delta\lambda] \left(\frac{1}{N+1}\right), \end{aligned} \tag{5.17}$$

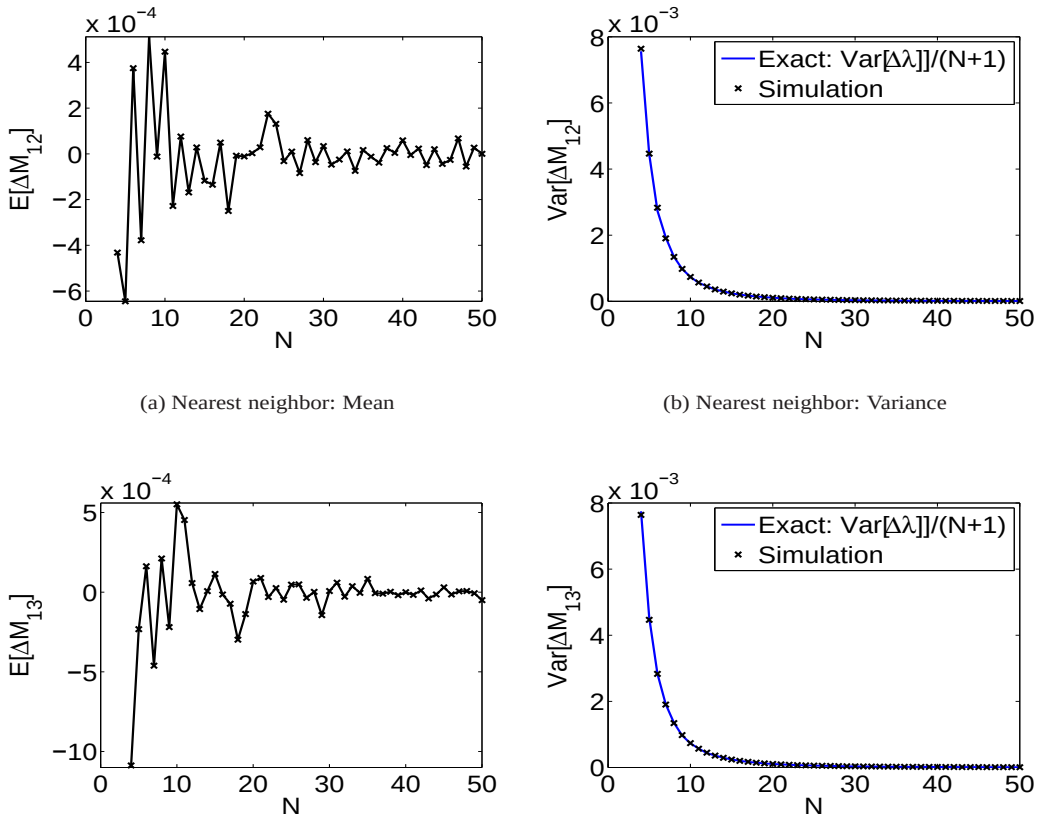

(a) Nearest neighbor: Mean

(b) Nearest neighbor: Variance

(c) Next-to-nearest: Mean

(d) Next-to-nearest: Variance

Figure 5.4: Error versus N: Exact eigenvalues of a tridiagonal symmetric matrix of size N were perturbed by values chosen from a uniform random distribution with variance chosen to be ten percent of the first eigenvalue. The variance and mean of the reconstructed nearest-neighbor coupling and next-to-nearest-neighbor coupling coefficients are plotted, calculated from a distribution of coupling matrices generated by 10^5 iterations, showing that Eq. (5.18) is a good predictor of the reconstruction accuracy.

and the same result is obtained for Var$[\Delta M_{j-1\,j+1}]$.

Summarizing the results,

$$\begin{aligned} &\text{Nearest neighbor:} \quad E[\Delta M_{j\,j+1}] = 0, \quad \text{Var}[\Delta M_{j\,j+1}] = \text{Var}[\Delta\lambda]/(N+1), \\ &\text{Next-to-nearest:} \quad E[\Delta M_{j-1\,j+1}] = 0, \quad \text{Var}[\Delta M_{j-1\,j+1}] = \text{Var}[\Delta\lambda]/(N+1). \end{aligned} \tag{5.18}$$

Numerical calculations, shown in Fig. 5.4 confirm Eq. (5.18). (Numerical calculations show that the same relations are seen to hold in the case of non-identical waveguides, in which case the off-diagonal terms of the coupling matrix are not identical along the

sub-diagonals, and also for slightly asymmetric matrices.)

These results show that the error in reconstructing the coupling coefficients decreases, rather than increases, as the number of inaccurately-measured eigenvalues increases. This results from (spectral) averaging: each reconstructed coupling coefficient averages over the entire spectrum of eigenvalues, and therefore, benefits from the law of averages. In contrast, directly measuring a coupling coefficient e.g., by a local near-field probe of the field in the coupling region, does not benefit from any ensemble averaging.

5.2.2 Next-to-nearest-neighbor Coupling

As Table 1 shows (calculated at one specific value of the waveguide separation distance), M contains useful information about non nearest-neighbor coupling. One may read off whichever coupling coefficients are needed: in particular, one may calculate the ratio $|\kappa_{13}/\kappa_{12}|$, i.e., the ratio of next-to-nearest-neighbor coupling coefficient to the nearest-neighbor coupling coefficient.

Table 5.1: An example of a reconstructed coupling (M) matrix from FDFD calculations of eigenmodes and eigenvalues. Si/SiO_2, TE polarization, separation s = 350 nm, $\beta_0 = 2.26128\,(2\pi/\lambda)$. Although the nearest-neighbor coupling coefficients dominate, the self-coupling and off-tridiagonal coupling terms are non-zero.

$$M = \text{diag}\left\{{\beta_0}^2\right\} + \begin{pmatrix} -0.00636 & +0.12794 & -0.00641 & +0.00057 & -0.00004 \\ +0.12789 & -0.01263 & +0.12838 & -0.00643 & +0.00050 \\ -0.00635 & +0.12839 & -0.01271 & +0.12839 & -0.00635 \\ +0.00050 & -0.00643 & +0.12838 & -0.01263 & +0.12789 \\ -0.00004 & +0.00057 & -0.00641 & +0.12794 & -0.00636 \end{pmatrix}$$

First we estimate the expected dependency of this ratio of coupling coefficients to the edge-to-edge separation, s. Using Kuznetsov's solution for the coupling coefficients of two slab waveguides [21], we observe that κ in both the TE and TM cases varies with s as $\kappa \sim e^{-ps}$ where p is the field decay length in the cladding. Therefore,

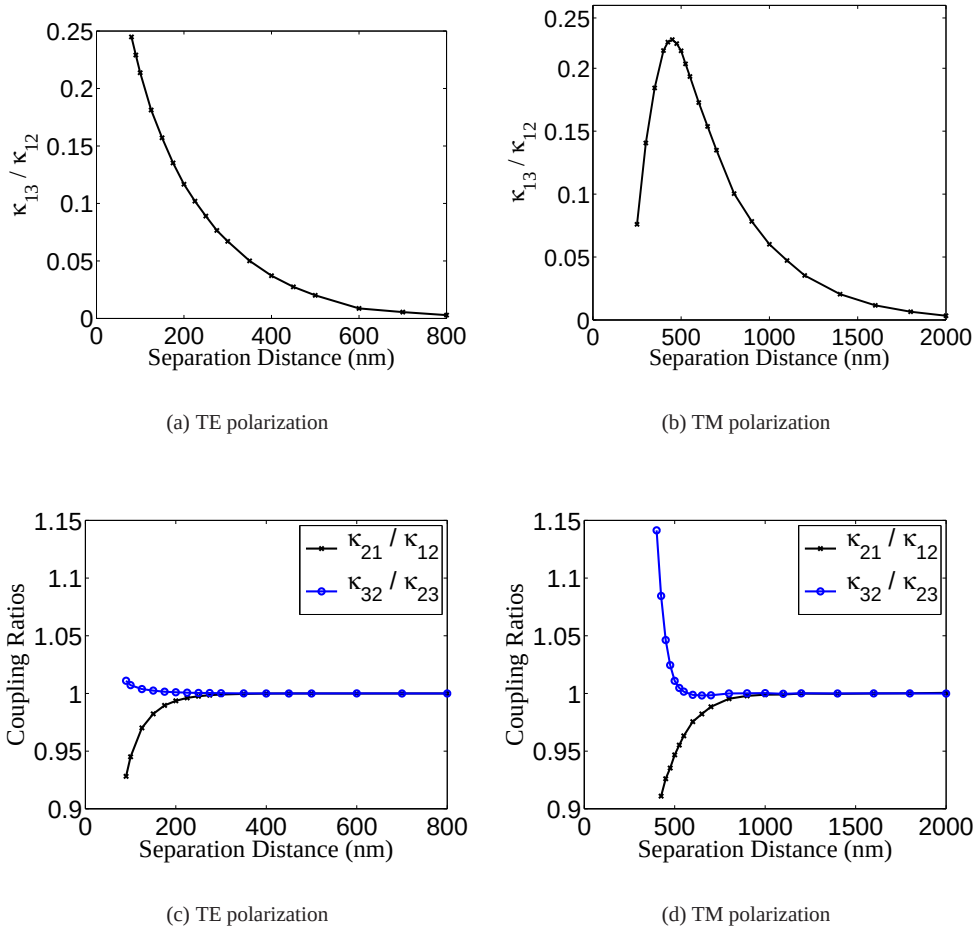

(a) TE polarization

(b) TM polarization

(c) TE polarization

(d) TM polarization

Figure 5.5: Ratio of coupling coefficients for different separation distances extracted from Eq. (5.9), which was reconstructed using an algorithm described in the text. (a) *TE Polarization* An exponential fit expected from a simple nearest-neighbor-coupling theory holds throughout this regime. (b) *TM Polarization* At a separations less than 450 nm, the ratio deviates significantly from the predicted behavior. (c) *TE Polarization* The ratio of cross coupling coefficients show that the reconstructed coupling matrix M becomes asymmetric as the waveguide separation is reduced. (d) *TM Polarization* The asymmetry of the coupling matrix begins at a larger separation.

the ratio κ_{13}/κ_{12} for both polarizations has the following expression (to leading order),

$$\frac{\Delta_3 I_{13} + \kappa_{13}}{\Delta_2 I_{12} + \kappa_{12}} \approx \frac{\kappa_{13}}{\kappa_{12}} = \frac{e^{-p(2s+w)}}{e^{-ps}} = e^{-p(s+w)} \tag{5.19}$$

i.e., the ratio of next-to-nearest-neighbor coupling coefficient to the nearest-neighbor coupling coefficient should fall off exponentially with increasing separation.

Fig. 5.5 shows the calculations of this ratio using the above algorithm. The ex-

ponential fit describes the TE polarization much better than it does the TM polarization, indicating that some of the central assumptions of CMT are starting to fail for the TM polarization at short distances. The next section will describe another symptom of the failure of CMT, obtained by looking at the eigenvalues, i.e., the propagation constants, of the supermodes.

5.2.3 Eigenvalue Fanout: Effective Index of the Supermodes versus Separation Distance

Another way to evaluate the predictions of CMT is the theory behind the eigenvalues of Eq. (5.9), which predicts that the effective index of the m-th supermode is given by the equation

$$\beta^{2^{(m)}} = {\beta_0}^2 + \kappa_{\text{self}} + 2\left(\kappa + \Delta_0 I\right)\cos\frac{m\pi}{N+1} - 2\frac{\delta\kappa_{\text{self}}}{N+1}\left(\sin^2\frac{m\pi}{N+1} + \sin^2\frac{Nm\pi}{N+1}\right), \tag{5.20}$$

where β_0 is the propagation constant of a single waveguide in isolation. Note that for $N = 5$, the $m = 3$ supermode has the special property that the right-hand-side of the above expression , i.e., the index of that supermode does not change with the coupling coefficient κ. Hence, $n_{\text{eff}}^{(3)}$ is only weakly dependent on the separation distance (through the self-coupling coefficients, $\kappa_{11}, \kappa_{22}, \ldots, \kappa_{55}$).

To verify this prediction, Fig. 5.6 shows the effective index calculated by FDFD for each of the five supermodes at various separation distances in three different silicon-based material systems. These values of the effective index take into account coupling-induced frequency shifts (CIFS, [22]) because M itself results from a numerical calculation of the supermodes (and their eigenfrequencies), rather than individual waveguide modes and the propagation constants of isolated waveguides.

In the limit of large separation, the effective indices of all the supermodes tends to that of the single waveguide. As the separation distance is decreased, the coupling coefficients increase, and the effective indexes of the different modes separate [23]. The first three modes remain guided even as s shrinks to zero, since their effective indices are higher than that of the single waveguide. From Fig. 5.6, one can read off the waveguide separation distance at which conventional CMT is expected to fail, and more

accurate design tools, such as FDFD calculations, should be used to accurately predict the coupling coefficients.

An interesting observation obtains from the $m = 3$ supermode: at a certain (small) waveguide separation, $n_{\text{eff}}^{(3)}$ is no longer independent of s and begins to deviate substantially from a straight line, contrary to the prediction of Eq. (5.20). This deviation is much more pronounced in the case of the TM polarization.

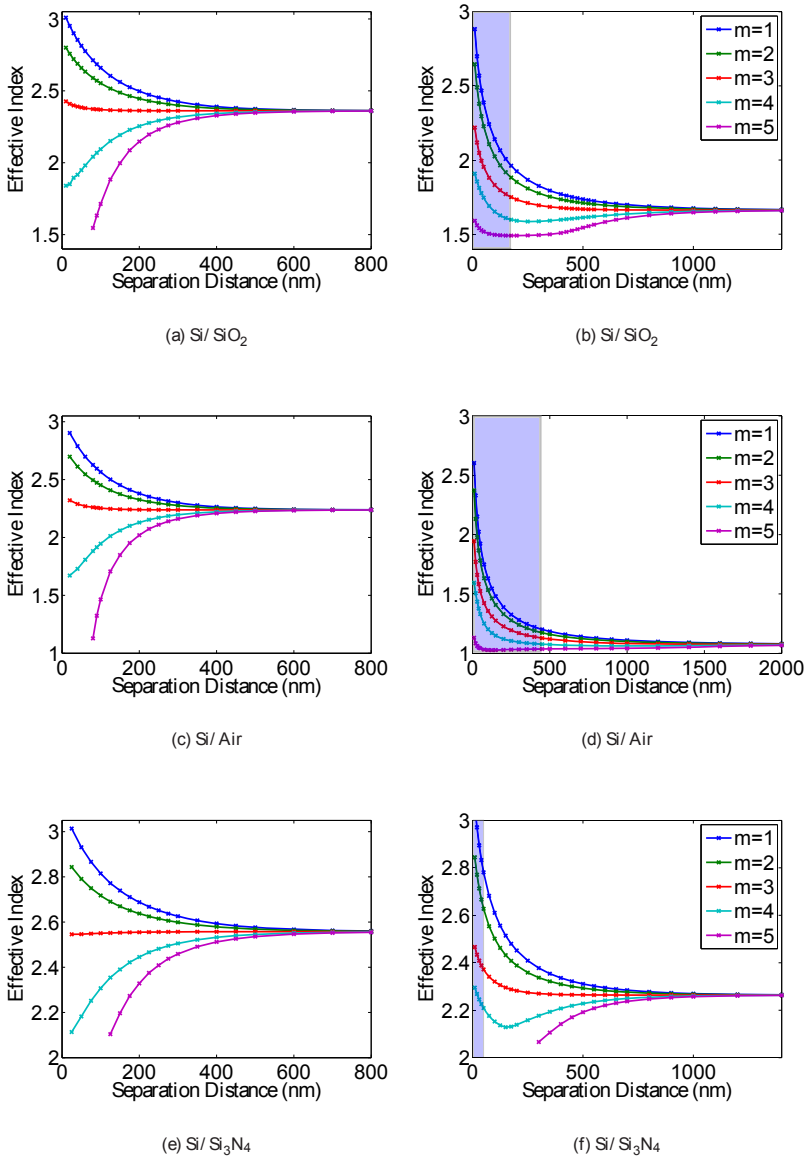

Figure 5.6: Left column: TE Polarization, and Right column: TM polarization. Effective index of the five supermodes for different separation distances with n_{core} = 3.47, and (a,b) n_{clad} =1.46, (c,d) n_{clad} = 1 (e,f) n_{clad} = 2.05. For each case as the separation between the waveguides increases, the effective indexes of the modes converge to that of the single waveguide. These values are (a) n_{eff} = 2.36 and (b) n_{eff} = 1.66 for oxide cladding, (c) n_{eff} = 2.24 and (d) n_{eff} = 1.07 for air cladding, (e) n_{eff} = 2.56 and (f) n_{eff} = 2.26 for nitride cladding. The shaded regions indicate $> 5\%$ deviation of n_{eff} for the m=3 supermode from its theoretical value, which as discussed in the text, is predicted by CMT to be independent of the separation distance.

5.3 Electric Field Perturbations from Strong Coupling

In the previous section, it was detailed how the predictions of coupled mode theory are no longer valid at short separation distances. Here, we will show exactly what is happening to the coupled-modes themselves at these distances. As described in section 1.4.1, at short separation distances, the reconstructed matrix M can become non-symmetric (non-Hermitian), although the eigenvalues remain strictly real as long as the mode is above cut-off. This can be seen in fact in the matrix written in Table 1 and Fig. 5.5(c,d): $\kappa_{12} \neq \kappa_{21}$ and $\kappa_{13} \neq \kappa_{31}$, etc.

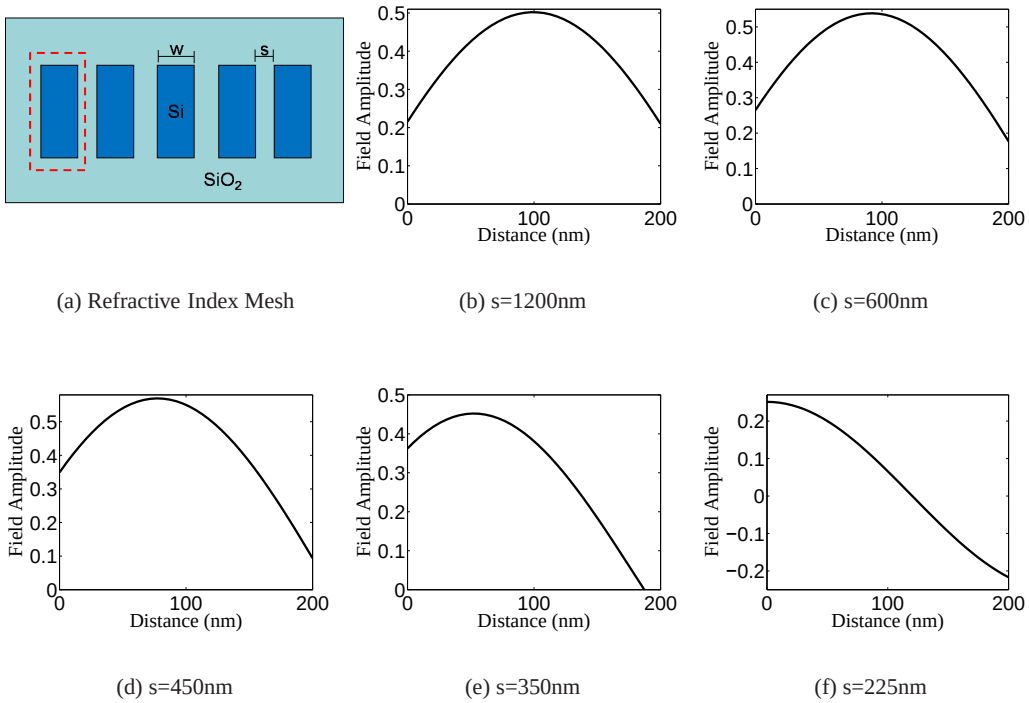

(a) Refractive Index Mesh (b) s=1200nm (c) s=600nm

(d) s=450nm (e) s=350nm (f) s=225nm

Figure 5.7: *TM Polarization* E_x: The field profile of the fifth eigenmode in the first waveguide. When the separation is decreased below 450 nm, the peak of the field in the high-index rib indicated by the dotted red line in (a) is no longer centered, and the mode shape is considerably altered, thereby changing both κ and n_{eff}. Consequently, CMT can no longer accurately predict the mode coupling.

The reason for this asymmetry is that the fields within the individual waveguides are no longer centered between the dielectric boundaries. As shown in Fig. 5.7, the

modal profile starts to deviate in the location of its maxima and minima. For example, the peaks of the field in the outermost ribs are skewed and no longer centered in the middle of the dielectric boundaries, and can even reach the boundaries of the high-index and low-index regions. It is no longer accurate to read off the peak amplitudes of the supermode in order to write the eigenvectors $A^{(m)}$ in Eq. (5.11)—doing so would result in asymmetric M matrices.

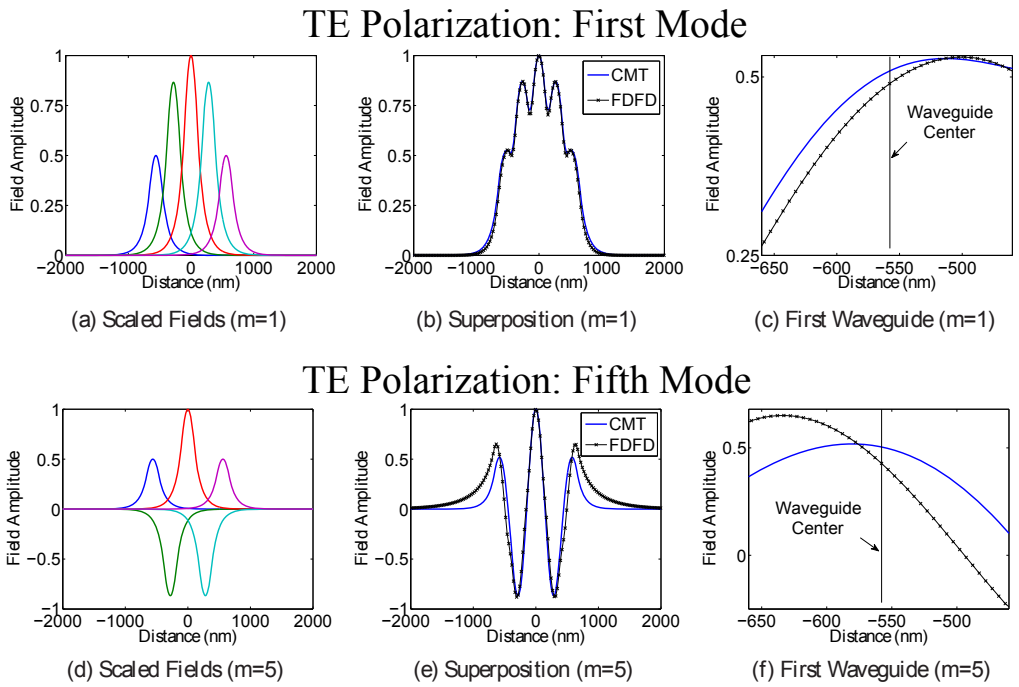

Figure 5.8: *TE Polarization* E_y: Using the exact solution from a FDFD simulation of a single waveguide, the horizontal cross section is extracted and five copies are shifted from one another so that their separation corresponds to a waveguide separation of 80 nm. (a) These individual waveguide modes are scaled in accordance with Eq. (5.11) for the fundamental mode (m=1). (b) The summation of the individual waveguide modes; superimposed is the FDFD solution of the entire five waveguide structure. (c) Zoomed in to just the first waveguide. CMT and FDFD show a shift of the mode towards the center of the waveguide structure. (d-e) The fifth mode, both CMT and FDFD show a shift towards the edge of the waveguide structure however FDFD shows a shift of greater magnitude.

At a short separation distance of 80 nm, Fig. 5.8 shows the coupled-mode theory used to reconstruct the $m = 1$ and $m = 5$ supermode (plotted with continuous lines) and the supermode calculation of FDFD (with crosses). Note that in both cases the field

is asymmetrically centered within the dielectric boundaries of the outer waveguides. Recall that CMT is based on writing the field as a summation of the scaled individual waveguide modes, Fig. 5.8(a,d), each of which is centered within its own core-cladding boundaries. At short separation distances, when, for example, there is a significant contribution of the (asymmetric) tail from the field in the second waveguide to the (symmetric) mode of the first waveguide, CMT itself predicts a lateral shift of the peak (of the sum) away from the exact center of the waveguide. The scaling relationships from Eq. (5.11) will enhance this effect for a multi-waveguide arrayed structure compared to a (twin-waveguide) directional coupler.

For the fundamental mode, Fig. 5.8(a-c), the summation of the fields associated with the first (blue) and second (green) waveguides results in the peak shifting towards the center of the five waveguide structure, which qualitatively agrees with the FDFD simulation. But the FDFD result for the fifth mode shows a shift of greater magnitude, now towards the outer edge of the waveguide structure, indicating that CMT no longer accurately predicts the modal profile of the supermode. TM polarized modes start to shift at a larger separation, due to the field discontinuities at the waveguide boundaries and electric field enhancement in the cladding regions.

To emphasize this fact, Fig. 5.9 plots the locations of the field peaks in the arrayed waveguide structure for each of the supermodes as the separation distance between the waveguides is reduced. Note that for large separation distances all of the peaks are located at the center of the dielectric boundaries for each of the five supermodes. However, as the separation distance is further reduced the field peaks begin to shift, and, as shown for both the fundamental and fifth supermode, at sub-50 nm separation distance the field peaks for the two outer waveguides have completely left their dielectric boundaries (this is very different from the conventional picture of supermodes in weakly coupled arrays [16]). As outlined in Fig. 5.8, the direction of the shift of an individual waveguide's peak for each supermode is completely determined by the scaled magnitude and phase of the evanescent tail of the neighboring waveguide. This shifting of the modal peaks for each of the supermodes is accompanied by a change of the effective index of each of the supermodes, Fig. 5.6. As shown in Chapter 4, this "eigenvalue fanout" is a well known prediction of CMT with strong practical applications. For

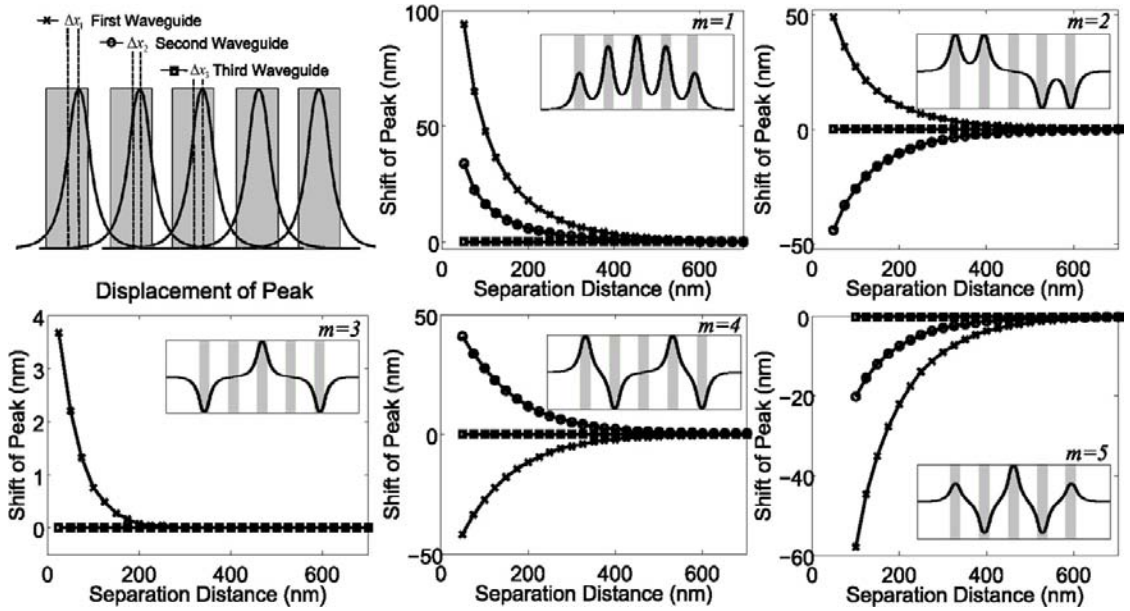

Figure 5.9: Displacement of the field peaks for each of the five supermodes shown in Fig. 1 as the separation distance is varied. As the separation is reduced, the modal profiles become strongly perturbed, while at large separations each of the field peaks is exactly centered within its dielectric boundaries. The modal profiles were obtained from a finite difference frequency domain algorithm [24].

example, a result of this fanout is the dephasing of the symmetric and antisymmetric supermode of an N = 2 arrayed waveguide structure, which completely determines the directional coupler's beat length [25].

Note also, as shown in Fig. 5.8(e), that FDFD predicts a different exponential decay constant of the field wings, compared to CMT. This is a fundamental failure of CMT in the sense that the eigenmode of the composite structure can no longer be written as the sum of modes of individual waveguides (in isolation from each other). In addition to perturbations of the electric field within the high-index silicon regions, strong coupling also affects the decay rate of each of the supermodes outside the arrayed waveguide structure. It is the fields in this region that are responsible for determining coupling length, cross talk, and circuit integration density.

5.3.1 Evanescent Tail Fanout

The electric field in the cladding region decays exponentially with distance. Conventional CMT for arrayed slab waveguides predicts that the m^{th} supermode decays with some spatial constant p,

$$E^{(m)}_{\text{cladding}}(x) = \sum_{l=1}^{N} A_l^{(m)} e^{-p(|x|-(l-1)d)} = C^m e^{-p|x|}, \tag{5.21}$$

where d is the center-to-center spacing between individual waveguides and,

$$C^m = \sum_{l=1}^{N} A_l^{(m)} e^{p(l-1)d}, \tag{5.22}$$

where

$$A_l^{(m)} = \left(\frac{2}{N+1}\right)^{1/2} \sin\frac{lm\pi}{N+1}, \quad \begin{matrix} m = 1, 2, \ldots, N \\ l = 1, 2, \ldots, N \end{matrix}. \tag{5.23}$$

Since C^m is a constant for the m^{th} supermode, CMT predicts the same decay rate for each supermode regardless of separation.

Fig. 5.10 (markers) shows the exact decay constant of each of the five supermodes of the arrayed waveguide structures studied here as the waveguide separation is

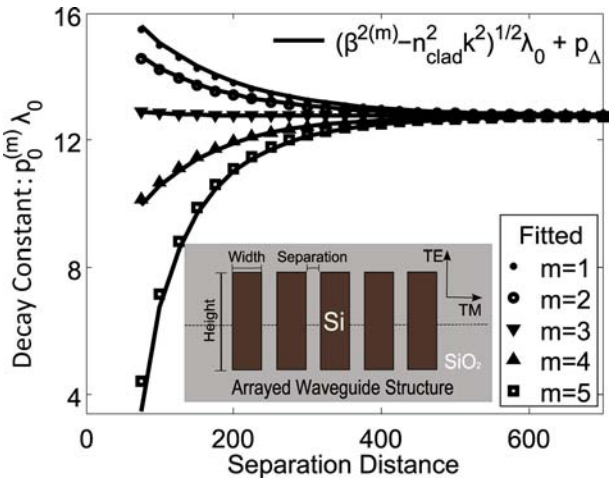

Figure 5.10: Decay constant of the five supermodes for different separation distances with height 500 nm and width 200 nm. The evanescent tail is fitted around 50 nm from the edge of the waveguide. Also included is the slab waveguide predictions (solid-line) for each of the five supermodes, offset by a constant, p_Δ, as described in the text.

reduced. The decay constant is determined by numerically fitting the evanescent tail to an exponential form, $e^{p_0^{(m)}x}$, around 50 nm from the edge of the waveguide. Also included is the slab waveguide solution of the decay constant (solid-line), which is calculated from the corresponding supermode's effective index, and is offset by a constant, p_Δ, to be described in the next section. It can be seen that despite the CMT prediction of the same decay rate across each of the supermodes, there is indeed a strong dependence of the supermode's decay rate on the supermode's effective index, which is a well known correspondence for optical modes as shown in both the analytical solutions for the higher order modes of a single slab waveguide and an optical fiber [26]. At large separation distances, or in the "weakly-coupled" regime, the decay rate of each of the supermodes converges to that of the single isolated waveguide and will have asymptotically identical decay rates. As the separation distance is reduced, the decay rates fan out, with the fundamental mode decaying the quickest in the cladding region.

We will next show that in addition to these strong coupling effects—shifting of the electric field peak locations and evanescent tail fanout—another perturbative effect on the arrayed waveguide structure is due to the vertical confinement of the mode.

5.3.2 Effects of Modal Confinement on the Isolated Waveguide

The framework of CMT is built upon writing the coupled-waveguide's electric field profile in terms of a linear superposition of the individual isolated waveguide modes. It is therefore necessary to have an accurate understanding of how confinement of the optical mode affects the basis set used in reconstructing the supermode profiles of an arrayed waveguide.

As shown in Fig. 5.11(a), in order to demonstrate the effects of optical confinement on the waveguide mode we fit the evanescent tail of the transverse electric field profile, E_y, at the center cross section of an isolated single waveguide (height = 250 nm), every 25 nm around 50 nm to an exponential form, $e^{p(x)x}$. The mode profiles were obtained from a finite element mode solver (COMSOL). Fig. 5.11(b) shows that for a single waveguide of 500 nm height, the field in the cladding decays exponentially with a *spatially varying* (i.e., chirped) decay constant $p(x)$, with the mode decaying faster

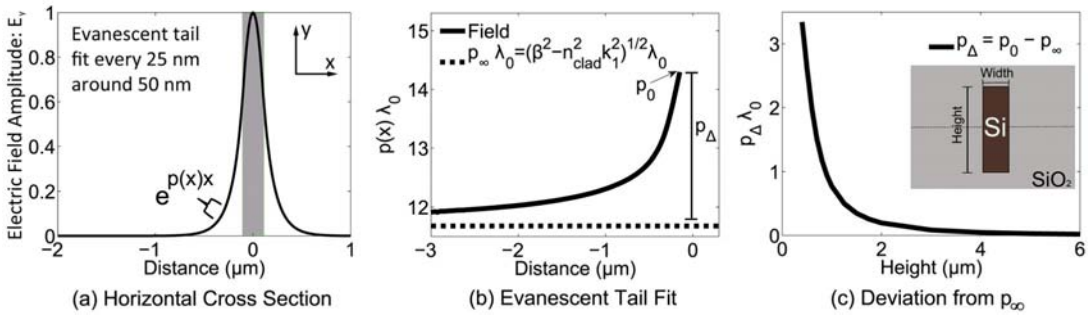

Figure 5.11: (a) Method of extracting the spatially dependent decay constant: The evanescent tail is fitted at the center cross section of an isolated single waveguide (height = 250 nm), every 25 nm around 50 nm to an exponential form, $e^{p(x)x}$. (b) A spatial dependence of the decay rate is introduced due to the vertical confinement of the waveguide. (c) As the height of the waveguide is increased, the maximum decay rate, p_0, approaches the slab waveguide solution, p_∞.

near the edge of the waveguide, where $p(x = 0) \equiv p_0$. We find that the reason for this novel spatial dependence of the decay constant is due to the vertical confinement of the mode. In Fig. 5.11(c), we show the dependence of p_0 on the height of the waveguide: for large heights p_0 approaches the spatially-independent slab-waveguide solution, $\mathrm{p}_\infty = \sqrt{\beta^2 - \mathrm{n}^2_{\mathrm{clad}} k^2}$. We define p_Δ as the difference between p_0 and p_∞. We will next show how this spatial dependence of the decay constant affects the supermodes when five such waveguides are coupled together.

5.3.3 Effects of Modal Confinement on the Arrayed Waveguide

A similar analysis as demonstrated in the previous section is performed on the supermodes of the arrayed waveguide. Fig. 5.12 shows the decay rate $p^{(m)}$ of the five supermodes of the arrayed waveguide structure, calculated numerically from FEM simulations at a separation of 80 nm. It can be seen that the spatial dependence of the decay rate of the single isolated waveguide is impressed onto the supermodes of an arrayed waveguide structure. Note that each of the five supermodes asymptotically approaches its respective $\mathrm{p}^{(m)}_\infty$ (dashed-line), and that these asymptotic values have "fanned out" due to the strong coupling at this separation distance. The isolated single waveguide solution

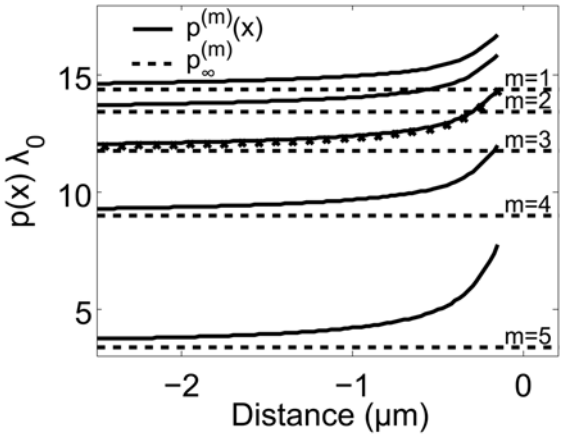

Figure 5.12: Spatially-dependent decay rate of the five supermodes at a separation distance of 80 nm, showing the super-exponential decay of the fields close to the high-index contrast dielectric boundaries. Farther away from the boundaries, the fields are well described by an exponential decay constant $\mathrm{p}_{\infty}^{(m)}$ (dashed-line). The isolated, single waveguide solution (black crosses) is located slightly below the m = 3 supermode.

(black crosses) is plotted slightly below the m = 3 supermode, where it is known from CMT that for this mode only next-to-nearest neighbor coupling affects the modal profile and effective index, which explains the high degree of agreement between the two trends. The dependence of the decay-rate on both confinement and coupling is outlined in Fig. 5.13 and Fig. 5.14. As the waveguide separation is increased, both $\mathrm{p}_{\infty}^{(m)}$ and $\mathrm{p}_{0}^{(m)}$ approach that of the single waveguide for each of the supermodes.

5.4 Modifying the CMT Basis for Reconstruction

There has been a significant amount of research with the aim of developing more accurate versions of CMT [27, 28, 14, 15, 25], and while they can offer improved accuracy for many waveguide devices compared with conventional CMT, they can also be less intuitive to incorporate into a specific design; not to mention that many of these improved methods are developed within the limitations of the effective index method for ridge waveguide structures. Here, we show how one may extend CMT to incorporate these perturbative effects, thus retaining much of the simplicity and intuitiveness often

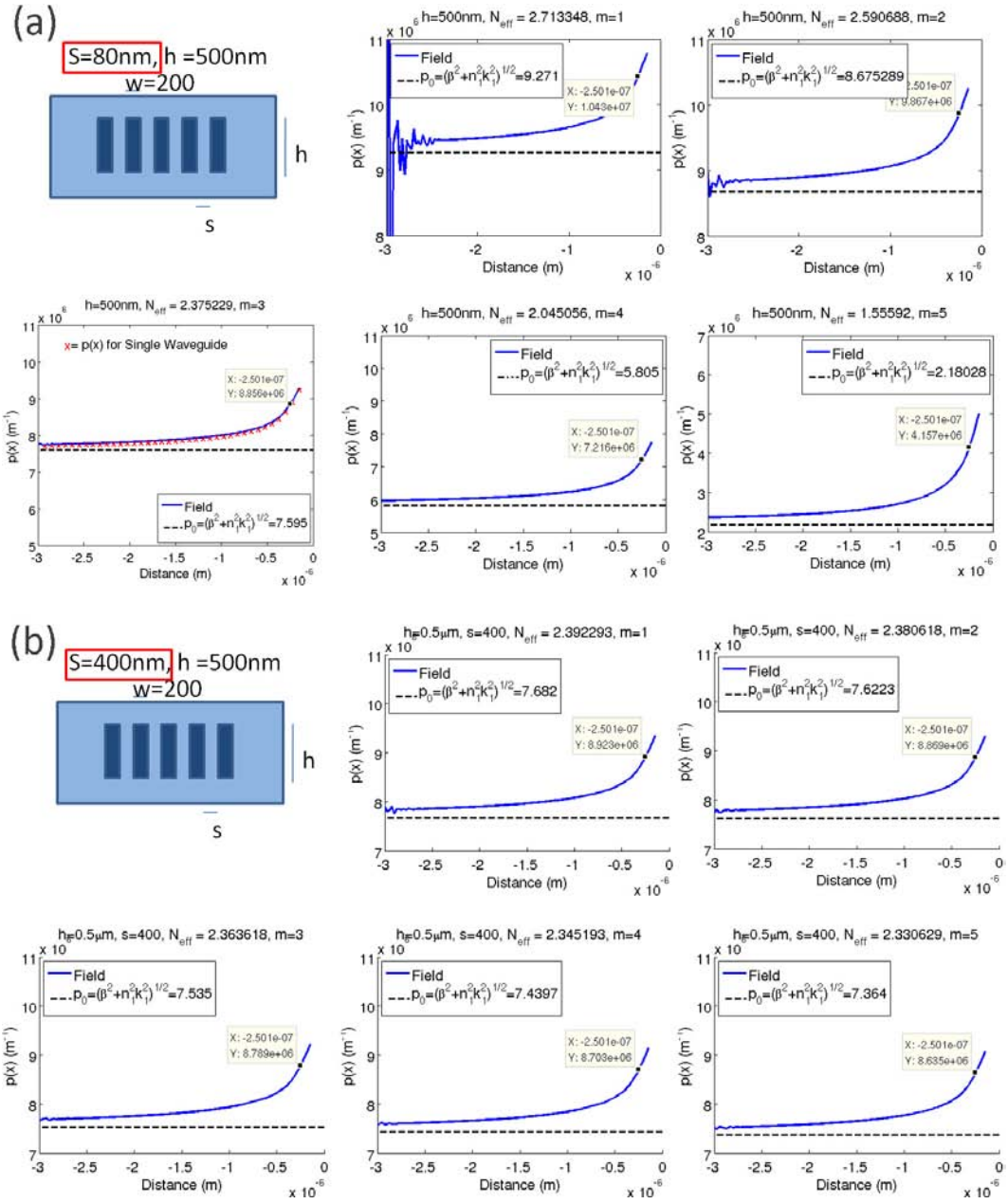

Figure 5.13: (a) Spatially-dependent decay rate of the five supermodes at a separation distance of 80 nm, and a height of 500 nm. Note that the supermodes decay to different assymptotic values. (b) By increasing the separation between the waveguides, the spatial dependence of the decay rate remains—that of the single isolated waveguide—however, each mode decays to the same asymptotic value.

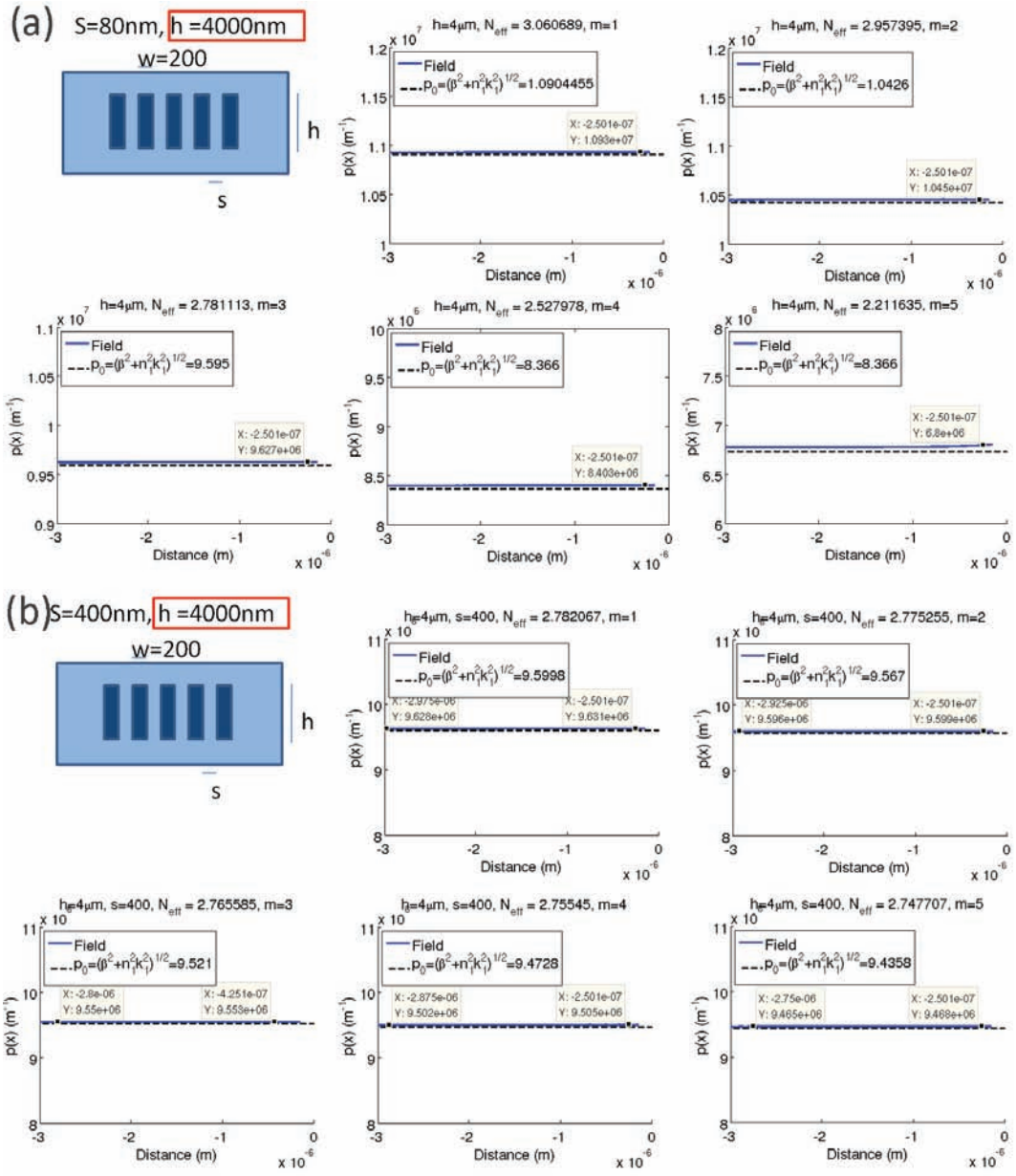

Figure 5.14: (a) By increasing the height of the waveguide, each of the five supermodes no longer has a spatially dependent decay rate, however, at a separation of 80 nm each of the supermodes decays at a different (constant) rate. (b) For a 400 nm separation and a 4 μm height, the supermodes have no spatial dependence, and decay at the same rate (and thus satisfy the requirements of CMT)

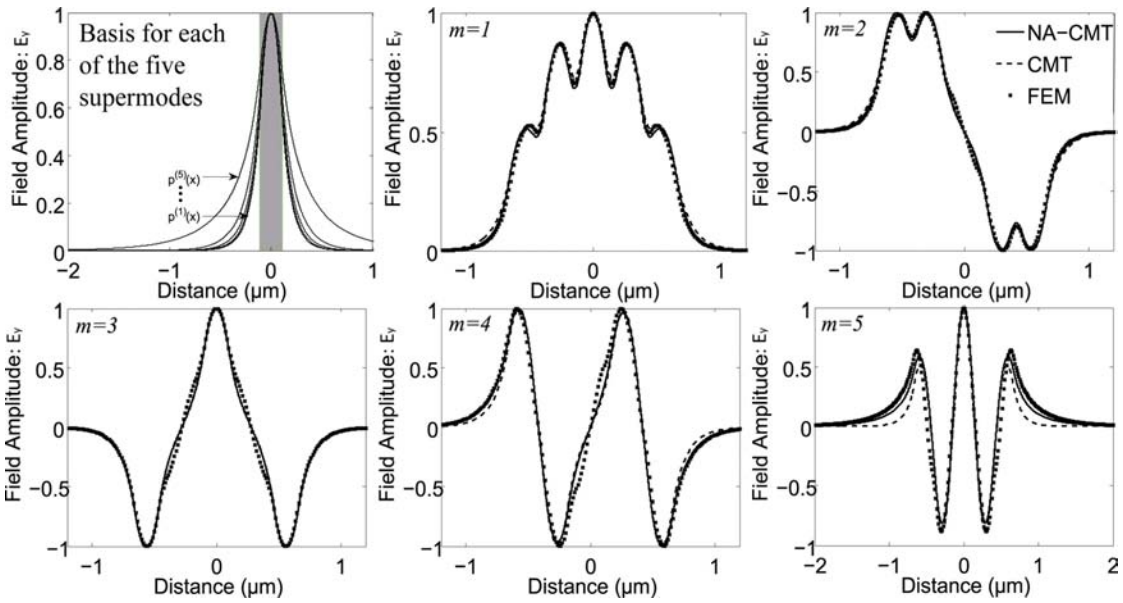

Figure 5.15: Comparison of the modes generated at a separation of 80 nm from both traditional CMT and the new basis set; the latter accounts for the spatial dependence of the field decay coefficients. To obtain the composite field, five copies are made of an individual waveguide mode, laterally shifted from one another, scaled according to the usual supermode ratios [25, Eq. (13)], and summed.

associated with CMT while also providing improved modal profile predictions compared with conventional CMT [29]. This coupled mode theory analysis assumes that the evanescent tail of a single waveguide can be calculated (or measured), e.g., using a standard finite element or finite difference method. For the transverse electric polarization, which requires continuity of the electric field across the waveguide boundaries in the coupling region, it will be shown how conventional CMT can be adapted by accounting for a simple spatial dependency of the parameters that enter into the basis set of solutions to the coupled mode equations. This “running” of the parameters is unique in the development of optical coupled mode theory. More accurate modal profiles allow for improved estimation of coupling lengths and crosstalk in multi-waveguide and inter-connect structures.

5.4.1 Calculating the Transverse Field Profile

Here, the problem of reconstructing (or predicting) the mode profiles accurately is analyzed, by taking as our starting point measurements or numerical estimates of the spatially dependent decay rate, $p^{(m)}(x)$, such as shown in Fig. 5.11. This method assumes—as usual—that within the high index regions, the field has a dependence of the form $\cos(h^{(m)}x)$. The relationship between $p_0^{(m)}$ and $h^{(m)}$ is of the same form as for a slab waveguide, i.e., satisfying the requirement of continuity and differential continuity across the waveguide boundary,

$$p_0^{(m)}(s) = h^{(m)}(s)\ \tan[h^{(m)}(s)w], \tag{5.24}$$

where $2w$ is the width of each silicon waveguide. Then, we assemble the field as usual,

$$\hat{E}^{(m)}(x;s) = \sum_{l=1}^{N} A_l^{(m)} \times \begin{cases} \cos\left[h^{(m)}(s)(|x| - (l-1)d)\right], \\ \qquad x \in ([l-1]d - w, [l-1]d + w) \\ \cos\left[h^{(m)}(s)w\right] e^{-p^{(m)}(x,s)(|x-(l-1)d|-w)}, \\ \qquad \text{otherwise} \end{cases} \tag{5.25}$$

In words, $\hat{E}^{(m)}(x;s)$ represents the scaled summation of shifted replicas of the single-waveguide modal solution, where the latter are renormalized by the running of the p and h constants with the inter-waveguide separation distance, s. By way of comparison, in conventional CMT, although the superposition coefficients may be spatially dependent (as in the analysis of tapered couplers), the modal basis set is not.

From Fig. 5.15 it can be seen that the conventional CMT profile overshoots the exact FEM simulations for both the first and second supermode but remains quite accurate for the third mode. This is to be expected, since, as pointed out in section 1.3.2, the $m = 3$ mode in the case of $N = 5$ coupled waveguides has the special property that the effective index does not change with the cross-coupling coefficient. For the fourth and fifth mode, the conventional CMT profile undercuts the FEM solutions. In fact, at a waveguide separation of 80 nm, where the fifth mode is close to cutoff, conventional CMT does a very poor job of describing how this mode decays into the cladding region, compared with the improved method presented here.

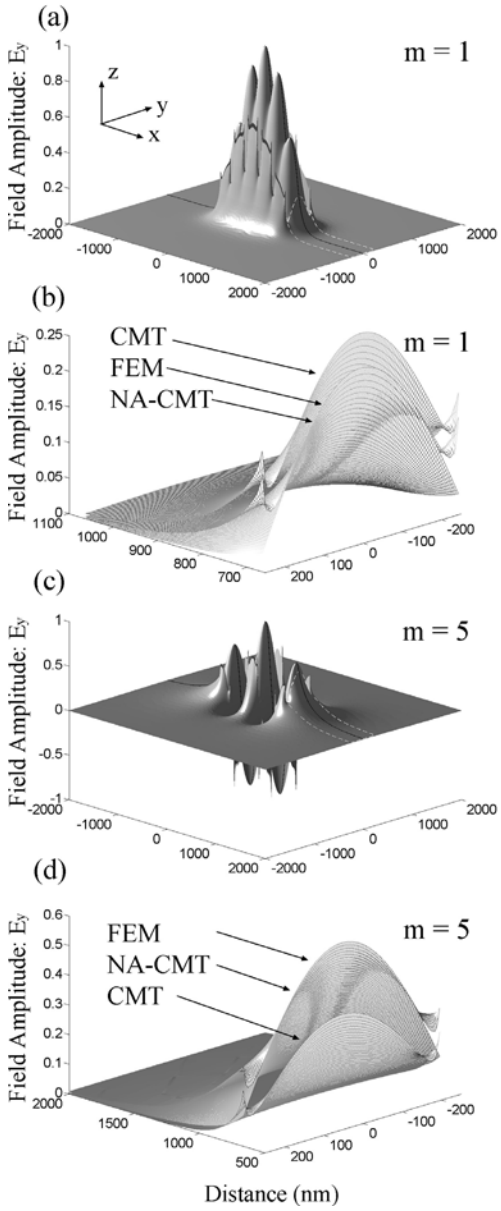

Figure 5.16: (a) FEM solution of the fundamental supermode of a silicon-on-insulator arrayed waveguide at a separation distance of 80 nm. The solid black line represents the field profiles shown in Fig. 6, whereas the region indicated by the white dashed lines represents the decaying region of the supermode. (b) The rate of decay of the fundamental supermode in the region indicated by the white dashed lines in (a), comparing the accuracy of CMT, NA-CMT with that of FEM. (c) FEM solution of the fifth supermode. (d) Calculated decay rate of the region indicated by the dashed lines in (c), showing the improved accuracy of NA-CMT compared with CMT.

5.4.2 Calculating the 2-D Field Profile

Coupling to nearby devices, whether desired or unintentional, is not solely dependent on the rate of decay at the center cross section of the device; rather, it is the entire 2-D profile that decays into the cladding region that will perturb a neighboring device. To calculate the 2-D mode profile, we determine the spatially dependent decay constant along the *height* of the waveguide near the waveguide's boundary. The method is identical to that described in the previous section, only it is now performed at different "slices" of the arrayed waveguide. By taking into account the evanescent tail fanout of the different supermodes, a non-linear least-squares fit to the form $\cos(h_y^{(m)}y)$ may be performed to generate the 2-D cross section. Fig. 5.16(a,c) shows the exact FEM solutions for the fundamental and fifth supermode respectively, where the solid black line located at the center region represents the field profiles shown in Fig. 5.15. The region included by the white dashed lines is the focus of the 2-D reconstruction. Shown in Fig. 5.16(b,d), the generated 2-D profile of the electric field decaying into the cladding region shows improved agreement with the FEM method. Similar to the last section, CMT overshoots the rate of decay for the fundamental supermode and undershoots for the fifth supermode, which is located a few nanometers from modal cut-off.

5.5 Summary

In this Chapter, the validity of coupled mode theory CMT for high-index contrast (e.g., silicon-based) optical waveguiding structures was analyzed. A fully vectorial finite-difference frequency-domain (FDFD) algorithm was used to obtain the modal profiles and effective indices of the supermodes in a non-perturbative way. When the modal profiles can be "discretized" to read off peak amplitudes within each of the waveguide cores, a theorem from matrix algebra can be employed to solve the "inverse problem"—to reconstruct accurately the matrix of coupling coefficients M (a procedure we have called numerically-assisted coupled-mode theory, NA-CMT). The NA-CMT framework can be used to find out when the nearest-neighbor-coupling approximation breaks down.

Of concern was also the physical phenomena that occur when waveguides become strongly coupled and fully confined in a high-index contrast medium. It was

shown that at large separation distances these perturbative effects can be ignored, while at short separation distances the effects of these perturbations may be taken into account through the choice of basis used in reconstructing the fields. Utilizing the evanescent tail fanout, which can be obtained from either measurement or simulations, we showed that one can generate a more accurate basis set. As the separation distance between waveguides is decreased, the decay constants of the fields fan out (Fig. 3) and depend upon the transverse coordinate x. Ignoring this "running" of the p and h constants leads to inaccurate prediction of the mode profiles in the strongly coupled regime and, in particular, of the evanescent tails, which determine cross talk, allowable bending radius, the coupling between rings and bus waveguides, etc. Finally, we show how a NA-CMT can be used to construct the 2-D waveguide profile that is responsible for coupling to nearby devices. We emphasize that the only required piece of information for reconstructing modes of strongly coupled, arrayed waveguides is the rate of their decay into the cladding, which is experimentally measurable using a variety of non-destructive techniques.

References

[1] F. Xia, L. Sekaric, and Y. Vlasov, "Ultracompact optical buffers on a silicon chip," *Nature Photonics*, vol. 1, pp. 65 –71, 2007.

[2] Q. Xu, D. Fattal, and R. G. Beausoleil, "Silicon microring resonators with 1.5-μm radius," *Optics Express*, vol. 16, pp. 4309 –4315, 2008.

[3] F. Xia, M. Rooks, L. Sekaric, and Y. Vlasov, "Ultra-compact high order ring resonator filters using submicron silicon photonic wires for on-chip optical interconnects," *Optics Express*, vol. 15, pp. 11934 –11941, 2007.

[4] A. Liu, R. Jones, L. Liao, D. Samara-Rubio, D. Rubin, O. Cohen, R. Nicolaescu, and M. Paniccia, "A high-speed silicon optical modulator based on a metal oxide-semiconductor capacitor," *Nature*, vol. 427, pp. 615 –618, 2004.

[5] Q. Xu, B. Schmidt, S. Pradhan, and M. Lipson, "Micrometer-scale silicon electro-optic modulator," *Nature*, vol. 435, pp. 325 –327, 2005.

[6] W. M. J. Green, M. J. Rooks, L. Sekaric, and Y. A. Vlasov, "Optical modulation using anti-crossing between paired amplitude and phase resonators," *Optics Express*, vol. 15, pp. 17264 –17272, 2007.

[7] X. Liu, I. Hsieh, X. Chen, M. Takekoshi, J. I. Dadap, N. C. Panoiu, R. M. Osgood, W. M. Green, F. Xia, and Y. A. Vlasov, "Design and fabrication of an ultra-compact silicon on insulator demultiplexer based on arrayed waveguide gratings," in *Lasers and Electro-Optics (CLEO) and Quantum Electronics and Laser Science Conference (QELS), 2010 Conference on*, p. CTuNN1, 2010.

[8] P. Cheben, J. H. Schmid, A. Delage, A. Densmore, S. Jannz, B. Lamontagne, J. Lapointe, E. Post, P. Waldron, and D. C. Xu, "A high-resolution silicon-on-insulator arrayed waveguide grating microspectrometer with sub-micrometer aperture waveguides," *Optics Express*, vol. 15, pp. 2299 –2306, 2007.

[9] K. Sasaki, F. Ohno, A. Motegi, and T. Baba, "Arrayed waveguide grating of 70x60 μm^2 size based on si photonic wire waveguides," *Electron. Lett.*, vol. 41, pp. 801 –802, 2007.

[10] P. Dumon, W. Bogaerts, D. V. Thourhout, D. Taillaert, and R. Baets, "Compact wavelength router based on a silicon-on-insulator arrayed waveguide grating pigtailed to a fiber array," *Optics Express*, vol. 14, pp. 664–669, 2006.

[11] H. Kogelnik and C. V. Shank, "Coupled-mode theory of distributed feedback lasers," *Appl. Phys.*, vol. 43, p. 2327 Ű2335, 1972.

[12] A. Hardy and W. Streifer, "Coupled-mode theory of parallel waveguides," *J. Lightwave Technol.*, vol. LT-3, pp. 1135 –1146, 1985.

[13] W. P. Huang, "Coupled-mode theory for optical waveguides: An overview," *J. Opt. Soc. Am. A*, vol. 11, pp. 963 –983, 1994.

[14] K. S. Chiang, "Coupled-zigzag-wave theory for guided waves in slab waveguide arrays," *J. Lightwave Technol.*, vol. 10, pp. 1380 –1387, 1992.

[15] F. P. Payne, "An analytical model for the coupling between the array waveguides in awgs and star couplers," *Opt. Quantum Electron.*, vol. 38, pp. 237 –248, 2006.

[16] E. Kapon, J. Katz, and A. Yariv, "Supermode analysis of phase-locked arrays of semiconductor lasers," *Optics Letters*, vol. 10, pp. 125 –127, 1984.

[17] A. Klekamp and R. Munzner, "Calculation of imaging errors of awg," *J. Lightwave Technol.*, vol. 21, pp. 1978 –1986, 2003.

[18] P. Yeh, *Optical Waves in Layered Media*. New York: John Wiley & Sons, Inc., 2005.

[19] S. H. Yang, M. L. Cooper, P. R. Bandaru, and S. Mookherjea, "Giant birefringence in multi-slotted silicon nanophotonic waveguides," *Optics Express*, vol. 16, pp. 8306 –8316, 2008.

[20] S. Mookherjea, "Spectral characteristics of coupled resonators," *J. Opt. Soc. Am. B*, vol. 23, pp. 1137 –1145, 2006.

[21] M. Kuznetsov, "Expressions for the coupling coefficient of a rectangular waveguide directional coupler," *Optics Letters*, vol. 8, pp. 499 –501, 1983.

[22] M. Popovica, C. Manolatou, and M. Watts, "Coupling-induced resonance frequency shifts in coupled dielectric multi-cavity filters," *Optics Express*, vol. 14, pp. 1208 –1222, 2006.

[23] G. Lenz and J. Salzman, "Eigenmodes of multiwaveguide structures," *J. Lightwave Technol.*, vol. 8, pp. 1803 –1809, 1990.

[24] C. L. Xu, W. P. Huang, M. Stern, and S. K. Chaudhuri, "Full-vectorial mode calculations by finite difference method," *IEE Proc.-Optoelectron.*, vol. 141, pp. 281 –286, 1994.

[25] M. L. Cooper and S. Mookherjea, "Numerically-assisted coupled-mode theory for silicon waveguide couplers and arrayed waveguides," *Optics Express*, vol. 17, pp. 1583 –1599, 2009.

[26] G. P. Agrawal, *Nonlinear Fiber Optics*. New York: Academic Press, 2001.

[27] C. Minot, N. Belabas, J. A. Levenson, and J. M. Moison, "Analytical first-order extension of coupled-mode theory for waveguide arrays," *Optics Express*, vol. 18, p. 7158, 2010.

[28] K. C. Patra, S. Srivastava, and E. K. Sharma, "Power exchange in strongly coupled diffused channel waveguide arrays: an analytical approach," *Journal of Optics*, vol. 12, p. 085501, 2010.

[29] A. Yariv, "Coupled-mode theory for guided-wave optics," *Journal of Quantum Elec.*, vol. 9, pp. 919 –933, 1973.

1. Chapter 5 contains material published in:

   Michael L. Cooper and Shayan Mookherjea, “Numerically-assisted coupled-mode theory for silicon waveguide couplers and arrayed waveguides,” 17, pp. 1583-1599 (2009).

   The dissertation author was the primary author of this paper.

2. Chapter 5, in part, has been submitted for publication Journal of Lightwave Technology, 2010, M. L. Cooper and Shayan Mookherjea.

   The dissertation author was the primary author of this paper.

6 Characterization of Nanophotonic Devices

Measure what is measurable, and make measurable what is not so.
—Galileo Galilei

The previous two chapters laid out computational and analytical methods for predicting the characteristics of nanophotonic devices. In Chapter 3, methods of simulating the local enhancement of each resonator in a hundred-plus ring disordered CROW was detailed. Here, we will demonstrate a technique that allows them to be measured directly. Further, we will show how this technique may be used to characterize micro-ring resonators, and simultaneously measure 10 waveguide facets allowing for rapid diagnostics. In the second part of this chapter, different methods of measuring group delay will be outlined. Specifically, it will be shown how swept-wavelength interferometry allows for rapid delay characterization of an amplified device—without the need of an optical filter.

6.1 Quantitative Infrared Imaging

Silicon-on-insulator (SOI) integrated photonic circuits with one or several microring resonators are an active area of research. In multi-resonator circuits, such as shown in Fig. 6.1, the individual resonators often have no accessible ports, requiring such structures to be treated as a "blackbox," where the behavior of the individual resonators are probed through transmission measurements. For post-fabrication trimming methods this is far from ideal. For example, a common multi-ring device is the side cou-

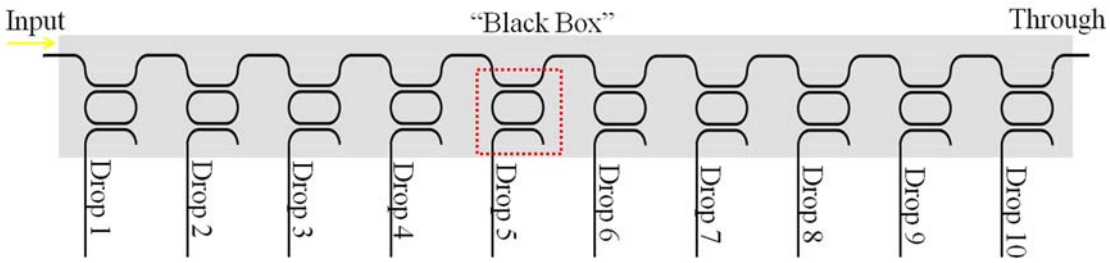

Figure 6.1: Typically resonator structures, such as this side coupled integrated spaced sequence of resonators, are probed by measuring each of the ports separately, where the structure itself is treated as a "black box," where it is unknown if measured resonance variations are due to a defective resonator, output coupler, etc.

pled integrated spaced sequence of resonators (SCISSOR) used as a delay line, which is composed of a linear array of identical resonators coupled together through one bus waveguide. Structural imperfections during fabrication can result in a variation of the microring resonant frequencies and coupling coefficients across the device. If a single resonator was off resonance, one could tell by noting an additional dip the transmission spectra measured at the *through* port using a lens-tipped fiber, however, they would be unable to decipher the specific resonator that was defective. It would be beneficial to know precisely which resonator caused this dip, so that it could then be tuned or trimmed through various methods. Wavelength resolved infrared imaging provides such information.

Rayleigh scattering due to sidewall roughness is a source of radiative loss in high-index contrast SOI waveguides at telecommunications wavelengths. Some of this light can be collected by imaging the device plane onto a high-sensitivity infrared camera through a microscope objective. This can be used to provide a local measure of the guided light-intensity, as the scattered light is directly proportional to the light-intensity guided in a waveguide or circulating within a resonator. Thus, using an infrared camera to image the photonic circuit at multiple wavelengths and processing the resulting images can yield spectral intensity-enhancement and transmittance data.

The ring resonator is ideal for measuring with an infrared camera. The reason being, that silicon has incredibly low material losses at telecommunication wavelengths, as such, a low intrinsic quality resonator is most often the result of high scattering losses.

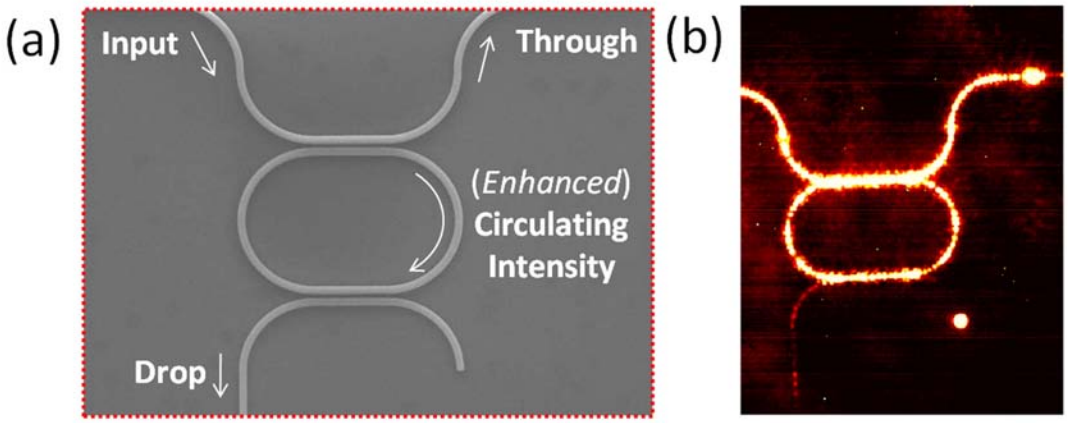

Figure 6.2: (a) A typical ring resonator: light within the resonator will become enhanced for wavelengths on resonance. (b) Infrared image of the resonator when excited by a resonant wavelength.

On the other hand, a high quality resonator will benefit from a significant enhancement of power circulating through the ring, which will again result in high (net) scattering. In other words, both "good" and "bad" rings scatter a significant amount of light. With a suitable integration time, an infrared camera can accurately measure the properties of these rings. Fig. 6.2(a) shows a typical micro-resonator that will be measured here, and Fig. 6.2(b) shows an IR image of the resonator when excited by a resonant wavelength. Light is clearly circulating within the resonator for this wavelength (the bright spot on the bottom right corner of the image is caused by light coupling to the counter propagating mode due to the periodic surface roughness seen by the propagating photons).

Fig. 6.3(a) shows a 2-D simulation (FDTD [1]) of the intensity enhancement of a single resonator. When light at one of the ring's resonant wavelengths is coupled into the resonator, energy builds up until the losses (from the couplers, absorption, or scattering) match the the power being supplied by the bus waveguide. However, to first order, light that is not within the Lorentzian response of the ring will simply bypass it. Shown in Fig. 6.3(b) are infrared images of the SCISSOR structure at three different wavelengths. Incidentally, we note that these resonators were originally designed to be the same size, but ended up having different resonant frequencies due to fabrication irregularities. Infrared imaging is thus able to tell you exactly which resonator is red-shifted of blue-shifted from the target value so that it may then be tuned. Contrary, a

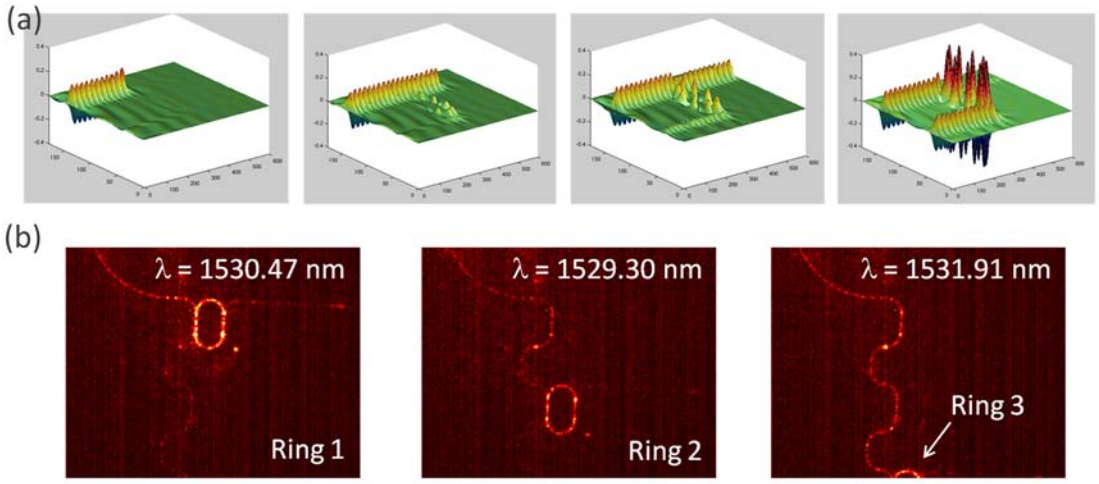

Figure 6.3: (a) Finite difference time domain simulations at four different time steps, showing the enhancement of energy in the ring for resonant wavelengths. (b) Infrared image of a circuit, excited with the resonant wavelength of three ring resonators.

simple transmission measurements at the through port—all that would be available if this device was operated as an optical buffer—would tell you that some of the rings were defective, but would not isolate which one.

6.1.1 Calibration of the Imaging Setup

Before the spectral variations of a multi-resonator circuit can be measured, the imaging setup must be properly calibrated. Perhaps the most important control nob is camera integration time (or equivalently, input optical power). If too high of an integration time is used, the images will become saturated and spectral features will be lost. For too low of an integration time, low-signal features will not be measured. Proper integration time was typically determined through a series of measurements, where the images where intentionally saturated at first, and then the integration time ramped down to the ideal level.

Once integration time has been chosen, one may determine the precise amount of power hitting the camera. To do this, laser light from a free space collimator is directly coupled onto the infrared camera (with the desired settings), as the laser power is tuned; Fig. 6.4 shows results of six different power levels. As the output power of the laser is precisely known, dividing each pixel by the sum of all pixels gives the percentage of

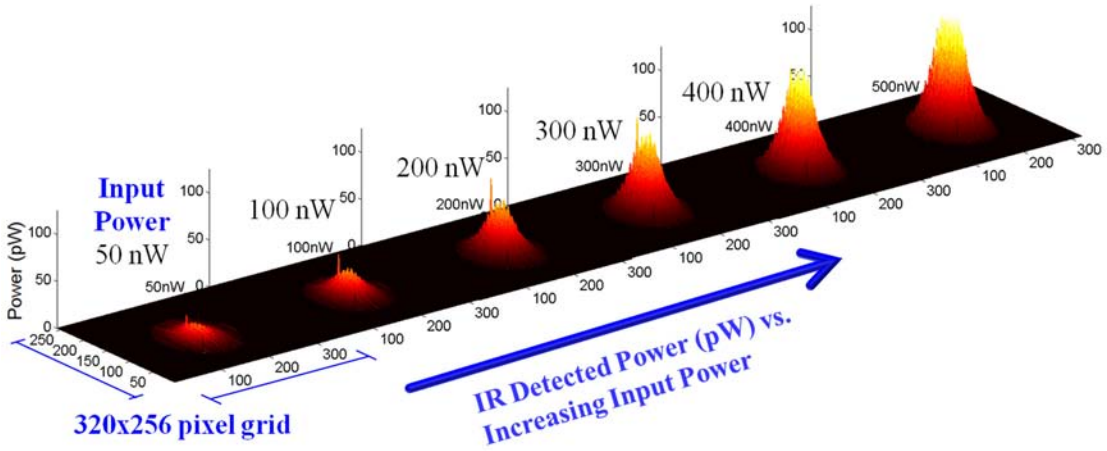

Figure 6.4: Using the camera settings reported here, light was collimated onto the infrared camera for different (known) power levels. Dividing each pixel by the sum of all pixels gives the percentage of power falling onto each pixel.

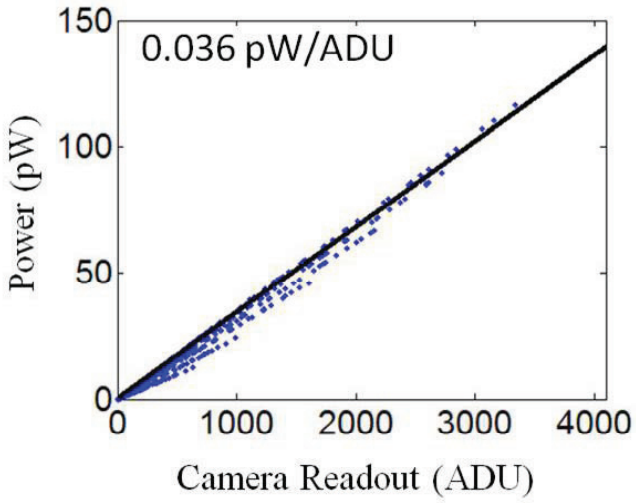

Figure 6.5: Correlation between camera ADU to the power hitting each pixel

power falling onto each pixel. By then multiplying by the total power delivered by the laser, one obtains the power that fell onto that pixel. As shown in Fig. 6.5, by correlating camera ADU to the power levels hitting the pixel, one can determine exactly how much light is being integrated by the camera for a given readout value. Once the camera has been properly calibrated, the photonic circuit may then be measured.

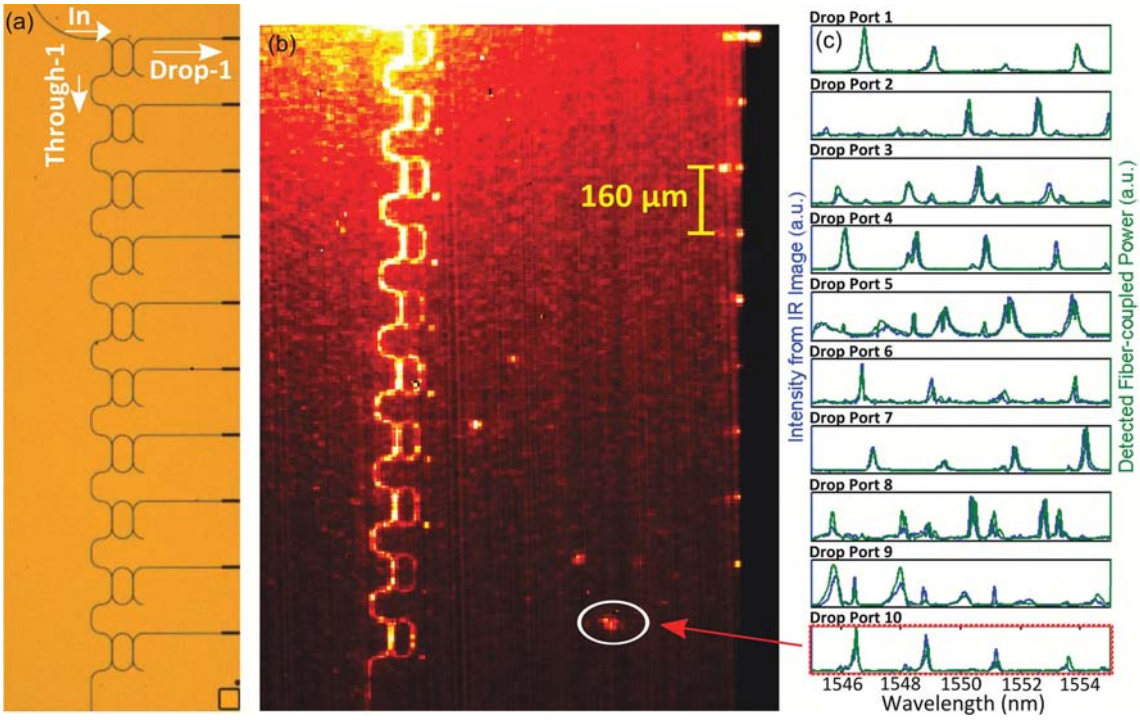

Figure 6.6: (a) Optical microscope image of 10-ring SCISSOR. (b) IR image of SCISSOR when excited by broadband source. (c) Using a tunable laser source, comparison of spectra obtained at the ten drop ports using IR images (blue line) and spectra obtained from detected drop port power using fiber-coupling (green line). The spectrum for Ring 10 was obtained by measuring at the encircled waveguide defect.

6.1.2 Multi-ring Structures

The particular multi-ring structure fabricated, tested and reported on here was the (SCISSOR), comprised of 10 racetrack resonators as shown in Fig. 6.1. Such devices may be used for slow-light [2], or as a linear, or nonlinear self-limiting, add-drop filter [3, 4]. In recent years, IR imaging using vertically scattered light has been used for loss characterization of planar and SOI photonic crystal waveguides [5, 6], and for the study of localization, polarization conversion and dispersion in disordered waveguides [7, 8, 9]. Here we use IR imaging to simultaneously characterize several SOI microring resonators.

The device was fabricated on an SOI wafer with 250 nm silicon thickness and 3 μm buried oxide thickness, using electron-beam lithography and dry-etching. The ring and bus waveguides have a top layer of 200 nm-thick hydrogen silsequioxane (HSQ),

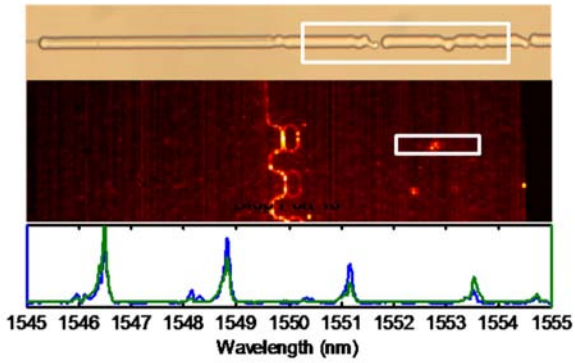

Figure 6.7: *Top*: Fabrication error that resulted in only a few nanowatts being measured using a lens-tipped fiber at the end-facet. *Middle*: The fabrication error "lights up" when light is coupled into the device and then imaged using an infrared camera. *Bottom*: Comparison of the spectral characteristics probed with the infrared camera, with the nano-Watt power levels that were measured using the lens-tipped fiber.

while air forms the side cladding. Using photolithography, 3x2 μm^2 SU-8 couplers are patterned over 150 μm-long silicon waveguide inverse tapers. The ring radius is 25 μm, and the straight track length is 40 μm.

Two light sources are used separately: a white-light source is used for broad-spectrum incoherent imaging of the chip, mainly for alignment purposes and determining averaging paths, as discussed later. Alternatively, TE-polarized coherent light from a tunable laser source is then coupled to the chip through polarization maintaining lens-tipped fiber, with 20-dB polarization extinction measured after the tip. A XEVA-FPA-1.7-320 12-bit IR camera (XenICs NV, Belgium, 320x256 pixel grid with a 30 μm-pitch) is used to spatially image the chip through a 5x microscope objective lens. The maximum and minimum detectable powers per pixel (area = 36 μm^2), for a camera integration time of 4ms, are 0.16 nW and 0.04 pW respectively. Fig. 6.6(b) shows a one-shot IR image of the entire SCISSOR device, when excited by a broadband source centered at a wavelength of 1570 nm. This image shows that for rings 1 through 9 (starting at the top of the image), the end points of the drop waveguides, along the cleaved facet of the chip, scatter sufficient light. With this technique, the desired spectral content could also be tapped anywhere on the chip using grating couplers[10]. For the 10^{th} ring, there was a fabrication defect that prevented the drop port from being measured accurately, and instead, the encircled defect, at a point along the waveguide was used.

Fig. 6.7 shows the fabrication defect that caused light to be radiated before making it to the end facet—where only nanowatts could be measured using the lens-tipped fiber. In the close vicinity of these measurement sites (both on the chip and at the end facet), a spatial average of 4x4 pixel intensities is computed from an array of IR images obtained at each wavelength, during a 10 pm step scan of the tunable laser source. Fig. 6.6(c) shows a comparison of the drop port transmission spectra obtained from imaging with the traditional method of measuring via a lensed fiber, translated (and re-aligned) sequentially from the first to the tenth drop port. Note that only a single alignment step (of the input) is necessary for the imaging approach, compared to eleven alignments (and ten tunable laser scans) for the lensed fiber approach. We observe very good agreement of data obtained from both methods.

By way of comparison, to get a sense of the spatial alignment required using the traditional lens-tipped fiber method, programmable piezo controllers were then used to map out the the wavelength-response of the first resonator, as the lens-tipped fiber was vertically translated at the drop port facet. Similar to the imaging setup, the piezo controllers move the lens-tipped fiber a few hundred nanometers, where a wavelength scan is performed, and then the process repeated. It can be seen in Fig.6.8(a), that such a mechanical method of automating the measurement of the drop ports would need micro-scale precision. To further map out the spatial profile of the radiated mode, the laser was then fixed at a given frequency, while both x and y axis were translated using piezo-controllers, as shown in Fig.6.8(b).

6.1.3 Resonant Frequency Locations Measured on Chip

IR imaging allows non-invasive measurement of the through port transmittance of each ring within a multi-ring cascade, as would be necessary to determine the waveguide cross-coupling coefficient κ, and the round-trip (amplitude) loss factor a [11, 12]. Compared to slower serial-scan probing methods such as near-field scanning optical microscopy [13], and optical fiber-based probes [14], IR imaging can measure several resonators simultaneously. The main disadvantage is the diffraction limited resolution.

Another set of images is obtained by scanning the tunable laser source wavelength and recording the IR images of Rings 1 and 2 at a higher magnification (20x).

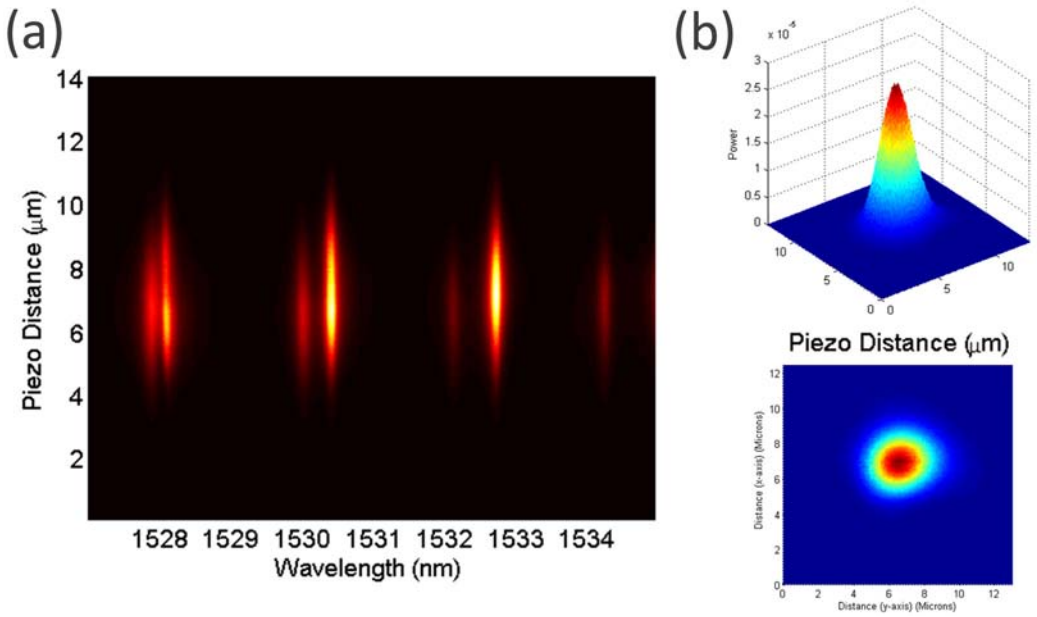

Figure 6.8: (a) Spatial dependence on the transmission spectrum of a resonator on the coupling alignment using a lens tipped fiber and a programmable piezo controller. The piezo controller was translated a few hundred nanometers, where a wavelength scan was then performed, and the process repeated. (b) Modal size of the radiated mode. Measured by fixing the laser at a single frequency, and taking power measurements while two piezo controllers were scanned in the plane perpendicular to the waveguide.

Fig. 6.10(a) shows a typical IR imaging profile at a wavelength of 1533.90 nm. The waveguide profile is obtained by using an ASE source to illuminate all 10 rings. This profile is then converted to a binary matrix, an example of which is shown in Fig. 6.9 for a single ring, which is used to extract the desired paths which correspond to the input port, the through port and the ring resonator. The pixel intensities are then averaged over these selected path lengths and normalized by the input to yield the spectra shown in Figs. 6.10(b) and 6.10(c). In order to compare between different areas, the averaging regions should contain the same number of bends, junctions or defects; otherwise, seemingly anomalous behavior can be observed for the magnitude of through port transmittance for Ring 1 (magnitude of the path-averaged output $>$ path averaged input). We emphasize that it is the ratios of the 'on' and 'off' resonance transmission values that are used to characterize the microrings [11, 12].

The free spectral range FSR, resonator bandwidth BW, and normalized through port transmittance T_{min} are obtained from the through port transmission spectrum. For

Figure 6.9: Binary Matrix used to mask and average over each of the rings separately.

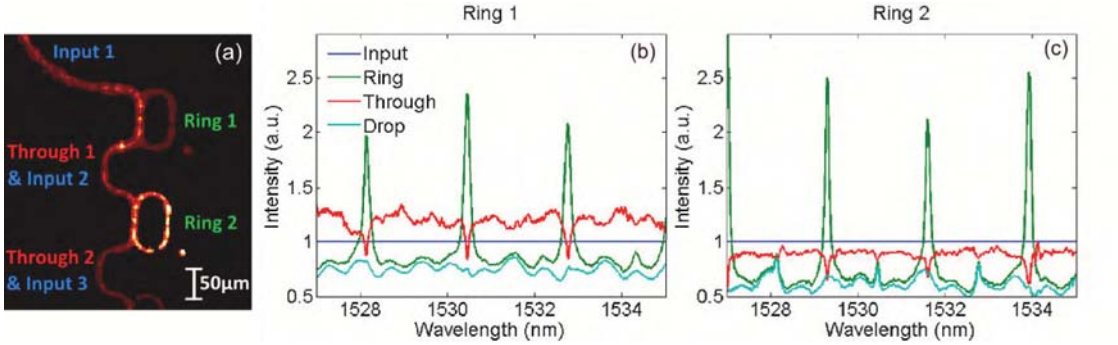

Figure 6.10: (a) IR image of Rings 1 and 2, at an input wavelength of 1533.90 nm, used towards obtaining spectra for through port, drop port and circulating ('Ring') powers, normalized by the input, for (a) Ring 1 and (b) Ring 2.

a Ring 1 resonance at λ_{res}=1530.45 nm, FSR=2.31 nm (296 GHz), BW=0.12 nm (15 GHz), and T_{min}=0.65. Using the expressions in Ref. 10, the relevant ring parameters are extracted and summarized in Table 1. α_{RT} is the loss (in dB) per round trip in the ring. I_{calc} is the intensity enhancement factor of the ring, calculated as the number of round-trips N of a circulating photon, which is the ratio of the photon lifetime τ_{ph} and the time taken to complete one round-trip of the ring, T_{RT}.

$$N = \frac{\tau_{ph}}{T_{RT}} = \frac{Q/\omega_0}{1/FSR_{freq}} = \frac{FSR_{freq}}{BW}\frac{1}{2\pi} = \frac{F}{2\pi}, \tag{6.1}$$

where ω_0 is the radial resonance frequency, and F is the finesse of the resonator. In Table 1, $I_{calc} = N$ is compared against I_{meas}, which is the peak circulating intensity at a resonant wavelength, read off from Figs. 6.10(b) and 6.10(c).

Scanning electron microscope (SEM) images convey a waveguide width of 540

Table 6.1: Extracted Resonator Parameters

	Ring 1		Ring 2	
λ_{res} (nm)	1530.45	1532.77	1529.30	1531.60
κ^2	0.032	0.035	0.022	0.020
a	0.859	0.832	0.878	0.861
α_{RT} (dB)	1.32	1.60	1.13	1.30
I_{calc}	3.06	2.64	3.66	3.34
I_{meas}	2.36	2.08	2.50	2.11

nm and a resonator-waveguide gap of 310 nm. Using an effective coupler length [15] of 51 μm, we estimate κ^2 to be 0.036, which is close to the values extracted from the imaging data. The high loss is consistent with the $\geq$ 10 nm sidewall roughness [16] observed using the SEM. The corresponding intrinsic quality factor is 15,900, while the loaded Q is 12,750. For high-Q resonators, the enhancement factor will compensate for low intrinsic scattering losses. For our ring structure, the enhancement factor will compensate for an intrinsic scattering loss as low as 0.001 dB/cm, which corresponds to an intrinsic Q-factor of 7.6×10^8.

In summary, infrared imaging has been applied for characterization of individual rings in a multi-ring structure, towards understanding the overall device performance, and desired post-fabrication tuning. This technique is readily scalable to measure multiple devices using larger fields of view and cameras with an increased number of pixels.

6.1.4 Waveguide Bends

As mentioned in Section 1.2, waveguide bends can also be a source of radiative loss in a photonic circuit. The reason being, that a mode shifts away from its radial center when going around a bend. This causes a mode mismatch between the straight and bent waveguide regions, and also increases the electric field at the waveguide boundary, both of which result in higher scatting losses [17, 18]. As was shown in the previous sections, infrared imaging can be used to spot fabrication defects, or “holes” in a photonic circuit. Similarly, it can also give a measure of where a device loses energy so that it can then be properly redesigned or trimmed. Fig. 6.11 shows a 4.15 cm long straight waveguide that folds upon itself seven times. One can see that the waveguide bends indeed scatter

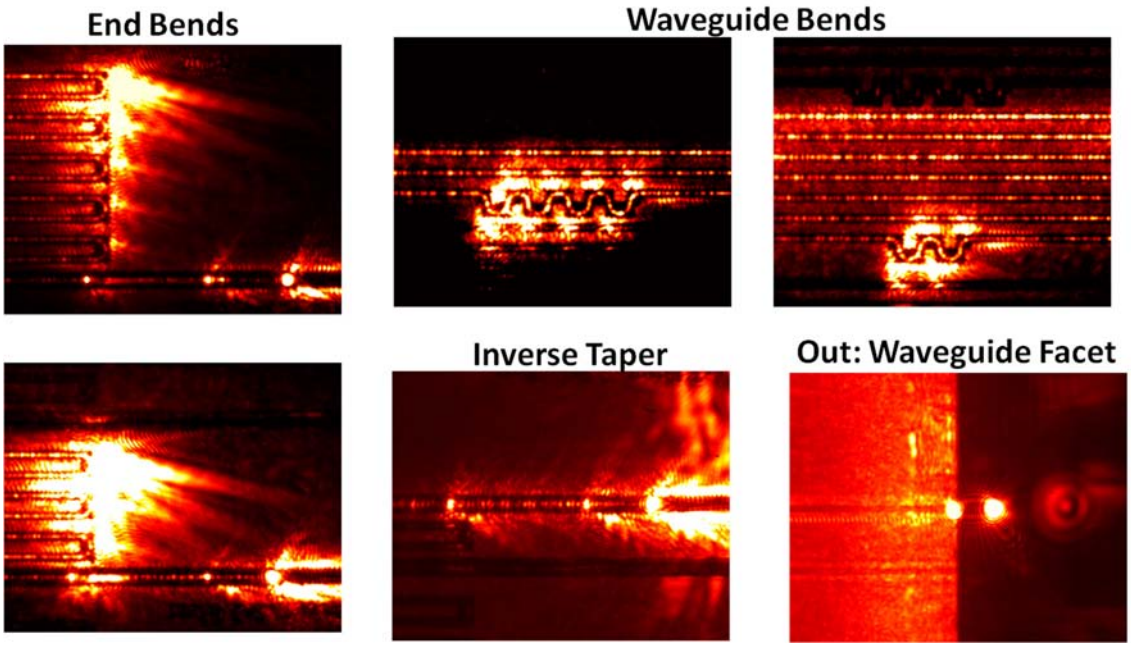

Figure 6.11: Infrared image of a 4.15 cm long straight waveguide that folds upon itself seven times. As discussed in the text, the waveguide bends scatter a significant amount of light compared with the straight sections. Also, the inverse taper coupler shows significant scattering at the silicon/SU8 transition regions. The bottom right corner shows light being scattered off of the output coupler due to reflections and mode-missmatch.

a significant amount of light compared with the straight sections. Further, one can see that the inverse taper couplers also scatter a significant amount of light. Most notably, light is scattered within the SU8 coupler where the silicon waveguide begins, and also when the SU8 coupler is terminated. In the bottom right figure is an image of light being coupled to the output fiber, where again one can see high scattering losses due to reflections and modal-mismatch. This is another benefit to using an infrared camera to probe "leaks" in photonic circuits, analogous to submerging a pumped bicycle tire into a bucket of water to spot air-holes.

6.1.5 Imaging CROWs

Infrared imaging provides a method of determining the wavelength response of individual rings. There is perhaps no device where this would be more beneficial then the coupled resonator optical waveguide—where by definition—the individual rings

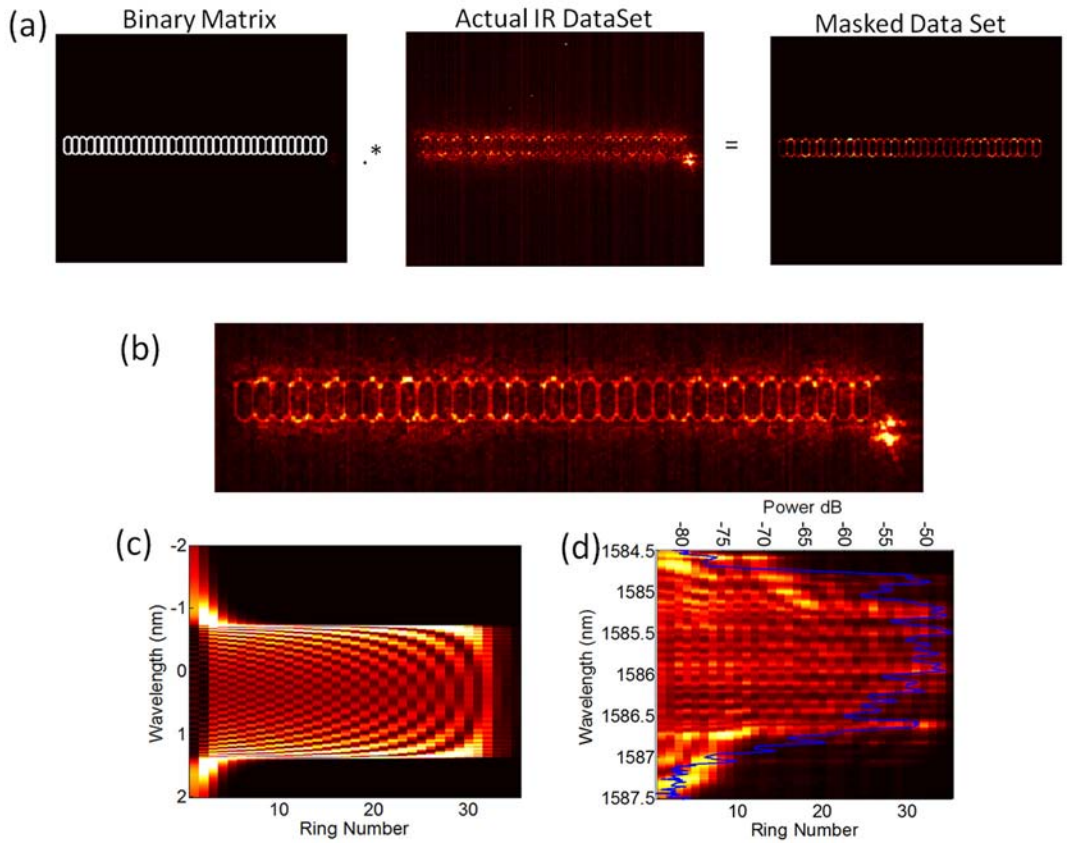

Figure 6.12: (a) Method of extracting the spectral characteristics of a 35-ring CROW. 35 single-ring binary matrices (shown is their summation), are superimposed onto the wavelength resolved infrared imaging dataset. (b) Enlarged image of a semi-transparent mask superimposed onto the 35-ring CROW. (c) Simulation of how the field profiles of a disorder-free CROW would look. (d) Wavelength resolved IR image of a 35-ring CROW: each of the masks were averages over their corresponding ring at each wavelength to produce the image shown.

have no accessible ports, leaving one with little information from a transmission spectrum on how an individual ring behaves. The characteristics of CROWs were discussed in detail in Section 2.1. Here, we extend the imaging technique described in the previous section to that of a CROW. Fig. 6.12(a) outlines the method of extracting the spectral response of the individual coupled-microrings. The data acquisition technique for the CROW is identical to that of the SCISSOR: a tunable laser source is synchronized with an infrared camera to obtain wavelength resolved imaging. Fig. 6.12(a) shows the binary mask used for the CROW. This mask consists of 35 rings (used to measure a 35

ring CROW), that is actually the summation of 35 individual *single ring* masks such as shown in Fig. 6.9. This mask is then superimposed onto the dataset. For each ring, camera pixels that align with the binary mask's "1's" are averaged. Computationally, the way this is done is that the mask and the dataset are dot-multiplied, and then all non-zero elements averaged. Fig. 6.12(b) shows an enlarged image of a semi-transparent mask superimposed on a 35-ring CROW. A method for simulating the response of the individual rings of a CROW was detailed in Chapter 4. In Fig. 6.12(c) we recall a typical image of how the field profiles of a disorder-free CROW should look from simulation. In Fig. 6.12(d) the measured (averaged) response of the individual microrings of a 35-ring CROW is shown. Also shown (blue line), is the transmission spectrum for the corresponding band. One can indeed see that there is a direct correlation between where the resonators "light-up" and the power measured at the CROW's drop port. Also, increased intensity can be observed at the band-edge, which will be discussed more later, similar to that of the simulation.

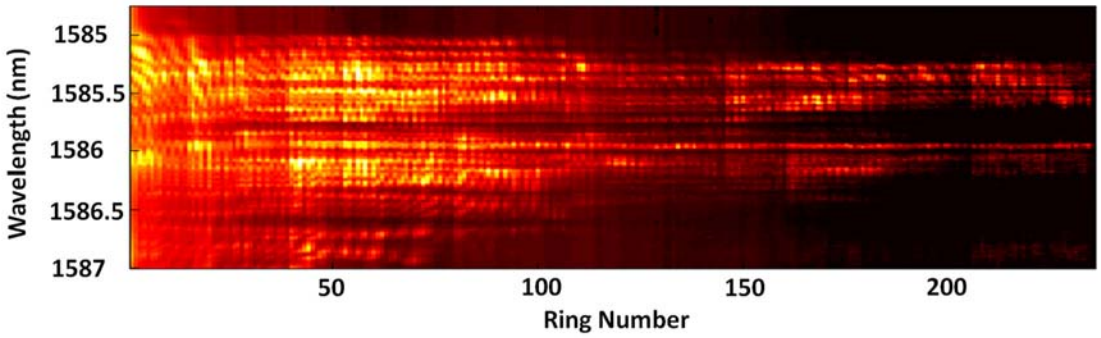

Figure 6.13: Wavelength resolved infrared image of a 235-ring CROW.

Wavelength dependent eigenvectors of a disordered 235-ring CROW

The imaging process was then performed for the 235-ring CROW as shown in Fig. 6.13. As the infrared camera is only 320 pixels, it is not feasible to take the images in a single shot as was done for the 35-ring CROW. For the 235-Ring CROW, 16 datasets were taken where each ring in a given dataset was then averaged using a binary mask 15-rings wide. The results of which were then stitched together to form the 235-ring CROW spectral response shown in Fig. 6.13. From these images, one can simply extract

the desired ring's transmission response from the dataset. Shown in Fig. 6.14 are cross sections of a single dataset measured near the start of the CROW. Comparing the 4th and 14th ring in this dataset, one can see that the individual rings in a CROW undergo very different spectral responses.

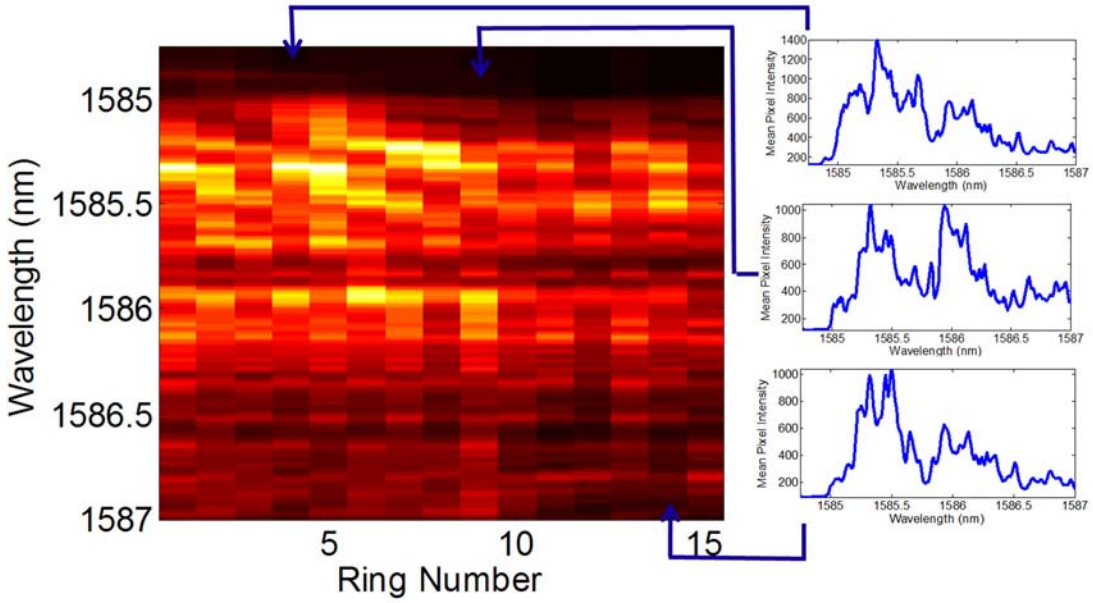

Figure 6.14: Typical dataset, measured near the beginning of the CROW shown in Fig. 6.13. As shown, one may extract the response of the individual microrings of a CROW using infrared imaging. Comparing the 4th and 14th ring in this dataset, one can that the individual rings in a CROW undergo very different spectral responses.

Band edge enhancement

The CROWs imaged thus far were done so under a semi-transparent polymer (PMMA), used to reduce the losses of the CROW. The effects of this polymer on the infrared images is to blur the responses of the individual microrings. In order to analyze band-edge phenomena the PMMA cladding was then removed by soaking the chip in acetone, with the intent of specifically looking at interesting high spectral resolution band-edge characteristics. Shown in Fig.6.15(a) is the spectral response of a 35-ring CROW on chip W2F9 (see Fig.2.2). Fig.6.15(b) shows the band-edge transmission spectrum outlined by the green box in Fig.6.15(a). One can see that while losses have

increased due to the air cladding, well defined peaks can still be observed at the band-edge.

The wavelength resolved infrared image data was taken only at the band-edge, shown in Fig. 6.15(c), where a 1-pm step scan was used to obtain ultra-fine band-edge resolution. Indeed, the air cladding allows the imaged responses of the individual micro-rings to be considerably well defined. Outlined by a green box in Fig. 6.15(b) is an enhanced localized mode of the 35-ring CROW where the light intensity is three times higher in the central region of the CROW compared with rings on either side. Note that the CROW has a high insertion loss of 86 dB at this wavelength. Fig. 6.15(d) shows the IR camera measured intensity of the CROW at each resonator for a wavelength within the region indicated by the green box in Fig. 6.15(c). In the top portion of this image, the raw image of the 35-ring crow is shown (no mask is being applied). IR imaging is thus capable of probing the entire disordered response of a CROW, where as a transmission spectrum would provide no information on the response of the individual micro-rings.

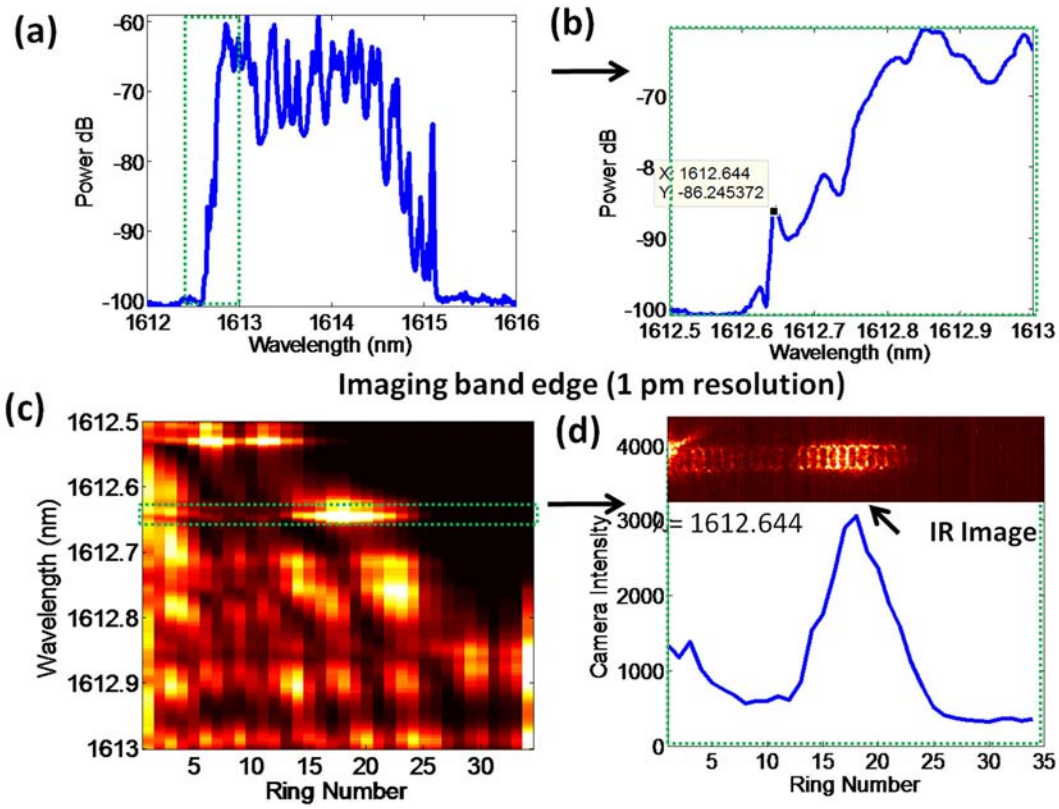

Figure 6.15: (a) Transmission spectra a 35-ring CROW on chip W2F9. (b) Band-edge transmission response of the CROW as outlined by the green-box in (a). (c) Wavelength resolved infrared image at the band-edge using an ultra-fine 1 pm step-size. (d) Response of the CROWs for the localized mode outlined by the green box in (c). Shown in the top is the actual IR image of the CROW at this wavelength.

6.2 Group Delay Measurements

The previous section outlined a novel technique for measuring the spectral dependence of the intensity enhancement of a micro-ring resonator. This section focuses on measurements of group-delay. Physiologically, these are the same thing. The enhancement of a micro-ring resonator is due to photons tunneling into the micro-ring where they are then "trapped," for a time determined by the coupling coefficient and the losses of the cavity (i.e., chance to escape). While these photons are trapped in the ring, additional photons are continuously being pumped into the cavity by the laser source, which is the cause of the enhancement. Group delay on the other hand is the measure of propagation time for a device. For micro-resonators, propagation time is increased due

to photons taking several passes around the microring before coupling out—which is again, the cause of the cavity enhancement. There are numerous methods of measuring group delay, with perhaps the most popular being the phase shift method using an vector network analyzer. Here, we look at another technique, swept-wavelength interferometry, and specifically the role of amplification.

6.2.1 Introduction

Measurements of wavelength-dependent group delay are important in optical filters, delay lines and interferometers, with applications in RF photonics, slow light and optical communications [19, 20, 21]. While the rationale for using erbium-doped fiber amplifiers (EDFA) in the operation and testing of fiber systems and networks is evident [22], and although much of the same intuition applies to testing photonic devices, there are significant differences between the two cases. Adding an EDFA with 50 meters of optical fiber and additional noise contributions to a device-under-test path previously consisting of a chip that may be only a few millimeters long requires special considerations, when the goal is that of measuring group delay with sub-picosecond accuracy [23, 24, 25].

Considerable cost, effort and time can be taken up by the packaging of bare-die photonic chips into fiber-pigtailed devices. Additional complexity of lithography is associated with fabricating mode-size converters in order to achieve a low-loss interface between fibers and single-mode silicon-on-insulator (SOI) waveguides [26, 27, 28, 29, 30]. Whereas researchers are reluctant to devote excessive time towards perfecting couplers at the preliminary stages of designing a novel chip, they would nevertheless like to accurately know the group delay and dispersion characteristics of the device under test, which is the main focus of the research. Thus, during testing, coupling efficiencies of -5 to -10 dB at each of the input and output interfaces may be anticipated, as often reported in the literature.

Furthermore, an intrinsic propagation loss of -5 to -10 dB should also be expected, since nanometer-scale sidewall roughness of SOI waveguides can lead to a significant propagation loss [31, 32]. For example, an SOI waveguide which provides 0.5 ns of delay is about 4 cm long. After a post-lithographic surface roughness reduction

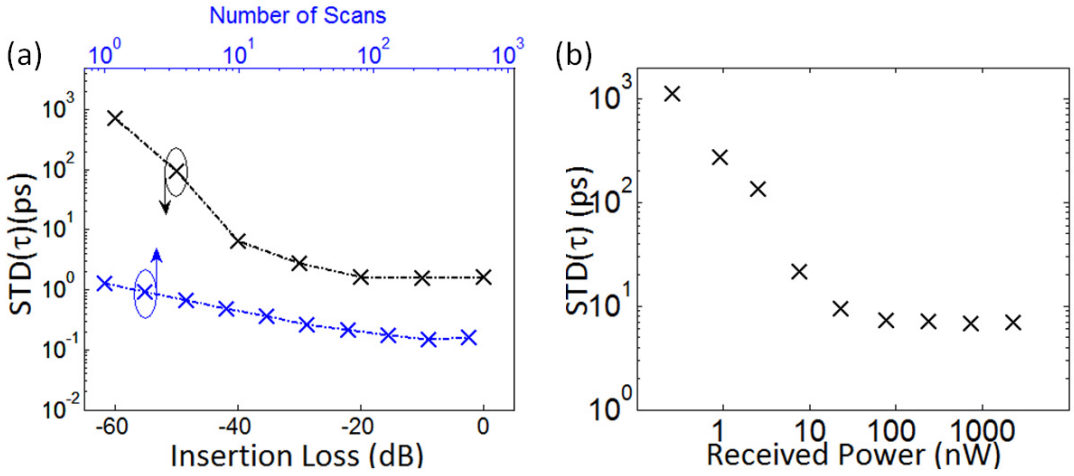

Figure 6.16: (a) Top Axis: Measurement of the group delay ripple (ps) of a 1.2 m long fiber patchcord, over a 40 nm wavelength span in the L-band, for increasing number of averaged scans. Bottom axis: Group delay ripple (ps) a device-under-test consisting of 76 m of single-mode fiber and Erbium doped fiber, and a programmable attenuator (JDS Uniphase HA9), whose setting was increased sequentially to simulate the effect of decreased coupling efficiency. (b) Measurement of the group delay ripple (ps) of a 4.15 cm single-mode silicon-on-insulator waveguide over a 40 nm wavelength span in the L-band.

process, it may have a (low) absorption coefficient of -1.25 dB/cm, thus yielding an insertion loss of -5 dB. In fact, single-mode SOI waveguide losses of -2.5 dB/cm (for a total insertion loss of -10 dB) are still considered low-loss by today's standards.

Since the goal of many novel devices is to realize filters, switches or modulators with $>$ 30 dB dynamic range, an accurate measurement of GD is needed not just at the peaks of the transmissions spectrum but also at the valleys, i.e., at a detected power level, relative to the source, of -45 to -60 dB. Typically, the input power level to an SOI waveguide cannot exceed +10 dBm before nonlinear effects are observed. Therefore, SOI chip-scale devices usually need accurate measurements of group delay (GD) over a wide range of detector power levels, from -5 dBm to -50 dBm. At the power levels considered here, $<$ -10 dBm, the dominant receiver noise contribution comes from the electronic amplifier noise[33, Fig. 5.27]. However, as we will see later, the situation may change for amplified measurements using an EDFA, but in general, depends on the device that is being measured.

6.2.2 Coupling Measurements

Group delay measurements were done using an optical vector network analyzer (OVA 5000 from Luna Technologies, [34]), based on the principle of swept-wavelength interferometric polarimetry [35, 36]. A mode-hop free rapidly-tunable telecommunications wavelength laser source was used along with Mach-Zehnder interferometers, polarization controllers and photodiodes to measure the four elements of the Jones matrix of the device under test (two for each polarization). A discrete Fourier transform of the raw data, followed by time-domain windowing, reveals the time-domain impulse response of the device under test. The instrument measures up to 6 ns of group delay with a wavelength resolution of 1.4 pm, which is determined by the window of the time-domain filter. The procedure used to calculate group delay from the measured transfer function, and its calibration against a known standard (e.g., acetylene gas cell) are described in [37].

To confirm that the measured group delay statistics reported here were above the detection limit of the optical vector network analyzer, measurements of the standard deviation of group delay for a 1.2 m long single-mode fiber patchcord were performed with increasing number of averaged scans, shown in the top axis of Fig. 1(a), yielding a very low intrinsic variation of 0.15 ps over a 40 nm wavelength span in the L-band. To maintain this high level of accuracy, all subsequent measurements were done with 64 averages.

Data shown in the bottom axis of Fig. 1(a) was measured when light was coupled through lensed tapered fibers, and attenuation of the amplified source was increased sequentially by using a programmable attenuator (JDS Uniphase HA9) to simulate the effect of decreased coupling efficiency, or increased insertion loss. We have verified that the attenuator, by itself, does not change the standard deviation of the measured group delay, i.e., the noise statistics. In fact, it is well-known that attenuated Poisson or Bose-Einstein distributions remain Poisson or Bose-Einstein distributions, respectively [38]. As can be seen, the standard deviation of the measured GD starts to increase once the received power decreases below 10 nW. This is similar to the degradation of the bit error rate in a fiber optic communication link once the received power drops below the noise floor.

For purposes of this discussion, we assume that a standard avalanche photodiode (APD) is used for detection, and that a signal-to-noise ratio of unity is the minimum threshold to measure GD reliably. We can thus attribute the flat ŞfloorŤ at the higher power levels to the effects of the photoreceiver electronics noise, with a root-mean-squared equivalent input noise of the electronic amplifier circuitry of $\langle i_{\text{amp}} \rangle_{\text{rms}} = 200\,\text{nA}$, and photoreceiver bandwidth $\Delta f_{\text{sig}} = 2$ GHz. These values are similar to those of a 2.5 Gbps APD receiver, for example, from Archcom Tech. (AC6522 Series), which has a responsivity of 0.9 A/W and an equivalent input noise current density of 5 pA/$\sqrt{\text{Hz}}$. In earlier published work using the same type of instrument [39], this noise floor was indeed attributed to electronic amplifier noise, rather than laser noise, shot noise or thermal noise.

6.2.3 Amplified Waveguide Measurements

Now, we consider optically amplified measurements of GD of a silicon waveguide chip, using the experimental setup shown in Fig. 2(a). Chips were fabricated at the IBM Microelectronics Research Laboratory using a CMOS compatible process on 200 mm SOI wafers. The waveguides are single-mode (TE polarization, with the electric field parallel to the plane of the chip), with transverse dimensions approximately $0.50\ \mu\text{m} \times 0.22\ \mu\text{m}$. The group index of the waveguides is measured to be $n_{\text{g}} = 4.25$ over the range of wavelengths used in this measurement.

The output of the tunable laser (average power $200\ \mu\text{W}$) is directly input to the EDFA which is used in the saturation regime (output power +18 dBm). In order to cover the range of wavelengths spanned by the tunable laser (1530 to 1610 nm), the EDFA actually consists of two EDFAs in parallel, with a splitter at the input: a C-band EDFA, with 200 mA of drive current to the pump laser diode, and an L-band EDFA with 700 mA of drive current.

Similar to Fig. 1(a), Fig. 1(b) shows the increase of measured GD ripple of a 4.15 cm waveguide as the insertion loss is increased. The waveguide loss is -1.5 dB/cm, measured by comparing the insertion loss of four waveguides of different lengths. By extrapolating these measurements to a null-length waveguide, the coupling efficiency is estimated to be -15 dB for the combination of input and output couplers. So as to have

the least perturbative effect on the noise contribution of the waveguide itself, the effects of increasingly worse coupling efficiencies are simulated by increasing the loss setting on the programmable attenuator, rather than adjusting the tapered fibers, which could possibly couple to a higher-order optical mode.

There are several reasons for using a saturated amplifier immediately after the tunable laser source, rather than a higher-gain unsaturated amplifier after the chip:

1. With pre-amplification, a rapidly-tunable (the tuning speed of the laser is 70 nm/s) narrow-band optical band-pass filter is not needed after the EDFA, since a interferometric detection scheme is used, and the ASE is suppressed effectively, and further attenuated by the coupling and insertion losses of the chip before reaching the photoreceiver,

2. The noise figure of the amplifier is possibly lowered, or at least not substantially worsened [40, 41], in the gain-compressed regime, and

3. Since the input power to the EDFA is maintained constant as the laser tunes in wavelength, the amplifier remains in the same operating condition, and contributes more or less the same ASE noise versus wavelength. In contrast, if the EDFA was used after a chip consisting of, e.g., a wavelength-selective filter with 30 dB contrast in the transfer function, the amplifier would see 30 dB variations in the input power as the wavelength was scanned, and both its output power and noise characteristics could vary, depending on the tuning speed of the laser.

We have verified, as shown in Fig. 2(b), that there is only a small penalty, of less than 1 picosecond, in the measurement of group delay due to the addition of the EDFA. This can easily be neglected in the measurement of photonic devices whose intrinsic group delay ripple exceeds this noise penalty.

In contrast, the benefit of using an EDFA to boost the detector signal power of a poorly-coupled chip is considerable. Fig. 3(a) shows the benefits of using optical amplification to boost the detected power at the output of a 4.15 cm waveguide. Measurements that were previously “lost” at detected power levels as low as 0.5 nW, which resulted in significantly higher noise in GD measurement, were successfully “brought back” to the low noise regime.

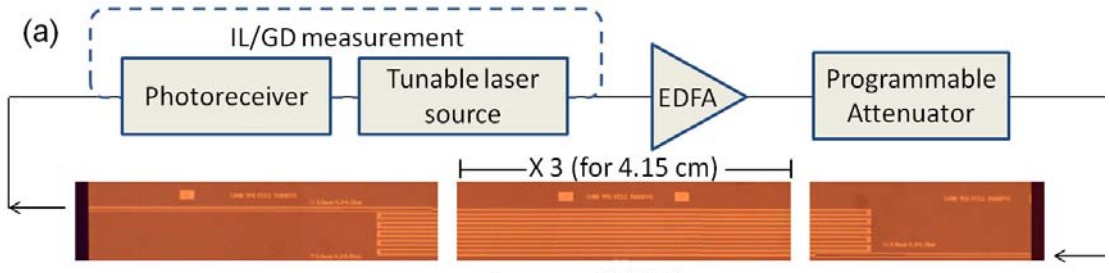

(b)

Averaged STD(τ)

	No EDFA	EDFA	Δ
C-Band	6.71 (ps)	7.09 (ps)	0.38 (ps)
L-Band	7.05 (ps)	7.19 (ps)	0.14 (ps)

Figure 6.17: (a) Light was coupled on and off the chip using a pair of lensed tapered optical fibers mounted on piezoelectrically actuated alignment stages. As in Fig. 1, the programmable attenuator setting was increased in steps of 10 dB to simulate the effect of decreased coupling efficiency. (b) Table of of the averaged GD ripple increase, as a consequence of using the EDFA.

It is important to note that both the measurement speed and the measured group delay statistics are unaffected. Fig. 3(b) shows the probability distribution, P, of the measured group delay in the unamplified and amplified measurements at the same level of net insertion loss. A more detailed discussion of the noise performance of the measurement system will be subject of the next section.

Fig. 4 shows the measured amplitude and group delay spectral measurements of a coupled-resonator optical waveguide (CROW) [25]. Note that while much of the amplitude response can be measured without amplification, the measurement of group delay benefits considerably from amplification. In particular, the unamplified insertion loss measurement shows peaks and valleys that mostly line up, versus wavelength, with the amplified measurement, but the dynamic range is clearly compressed by the noise floor at -60 dB. Adding the EDFA to the setup raises the noise floor by a few dB, as seen in the stop-band of the filter response, but significantly improves the accuracy of the dynamic range, and greatly improves the precision of the measurement of group delay.

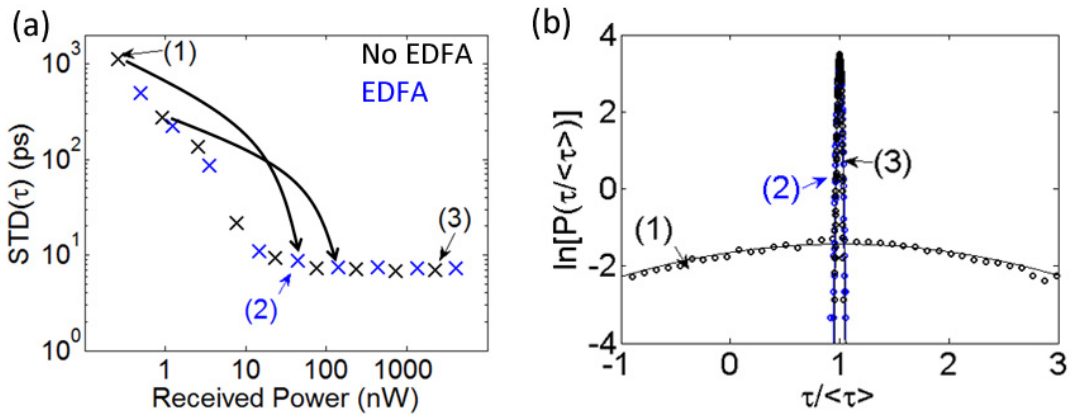

Figure 6.18: (a) Improvement in the standard deviation and of measured group delay, i.e. the group delay ripple, as a consequence of using the EDFA to boost the detected signal power. (b) Histograms of the normalized group delay $\hat{\tau} \equiv \mathrm{GD}/\langle \mathrm{GD} \rangle$, in three cases: (1) un-amplified measurement at 0.5 nW, (2) which is then boosted, using an EDFA, to 20 nW, and (3) compared with a measurement that was neither amplified nor attenuated. The comparison shows that amplification is successful at measuring the correct group delay ripple statistics of a waveguide that would otherwise be too lossy to measure accurately.

6.2.4 Discussion

Because of the presence of an optical amplifier in the signal path, there is a noise component to the detector output current. We refer to the diagram in Fig. 2(a). Under typical power levels as described earlier, the only significant source of the amplifier-added noise is the ASE-signal beat noise, and the mean-squared current that arises from this contribution to the total photocurrent is

$$\langle {i_{\text{ASE-signal}}}^2 \rangle = 4R^2 S N_{\text{A}} \tag{6.2}$$

where $R = e\eta/(h\nu)$ is the responsivity (A/W) of the photoreceiver,

$$S = GLP_{\text{in}} \tag{6.3}$$

is the optical power of the signal component of the light that is incident on the photodetector, and (Haus p.337)

$$N_{\text{A}} = GL\, h\nu\, \Delta f_{\text{sig}} (\text{NF}_{\text{ASE}} - 1) \tag{6.4}$$

is the optical power of the amplified spontaneous emission added by the amplifier, in terms of the quantity $(\text{NF}_{\text{ASE}} - 1)$, which is the excess noise figure of the amplifier. We

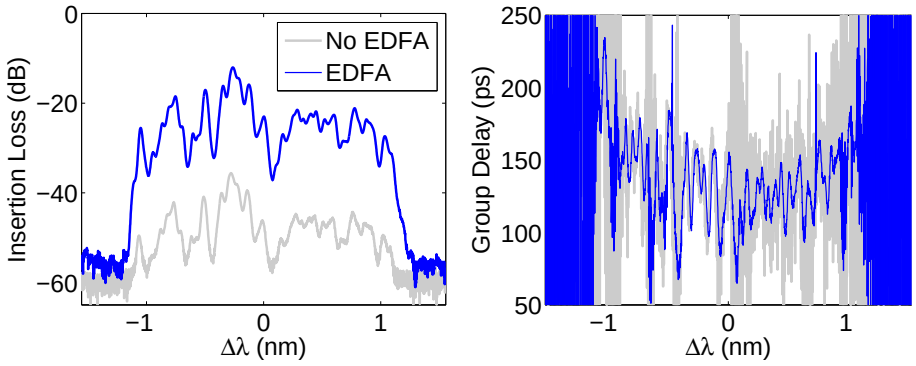

Figure 6.19: Example of measurements of (a) the amplitude and (b) the group delay versus wavelength of a silicon microring coupled-resonator optical filter which has a delay of about 135 ps at band-center [25]. Notice that poor coupling through the device affects the amplitude and group delay response differently. Whereas the unamplified insertion loss measurement is mostly spectrally accurate but dynamically compressed, i.e., the peaks and valleys line up with the more accurate amplified measurement versus wavelength, meaningful measurements of group delay are nearly impossible without amplification, in accordance with Fig. 3.

assume, in keeping with the experimental results reported here, that only one polarization state of light (TE polarized) is transmitted through the device; otherwise, Eq. (6.4) should be multiplied by 2. We also assume that the optical signal bandwidth Δf_{sig} in the expression for N is also the electronic bandwidth in the photodetector [42].

$$(GL) \leq \frac{\langle i_{\text{amp}} \rangle_{\text{rms}}}{\left[4R^2 h\nu\, \Delta f_{\text{sig}} (\text{NF}_{\text{ASE}} - 1)\, P_{\text{in}}\right]^{1/2}} \tag{6.5}$$

At equality between the left-hand side and right-hand side of Eq. (6.5), the ASE-signal beat noise equals the intrinsic noise of the amplifier electronics. Increasing the amplifier gain further, so that the beat noise term grows above the electronics noise, does not improve the signal-to-noise (SNR) ratio any further, but does not alter it, since signal power and noise variance both scale with $(GL)^2$.

There is no obvious benefit to significantly larger gain. Eq. (6.5) can be numerically evaluated to solve for the amplification level which should be used, given the laser power into the EDFA, P_{in}, and the estimated loss, L, e.g., -15 dB for a single-mode waveguide delay line with no resonant spectral features, or -50 dB for the resonance dip of a microring resonator or optical filter.

As stated before, we assume $\Delta f_{\text{sig}} = 2$ GHz and $R = 1$. Since the EDFAs are used in the saturation regime, the gain G is compressed,

$$G = G_0 \ \exp\left(-\frac{G-1}{G}\frac{P_{\text{out}}}{P_{\text{sat}}^{\{\text{C,L}\}}}\right) \tag{6.6}$$

where G_0 is the nominal (unsaturated) gain, $P_{\text{sat}}^{\text{C}} = 16.5\,\text{dBm}$ and $P_{\text{sat}}^{\text{L}} = 18.23\,\text{dBm}$ are the saturation powers of the C-band and L-band EDFAs used in the measurement. The excess noise of the amplifier in the saturated regime is also function of G, but does not vary much over the typical range of values used here, and is conservatively taken to be a constant equal to 6 dB.

We consider two examples based on evaluating Eq. (6.5), assuming a tunable laser power of $P_{\text{in}} = 0.1$ mW. For a long single-mode waveguide delay line, with small variations in insertion loss versus wavelength, a typical value of $L = -20$ dB, we need $G \geq 15.6$ dB to reach the beat-noise limited regime. This can be achieved by a saturated EDFA as long as the gain compression is not excessive.

On the other hand, to measure a microring resonator add-drop filter on resonance, we may encounter a typical value of $L = -40$ dB (on resonance), and we need $G \geq 36$ dB to reach the beat-noise limited regime. This is beyond the regime of saturated EDFAs, and in any case, such an amplifier would boost the optical power levels input to the chip to nearly 1 W, i.e., into the nonlinear regime of silicon waveguides. Thus, the measurement of the valleys in the pre-amplified configuration regime must be in the detector-noise limited regime. This has not been a limitation for the measurements reported in this paper, but recent studies of the statistics of light transmission and back-reflection in waveguides may be influenced by which noise regime happens to describe the measurements, when pushed to more sensitive limits in the future [43, 44, 45].

As stated before, the benefit to using saturated EDFAs before the chip, rather than an unsaturated EDFA after the chip, is that the measured variations and noise statistics of insertion loss or group delay can be conclusively attributed to the device under test, since the input light to the EDFA, directly from the tunable laser, does not vary in intensity. For measurements focused on the ripple statistics of waveguides or filters, this is an important benefit to pre-amplification.

Post-chip amplification may be used if high values of gain are required, e.g., in photonic crystal structures [46, 47], or the critical-coupling slope of a microring res-

onator [48]. In such cases, the spectral range of the measurements should be limited in order to prevent the amplifier from saturating as the shoulders of the transmission nulls are encountered. The large variation in input power to the EDFA would introduce nonlinearity in the measured transfer function, and also change the noise properties of the measured group delay.

For such applications, the modulation-phase shift method, based on a stepped wavelength scan of the tunable laser along with an RF modulation source and detection by an electronic vector network analyzer, may be more versatile. However, the data acquisition time is greatly increased, from a few seconds to many minutes, to achieve comparable accuracy [22].

6.3 Summary

Infrared imaging is a powerful technique for probing photonic circuits. By utilizing the intensity enhancement, a microring resonator can be measured that in practice would have no drop ports. The method consists of taking sequential images of a photonic circuit that directly correspond with a step scan of a tunable laser source. This method was also used to simultaneously measure the response of 10 rings at their drop ports from a single data set.

Further, the benefits of optical amplification in the rapid measurement of group delay (GD) of chip-scale photonic devices with high insertion loss was shown. By using an EDFA before the chip, in the saturation regime, we have ensured that the amplifier itself does not contribute noticeably to the measured GD ripple at less than the picosecond scale. Filtering of the amplified spontaneous emission was not needed, and there is no penalty to the measurement speed of the instrument. The rapid speed of the tunable laser (70 nm/s) used in the Luna OVA5000 enables almost video-rate measurements of group delay of a nanophotonic device.

Measurements that were previously “lost” at detected power levels as low as 0.5 nW, which previously resulted in significantly higher noise in GD measurement, were successfully “brought back” to the low noise regime. These group delay measurements are at the lowest-reported power values for any photonic chip to date, and

further improvement into the low-power regime may enable rapid and routine delay and dispersion measurements with sub-picosecond accuracy of novel nanophotonic devices [46, 49, 25] without having to worry, at least initially, about optimizing the coupling into and out of the devices.

References

[1] A. F. Oskooi, D. Roundy, M. Ibanescu, P. Bermel, J. D. Joannopoulos, and S. G. Johnson, "Meep: A flexible free-software package for electromagnetic simulations by the fdtd method," *Computer Physics Communications*, vol. 181, p. 687Ű702, 2010.

[2] J. E. Heebner, P. Chak, S. Pereira, J. E. Sipe, and R. W. Boyd, "Distributed and localized feedback in microresonator sequences for linear and nonlinear optics," *J. Opt. Soc. Am. B*, vol. 21, p. 1818, 2004.

[3] S. T. Chu, B. E. Little, W. Pan, T. Kaneko, S. Sato, and Y. Kokubun, "An eight-channel add-drop filter using vertically coupled microring resonators over a cross grid," *IEEE Photon. Technol. Lett.*, vol. 11, p. 691, 1999.

[4] S. Mookherjea and M. A. Schneider, "The nonlinear microring add-drop filter," *Optics Express*, vol. 16, p. 15130, 2008.

[5] V. Aggarwal and S. Aditya, "Measurement of loss and mode-profile for integrated-optic waveguides using a camera," *Proc. SPIE*, vol. 4579, p. 310, 2001.

[6] S. J. McNab, N. Moll, and Y. A. Vlasov, "Ultra-low loss photonic integrated circuit with membrane-type photonic crystal waveguides," *Optics Express*, vol. 11, p. 2927, 2003.

[7] J. Topolancik, F. Vollmer, R. IIic, and M. Crescimanno, "Out-of-plane scattering from vertically asymmetric photonic crystal slab waveguides with in-plane disorder," *Optics Express*, vol. 17, pp. 12470–12480, 2009.

[8] S. Mookherjea, J. S. Park, S. H. Yang, and P. R. Bandaru, "Localization in silicon nanophotonic slow-light waveguides," *Nature Photonics*, vol. 2, p. 90, 2008.

[9] N. L. Thomas, V. Zabelin, R. Houdre, M. V. Kotlyar, and T. F. Krauss, "Influence of residual disorder on the anticrossing of bloch modes probed in k space," *Phys. Rev. B*, vol. 78, p. 125301, 2008.

[10] G. Roelkens, D. V. Thourhout, and R. Baets, "High efficiency grating coupler between silicon-on-insulator waveguides and perfectly vertical optical fibers," *Optics Letters*, vol. 32, p. 1495, 2007.

[11] S. Xiao, M. H. Khan, H. Shen, and M. Qi, "Modeling and measurement of losses in silicon-on-insulator resonators and bends," *Optics Express*, vol. 17, pp. 10553–10561, 2007.

[12] F. Xia, L. Sekaric, and Y. A. Vlasov, "Mode conversion losses in silicon-on-insulator photonic wire based racetrack resonators," *Optics Express*, vol. 14, pp. 3872–3886, 2006.

[13] G. H. V. Rhodes, B. B. Goldberg, M. S. U. abd S. T. Chu, and B. E. Little, "Internal spatial modes in glass microring resonators," *IEEE J. Sel. Top. Quantum Electron.*, vol. 6, p. 46, 2000.

[14] K. Srinivasan, P. E. Barclay, M. Borselli, and O. Painter, "Optical-fiber-based measurement of an ultrasmall volume high-q photonic crystal microcavity," *Phys. Rev. B*, vol. 70, p. 081306(R), 2004.

[15] G. Gupta, Y. H. Kuo, H. Tazawa, W. Steier, A. Stapleton, and J. D. O'Brien, "Analysis and demonstration of coupling control in polymer microring resonators using photobleaching," *Applied Optics*, vol. 48, p. 5324, 2009.

[16] F. Grillot, L. Vivien, S. Laval, D. Pascal, and E. Cassan, "Size influence on the propagation loss induced by sidewall roughness in ultrasmall soi waveguides," *IEEE Photon. Technol. Lett.*, vol. 16, p. 1661, 2004.

[17] E. G. Neumann and R. Nat, "Curved dielectric optical waveguides with reduced transition losses," *IEE Proc., Pt. H*, vol. 129, pp. 278–280, 1983.

[18] J. P. R. L. F. P. Payne, "A theoretical analysis of scattering loss from planar optical waveguides," *Opt. Quantum Electron.*, vol. 26, pp. 977–986, 1994.

[19] C. Scheerer, C. Glingener, G. Fischer, M. Bohn, and W. Rosenkranz, "System impact of ripples in grating group delay," in *Transparent Optical Networks, 1999. International Conference on*, pp. 33 –36, 1999.

[20] J. Mok, J. Blows, and B. Eggleton, "Investigation of group delay ripple distorted signals transmitted through all-optical 2R regenerators," *Opt. Express*, vol. 12, no. 19, pp. 4411–4422, 2004.

[21] P. Q. Thai, A. Alphones, and D. Lim, "Limitations by group delay ripple on optical beam-forming with chirped fiber grating," *Lightwave Technology, Journal of*, vol. 27, pp. 5619 –5625, dec.15, 2009.

[22] R. Hui and M. O'Sullivan, *Fiber Optic Measurement Techniques*. San Diego: Academic Press, 2009.

[23] M. R. Bell, M. Mazilu, S. J. White, T. J. Karle, T. F. Krauss, and A. Miller, "High resolution, dispersion measurement of photonic waveguides," in *Conference on Lasers and Electro-Optics/Quantum Electronics and Laser Science Conference and Photonic Applications Systems Technologies*, p. JTuD37, Optical Society of America, 2006.

[24] M. Sagues, M. Pérez, and A. Loayssa, "Measurement of polarization dependent loss, polarization mode dispersion and group delay of optical components using swept optical single sideband modulated signals," *Opt. Express*, vol. 16, no. 20, pp. 16181–16188, 2008.

[25] M. L. Cooper, G. Gupta, W. M. J. Green, S. Assefa, F. Xia, Y. A. Vlasov, and S. Mookherjea, "235-ring coupled-resonator optical waveguides," in *Lasers and Electro-Optics (CLEO) and Quantum Electronics and Laser Science Conference (QELS), 2010 Conference on*, p. CTuHH3, 16-21 2010.

[26] A. R. Mickelson, N. R. Basavanhally, and Y. C. Lee, *Optoelectronic Packaging*. New York: Wiley-Interscience, 1997.

[27] T. Shoji, T. Tsuchizawa, T. Watanabe, K. Yamada, and H. Morita, "Spot-size converter for low-loss coupling between 0.3- mu;m-square si wire waveguides and single-mode fibers," in *Lasers and Electro-Optics Society, 2002. LEOS 2002. The 15th Annual Meeting of the IEEE*, vol. 1, pp. 289–290, 2002.

[28] D. Taillaert, H. Chong, P. I. Borel, L. H. Frandsen, R. M. De La Rue, and R. Baets, "A compact two-dimensional grating coupler used as a polarization splitter," *IEEE Photonics Technology Letters*, vol. 15, no. 9, pp. 1249–1251, 2003.

[29] V. R. Almeida, R. R. Panepucci, and M. Lipson, "Nanotaper for compact mode conversion," *Optics Letters*, vol. 28, no. 15, pp. 1302–1304, 2003.

[30] F. Van Laere, G. Roelkens, M. Ayre, J. Schrauwen, D. Taillaert, D. Van Thourhout, T. Krauss, and R. Baets, "Compact and highly efficient grating couplers between optical fiber and nanophotonic waveguides," *J. Lightwave Technol.*, vol. 25, no. 1, pp. 151 –156, 2007.

[31] Y. A. Vlasov and S. J. McNab, "Losses in single-mode silicon-on-insulator strip waveguides and bends," *Opt. Express*, vol. 12, pp. 1622–1631, 2004.

[32] F. Grillot, L. Vivien, S. Laval, and E. Cassan, "Propagation loss in single-mode ultrasmall square silicon-on-insulator optical waveguides," *J. Lightwave Technol.*, vol. 24, no. 2, pp. 891–896, 2006.

[33] E. Säckinger, *Broadband Circuits for Optical Fiber Communication*. New Jersey: John Wiley & Sons, Inc., 2005.

[34] L. Technologies, "Optical vector analyzer (model 5000)." http://www.lunatechnologies.com/products/ova/files/OVA5000_Data_Sheet.

[35] B. Heffner, "Deterministic, analytically complete measurement of polarization-dependent transmission through optical devices," *IEEE Photon. Technol. Lett.*, vol. 4, no. 5, pp. 451 –454, 1992.

[36] M. Froggatt, E. Moore, and M. Wolfe, "Interferometric measurement of dispersion in optical components," in *Optical Fiber Communication Conference and Exhibit, 2002. OFC 2002*, pp. 252 – 253, 17-22 2002.

[37] D. K. Gifford, B. J. Soller, M. S. Wolfe, and M. E. Froggatt, "Optical vector network analyzer for single-scan measurements of loss, group delay, and polarization mode dispersion," *Appl. Opt.*, vol. 44, no. 34, pp. 7282–7286, 2005.

[38] H. A. Haus, *Electromagnetic Noise and Quantum Optical Measurements*. Berlin: Springer, 2000.

[39] B. J. Soller, D. K. Gifford, M. S. Wolfe, and M. E. Froggatt, "High resolution optical frequency domain reflectometry for characterization of components and assemblies," *Optics Express*, vol. 13, no. 2, pp. 666–674, 2005.

[40] M. Movassaghi, M. Jackson, V. Smith, and W. Hallam, "Noise figure of erbium-doped fiber amplifiers in saturated operation," *J. Lightwave Technol.*, vol. 16, no. 5, pp. 812 –817, 1998.

[41] K. Bertilsson, P. Andrekson, and B. Olsson, "Noise figure of erbium doped fiber amplifiers in the saturated regime," *IEEE Photon. Technol. Lett.*, vol. 6, no. 2, pp. 199 –201, 1994.

[42] A. Yariv, *Optical Electronics in Modern Communications*. New York: Oxford, fifth ed., 1997.

[43] B. Wang, S. Mazoyer, J. P. Hugonin, and P. Lalanne, "Backscattering in monomode periodic waveguides," *Phys. Rev. B*, vol. 78, p. 245108, Dec 2008.

[44] S. Mazoyer, P. Lalanne, J. Rodier, J. Hugonin, M. Spasenović, L. Kuipers, D. Beggs, and T. Krauss, "Statistical fluctuations of transmission in slow light photonic-crystal waveguides," *Opt. Express*, vol. 18, no. 14, pp. 14654–14663, 2010.

[45] F. Morichetti, A. Canciamilla, C. Ferrari, M. Torregiani, A. Melloni, and M. Martinelli, "Roughness induced backscattering in optical silicon waveguides," *Phys. Rev. Lett.*, vol. 104, p. 033902, Jan 2010.

[46] J. S. Foresi, P. R. Villeneuve, J. Ferrera, E. R. Thoen, G. Steinmeyer, S. Fan, J. D. Joannopoulos, L. C. Kimerling, H. I. Smith, and E. P. Ippen, "Photonic-bandgap microcavities in optical waveguides," *Nature*, vol. 390, pp. 143–145, 1997.

[47] S. Y. Lin, E. Chow, V. Hietala, P. R. Villeneuve, and J. D. Joannopoulos, "Experimental demonstration of guiding and bending of electromagnetic waves in a photonic crystal," *Science*, vol. 282, pp. 274–276, 1998.

[48] A. Yariv, "Coupled-mode theory for guided-wave optics," *Journal of Quantum Elec.*, vol. 9, pp. 919 –933, 1973.

[49] J. C. Prangsma, D. van Oosten, R. J. Moerland, and L. Kuipers, "Increase of group delay and nonlinear effects with hole shape in subwavelength hole arrays," *New Journal of Physics*, vol. 12, p. 013005, 2010.

1. Chapter 6 contains material published in:

   M. L. Cooper, G. Gupta, J. S. Park, M. A. Schneider, I. B. Divliansky, and S. Mookherjea, “Quantitative infrared imaging of SOI microring resonators,” *Optics Letters*, 35, 2010.

   The dissertation author was the primary author of this paper.

2. Chapter 6 contains material submitted to *Photonics Technology Letters*:

   M. L. Cooper, Mark A. Schneider, Greeshma Gupta, and Shayan Mookherjea, “Filter-less amplification for rapid swept-wavelength interferometric measurement of silicon nanophotonic waveguide group delay statistics,” submitted to *Photonics Technology Letters*.

   The dissertation author was the primary author of this paper.

A Graphical User Interfaces

Numerous graphical user interfaces were developed to facilitate the research presented in this dissertation, all of which were written in Matlab. Listed here are among the few that were indispensable to its development.

A.1 Efield

Solves for the exact eigenvectors (modes) and eigenvalues (propagation constants) of high-index contrast waveguides. This program was used extensively for the results presented in Chapter 4. Further, it was used for the dispersion engineering calculations in Chapter 3.

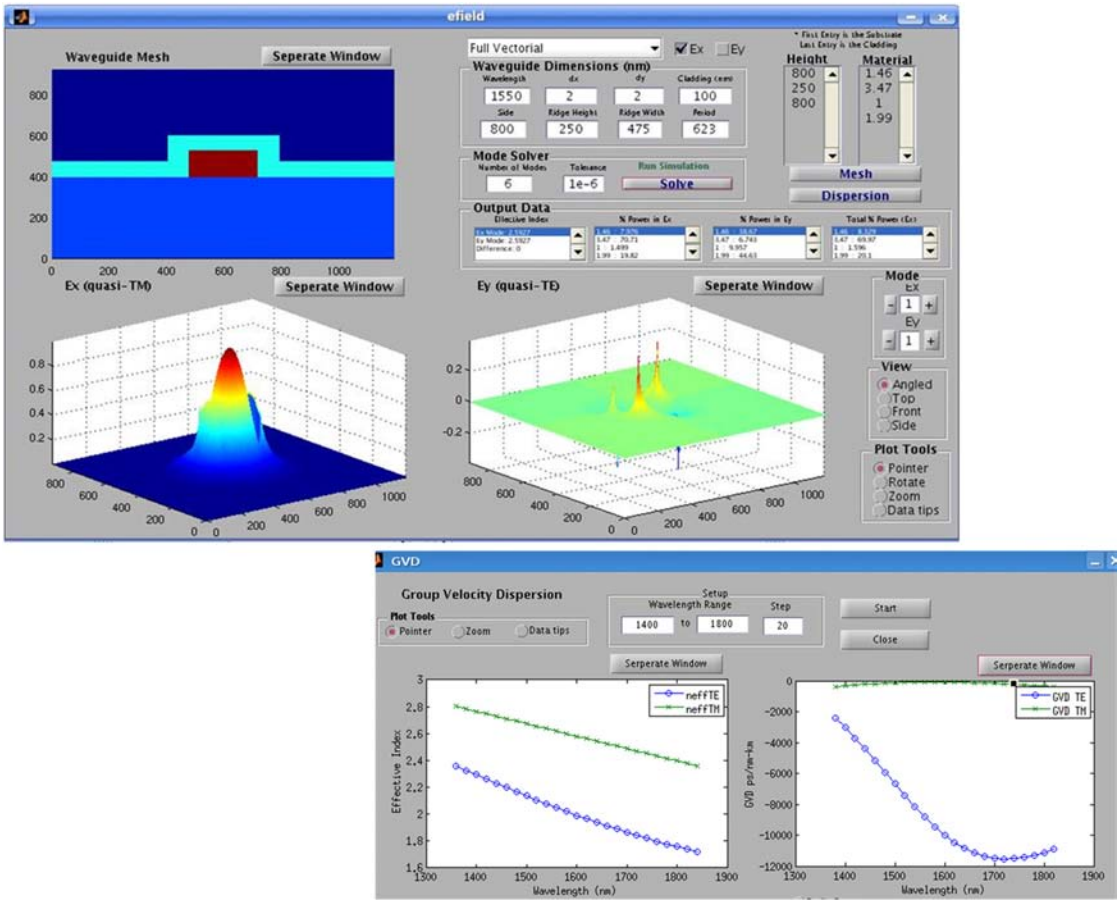

Figure A.1: Users input waveguide (array or single) device dimensions, materials, wavelength, desired discretization, and program solves for the transverse eigenvectors and eigenvalues, (electric field and propagation constant), with Dirichlet boundary conditions. Also calculates waveguide group index, field concentration, and group velocity dispersion with built in Sellmeier equations for Oxide, Silicon Nitride, PMMA, and Silicon. For a mathematical description, see Section 3.1

A.2 IRCAM and LScan

Synchronize a tunable laser source with an infrared camera for extracting micro-ring resonator parameters from wavelength resolved infrared imaging. This program was used extensively for the results presented in Chapter 5, and also published in, M. L. Cooper, et al., "Quantitative infrared imaging of SOI microring resonators," *Optics Letters*, 35, (2010)—in which the optics letters manuscript received a spotlight from OSA with commentary from Dr. John E. Heebner (March 2010).

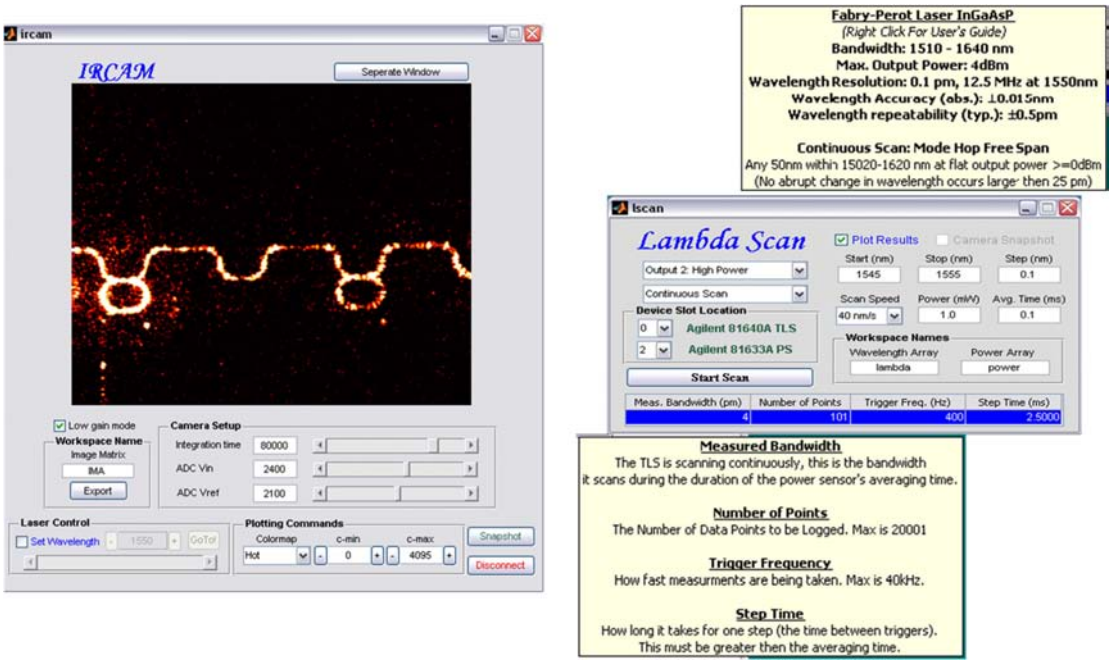

Figure A.2: Users input slot location of the tunable laser source (Agilent 81640A), power sensor (Agilent 81633A or Agilent 81634B), and desired wavelength range, step size, integration time, input power, scan speed, and scan type (step or continuous). The program then runs the scan and returns wavelength and power data into an array in Matlab. Has the option in step scan to record 12-bit images at each wavelength, follow the TLS with an optical tunable filter (Santec OTF-910 (RS232)) for use with an inline EDFA, program Piezo controllers (RS232) for micron scale position vs. wavelength scan, and send the user a text message to his cell phone when scan completes.

A.3 SNIPER26

This program was used to facilitate analyzing over 5 Gb of data on the IBM wafers, the results of which were presented in Chapter 2.

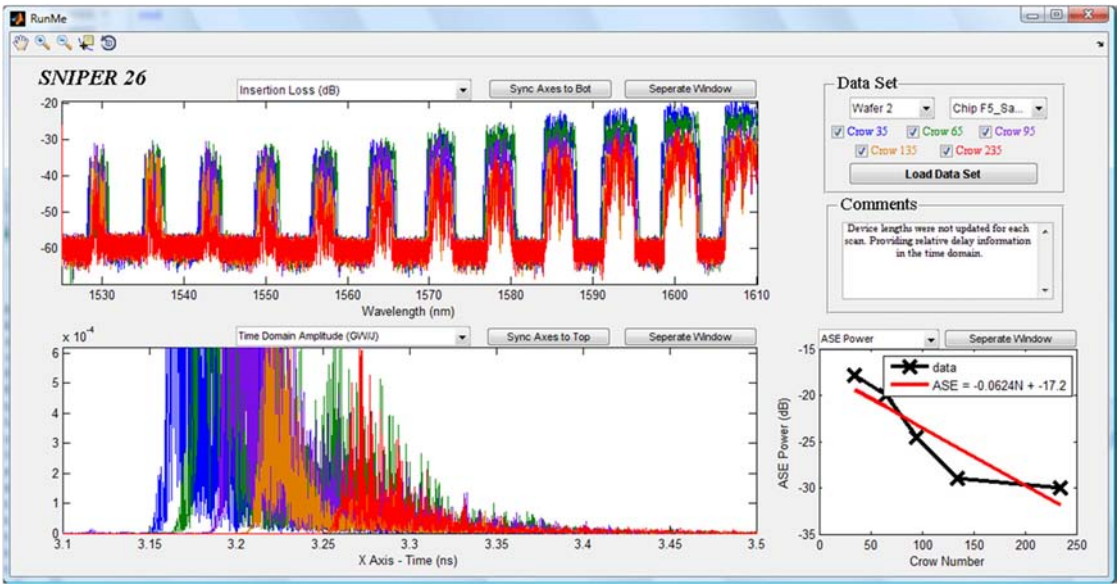

Figure A.3: The program facilitates analyzing >5 Gb of spectra data of 22 chips each with 5 sets of coupled resonator optical waveguides, returned from the LUNA OVA. It also displays user comments noted while the devices were being measured, the amplified spontaneous emission source (ASE) measurements, and the device length of each measurement.

B Final notes

I learned this, at least, by my experiment: that if one advances confidently in the direction of his dreams, and endeavours to live the life which he has imagined, he will meet with a success unexpected in common hours. He will put some things behind, will pass an invisible boundary; new, universal, and more liberal laws will begin to establish themselves around and within him; or the old laws be expanded, and interpreted in his favor in a more liberal sense, and he will live with the license of a higher order of beings. In proportion as he simplifies his life, the laws of the universe will appear less complex, and solitude will not be solitude, nor poverty poverty, nor weakness weakness. If you have built castles in the air, your work need not be lost; that is where they should be. Now put the foundations under them.

—Henry David Thoreau, “Walden,” 1854